eISSN 2500-0632

МИСИС
УНИВЕРСИТЕТ

Mining Science and Technology

Горные науки и технологии

Vol. Том 11 № 1
2026

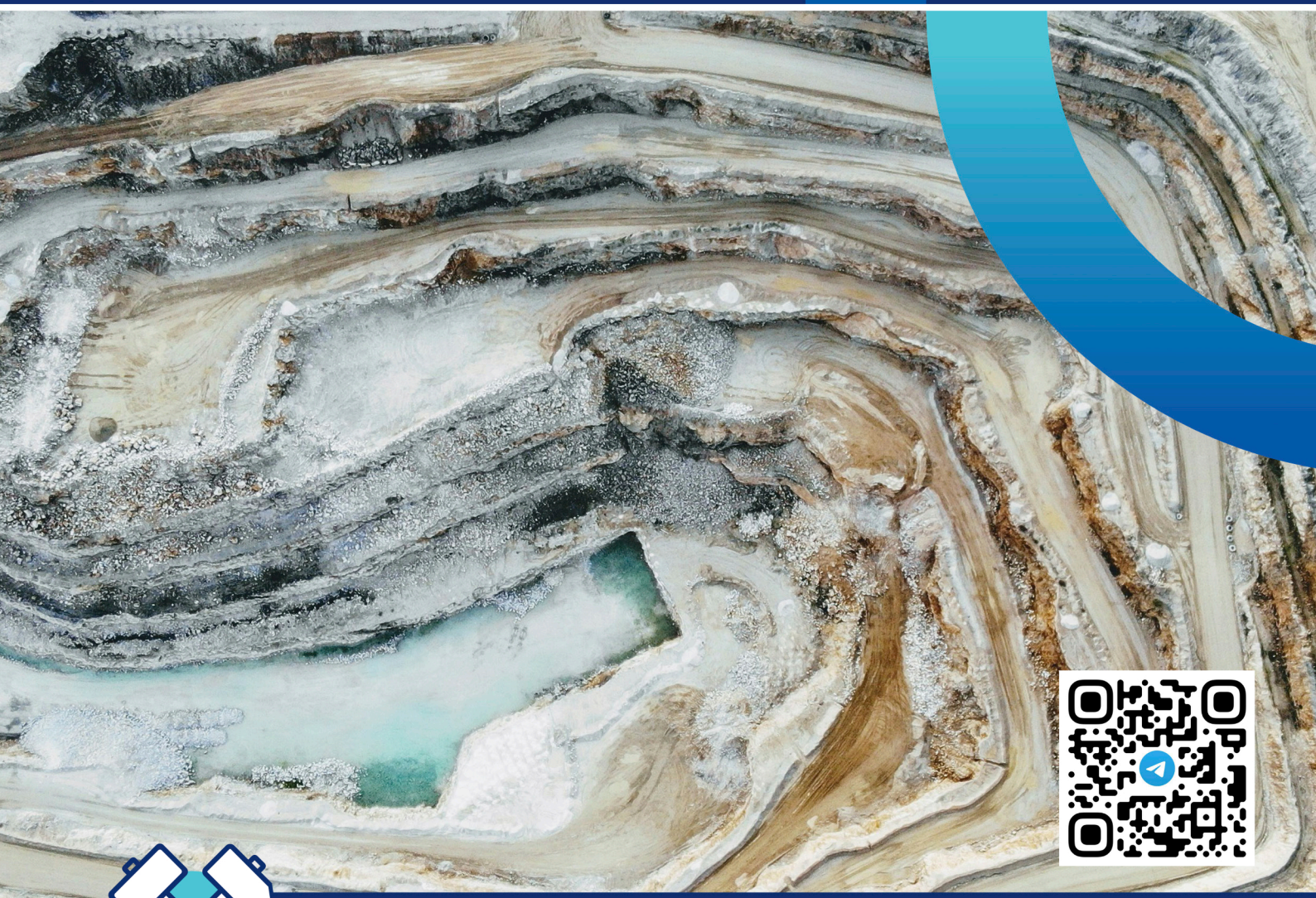

https://mst.misis.ru/

https://t.me/MinSciTech

Photo by Dion Beetson on Unsplash

MINING SCIENCE AND TECHNOLOGY (Russia)

Горные науки и технологии

SCIENTIFIC AND PRACTICAL E-JOURNAL

eISSN 2500-0632

2026
Vol. 11, no. 1

https://mst.misis.ru/

Activities of the *Mining Science and Technology (Russia) (Gornye nauki i tekhnologii)* international journal are aimed at developing international scientific and professional cooperation in the field of mining.
The journal target audience comprises researchers, specialists in the field of mining, representatives of academic and professional communities.
The journal publishes original papers describing research findings, experience in the implementation of projects in mining industry, review publications.
The journal seeks to develop interdisciplinary areas that contribute to progress in mining, for example, technological and environmental safety, project organization and management in mining industry, development of territories, legal aspects of natural resource use, and other areas studied by researchers and practitioners. The journal always welcomes new developments. Papers are accepted in English or Russian.

QUARTERLY

FOUNDED in 2016

REGISTRATION
The journal science and applied research journal is registered by the Federal Service for Communication, IT and Mass Communication Control on August 10, 2015.
Registration Certificate E-No. ФС77-62652

INDEXATION
Scopus, CAS, EBSCO, DOAJ, РИНЦ, ВИНИТИ РАН, Dimensions, BASE, J-Gate, Jisc Library Hub Discover.

FOUNDER AND PUBLISHER

MISIS UNIVERSITY University of Science and Technology MISIS

CONTACT
4 Leninsky Prospect, Moscow 119049, Russian Federation
Phone: +7 (495) 955-00-77
e-mail: send@misis.ru

ГОРНЫЕ НАУКИ И ТЕХНОЛОГИИ
Mining Science and Technology (Russia)
ЭЛЕКТРОННЫЙ НАУЧНО-ПРАКТИЧЕСКИЙ ЖУРНАЛ

eISSN 2500-0632
2026
Т. 11, № 1
https://mst.misis.ru/

Деятельность научно-практического журнала «Горные науки и технологии» (Mining Science and Technology (Russia)) направлена на развитие международного научного и профессионального сотрудничества в области горного дела.
Целевая аудитория журнала – исследователи, специалисты в области горного дела, представители академического и профессионального сообществ.
В журнале публикуются оригинальные статьи, описывающие результаты исследований, опыт реализации проектов в горнопромышленном комплексе, обзорные публикации.
Журнал стремится развивать такие междисциплинарные направления, как технологическая и экологическая безопасность, организация и управление проектами в горной промышленности, развитие территорий, правовые аспекты использования природных ресурсов и другие, которые способствуют прогрессу в горном деле и реализуются исследователями и практиками.

ПЕРИОДИЧНОСТЬ 4 раза в год

ОСНОВАН в 2016 году

РЕГИСТРАЦИЯ
Зарегистрирован Федеральной службой по надзору в сфере связи, информационных технологий и массовых коммуникаций 10 августа 2015 года.
Свидетельство о регистрации Эл № ФС77-62652.

ИНДЕКСИРОВАНИЕ
Scopus, CAS, EBSCO, DOAJ, РИНЦ, ВИНИТИ РАН, Dimensions, BASE, J-Gate, Jisc Library Hub Discover.

OPEN ACCESS Журнал открытого доступа.

УЧРЕДИТЕЛЬ И ИЗДАТЕЛЬ
МИСИС Университет науки и технологий МИСИС

АДРЕС УЧРЕДИТЕЛЯ И ИЗДАТЕЛЯ
119049, г. Москва, Ленинский проспект, д. 4

КОНТАКТЫ РЕДАКЦИИ
Адрес: 119049, г. Москва, Ленинский проспект, д. 4
Телефон: +7 (495) 955-00-77
e-mail: send@misis.ru

MINING SCIENCE AND TECHNOLOGY (Russia)
Горные науки и технологии
SCIENTIFIC AND PRACTICAL E-JOURNAL
eISSN 2500-0632
2026
Vol. 11, no. 1
https://mst.misis.ru/

CONTENTS

ГОРНЫЕ НАУКИ И ТЕХНОЛОГИИ
Mining Science and Technology (Russia)
ЭЛЕКТРОННЫЙ НАУЧНО-ПРАКТИЧЕСКИЙ ЖУРНАЛ
eISSN 2500-0632
2026
Т. 11, № 1
https://mst.misis.ru/

СОДЕРЖАНИЕ

MINERAL RESOURCES EXPLOITATION

Research paper

https://doi.org/10.17073/2500-0632-2026-02-1107
UDC 622.363.2

Recovery of barrier pillar reserves during deep potash seam mining

E.R. Kovalsky, Ch.B. Kongar-Syuryun ✉
Empress Catherine II Saint Petersburg Mining University, Saint Petersburg, Russian Federation
✉ *kongarsiuriun@gmail.com*

Abstract
Mining potash deposits at great depths is associated with increasing extraction losses. Conventional room-and-pillar mining systems that leave barrier pillars between panels prevent their subsequent recovery because of progressive stress accumulation and deterioration of excavation stability, which necessitates the development of new technological solutions. This study proposes and substantiates a mining approach for gently dipping potash seams at great depths aimed at reducing ore losses through secondary recovery of barrier pillars between panels while controlling the rock mass stress state by backfilling. The study was conducted using finite element modeling with a Mohr–Coulomb elastoplastic constitutive model. The model was calibrated against field measurements of roof subsidence for mining conditions at a depth of 1100 m. The influence of extraction thickness, chamber filling ratio, and deformation properties of backfill materials (dry fill, hydraulic fill, and cemented backfill) on the stress state of the barrier pillar was evaluated. The results show that in the absence of backfilling, stresses in the barrier pillar at the stage of ground movement stabilization exceed the geostatic stress level by more than six times, which precludes its subsequent extraction. An empirical relationship between the stress concentration factor and the properties of the backfill mass was derived, enabling the prediction of safe mining conditions. A configuration of inter-chamber pillars with variable width, increasing from the center toward the periphery, is proposed to achieve a more uniform load distribution. A method was developed for calculating the width of first-stage pillars, ensuring that the factor of safety remains above the regulatory threshold (>1). Simultaneous mining and backfilling operations limit stress buildup in the barrier pillar. This creates conditions for the safe recovery of the pillar using second-stage chambers. The proposed technology enables additional recovery of mineable reserves, does not require major modifications to the existing development layout, and allows mining waste to be used as backfill material.

Keywords
mining, potash seam, pillar, barrier pillar, backfilling, mined-out space, two-stage extraction, reserves, secondary recovery, inter-chamber pillars, numerical modeling, finite element method

For citation
Kovalsky E.R., Kongar-Syuryun Ch.B. Recovery of barrier pillar reserves during deep potash seam mining. *Mining Science and Technology* (*Russia*). 2026;11(1):5–15. https://doi.org/10.17073/2500-0632-2026-02-1107

РАЗРАБОТКА МЕСТОРОЖДЕНИЙ ПОЛЕЗНЫХ ИСКОПАЕМЫХ

Научная статья

Извлечение запасов из опорных целиков при разработке калийных пластов на больших глубинах

Е.Р. Ковальский, Ч.Б. Конгар-Сюрюн ✉
Санкт-Петербургский горный университет императрицы Екатерины II, г. Санкт-Петербург, Российская Федерация
✉ *kongarsiuriun@gmail.com*

Аннотация
Разработка калийных месторождений на больших глубинах сопровождается ростом эксплуатационных потерь полезного ископаемого. Традиционные камерные системы с оставлением опорных целиков не позволяют в дальнейшем извлекать эти запасы из-за прогрессирующего роста напряжений и потери устойчивости выработок, что определяет необходимость поиска новых технологических решений.

Исследование ставит перед собой цель – обоснование параметров технологии выемки пологих калийных пластов на больших глубинах, обеспечивающей снижение потерь руды за счет доизвлечения опорных межучастковых целиков при управлении напряженным состоянием массива с помощью закладки. Исследование выполнено на основе моделирования методом конечных элементов с использованием упруго-пластической модели Мора–Кулона. Модель откалибрована по натурным данным оседания кровли для условий глубины 1100 м. Оценено влияние вынимаемой мощности, степени заполнения камер и деформационных свойств закладочного материала (сухая, гидравлическая, твердеющая закладка) на напряженное состояние опорного целика. Установлено, что при отсутствии закладки напряжения в опорном целике к моменту стабилизации сдвижений превышают геостатический уровень более чем в 6 раз, что исключает его последующую отработку. Получена эмпирическая зависимость коэффициента концентрации напряжений от параметров закладочного массива, позволяющая прогнозировать условия безопасности ведения горных работ. Предложена конфигурация междукамерных целиков переменной ширины (увеличивающейся от центра к периферии), обеспечивающая равномерное распределение нагрузок. Разработан способ расчета ширины целиков первой очереди, при котором коэффициент запаса прочности сохраняется выше нормативного значения (>1). Одновременное ведение очистных и закладочных работ позволяет ограничить рост опасных напряжений в опорном целике, что создает условия для безопасной выемки целика камерами второй очереди. Предлагаемая технология обеспечивает дополнительное извлечение балансовых запасов, не требует коренной перестройки подготовительных выработок и способствует утилизации техногенных отходов.

Ключевые слова

добыча, калийный пласт, целик, опорный целик, закладка, выработанное пространство, двухстадийная выемка, запасы, доизвлечение запасов, междукамерные целики, моделирование, метод конечных элементов

Для цитирования

Kovalsky E.R., Kongar-Syuryun Ch.B. Recovery of barrier pillar reserves during deep potash seam mining. *Mining Science and Technology* (*Russia*). 2026;11(1):5–15. https://doi.org/10.17073/2500-0632-2026-02-1107

Introduction

Mining potash deposits becomes increasingly challenging as operations progress to greater depths, where operational losses of mineral reserves increase significantly. In global mining practice, such conditions are typically addressed using room-and-pillar mining with barrier pillars left between extraction panels [1]. However, previous attempts to reduce losses through partial extraction of pillars or reduction of their width have not yielded positive results [2–4].

Possible approaches to increasing recovery include mining the inter-chamber pillars within the panels, as well as recovery of reserves contained in the barrier pillar. However, earlier studies [5] have shown that achieving a practical reduction of losses through secondary extraction of inter-chamber pillars within the life of a mining block is almost impossible. In particular, it is difficult to ensure an acceptable time lag between the secondary extraction operations and the primary stoping activities within the panel. By the time the technological conditions allow secondary extraction to begin, the inter-chamber pillars have already entered a critical stress-strain state due to rheological deformation processes.

Observations at potash mines operating at depths of approximately 1000–1200 m indicate that salt pillars undergo plastic deformation. As a result, the mined-out chambers gradually close, eventually forming a continuous technogenic rock mass. Roof subsidence during the first year after stoping reaches 150–200 mm, and after 2–3 years the excavations become non-operational. At the same time, stresses in the retained barrier pillars increase several-fold relative to the natural geostatic stress level, making it impossible to conduct mining operations in their vicinity without risking instability of the entire mining system.

This situation creates a fundamental contradiction: barrier pillars are required to maintain the stability of mining panels during extraction, yet a substantial portion of the reserves remains locked within these pillars and cannot be recovered using conventional methods. One possible solution is the implementation of a two-stage mining approach, which allows secondary recovery of reserves while protecting overlying aquifers through backfilling of the mined-out space. Timely filling of first-stage chambers with backfill material can limit stress buildup in the barrier pillar and prevent excessive deformation. After backfilling of adjacent panels is completed, the barrier pillar can be mined using second-stage chambers, leaving only the technologically required inter-chamber pillars.

In this context, the paper proposes a two-stage scheme for barrier pillar extraction, enabling secondary recovery of reserves while ensuring protection of

overlying aquifers through backfilling of the mined-out space.

The objective of this study is to develop and justify a mining technology for gently dipping potash seams at great depths that minimizes extraction losses.

To achieve this objective, the following tasks were addressed:

– forecasting geomechanical processes in the salt rock mass under different mining scenarios and assessing the influence of time-dependent factors on the stress state of barrier pillars;

– developing methods to reduce stresses in the barrier pillar through optimization of backfill parameters and inter-chamber pillar configuration;

– investigating the influence of mined-out space backfilling (degree of chamber filling and type of backfill material) on the stress state of the barrier pillar;

– developing an algorithm for determining the parameters of the proposed technology (number of chambers and width of inter-chamber pillars) based on numerical modeling results.

Methods

To achieve the study objective and address the research tasks, computer-based numerical modeling was employed [6, 7]. In modern geomechanics, numerical modeling is widely recognized as an effective tool for assessing the stress–strain state of rock masses. The simulations were performed using the software package developed by Rocscience, which implements the finite element method (FEM). This software is widely used to solve a broad range of geomechanical problems, including the evaluation and justification of engineering design solutions in mineral deposit development [8, 9]. The selection of this software was determined by its ability to efficiently construct and analyze complex multistage numerical models, requiring significantly less effort than physical modeling. This capability is particularly important for investigating geomechanical processes in salt rock masses.

Model geometry and parameters

The model represents a two-dimensional fragment of a room-and-pillar mining system including the roof and floor strata as well as the main productive seam. The model incorporates inter-chamber pillars within the mining panel and a barrier pillar separating adjacent panels. Because the stress–strain state is symmetric with respect to the vertical axis of the barrier pillar, the calculations consider half of the pillar width and half of the adjacent mining panel. The model geometry and layout of structural elements are shown in Fig. 1.

Boundary conditions and loading

At the lateral boundaries of the model, horizontal displacements were constrained, while vertical displacement was restricted along the bottom boundary. A distributed load corresponding to the weight of the overlying rock mass was applied to the upper boundary. The initial stress state of the rock mass was assumed to be hydrostatic, which corresponds to the conditions of deep potash seam occurrence. The simulations were carried out within an elastoplastic framework using the Mohr–Coulomb strength criterion, which adequately describes the mechanical behavior of salt rocks within the considered stress range.

Modeling of the backfill mass

To evaluate the influence of backfilling operations on the stress state of the barrier pillar, the model includes the filling of mined chambers with material characterized by specified strength and deformation properties [10–12]. The variable parameters were the degree of chamber filling (the ratio of backfill volume to the volume of the mined-out space) and the mechanical properties of the backfill mass, which allowed different backfill types to be considered, ranging from dry fill to cemented backfill. Varying these parameters made it possible to perform parametric analyses aimed at identifying the most suitable type of backfill material for specific mining and geological conditions [13, 14].

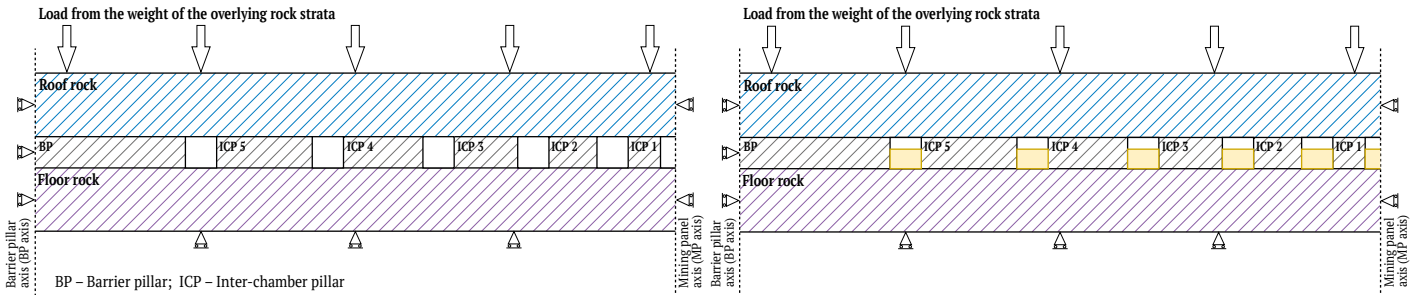

Fig. 1. Geometry of the geomechanical model used in the study: *a* – without chamber backfilling; *b* – with chamber backfilling

The adopted modeling approach enables quantitative evaluation of the influence of each factor on the stresses acting within the barrier pillar, providing a basis for developing recommendations on the parameters of the proposed two-stage mining technology. The simulations used average values of the strength and deformation properties of the salt rocks forming the modeled stratigraphic sequence [15–17].

Results

1. Prediction of geomechanical processes

The evolution of geomechanical processes was evaluated using vertical roof convergence as the primary indicator (Fig. 2). Field observations at a Russian potash deposit, where the productive seams occur at a depth of approximately 1100 m, show that roof subsidence in extraction chambers during the first year after mining reaches up to 200 mm. Since further monitoring of chamber conditions was not conducted, the numerical model was calibrated using data reported in previous studies [18–20]. Earlier investigations [21, 22] have shown that salt pillars deform plastically, resulting in gradual closure of the mined-out chambers and eventually forming a continuous technogenic rock mass. Maximum roof subsidence typically ranges from 30–40% of the extraction thickness and depends on the ratio of pillar area to the total panel area. To evaluate the time-dependent evolution of stresses in the barrier pillar, pillar deformability was varied in the model. The results show that stresses in the barrier pillar increase progressively as deformation of the seam develops (Fig. 3).

The stress increase occurs gradually rather than instantaneously. Calibration of the model using the observed roof convergence made it possible to track the evolution of stresses in the barrier pillar. The simulations indicate that after one year the stresses in the barrier pillar exceed the natural geostatic stress level by approximately 1.5 times, and by more than six times at the final stage of ground movement stabilization.

The resulting stress distribution across the pillar cross-section at the final stage of deformation shows pronounced stress concentration near the pillar edges, where maximum stresses are 1.4–1.7 times higher than the average stress level. When evaluating the potential for secondary recovery of reserves, it is therefore necessary to consider the maximum stresses acting within the barrier pillar, since these highly stressed zones complicate the determination of the required width of second-stage inter-chamber pillars (ICPs).

An increase in the time interval between mining and backfilling operations leads to higher stress levels and also complicates backfilling operations.

Results of visual and instrumental observations conducted at the deposit on deformation processes in ICPs and extraction chambers indicate that mine workings become non-operational within 1–2 years after the completion of mining operations. Other studies [23, 24] report that pillar wall failure in deep salt deposits occurs approximately 250 days after chamber extraction, although in those cases no backfilling was performed.

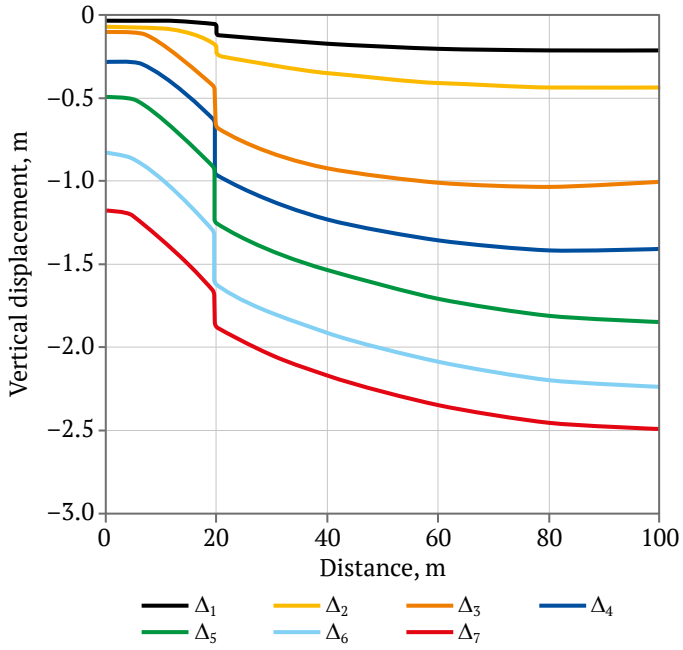

Fig. 2. Roof convergence in the mining panel

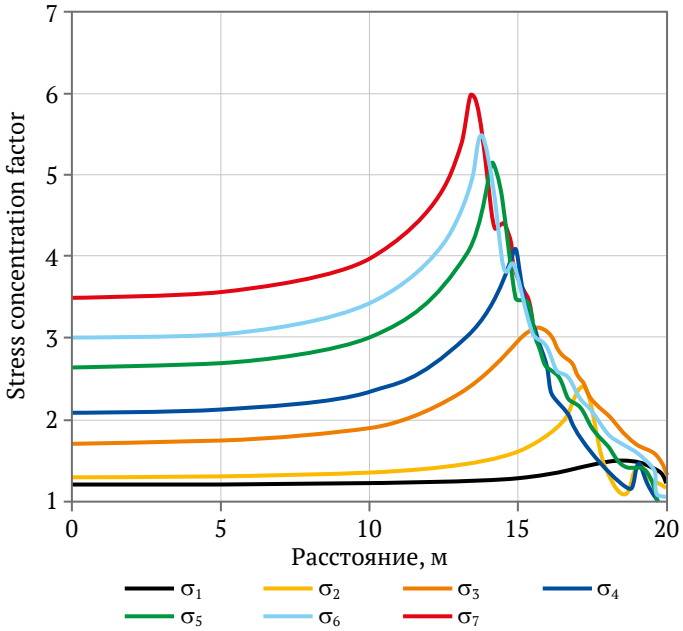

Fig. 3. Stresses in the barrier pillar

Backfilling of chambers reduces the deformation rate of the seam, decreases roof subsidence, and consequently limits stress growth in the barrier pillar.

Clearly, minimizing the delay between mining and backfilling operations is advantageous. However, these processes must be coordinated both spatially and temporally [25–27], taking into account that the backfill mass does not provide mechanical support immediately after placement.

The potential amount of secondary reserve recovery (i.e., the number of chambers that can be extracted) from the barrier pillar depends on the stress level within the pillar. When the delay between mining and backfilling operations is minimized, roof convergence remains small and stresses in the barrier pillar do not increase; in some cases they may even approach the natural geostatic stress level.

To assess the influence of backfill parameters on the stress state of the barrier pillar, the simulations varied the seam extraction thickness, degree of chamber filling, and the strength and deformation properties of the backfill material.

For the range of conditions considered in this study, the stresses acting in the barrier pillar during backfilling operations can be estimated using the following relationship:

$$\sigma_{bp} = k \cdot \sigma_{nat},$$

where σ_{nat} – natural stress level at the mining depth; k – coefficient derived from numerical simulations for estimating stresses acting in the barrier pillar σ_{bp} (Fig. 4), defined as:

$$k = A \cdot x^{-B},$$

where x – degree of chamber filling with backfill material; A and B – empirical coefficients depending on mining parameters of adjacent panels (A is a function of the extraction thickness, while B depends on the deformation properties of the backfill mass).

The coefficient A can be expressed as a function of the seam extraction thickness m (m) with a coefficient of determination $R^2 = 0.9241$:

$$A = X \cdot e^{0.01m},$$

where X – is a coefficient depending on the type of backfill (0.8 for cemented backfill; 1.5 for hydraulic backfill; 2.9 for dry backfill).

The exponent B is described by a second-order polynomial function depending on the elastic modulus E (MPa) of the backfill mass; the coefficient of determination is $R^2 = 0.9458$:

$$B = -0.000002 \cdot E^2 + 0.0033 \cdot E + 0.5598.$$

When first-stage chambers are filled, a monolithic backfill structure is formed that prevents further stress accumulation in the barrier pillar and allows it to remain in a relatively unloaded state. The obtained relationships are valid for typical conditions of gently dipping potash seams occurring at depths of about 1100 m, with extraction thickness ranging from 5 to 20 m, provided that the required pillar loading conditions are maintained.

The stress level in the barrier pillar depends strongly on backfill characteristics. Dry backfilling of chambers has little effect on pillar stability [5, 28]. Hydraulic backfill provides some improvement but does not fully realize the potential of the proposed technology. Maximum recovery of second-stage chambers, with stresses in the barrier pillar reduced to the natural geostatic stress level, can only be achieved when cemented backfill is used.

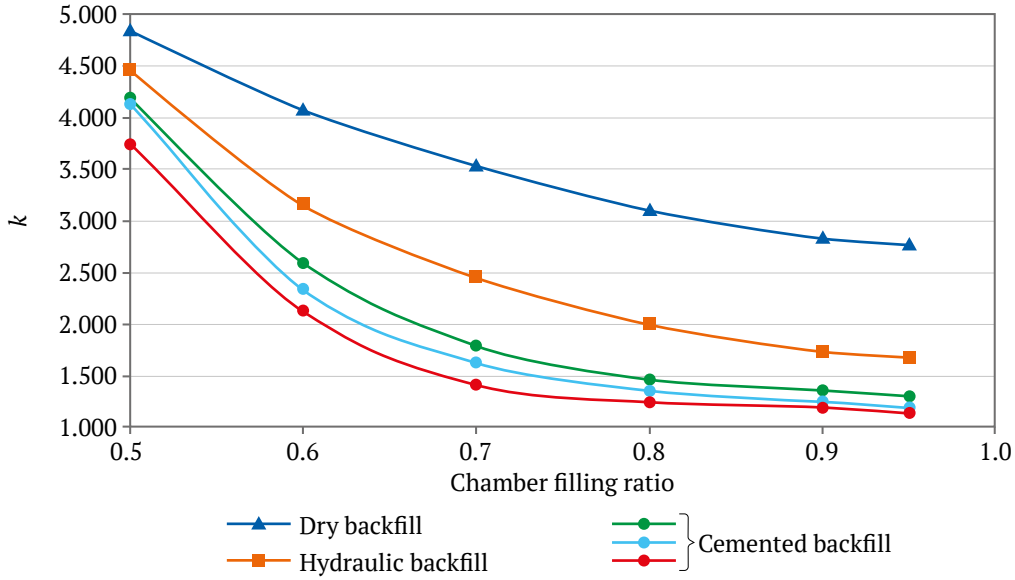

Fig. 4. Stress concentration coefficient as a function of backfill deformation properties and chamber filling ratio

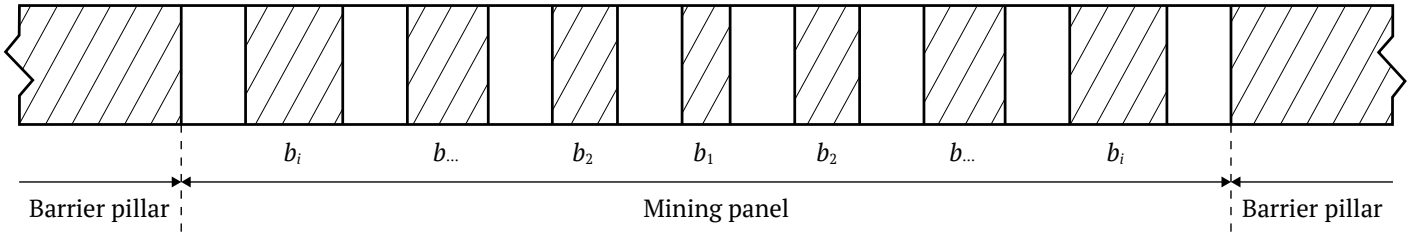

Fig. 5. Configuration of ICPs with variable width

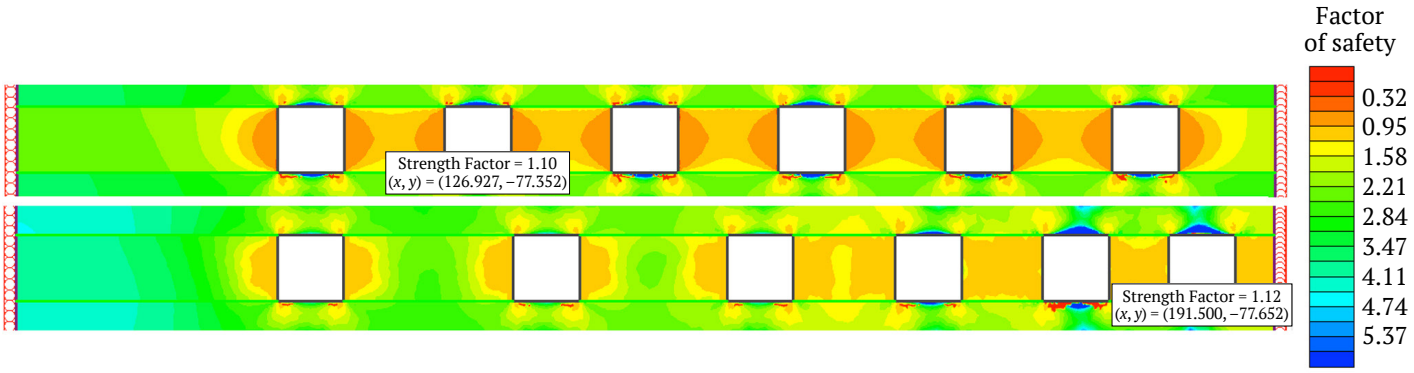

Fig. 6. Factor of safety of ICPs

2. Development of a mining technology for gently dipping seams

The concept of limiting stress growth in the barrier pillar can be implemented when mining and backfilling operations are conducted simultaneously. The proposed method for mining deep potash seams is implemented as follows[1].

The mining field is divided into extraction panels, separated by inter-panel barrier pillars. The width of the barrier pillars is calculated for conditions of complete undermining, in which the pillars are subjected to the load of the entire overburden column extending to the surface. Within each panel, mining is carried out using first-stage chambers, leaving rib pillars between them. These pillars are subjected to the load of the overlying rock mass within the natural arch of equilibrium.

As each first-stage chamber is completed, backfilling operations are initiated, so that mining and backfilling proceed simultaneously within the panel.

After adjacent panels have been backfilled, the inter-panel barrier pillar is mined using second-stage chambers. The number of second-stage chambers is determined by the width of the barrier pillar while accounting for the required width of the ICPs left between them. The width of these pillars is calculated based on the stress level acting in the barrier pillar after backfilling.

The proposed technology involves a pillar configuration in which the width of inter-chamber pillars decreases from the panel boundaries toward its central part (Fig. 5).

The minimum width of ICPs is determined based on the degree of pillar loading, taking into account the time lag between mining and backfilling operations within the block, and is calculated using established empirical design relationships.

The width of the intermediate ICPs b^i_{ICP} increases linearly from the center toward the boundaries of the mining panel, while the average loading coefficient of ICPs within the panel C_{avg} must not exceed the maximum value permitted by regulatory guidelines:

$$C_{avg} = \frac{\sum b^i_{ICP} C_i}{\sum b^i_{ICP}}.$$

The presence of a zone with variable pillar width smooths the roof subsidence curve and reduces the stress level in the barrier pillar compared with the case where ICPs of uniform width are left within the mining panel. At the same time, the factor of safety of ICPs in the proposed configuration is not lower than in the baseline case and remains greater than 1 (Fig. 6), indicating that the proposed method does not reduce the level of operational safety.

[1] Kovalsky E.R., Kongar-Syuryun Ch.B., Sirenko Yu.G., Karpov G.N. Method for mining potash seams at great depths. Russian Federation patent application No. 2025136780; filed December 18, 2025.

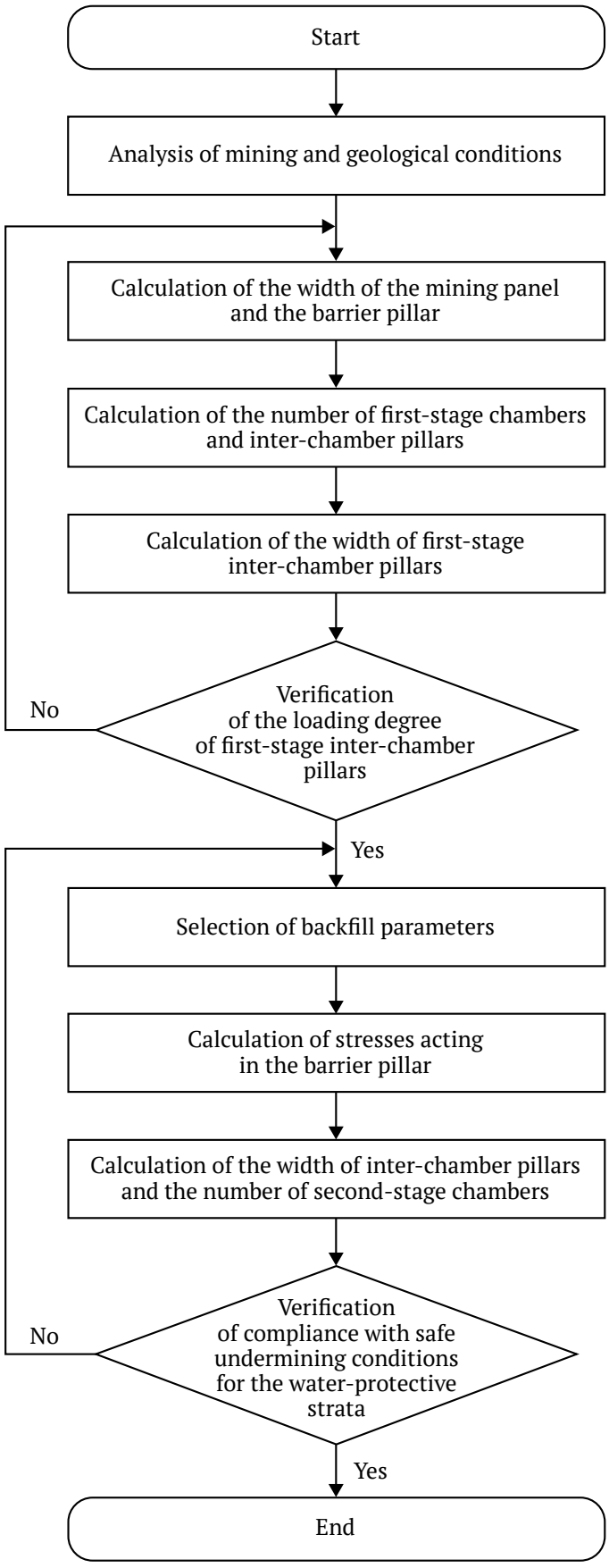

Fig. 7. Algorithm for determining the parameters of the proposed mining method for gently dipping potash seams at great depths

The backfill material is selected so that the calculated value of the empirical function k is minimized, which allows the stresses in the barrier pillar to be reduced as much as possible.

Based on the results of numerical modeling and current regulatory and technical standards governing potash mining operations, a methodology was developed for determining the parameters of the proposed technology for mining gently dipping potash seams at great depths with reduced ore losses. The algorithm of the proposed methodology is presented in Fig. 7.

Discussion

A key issue in assessing the feasibility of the proposed technology is the need for backfilling operations, which has traditionally been regarded as a factor increasing both capital costs and the organizational complexity of mining operations [29]. Indeed, the construction and operation of a backfilling system require additional investment and are associated with a number of technological challenges [30, 31]. However, under modern deep potash mining conditions, backfilling of the mined-out space is no longer merely a desirable improvement but has become a practical necessity.

This conclusion is supported by the negative experience of several potash mines where the absence of backfilling operations in the past resulted in serious geomechanical and hydrogeological problems, including uncontrolled ground movements, brine inflows, and loss of excavation stability [32–34]. Preventing such phenomena at newly designed and operating mines requires the use of backfilling systems regardless of the selected mining method. In this context, the costs associated with the construction of a backfilling system, as well as the related organizational and technological challenges, should not be regarded as disadvantages of the proposed two-stage extraction method. Rather, they should be considered inevitable conditions for ensuring the safe and sustainable mining of deep potash seams.

An important advantage of the proposed technological solution lies in its compatibility with existing mine development and panel layout schemes. Implementation of two-stage extraction with backfilling does not require the development of a large number of additional access or development workings and does not imply a fundamental restructuring of the technological scheme adopted at the mine. This considerably reduces the barriers to practical implementation and allowing the proposed method to be implemented at operating mines with minimal changes to existing infrastructure.

Another important advantage of the proposed technology is the possibility of using large volumes of processing waste and waste rock in backfill mixtures. This approach makes it possible not only to address the problem of waste storage at the surface but also to reduce the negative environmental impact associated with mining operations. Consequently, the benefits of the proposed technology are multifaceted and consist of two main components. The first is a direct economic benefit resulting from the additional recovery of mineable reserves from barrier pillars. The second is an environmental and economic benefit associated with reducing the area occupied by waste storage facilities and preventing environmental contamination [35]. Taken together, these considerations indicate that the proposed technology, despite the objective challenges associated with the need for backfilling, represents not only a geomechanically justified but also a technologically feasible solution. Its implementation makes it possible to increase the completeness of reserve recovery while simultaneously addressing the tasks of industrial safety and environmental protection.

Conclusion

As a result of this study, a method for mining gently dipping potash seams at great depths has been developed and substantiated. The proposed method makes it possible to reduce operational losses through the secondary recovery of inter-panel barrier pillars. A key condition for implementing the proposed approach is the simultaneous execution of mining and backfilling operations, which limits stress growth in the barrier pillars and creates favorable conditions for their subsequent extraction using second-stage chambers.

For typical conditions of potash mining (depth 1100 m, seam extraction thickness 5 m), the results show that the use of cemented backfill reduces stress concentration in the barrier pillar to a level characterized by a coefficient k = 1.2. In contrast, when backfilling is not applied, this coefficient reaches k = 5.0. The resulting fourfold reduction in stresses makes it possible to carry out second-stage chamber mining within the boundaries of the barrier pillar, thereby enabling additional recovery of mineable reserves. Based on the results of the study, the following main conclusions can be drawn:

1. Stress in barrier pillars increases gradually over time. According to the modeling results, one year after mining operations the stresses exceed the natural stress level by approximately 1.5 times, and at the final stage of ground movement stabilization they exceed it by more than six times. Increasing the time interval between mining and the start of backfilling results in irreversible stress growth. Therefore, mining and backfilling operations should be synchronized within 1–2 years of excavation, while the workings still remain operational.

2. The stress state of the barrier pillar is controlled by two key factors: the use of inter-chamber pillars with variable width (increasing from the center toward the boundaries of the mining panel) and the simultaneous execution of mining and backfilling operations. Under these conditions, the factor of safety of inter-chamber pillars remains greater than 1, which confirms the stability of the proposed method.

3. The stress level in the barrier pillar after backfilling of first-stage chambers is described by an empirical function obtained from numerical modeling. This function takes into account the deformation properties of the backfill material (elastic modulus from 100 to 1000 MPa) as well as the degree of chamber filling (0–100%). The reliability of the obtained relationships is confirmed by coefficients of determination R^2 = 0.9241 for parameter A and R^2 = 0.9458 for parameter B.

4. The developed algorithm for determining the parameters of two-stage extraction is based on calculating stresses in the barrier pillar, which determine both the allowable number of second-stage chambers and the width of the inter-chamber pillars left between them.

Thus, the proposed method represents a geomechanically substantiated solution aimed at increasing the completeness of reserve recovery while ensuring safe mining operations. An additional benefit of the technology is the possibility of utilizing processing waste in backfill mixtures, which contributes to reducing the environmental impact of mining activities.

References

1. Kovalski E.R., Kongar-Syuryun Ch.B., Petrov D.N. Challenges and prospects for several-stage stoping in potash mining. *Sustainable Development of Mountain Territories.* 2023;15(2):349–364. (In Russ.) https://doi.org/10.21177/1998-4502-2023-15-2-349-364
2. Soloviev V.A., Sekuntsov A.I., Chernopazov D.S. Development and application of sylvinite seams excavation technology with pillar-and-chamber method in Verchnekamsk potash deposit. *News*

of the Ural State Mining University. 2013;(4):41–46. (In Russ.) URL: https://iuggu.ru/index.php/archive/xxi-vek/2013/4-13/78-ru/195-4-13-07

3. Golovaty I.I., Petrovskij A.B., Prushak V.Y. Substantiation of the possibility of developing reserves of the Third potash horizon of the Starobin deposit, previously worked out by the chamber system. *Proceedings of the National Academy of Sciences of Belarus. Physical-Technical Series*. 2019;64(4):497–510. (In Russ.) https://doi.org/10.29235/1561-8358-2019-64-4-497-510
4. Toksarov V.N., Evseev A.V., Kuzmin V.S. Determination of mechanical properties of salt rocks in the mined-out part of the mine field at the BKPRU-2 mine. *Nauchnye Issledovaniya i Innovatsii*. 2011;5(2):154–156. (In Russ.)
5. Kovalskiy E.R., Kongar-Syuryun Ch.B., Sirenko Yu.G., Mironov N.A. Modeling of rheological deformation processes for room and pillar mining at the Verkhnekamsk potash salt deposit. *Sustainable Development of Mountain Territories*. 2024;16(3):1017–1030. (In Russ.) https://doi.org/10.21177/1998-4502-2024-16-3-1017-1030
6. Belyakov N.A., Belikov A.A. Prediction of the integrity of the water-protective stratum at the Verkhnekamskoye potash ore deposit. *Mining Informational and Analytical Bulletin*. 2022;(6–2):33–46. (In Russ.) https://doi.org/10.25018/0236_1493_2022_62_0_33
7. Toksarov V.N., Polyakov I.V., Beltyukov N.L. et al. Rock mass stress state at the Gremyachinskoe potassium deposit. *Mining Informational and Analytical Bulletin*. 2025;(1):100–113. (In Russ.) https://doi.org/10.25018/0236_1493_2025_1_0_100
8. Karasev M.A., Petrushin V.V., Rysin A.I. The hybrid finite/discrete element method in description of macrostructural behavior of salt rocks. *Mining Informational and Analytical Bulletin*. 2023;(4):48–66. (In Russ.) https://doi.org/10.25018/0236_1493_2023_4_0_48
9. Protosenya A.G., Belyakov N.A., Bouslova M.A. Modelling of the stress-strain state of block rock mass of ore deposits during development by caving mining systems. *Journal of Mining Institute*. 2023;262:619–627.
10. Ryl'nikova M.V., Berger R.V., Yakovlev I.V. et al. Backfill Technologies and designs for deep-level sylvinite mining. *Journal of Mining Science*. 2024;60(2):332-340. https://doi.org/10.1134/S1062739124020145 (Orig. ver.: Ryl'nikova M. V., Berger R. V., Yakovlev I. V. et al. Backfill Technologies and designs for deep-level sylvinite mining. *Fiziko-Tekhnicheskie Problemy Razrabotki Poleznykh Iskopaemykh*. 2024;(S2):167–176. (In Russ.) https://doi.org/10.15372/FTPRPI20240214)
11. Ilinov M.D., Korshunov V.A., Pospekhov G.B., Shokov A.N. Integrated experimental research of mechanical properties of rocks: Problems and solutions. *Gornyi Zhurnal*. 2023;(5):11–18. (In Russ.) https://doi.org/10.17580/gzh.2023.05.02
12. Gilev M.V., Konstantinova S.A., Marakov V.E., Chernopazov S.A. Stowing of goaf during sylvinite seams mining as a structural element of mining system. *Mine Surveying Bulletin*. 2007;(1):33–40. (In Russ.)
13. Tyulyaeva Y.S., Khayrutdinov A.M., Galachieva I.D., Totrukova I.K. Creation of a high-strength backfill composite based on sulfide-bearing technogenic waste from mining production. *Sustainable Development of Mountain Territories*. 2024;16(3):1384–1396. (In Russ.) https://doi.org/10.21177/1998-4502-2024-16-3-1384-1396
14. Agafonov V.V., Oganesyan A.., Solovykh D.Ya., Kozlova O.Yu. Effect of polypropylene fiber on cement backfill based on tailings. *Sustainable Development of Mountain Territories*. 2023;15(4):1108–1118. (In Russ.) https://doi.org/10.21177/1998-4502-2023-15-4-1108-1118
15. Kozlovskiy E.Y., Zhuravkov M.A. Determination and verification of the calculated model parameters of salt rocks taking into account softening and plastic flow. *Journal of Mining Institute*. 2021;247:33–38. https://doi.org/10.31897/PMI.2021.1.4
16. Protosenya A.G., Katerov A.M. Substantiation of rheological model parameters for salt rock mass. *Mining Informational and Analytical Bulletin*. 2023;(3):16–28. https://doi.org/10.25018/0236_1493_2023_3_0_16
17. Karasev M.A., Petrushin V.V. Methodological issues in determination of initial parameters for modeling deformation of rock salt as a polycrystalline discrete medium. *Mining Informational and Analytical Bulletin*. 2024;9:47–64. https://doi.org/10.25018/0236_1493_2024_9_0_47
18. Kratzsch H. Bergschadenkunde. Berlin: Springer-Verlag; 1974. 582 p. (In German) (Trans. ver.: Kratzsch H. *Rock mass displacement and protection of undermined structures*. Transl. from German by R.A. Muller and I.A. Petukhov (Eds.) Moscow: Nedra; 1978. 494 p. (In Russ.))

19. Toksarov V.N., Morozov I.A., Beltyukov N.L., Udarcev A.A. Deformation of underground excavations under conditions of the Gremyachinsk potassium salt deposit. *Mining Informational and Analytical Bulletin.* 2020;(7):113–124. (In Russ.) https://doi.org/10.25018/0236-1493-2020-7-0-113-124

20. Qu H., Yin H., Li C., Wang W. Deformation characteristics and mechanism of salt structure: Research and discussion based on seismic analysis and tectonic simulation and implications for rock salt migration and mineralization in complex tectonic regions. *Acta Geologica Sinica.* 2024;98(10):2916–2930. (In Chinese) https://doi.org/10.19762/j.cnki.dizhixuebao.2024300

21. Asanov V.A., Pankov I.L. Study of deformation features of salt rocks under long-term loading. *Mining Informational and Analytical Bulletin.* 2010;(1):105–110. (In Russ.)

22. Sidki-Rius N., Bascompta M., Sanmiquel L., Yubero M.T. Definition of characteristic subsidence parameters. A case study in the Catalan potassium basin. *Environmental Earth Sciences*. 2024;83(19):566. https://doi.org/10.1007/s12665-024-11849-y

23. Konstantinova S.A., Aptukov V.N. *Some problems of mechanics of deformation and fracture of salt rocks*. Novosibirsk: Nauka; 2013. 191 p. (In Russ.)

24. Zhang Y., Lapatsin S., Zhuravkov M. et al. The stability and failure of deep underground structures at potash mining deposits. *Applied Sciences.* 2024;14(20):9434. https://doi.org/10.3390/app14209434

25. Stadnik D.A., Gabaraev O.Z., Stadnik N.M., Tedeev A.M. Improvement of methodical framework for autonomous scheduling of mining operations during underground mine design and planning. *Mining Informational and Analytical Bulletin.* 2020;(11–1):189–201. https://doi.org/10.25018/0236-1493-2020-111-0-189-201

26. Zubov V.P., Sokol D.G. Technologies of intensive development of potash seams by longwall faces at great depths: current problems, areas of improvement. *Journal of Mining Institute*. 2023;264:874–885.

27. Sirenko Yu.G., Kovalsky E.R. Improvement of selective potash extraction using shortwall mining with partial backfill. *Gornyi Zhurnal*. 2016;(1):24–26. (In Russ.) https://doi.org/10.17580/gzh.2016.01.05

28. Kovalsky E., Kongar-Syuryun C., Morgoeva A., Klyuev R., Khayrutdinov M. Backfill for advanced potash ore mining technologies. *Technologies*. 2025;13(2):60. https://doi.org/10.3390/technologies13020060

29. Khayrutdinov M.M., Aleksakhin A.V., Kibuk T.N. et al. Technogenic waste in backfill composite is a paradigm of circular economy. *Mining.* 2025;5(3):57. https://doi.org/10.3390/mining5030057

30. Kazanin O.I., Evsiukova A.A. Justification of the parameters of the paired workings development technology with the extracting of the pillar between workings by continuous miner. *Mining Informational and Analytical Bulletin.* 2025;(11-1):23–37. (In Russ.) https://doi.org/10.25018/0236_1493_2025_111_0_23

31. Jin R., Wang X., Zhang S. et al. Slurry transportation characteristics of potash mine cemented paste backfills via loop test processing. *Processes*. 2024;12(12):2929. https://doi.org/10.3390/pr12122929

32. Schleinig J.-P., Höntzsch S., Barnasch J. et al. A new technology to increase the extraction rate in potash mining areas – an approach for a safe secondary mining concept. In: Tomás R., Cano M., Riquelme A. et al. (Eds.) *New Challenges in Rock Mechanics and Rock Engineering*. 1st ed. Boca Raton, FL, USA: CRC Press; 2024. Pp. 772–777.

33. Baryakh A.A., Lomakin I.S., Samodelkina N.A., Tenison L.O. Loading of rib pillars in multiple seam mining at the upper Kama salt deposit. *Mining Informational and Analytical Bulletin.* 2023;(1):5–19. https://doi.org/10.25018/0236_1493_2023_1_0_5

34. Sidki-Rius N., Sanmiquel L., Bascompta M., Parcerisa D. Subsidence Management and Prediction System: a case study in potash mining. *Minerals*. 2022;12(9):1155. https://doi.org/10.3390/min12091155

35. Perevoshchikova A.A., Perevoshchikov R.D., Malyshkina E.E., Mitrakova N.V. Waste management in potash mining companies. *Bulletin of the Tomsk Polytechnic University. Geo Assets Engineering*. 2024;335(1):19–35. (In Russ.) https://doi.org/10.18799/24131830/2024/1/4387

Information about the authors

Eugene R. Kovalsky – Cand. Sci. (Eng.), Associate Professor of the Department of Underground Mining, Empress Catherine II Saint Petersburg Mining University, Saint Petersburg, Russian Federation; ORCID 0000-0002-6656-9377, Scopus ID 57189600737, ResearcherID E-2477-2014, SPIN 8295-5373; e-mail kovalskiy_er@pers.spmi.ru

Cheynesh B. Kongar-Syuryun – PhD Student of the Department of Underground Mining, Empress Catherine II Saint Petersburg Mining University, Saint Petersburg, Russian Federation; ORCID 0000-0002-6097-905X, Scopus ID 57212406315, SPIN 2461-3893; e-mail kongarsiuriun@gmail.com

Received 05.02.2026
Revised 03.03.2026
Accepted 10.03.2026

GEOLOGY OF MINERAL DEPOSITS

Review paper

https://doi.org/10.17073/2500-0632-2025-08-1020
UDC 553.04:339.5:546.831

Global zirconium market as a critical mineral raw material

G. Yu. Boyarko, L. M. Bolsunovskaya
National Research Tomsk Polytechnic University, Tomsk, Russian Federation
gub@tpu.ru

Abstract

This study addresses the growing recognition of zirconium raw materials as a critical mineral resource in most industrialized countries and the need for a comprehensive assessment of the complex global zirconium market. Using statistical, graphical, and analytical methods, the study examines the zirconium resource base, the spatial distribution of zirconium deposits by geological type, global commodity flows (production, imports, exports, and consumption) by country, as well as prices and future production and consumption trends. The analysis shows that global consumption of zirconium raw materials has increased rapidly, from 39 kt in 1950 to 2.191 Mt in 2024. The main demand-side trend is the sharp rise in consumption in China, driven by rapid economic growth: from 84 kt (8.7% of the global market) in 1997 to 1.83 Mt (78%) in 2024. At the same time, growth of the global zirconium raw materials market is constrained by rising demand and prices, the high share of international trade, and conflicting interests between producing countries (Australia, South Africa, Mozambique, Indonesia, and Senegal) and the major consuming countries (China, the European Union, the United States, India, and Japan). Another major challenge is that a significant share of global reserves is located in complex endogenic deposits that are difficult to develop both technologically and economically. In most industrialized countries, zirconium is classified as a critical mineral resource. Global proven reserves of zirconium raw materials in developed deposits are estimated at 95 Mt, while forecast resources amount to 232 Mt. Production is currently concentrated mainly in titanium-zirconium placer deposits; however, zirconium also occurs in complex endogenic deposits in carbonatites and alkaline igneous rocks in the form of zircon, baddeleyite, and eudialyte. Global production of zircon concentrate increased from 537 kt in 1970 to 1.64 Mt in 2024 (+2.4% per year), while cumulative global production for 1950–2024 reached 59.7 Mt. Export supply of zircon concentrate to the global market, including re-exports, increased from 395 kt in 1970 to 1.86 Mt in 2024. In the 2010s, the share of exports in global zirconium raw material production ranged from 61% to 98%. High demand led to the emergence of a new group of producers developing placer deposits in Indonesia, Mozambique, Senegal, Kazakhstan, Madagascar, Kenya, Vietnam, and Sierra Leone. Their share of global exports increased from 0.2% in 1999 to 30% in 2024. Production from placer deposits may increase significantly in Mozambique, Madagascar, and Vietnam, while new mining operations may also emerge in Namibia and Tanzania. In addition to placer deposits, projects are being considered for the development of complex endogenic deposits in which zircon concentrate would be produced as a by-product, including Strange Lake and Thor Lake (Canada), Bear Lodge (USA), Baerzhe, Bozigor, and Tudiling (China), Khalzan-Buregtei (Mongolia), and Katuginskoye, Ulug-Tanzekskoye, and Zashikhinskoye (Russia). Development of deposits representing a new technological type—eudialyte ores, which constitute complex zirconium–rare-earth raw materials, is also possible. These projects include Nechalacho (Canada), Tanbreez–Kvanefjeld (Greenland), Toongi–Dubbo (Australia), Lovozerskoye (Russia), and Saima (China).

Keywords

critical mineral resources, zirconium, zircon, baddeleyite, eudialyte, proved reserves, forecast resources, production, export, import, consumption, prices

For citation

Boyarko G. Yu., Bolsunovskaya L. M. Global zirconium market as a critical mineral raw material. *Mining Science and Technology* (*Russia*). 2026;11(1):16–34. https://doi.org/10.17073/2500-0632-2025-08-1020

ГЕОЛОГИЯ МЕСТОРОЖДЕНИЙ ПОЛЕЗНЫХ ИСКОПАЕМЫХ

Обзорная статья

Мировой рынок циркония – критического минерального сырья

Г.Ю. Боярко, Л.М. Болсуновская
Национальный исследовательский Томский политехнический университет, г. Томск, Российская Федерация
gub@tpu.ru

Аннотация
Актуальность работы обусловлена статусом циркониевого сырья как критического минерального сырья, принятым в большинстве промышленно-развитых стран, и необходимостью получения максимально полной картины его сложного мирового рынка. На основе статистического, графического и логического методов проведено изучение минерально-сырьевой базы циркониевого сырья, пространственного размещения месторождений циркония по типам геологических формаций, динамики товарных потоков (производства, импорта, экспорта, потребления) по странам мира, а также мировых цен и перспектив добычи и потребления. Анализ показал, что мировое потребление циркониевого сырья стремительно растет – с 39 тыс. т в 1950 г. до 2,191 млн т в 2024 г. В динамике спроса главным является тренд его взрывного роста в Китае на фоне стремительного подъема национальной экономики: с 84 тыс. т (8,7 % от объемов мирового рынка) в 1997 г. до 1,83 млн т (78 %) в 2024 г. Развитие мирового рынка предложения циркониевого сырья при этом осложняется ростом объемов спроса и цен, значительной долей международной торговли при наличии противоречий интересов добывающих стран (Австралия, ЮАР, Мозамбик, Индонезия, Сенегал) и главных стран-потребителей (Китай, Евросоюз, США, Индия, Япония), а также нахождением значительной доли мировых запасов в комплексных эндогенных месторождениях, сложных для освоения как по технологическим, так и экономическим причинам. В большинстве промышленно-развитых стран цирконий рассматривается как критическое минеральное сырье. Мировые запасы циркониевого сырья в подготовленных для эксплуатации месторождениях оцениваются в 95 млн т, прогнозные ресурсы – в 232 млн т. В разработке находятся преимущественно месторождения титан-циркониевой россыпной формации, однако цирконий также присутствует в комплексных эндогенных месторождениях в карбонатитах и щелочных магматических породах в виде циркона, бадделеита и эвдиалита. Мировое производство цирконового концентрата выросло с 537 тыс. т в 1970 г. до 1,64 млн т в 2024 г. (+2,4 %/год), а накопленная мировая добыча за 1950–2024 гг. составила 59,7 млн т. Экспортное предложение цирконового концентрата на мировой рынок (включая реэкспорт) увеличилось с 395 тыс. т в 1970 г. до 1,86 млн т в 2024 г. При этом в 2010-е годы доля экспорта в мировой добыче циркониевого сырья составляла от 61 до 98 %. Высокий спрос привел к появлению на рынке пула новых производителей, разрабатывающих россыпные месторождения в Индонезии, Мозамбике, Сенегале, Казахстане, Мадагаскаре, Кении, Вьетнаме и Сьерра-Леоне. Их доля в мировом экспорте увеличилась с 0,2 % в 1999 г. до 30 % в 2024 г. В перспективе возможно значительное увеличение объемов добычи из россыпей в Мозамбике, Мадагаскаре, Вьетнаме, а также появление новых производств в Намибии и Танзании. Наряду с россыпными существуют проекты разработки комплексных эндогенных месторождений с получением цирконового концентрата: Стрейндж-Лейк и Тхор-Лэйк (Канада), Беар-Лодж (США), Балже, Бозигор и Тудилинг (Китай), Халзан-Бурегте (Монголия), Катугинское, Улуг-Танзегское и Зашихинское (Россия). Возможна также разработка месторождений нового технологического типа – эвдиалитовых руд, представляющих собой комплексное цирконий-редкоземельное сырье: Нечалачо (Канада), Танбриз-Кванефьелд (Гренландия), Тунги-Дуббо (Австралия), Ловозерское-эвдиалитовое (Россия) и Саима (Китай).

Ключевые слова
критическое минеральное сырье, цирконий, циркон, бадделеит, эвдиалит, балансовые запасы, прогнозные ресурсы, добыча, экспорт, импорт, потребление, цены

Для цитирования
Boyarko G. Yu., Bolsunovskaya L. M. Global zirconium market as a critical mineral raw material. *Mining Science and Technology* (*Russia*). 2026;11(1):16–34. https://doi.org/10.17073/2500-0632-2025-08-1020

Introduction

Since the 1920s, zirconium raw materials have been used primarily as refractories, anti-adhesion coatings and high-temperature ceramics, both in the form of zirconium silicate (natural zircon) and zirconium oxide – natural (baddeleyite) and synthetic, produced during the processing of zircon [1]. Beginning in the 1950s, a portion of zirconium raw materials has been processed to produce metallic zirconium used in the nuclear industry [2]. New zirconium dioxide-based materials have since been developed, including single crystals, thin-film coatings, microfibers, nanopowders, and composite materials. Accordingly, the range of applications for zirconium products has expanded.

The biocompatibility of zirconium products enables their use in medical devices, including dental implants, joint replacements and bone screws [3].

Global consumption of zirconium raw materials increased from 35–60 kt per year in the early 1950s to 1.83–2.34 Mt/year in the 2020s. In most developed industrial countries, zirconium is regarded as a critical mineral raw material [4–6]. The rapid growth in the consumption of zirconium raw materials necessitates assessing the adequacy of the global mineral resource base and analyzing changes in global commodity flows.

Methodology

To examine the mineral resource base of zirconium, data on global zirconium production for the period 1950–2022 were compiled[1]. Production is understood here as the mining of zirconium deposits followed by the production of concentrate. The volumes of mining, imports, exports, and consumption of zirconium raw materials (zircon and baddeleyite concentrates) are reported in metric tons. Prices for zirconium raw materials are given in USD per metric ton. Reserves and resources of zirconium raw materials are expressed in terms of 100 % ZrO_2.

For indicators of commodity flow volumes, the baseline data were taken from the U.S. Geological Survey (USGS). These data were compared with information from the British Geological Survey, the United Nations Data, the TrendEconomy platform, the Mineral Information and Analytical Center and national customs statistics of individual countries, primarily China. When discrepancies between sources were identified, values reported by at least two independent sources were adopted.

For a long period (1959–2014), USGS statistical reports did not contain direct data on zirconium raw material production; therefore, these values were determined indirectly based on the balance of available information on imports, exports, national consumption, and stock changes of these products. Data on zirconium raw material commodity flows in Australia for the period 2007–2024 are also nontransparent: the reported export figures (and, accordingly, production levels) are significantly lower than the import volumes of Australian zircon concentrate reported by importing countries (primarily China). For this period, Australian import and production figures were adjusted based on the difference between Australia's reported export volumes and China's reported imports from Australia.

Information on China's imports of zirconium raw materials prior to 1991 is almost entirely unavailable; therefore, the country's domestic consumption in the 1970s–1980s was most likely underestimated. Estimates of zirconium raw material production in China for the period 2006–2024 also vary considerably across different sources. Data on reserves and forecast resources for individual countries were compiled using the most recent information from the Mineral Information and Analytical Center, the U.S. Geological Survey (USGS), and national statistical agencies. These figures were further adjusted to account for extraction volumes (reserve depletion) and reported additions to reserves resulting from national geological exploration programs, reflecting the situation as of 2022.

Overview of global zirconium raw material production

Between 1950 and 2022, a total of 59.7 Mt of zirconium raw materials (zircon and baddeleyite concentrates) were produced worldwide (Fig. 1). From production levels of 33–75 kt per year in 1950–1955, concentrate supply increased to 1.52–1.63 Mt/year in 2020–2024 (Fig. 2), corresponding to an average annual supply growth rate of +5.7%.

Zircon concentrate, which accounts for about 99% of all zirconium raw materials produced, is obtained exclusively from the development of coastal marine placer deposits (both modern and buried). Baddeleyite concentrate, produced in very small quantities, is derived from ores of carbonatite deposits.

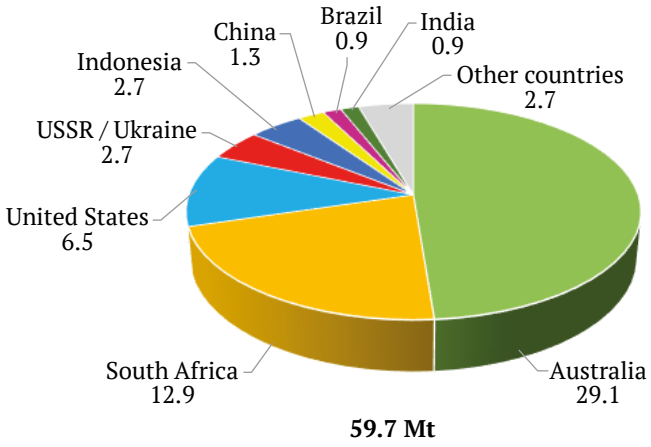

Fig. 1. Cumulative zirconium raw material production by country worldwide, 1950–2024, Mt

Sources: U.S. Geological Survey. URL: http://minerals.usgs.gov/minerals/pubs/commodity/tin/index.html#mcs; British Geological Survey. Commodities & Statistics. URL: https://www.bgs.ac.uk/; United Nations Data. URL: https://data.un.org/

[1] *Data sources*: U.S. Geological Survey. URL: http://minerals.usgs.gov/minerals/pubs/commodity/tin/index.html#mcs; British Geological Survey. URL: https://www.bgs.ac.uk/; United Nations Data. URL: https://data.un.org/; TrendEconomy. Open Data Portal. URL: https://trendeconomy.ru/; Mineral Information and Analytical Center. URL: https://www.mineral.ru/

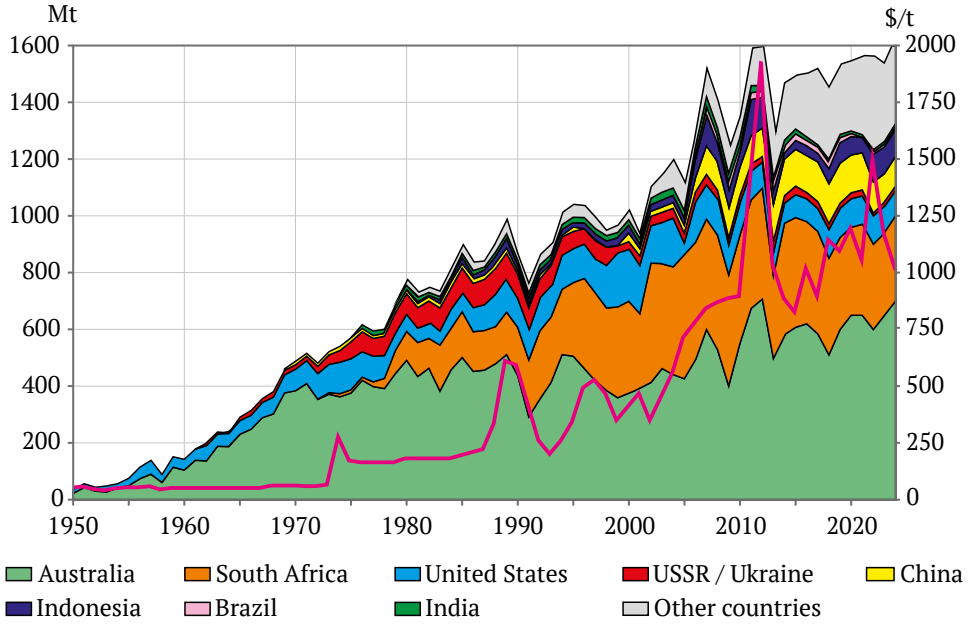

Fig. 2. Dynamics of global zircon concentrate production by countries with the largest cumulative output and its average global price, 1950–2024

Sources: U.S. Geological Survey. URL: http://minerals.usgs.gov/minerals/pubs/commodity/tin/index.html#mcs; British Geological Survey. Commodities & Statistics. URL: https://www.bgs.ac.uk/; United Nations Data. URL: https://data.un.org/

In the 1930s, global consumption of zirconium raw materials was below 5 kt per year. Zircon concentrate production at that time took place in Brazil (the leading producer until 1935), India, Senegal, Madagascar, and Japan. In 1928, the development of titanium-zirconium placers began in the United States (on a relatively small scale), followed by the start of production in Australia in 1932, which rapidly became the dominant global producer of zirconium raw materials.

The 1950s marked the beginning of a period of rapid growth in global zirconium raw material consumption, largely driven by a sharp increase in prices for metallic zirconium used in the nuclear industries of the United States, the USSR, and France. Demand for zirconium oxide used in refractory materials and high-temperature ceramics also increased. As a result, zircon concentrate production rose from 50 kt in 1952 to 465 kt in 1971, while global consumption expanded at a very high rate of +13.2% per year during this period. Australia accounted for 60–80% of global zirconium raw material production, while the United States contributed 15–25%. Beginning in 1962, zirconium raw material production also started in the USSR, reaching 3–4% of global output.

During the 1970–1990s, global zirconium raw material production increased from 510 kt in 1972 to 1.01 Mt in 1997. At the same time, the growth rate of global consumption slowed to +2.6% per year, slightly below the average global economic growth rate for that period (+3.24% per year). Production levels of the global leader, Australia, remained relatively stable at 350–520 kt per year, although its share of global output declined from 70% in 1972 to 50% in 1997. This reduction was largely due to the emergence of South Africa as a major new supplier, increasing its production from 15 kt in 1977 to 320 kt in 1996 (32% of global output). The USSR also expanded production during this period to 80–90 kt per year (8–11% of global output), while the United States, despite increasing production to 80–120 kt per year, saw its share of global supply decline to 8–13%, compared with 17–30% in the 1960s.

In the 21st century, global consumption of zirconium raw materials accelerated again (+3.5% per year, compared with global economic growth of +3.28% per year) and reached 2.34 Mt in 2024. The supply of zircon concentrate increased from Australia (up to 700 kt per year) and South Africa (up to 420 kt per year). Several new producers also emerged: China, which increased production from 15 kt in 1999 to 140 kt per year; Indonesia (up to 130 kt per year); Mozambique (up to 100 kt per year); Kenya (up to 90 kt per year); Kazakhstan (up to 78 kt per year); Senegal (up to 65 kt per year); and Vietnam (up to 40 kt per year). At the same time, production declined in Ukraine, which inherited zirconium production capacity from the USSR, decreasing from 60–80 kt per year in the 1990s to about 10 kt per year in the 2020s.

Australia accounts for 48.8% of cumulative global zirconium raw material production (29.1 Mt). Zircon mining in the country began in 1932 with the development of beach sand deposits at Greenbushes and Cheynes Beach in the Perth Basin of Western Australia. Following substantial production growth in the 1950–1970s, Australia became the dominant global supplier of zircon concentrate (accounting for 83% of global demand in 1970) and continues to hold up to 50% of the global zirconium raw material market, exporting up to 916 kt of zircon concentrate per year. Australia hosts some of the largest coastal placer basins in the world, containing numerous deposits: the Perth Basin (Coburn, Eneabba, South Tutunup, Keysbrook, Cataby, Cooljarloo, Thunderbird); the Eucla Basin (Jacinth, Ambrosia, Tripitaka); the Murray Basin (Douglas, Donald, Mindarie, Pooncarie, Euston); and deposits on the Tiwi Islands (Kilimiraka, Lethbridge South) [7–9] (Fig. 3). In addition to placer deposits, Australia also hosts primary zirconium ore deposits, including the large zirconium–rare earth (eudialyte) deposit Toongi, located in alkaline syenites [10]. This deposit is currently being prepared for development as part of the Dubbo Zirconium Project.

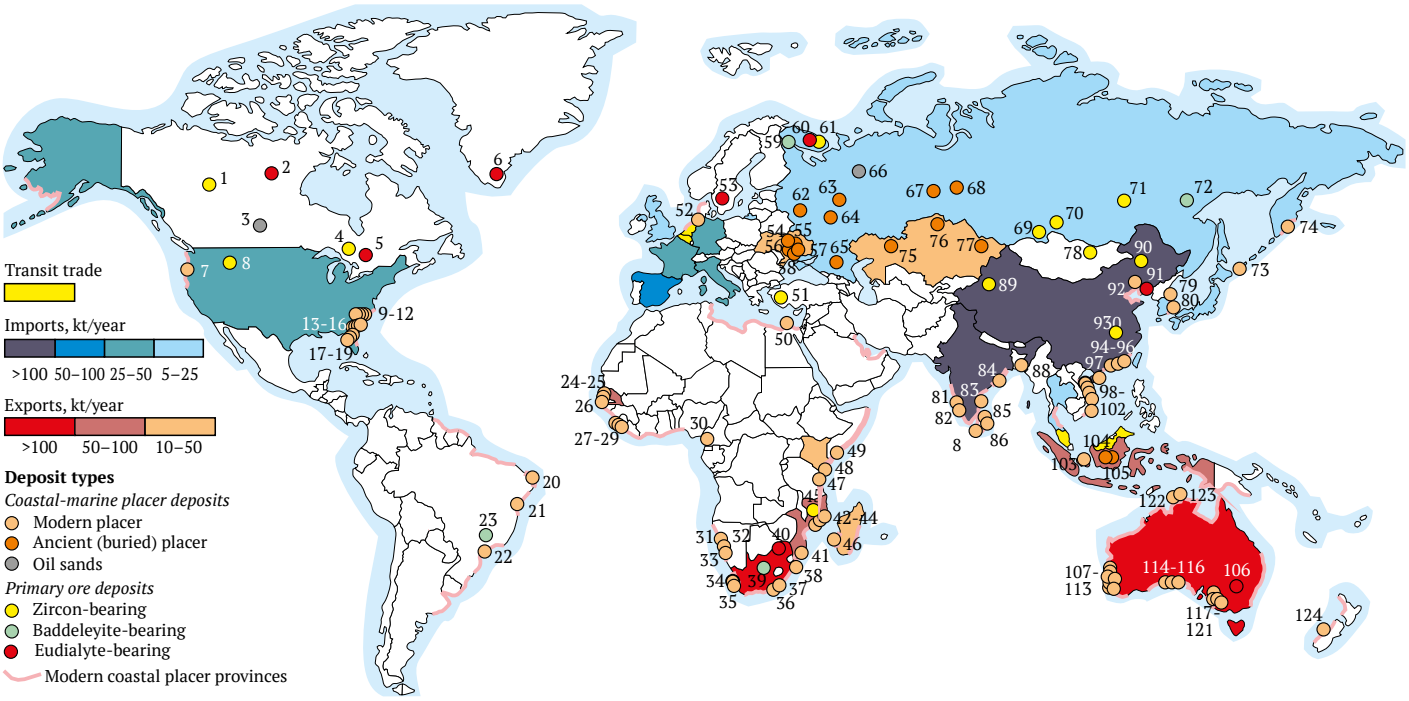

Fig. 3. World map showing the distribution of zirconium deposits and the leading producers, exporters, and importers of zirconium raw materials. Compiled using data from [7, 8].

Zirconium deposits: *1–4* – Canada (*1* – Thor Lake, *2* – Nechalacho, *3* – Athabasca, *4* – Strange Lake, *5* – Kipawa Lake); *6* – Greenland (Tanbreez–Kvanefjeld); *7–19* – United States (*7* – Coos Bay, *8* – Bear Lodge, *9* – Aurelian Springs, *10* – Hickory, *11* – Lulaton, *12* – Mission, *13* – Amelia, *14* – Folkston, *15* – Boulogne, *16* – Green Cove Springs, *17* – Brink, *18* – Concord, *19* – Trail Ridge); *20–23* – Brazil (*20* – Guai, *21* – Cumuruxatiba, *22* – Guaratiba, *23* – Poços de Caldas); *24–25* – Senegal (*24* – Diogo, *25* – Kayar–Lompoul); *26* – Gambia (Brufut); *27–29* – Sierra Leone (*27* – Sembekhan, *28* – Bradford–Rotifunk, *29* – Gbangbama–Mogbwemo); *30* – Cameroon (Tongo–Gandima); *31–33* – Namibia (*31* – Cape Cross, *32* – Omaruru, *33* – Swakopmund); *34–40* – South Africa (*34* – Namaqua, *35* – Tormin, *36* – Fairbreeze, *37* – Hillendale, *38* – Richards Bay, *39* – Palabora, *40* – Pilanesberg); *41–45* – Mozambique (*41* – Corridor Sands, *42* – Pilivili, *43* – Namalope, *44* – Sangage, *45* – pegmatites Muiane, Naimpa, Nanro, Macula, Morrua, Marropino); *46* – Madagascar (Toliara); *47* – Tanzania (Fungoni); *48* – Kenya (Kwale, Vipingo, Kilifi, and Mambrui); *49* – Somalia (Kismayo); *50* – Egypt (Rashid); *51* – Turkey (Büyük Kuluncak); *52* – Germany (Cuxhaven); *53* – Sweden (Norra Kärr); *54–58* – Ukraine (*54* – Stremigorodskoye, *55* – Irshanskoye, *56* – Malyshevskoye, *57* – Mezhdurechenskoye, *58* – Volchanskoye); *59–74* – Russia (*59* – Kovdor, *60* – Lovozero, *61* – Sakharyok, *62* – Unecha, *63* – Lukoyanovskoye, *64* – Tsentralnoye, *65* – Beshpagirskoye, *66* – Yaregskoye, *67* – Tarskoye, *68* – Tuganskoye, *69* – Ulug-Tanzekskoye, *70* – Zashikhinskoye, *71* – Katuginskoye, *72* – Algama, *73* – Rucharskoye, *74* – Khalaktyrskoye); *75–77* – Kazakhstan (*75* – Shakashskoye, *76* – Obukhovskoye, *77* – Karaotkel); *78* – Mongolia (Khalzan-Buregtei); *79* – North Korea (Samchon); *80* – South Korea (Dancheon); *81–84* – India (*81* – Kerala, *82* – Chavara, *83* – Chhatrapur, *84* – Srikurmam); *85–87* – Sri Lanka (*85* – Trincomalee, *86* – Pulmoddai, *87* – Beruwala); *88* – Bangladesh (Cox's Bazar Beach); *89–97* – China (*89* – Bozigor, *90* – Baerzhe, *91* – Saima, *92* – Bohaiwan, *93* – Tudiling, *94* – Lingshui, *95* – Wanning, *96* – Qionghai, *97* – Wenchang); *98–102* – Vietnam (*98* – Cam Hoa, *99* – Ky Ninh, *100* – Ke Sung, *101* – De Ji [Cat Khanh], *102* – Ham Tan); *103–105* – Indonesia (*103* – Bangka–Belitung, *104* – Mandiri, *105* – Tisma); *106–123* – Australia, including: *106* – Toongi; Perth Basin: *107–113* (*107* – Coburn, *108* – Eneabba, *109* – South Tutunup, *110* – Keysbrook, *111* – Cataby, *112* – Cooljarloo, *113* – Thunderbird); Eucla Basin: *114–116* (*114* –Jacinth, *115* – Ambrosia, *116* – Tripitaka), Murray Basin: *117–121* (*117* – Douglas, *118* – Donald, *119* – Mindarie, *120* – Pooncarie, *121* – Euston); Tiwi Islands: *122–123* (*122* – Kilimiraka, *123* – Lethbridge South); *124* – New Zealand (Barrytown)

South Africa, a traditional supplier of mineral raw materials, ranks second among producers and exporters of zirconium raw materials since the 1970s in terms of cumulative production of zirconium products (12.9 Mt, or 21.7% of total global cumulative production) [8, 11]. After the commissioning of the Richards Bay deposit in 1977, the country reached a production level of about 150 kt/year in the 1980s (14–22% of global production). In the 1990s, production increased to 230–320 kt/year (17–36%), in the 2000s to 320–420 kt/year (20–33%), in the 2010s to 320–380 kt/year (20–28%), and in the 2020s to 290–310 kt/year (18–21%) (see Figs. 2, 4 *a*, *b*). Coastal-marine placer deposits currently under development include Namakwa, Tormin, Fairbreeze, Hillendale, and Richards Bay [6, 7, 11] (see Fig. 3). At the Palabora copper-phosphate carbonatite deposit, by-product baddeleyite concentrate (5–13 kt/year) was recovered from the ore until 2001 [12]. In northern South Africa there is also the unique Pilanesberg zirconium rare-earth (eudialyte) deposit hosted by alkaline syenites [13]; however, its development is problematic because it lies within a national park.

The *United States*, which has supplied 6.5 Mt to the global market (10.8% of cumulative global production) and ranks third among zirconium raw material producers, has also long been the world's largest consumer of zirconium products. Domestic production of zirconium raw materials in the United States began in 1922 at the Pablo Beach placer deposit in Florida[2]. By 1960, zircon concentrate production reached up to 56 kt (30% of global production). In the 1960–1980s production remained at 60–80 kt/year (10–15%), increased to 100–110 kt/year (8–9%) in the 1990–2010s, and in 2019–2024 declared production remained at 100–110 kt/year (7–8%) (see Figs. 2, 4 *a*, *b*). Coastal-marine placer deposits are exploited on both the eastern coast (Coos Bay) and the western coast (Aurelian Springs, Hickory, Lulaton, Mission, Amelia, Folkston, Boulogne, Green Cove Springs, Brink, Concord, Trail Ridge) (see Fig. 3) [7]. Zirconium products may also be obtained as by-products during the development of the large complex Bear Lodge carbonatite deposit in Wyoming, which is being considered as an alternative source of rare-earth raw materials outside China [14].

In the *USSR*, the zirconium raw material production base was established in the 1960s with the development of placer titanium-zirconium deposits in Ukraine (Stremigorodskoye, Irshanskoye, Malyshevskoye, Mezhdurechenskoye, and Volchanskoye) [15, 16]. The cumulative production of zirconium raw materials in the USSR and post-Soviet Ukraine amounts to 2.7 Mt, or 4.6% of global production. Production levels in the 1960s ranged from 8–16 kt/year, in the 1970s from 16–73 kt/year, and in the 1980s from 75–90 kt/year (9–10% of global production). After Ukraine's independence, zirconium raw material production declined from 75 kt in 1992 to 25 kt in 1999, remaining at 20–30 kt/year in the 2000–2010s (1–3% of global production) and decreasing further to 8–10 kt/year in the 2020s (see Figs. 2, 4 *a*, *b*).

China accounts for 2.2% of cumulative global zirconium raw material production (1.3 Mt). Production began in 1969 with the development of coastal-marine placer deposits Bohaiwan, Lingshui, Wanning, Qionghai, and Wenchang (see Fig. 3). Production during the 1970–1990s was 10–15 kt/year. After increasing output from 15 kt in 1999 to 120 kt in 2004, Chinese zirconium mining has maintained zircon concentrate production at 100–140 kt/year (7–10% of global production) (see Figs. 2, 4 *a*, *b*). Zirconium is included in the list of critical materials for Chinese industry, and therefore projects are being considered for the development of ore deposits containing zirconium minerals: zircon in the carbonatite deposits Bozigor, Baerzhe, and Tudiling, as well as eudialyte in the alkaline syenites of the Saima deposit [6, 17].

In the 21st century, rising prices for zirconium raw materials led to the emergence of new suppliers on the global market: Vietnam (since 2003), Indonesia (since 2006), Mozambique (since 2007), Sierra Leone (since 2009), Kazakhstan (since 2011), Senegal (since 2014), and Kenya (since 2014).

Indonesia ranks fifth in cumulative global zirconium raw material production, with 2.7 Mt (4.4% of global production). Development of tin-rare-metal coastal-marine (Bangka and Belitung) and buried (Mandiri and Tisma) placer deposits began in 2006 [18] (see Fig. 3). In 2006–2015 the country produced 65–120 kt/year (5–8% of global production), but production later declined to 30–60 kt/year (2–3%) (see Figs. 2, 4 *a*, *b*). Zircon concentrate is also produced as a by-product during the exploitation of numerous placer tin deposits in Indonesia.

In *Mozambique*, coastal-marine placer deposits Corridor Sands, Pilivili, Namalope, and Sangage have been developed since 2007 (see Fig. 3). Cumulative production amounts to 1.1 Mt (1.2% of global production). In 2007–2013 concentrate production ranged from 25–45 kt/year, later increasing to 50–100 kt/year (3–5% of global production) (see Fig. 4, *a*). Projects are also being considered to develop rare-metal pegmatites containing zirconium and tantalum-niobium raw materials (Muiane, Naimpa, Nanro, Macula, Morrua, and Marropino) [19].

[2] U.S. Geological Survey. URL: http://minerals.usgs.gov/minerals/pubs/commodity/tin/index.html#mcs

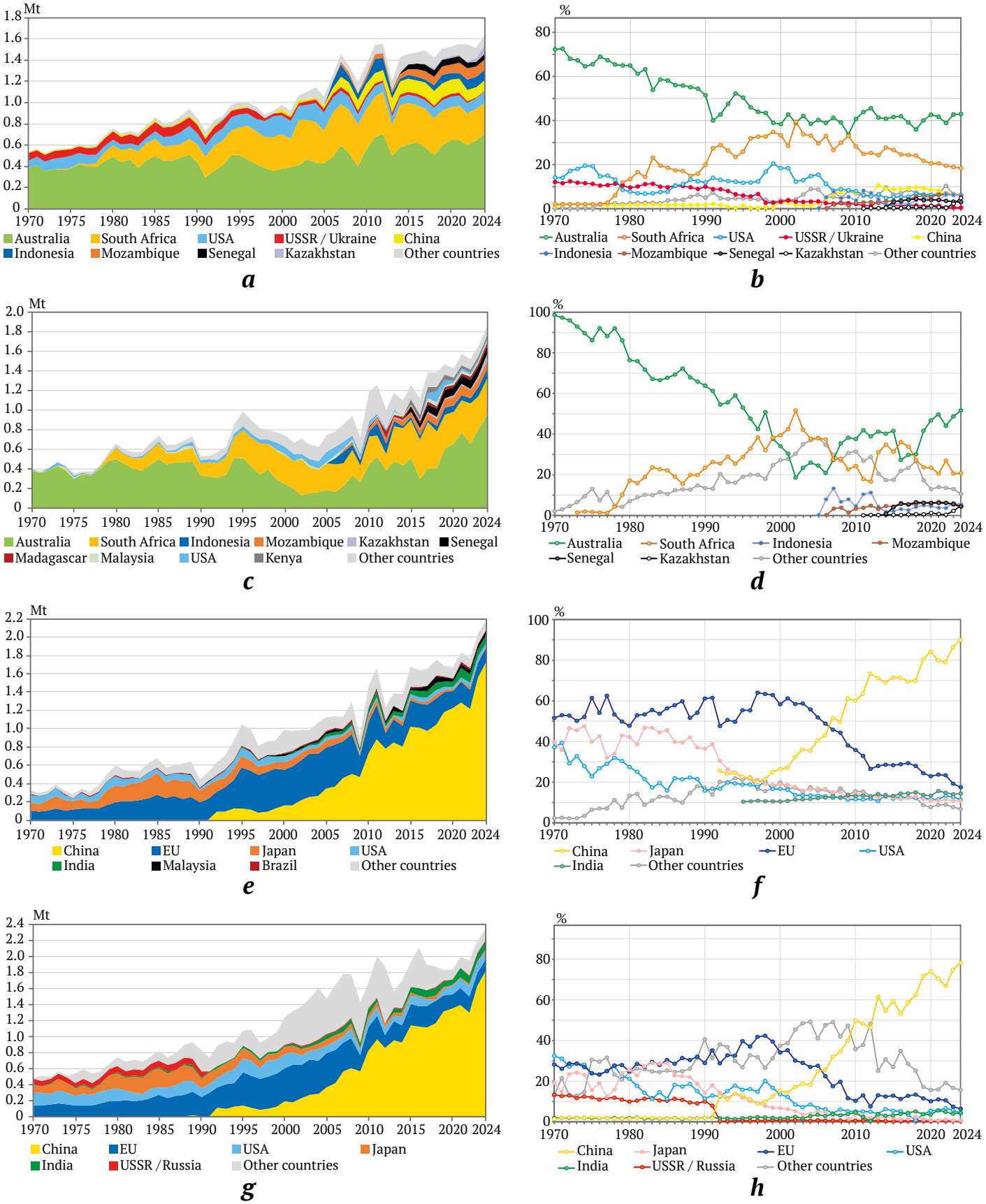

Fig. 4. Dynamics of zircon concentrate commodity flows by country in 1970–2022:
a, *b* – production (volumes and shares); *c*, *d* – exports (volumes and shares); *e*, *f* – imports (volumes and shares);
g, *h* – net consumption (volumes and shares)

Sources: U.S. Geological Survey. URL: http://minerals.usgs.gov/minerals/pubs/commodity/tin/index.html#mcs; British Geological Survey. Commodities & Statistics. URL: https://www.bgs.ac.uk/; United Nations Data. URL: https://data.un.org/

Coastal-marine titanium-zirconium deposits in *Senegal* have been developed since the 1930s, when the country was still a French colony. Production later ceased and resumed only in 2014 amid rising zirconium prices, at the Diogo and Kayar–Lompoul deposits (see Fig. 3) [20], reaching up to 64 kt/year (see Fig. 4, *a*). Cumulative production amounts to 613 kt (1.0% of global production).

In *Vietnam*, rising zirconium prices led to the start of zircon concentrate production in 2004 at offshore coastal-marine placer deposits Cam Hoa, Ky Ninh, Ke Sung, De Ji, Cat Khanh, and Ham Tan (see Fig. 3), with production volumes of 10–15 kt/year [21]. Cumulative production totals 416 kt (0.7% of global production).

Four placer titanium-zirconium deposits have been explored in *Kenya*: Kwale, Vipingo, Kilifi, and Mambrui (see Fig. 3). Mining began at the Kwale deposit in 2014 and continues to the present, with zircon concentrate production ranging from 26 to 90 kt/year [20]. Cumulative production amounts to 415 kt (0.7% of global production).

In *Kazakhstan*, development of the Obukhov titanium-zirconium deposit began in 2010 [22, 23], with production increasing to 78 kt in 2024 (see Figs. 2, 4 *a*). Cumulative production in Kazakhstan already amounts to 218 kt (0.4% of global production).

In *Madagascar*, the coastal-marine Toliara deposit has been developed since 2009, with annual production of up to 35 kt. Cumulative production in Madagascar amounts to 351 kt (0.6% of global production).

In *Sierra Leone*, zircon concentrate is produced as a by-product during the development of titanium (mainly rutile) coastal-marine placer deposits Bradford–Rotifunk, Gbangbama–Mogbwemo, and Sembekhan [24]. Although rutile placers have been mined since 1967, significant volumes of associated zirconium raw materials were marketed in 1991–1994 (up to 1.3 kt/year) and in 2009–2024 (3–11 kt/year) (see Fig. 4, *a*). Cumulative production amounts to 415 kt (0.7% of global production).

In *India*, coastal–marine placer mining began as early as the 1930–1940s, but a significant increase in zirconium raw material production at the Kerala, Chavara, Chhatrapur, and Srikurmam (see Fig. 3) deposits occurred in the 1970s [7, 25, 26]. Production volumes were 10–20 kt/year, increasing to 30–40 kt/year in 2007–2017, but declining again to about 20 kt/year by 2020 (see Fig. 2). Cumulative production in India amounts to 853 kt (1.4% of global production). Zirconium raw materials have been designated a critical resource for the nuclear industry in India [27].

In the 1930s *Brazil* was the global leader in zirconium raw material production. Initially mining was carried out from weathering crusts of eudialyte-bearing alkaline syenites at the Poços de Caldas deposit, with extraction of a colloform mixture of baddeleyite and zircon (brazilite)[3]. Later, coastal-marine titanium-zirconium deposits Guai, Cumuruxatiba, and Guaratiba were brought into production (see Fig. 3) [7, 28]. Production volumes in the 1950–1970s reached up to 5 kt/year, increasing to 20–25 kt/year in the 1980–2010s, but declining again to 6–11 kt/year in the 2020s (see Fig. 2). Cumulative production in Brazil amounts to 940 kt (1.6% of global production).

In *Sri Lanka*, as in India, zirconium raw materials were mined as early as the 1930–1940s, with a significant increase in production in the 1970s. Coastal-marine placer deposits Trincomalee, Pulmoddai, and Beruwala are currently exploited (see Fig. 3) [7, 29]. Production volumes were 1–5 kt/year, increasing to 10–25 kt/year in 1990–2010, but subsequently declining again to about 5 kt/year. Cumulative production amounts to 302 kt (0.5% of global production).

In *Russia*, zirconium raw materials are produced at the Kovdor Mining and Processing Plant during the beneficiation of apatite-magnetite ores from the Kovdor carbonatite deposit, with recovery of by-product baddeleyite concentrate (4–9 kt/year) [12, 30]. Zircon concentrate previously used in Russia was entirely imported (up to 15 kt/year), but following the launch in 2022 of the Tugan Mining and Processing Plant at the buried coastal-marine placer deposit of the same name, production is expected to reach up to 15 kt per year from 2025 [30, 31]. At the Yarega oil-sand deposit, which contains titanium–zirconium placers, extraction of these minerals is technologically difficult and economically inefficient [32]. In addition, several buried titanium-zirconium placer deposits have been (Tsentralnoye [33], Lukoyanovskoye [34], Beshpagirskoye [35], and Tarskoye [36]), as well as complex zirconium-bearing ore deposits (Katuginskoye [37], Ulug-Tanzekskoye [38], Zashikhinskoye [39], and Sakharyok [40]) hosted by alkaline granites, and the Lovozero eudialyte deposit in alkaline syenites [41] (see Fig. 3). The Algama baddeleyite deposit is also known in the weathering crusts of the Algama carbonatite massif [42].

Small-scale zirconium raw material production also occurs in Malaysia (up to 2 kt/year), Nigeria (up to 2 kt/year), Turkey (up to 1 kt/year), and Thailand (up to 1 kt/year).

Prepared reserves and forecast resources

The currently available prepared (proven) reserves of zirconium raw materials worldwide (95 Mt) are sufficient for 20 years at the current level of global consumption, assuming annual growth of +3.5% (Fig. 5).

[3] U.S. Geological Survey. URL: http://minerals.usgs.gov/minerals/pubs/commodity/tin/index.html#mcs

Of this total, 55 Mt, or 58% of global reserves, are concentrated in *Australia*, the undisputed and longstanding world leader in zirconium raw material production, supported by the largest resource base of numerous coastal–marine placer deposits along the southern and southwestern coasts of the continent.

Russia, with 12.4 Mt of zirconium raw materials recorded on its balance sheet, formally ranks second in the world. However, most of these reserves are associated with complex ore deposits in carbonatites, as well as in alkaline granites and syenites[4], whose development is problematic. Only the Kovdor apatite-iron ore deposit hosted by carbonatites has been under development, where baddeleyite has been recovered in small quantities as a by-product. The reserves of technologically favorable titanium-zirconium placer deposits in Russia amount to 2.3 Mt.

South Africa, which ranks third in reserves and second in production, holds 5.3 Mt (13% of global reserves) in placer deposits along the country's southern coast. *Ukraine* ranks fourth; although it is no longer among the top ten producers of zirconium raw materials, it still has a substantial prepared explored base of buried placer deposits amounting to 4 Mt (4.2% of global reserves). The decline in production is due to the fact that the Ukrainian deposits under development are buried placers, which increase operating costs, as well as to the complications arising under the current economic and political crisis.

India (fifth in reserves) and *Senegal* (sixth in reserves and eighth in production) also have fairly large prepared reserves of zirconium raw materials in coastal-marine placer deposits, amounting to 3.4 Mt and 2.6 Mt, respectively (3.6% and 2.7% of global reserves). However, whereas titanium-zirconium placer deposits in Senegal are being brought into production relatively actively, their development in India is constrained by the high cost of land acquisition in coastal zones.

[4] Ministry of Natural Resources and Environment of the Russian Federation. The State Report "On the State and Use of the Mineral Resources of the Russian Federation in 2023". URL: https://rosnedra.gov.ru/activity/documents/gosudarstvennyy-doklad-2023/

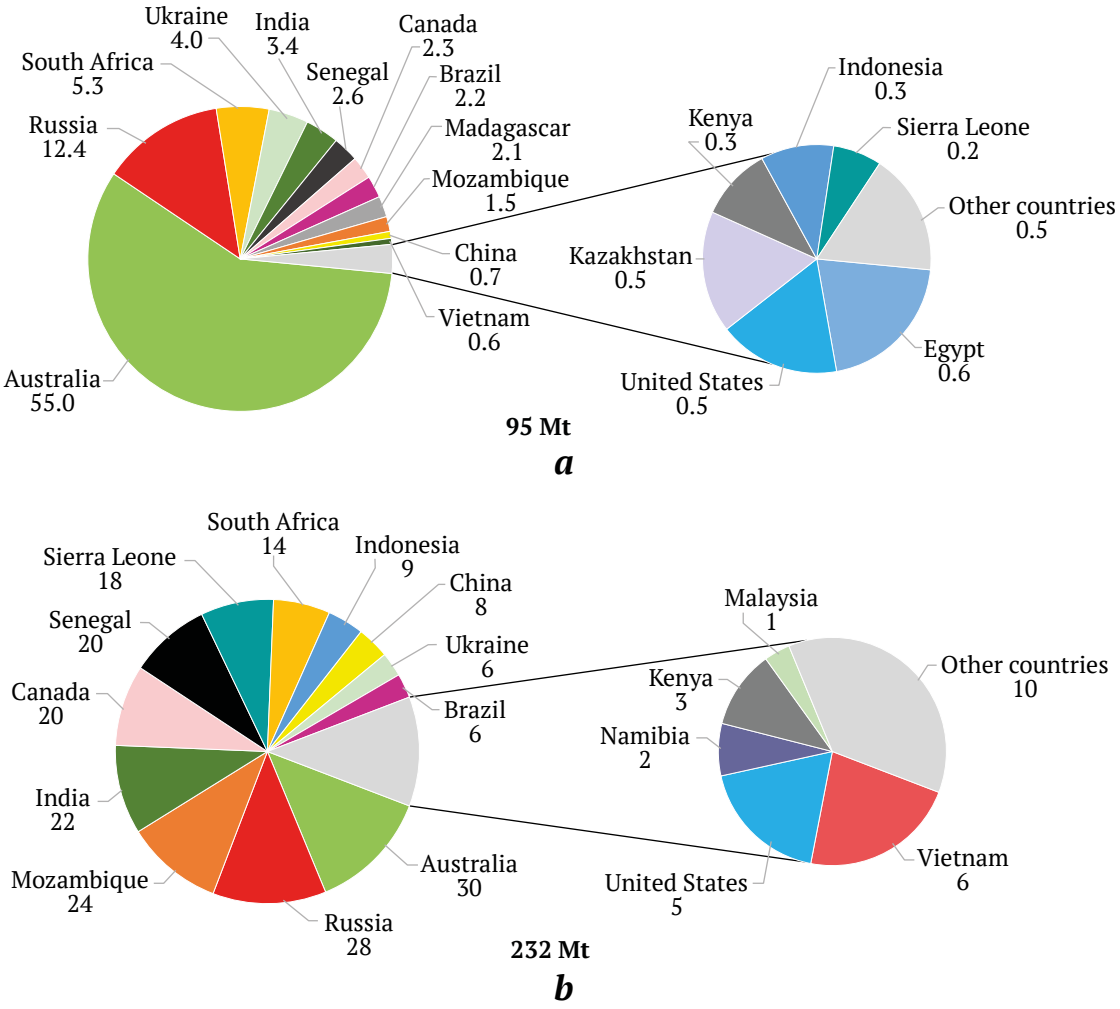

Fig. 5. Global proven reserves (*a*) and forecast resources (*b*) of zirconium as of 2024

Sources: U.S. Geological Survey. URL: http://minerals.usgs.gov/minerals/pubs/commodity/tin/index.html#mcs; Mineral Information and Analytical Center. URL: https://www.mineral.ru/

In *Canada*, zirconium raw materials are not currently mined, but several explored complex ore deposits are known: Strange Lake [43] in carbonatites; Thor Lake [44], Nechalacho [45], and Kipawa Lake [46] in alkaline syenites; as well as technogenic accumulations in the tailings of oil sand processing at the Athabasca deposit that have been evaluated for zirconium raw materials [47] (see Fig. 3). These deposits contain 2.3 Mt of zirconium raw materials (2.4% of global reserves), placing Canada seventh in terms of reserves. These deposits periodically attract interest as potentially promising business projects, but their development is complicated by technological and economic challenges associated with complex mineral raw materials.

The top ten countries in terms of prepared (proven) reserves of zirconium raw materials also include Brazil with 2.2 Mt (2.3% of global reserves), Madagascar with 2.1 Mt (2.2%), and Mozambique with 1.5 Mt (1.6%).

Zirconium raw material reserves are being explored not only in the traditionally major producing countries, but also in other states. Many deposits have been explored but have not yet been brought into production: Cape Cross, Omaruru, and Swakopmund in Namibia [48]; the Rashid deposit in Egypt [49]; Tongo-Gandima in Cameroon [50]; Shakashu [51] and Karaotkel [52] in Kazakhstan; and Cox's Bazar Beach in Bangladesh [53, 54]. The reasons for the delay in their commissioning include marginal project economics in some cases (Kazakhstan, Russia) and the high cost of acquiring coastal land occupied by settlements and agricultural land in others (the coasts of India, Sri Lanka, Bangladesh, Brazil, Turkey, and Germany).

There are notable differences between the ranking of countries by zirconium raw material resources (232 Mt) and by prepared reserves (see Fig. 5). While Australia remains the leader, with 30 Mt of zirconium raw material resources (mainly placer deposits), or 12.9% of global resources, Russia ranks second with 28 Mt (12.1%), predominantly in complex endogenic deposits. Mozambique ranks third (while fifth in the production ranking), with 24 Mt (10.3%): its coastline containing placer deposits remains only weakly developed, and extensive lateritic weathering crusts over alkaline granites are also considered prospective for zircon. Fourth and fifth places are occupied by countries with limited zirconium raw material production but substantial resources: coastal-marine deposits in India (22 Mt, or 9.5% of global resources) and complex ore deposits in Canada (20 Mt, or 8.6%). Senegal, which ranks eighth in zirconium raw material production, is sixth in resources, estimated at 20 Mt, or 8.6% of the global total. The top ten countries in terms of zirconium raw material resources also include Sierra Leone (18 Mt, 7.8%), South Africa (14 Mt, 6.0%), Indonesia (9 Mt, 3.9%), and China (8.0 Mt, 3.9%).

The resources of many countries remain underestimated because of limited geological knowledge in some cases and economic and political problems in others. New coastal-marine placer deposits of zirconium raw materials may be discovered along the marine coasts of Somalia, Libya, Madagascar, Liberia, Côte d'Ivoire, and Ghana in Africa; Indonesia and Papua New Guinea in Asia; and Uruguay, Guyana, Suriname, and French Guiana in South America (see Fig. 3).

Despite the traditional focus on technologically favorable placer deposits of zirconium raw materials, interest in ore deposits containing zirconium mineralization is increasing. As a rule, these are complex rare-metal deposits in carbonatites, alkaline granites, and syenites, as well as in weathering crusts developed over their ores and host rocks. The marketable zirconium products from such deposits are zircon, baddeleyite, and eudialyte.

Zircon concentrate is regarded as one of the saleable products of integrated development projects for zirconium-rare-earth deposits in carbonatites (Strange Lake [43] in Canada, Bear Lodge [14] in the United States, Baerzhe [55] in China, Khalzan-Buregtei [56] in Mongolia), as well as in alkaline granites (Katuginskoye [37], Ulug-Tanzekskoye [38], and Zashikhinskoye [39] in Russia) and in alkaline syenites (Thor Lake [44] in Canada, Bozigor [57] and Tudiling [58] in China).

Baddeleyite (natural zirconium oxide), previously mined at the carbonatite deposits of Poços de Caldas in Brazil and Palabora in South Africa, and currently produced at the Kovdor deposit in Russia, may become a target for future development at the Algama deposit [42] in Russia.

Eudialyte ores represent a complex zirconium-rare-earth raw material. Their deposits are known in alkaline syenite complexes: Nechalacho [45] in Canada, Tanbreez [59] and Kvanefjeld in Greenland, Norra Kärr in Sweden [60], the Lovozero eudialyte deposit [41] in Russia, Pilanesberg [13] in South Africa, Saima [62] in China, and Toongi (the Dubbo Project) [10] in Australia. The development of eudialyte ores is complicated by the production of several marketable products (zirconium and individual rare earths) that differ in value, are subject to price fluctuations and vary in market demand.

There is also some interest in zirconium deposits in weathering crusts, not only those developed over known primary zirconium occurrences (the carbonatites of Poços de Caldas in Brazil [61], and the rare-metal pegmatites Muiane, Naimpa, Nanro, Macula, Morrua, and Marropino in Mozambique [19]), but also

those developed over rocks with disseminated zirconium mineralization, for example over ultrabasic-alkaline complexes in Brazil and the Philippines [63] and over alkaline syenites in Turkey [64].

Technogenic dumps from old placer tin workings in Indonesia [18] and Malaysia, as well as old gold workings in New Zealand [65], may also potentially be used for zirconium raw material production.

Commodity flows of zirconium raw materials

The marketable products of zirconium raw materials are zircon concentrate and baddeleyite concentrate.

The supply of *baddeleyite* (natural zirconium oxide) on the global market is limited due to the rarity of its deposits and amounts to only 4–9 kt/year [12, 30], supplied primarily from Russia. It is used as an abrasive raw material and for the production of refractories. The share of baddeleyite concentrate in the total global production of zirconium raw materials accounts for only 0.3–0.7%.

Global production of *zircon concentrate* increased from 537 kt in 1970 to 1.64 Mt in 2024 (+2.4% per year) (see Fig. 4, *a*). Significant volumes of zircon concentrate are produced by a limited group of producer countries. While traditional producers of zirconium raw materials (Australia, South Africa, and the United States) continue to dominate, the contribution of new producing countries has increased over time, including Mozambique, Senegal, Indonesia, China, as well as Madagascar, Kenya, Sierra Leone, and Vietnam. Production of zirconium raw materials has declined at the enterprises remaining in Ukraine, which inherited production capacity from the former USSR, decreasing from 65 kt in 1991 to 10 kt in the 2020s. At the same time, stable but relatively small-scale production of zirconium raw materials continues in Brazil, India, and Sri Lanka.

Although the production volumes of the traditional leaders (Australia, South Africa, the United States, the USSR/Ukraine, Brazil, India, Sri Lanka, and Malaysia) increased in supplies to the global market from 455 kt in 1970 to 1,130 kt in 2024, their share in the global supply of this raw material declined from 92% in 1999 to 69% in 2024. In contrast, the production of zirconium raw materials in new producing countries (China, Mozambique, Senegal, Indonesia, Vietnam, Kenya, Madagascar, Sierra Leone, and Kazakhstan) increased from 2.2 kt in 1999 (0.2% of global exports) to 500 kt in 2024 (30%). The combined share of all other countries amounts to 0.2–2.5% of global production (Fig. 6).

The dynamics of total global exports of zircon concentrate (see Fig. 4, *c*) broadly correspond to the dynamics of its total global production (see Fig. 4, *a*). This relationship is explained by the extremely high share of total global exports (including re-exports) relative to production (61–98%). The supply of zircon concentrate to the global market (exports) increased from 395 kt in 1970 to 1.86 Mt in 2024. The growth rate of global zircon concentrate exports (+2.8% per year) slightly exceeds the growth rate of its production (+2.4% per year), which indicates incomplete or non-transparent reporting of production volumes by some countries. There is also a clear trend toward an increasing share of global zircon concentrate exports relative to its production, rising from 60–80% in the 1970s to 85–98% in the 2010s–2020s (Fig. 7).

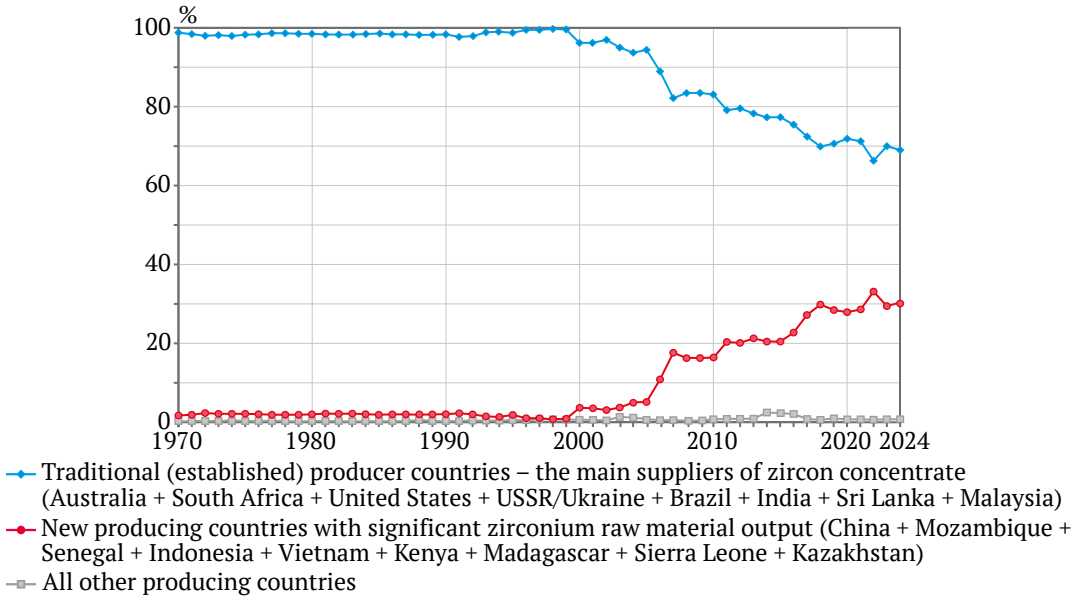

Fig. 6. Dynamics of the shares of zircon concentrate production in total global output, 1970–2024

Sources: U.S. Geological Survey. URL: http://minerals.usgs.gov/minerals/pubs/commodity/tin/index.html#mcs; British Geological Survey. Commodities & Statistics. URL: https://www.bgs.ac.uk/; TrendEconomy. Open Data Portal. URL: https://trendeconomy.ru/

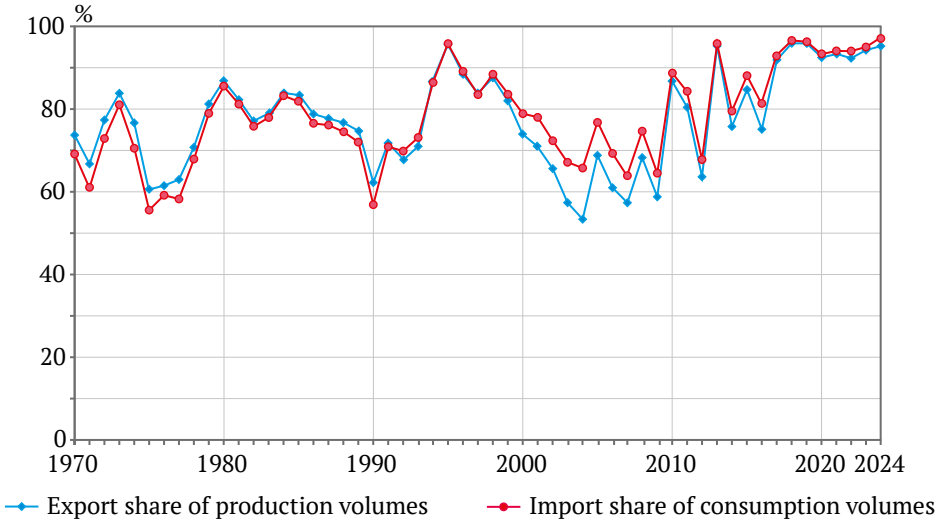

Fig. 7. Shares of global zircon concentrate exports and imports, 1970–2024

Sources: U.S. Geological Survey. URL: http://minerals.usgs.gov/minerals/pubs/commodity/tin/index.html#mcs; British Geological Survey. Commodities & Statistics. URL: https://www.bgs.ac.uk/; United Nations Data. URL: https://data.un.org/; TrendEconomy. Open Data Portal. URL: https://trendeconomy.ru/

Australia ranks first in exports of zircon concentrate as the undisputed global leader in its production. The country increased export volumes from 387 kt in 1970 to 950 kt in 2024 (adjusted to account for data on imports of Australian concentrate into China) (see Fig. 4, *c*), although its share in global zircon concentrate supply declined over this period from 98% to 50% (see Fig. 4, *d*). Australia exports 93–99% of the zircon concentrate it produces.

South Africa, which began large-scale production of zircon concentrate only in 1977, also exports 80–98% of its output. Its exports increased from 3 kt in 1977 to a peak of 465 kt in 2017, with a high export growth rate of +13.4% per year. In subsequent years, exports have remained relatively stable in the range of 340–400 kt/year. South Africa's share in international trade reached a maximum of 51% in 2002, but later declined to local minima of 16% in 2022 and 20% in 2023–2024, primarily due to the emergence of new suppliers of zirconium raw materials (see Fig. 4, *d*).

Among the established exporting countries, the *United States* shows a highly variable export flow (6–119 kt/year, accounting for 2–13.6% of global exports), while *Malaysia* contributes a smaller export stream (4–40 kt/year, or 0.8–4.8%) (see Fig. 4, *c*).

New producing countries rapidly expanded their exports, shipping almost all of the zircon concentrate they produce (see Fig. 4, *c*, *d*): *Mozambique* – exports since 2007, reaching 101 kt in 2021, with a global export market share of up to 6.8%; *Senegal* – since 2014, up to 92 kt/year, share up to 6.2%; *Madagascar* – since 2009, up to 68 kt/year, up to 6.8%; *Kenya* – since 2015, up to 69 kt/year, up to 4.8%; *Kazakhstan* – since 2011, up to 78 kt/year, up to 4.2%; *Vietnam* – since 2000, up to 25 kt/year, up to 1.9%.

Since 1991, international trade in zirconium raw materials has experienced a sharp increase in transit trade (re-exports), reaching 15–20% of total import volumes. Among the re-exporting countries, several traditional transit trading hubs without domestic production should be noted, exporting 60–100% of their import volumes: the *Netherlands* (up to 40 kt/year), *Belgium* (up to 37 kt/year), and *Hong Kong* (up to 70 kt/year). In the *United States*, re-exports of zircon concentrate amounted to 7–26 kt/year in the 1970s–1980s, representing 10–25% of imports, but in the 1990s–2010s they increased to 40–120 kt/year, reaching up to 100% of import volumes. Malaysia, while producing up to 26 kt/year of zirconium raw materials and importing up to 65 kt/year, simultaneously exports up to 40 kt/year (50–80% of its import volumes). Transit re-exports of zirconium raw materials also occur in Italy and Thailand, though at smaller shares of imports.

For total global imports of zircon concentrate, the share of imports relative to consumption shows a smoother dynamic than the changes in the share of exports relative to production, possibly due to the influence of re-export accounting and unreported changes in stock levels (see Fig. 7). Global imports of zircon concentrate (including the double counting associated with transit trade) increased from 319 kt in 1970 to 2.19 Mt in 2024. The ranking of importing countries includes both countries without domestic production capacity (Japan and the European Union) and producer countries (the United States, China, and India) (see Fig. 4, *e*, *f*).

In the 1970s–1980s, the *European Union* was the global leader in zircon concentrate imports, purchasing 100–280 kt/year, or 38–52% of global imports. In the 1990s–2000s, import volumes increased to 370–470 kt/year, although the EU share did not grow and began to decline as China's imports rose to 25% of global imports by 2010. Subsequently, volumes decreased due to declining domestic consumption, reaching 164 kt in 2024 (7.5% of global imports) (see Fig. 7, *e*, *f*).

Within the European Union, imports are distributed among Italy, Spain, Germany, France, the United Kingdom, and the Netherlands (Fig. 8, *a*). Italy, which imported 30–45 kt/year in the 1970s (10–15% of global imports), increased purchases to 55–80 kt/year (10–14%) in the 1980s and to 115–150 kt/year (11–16%) during 1992–2008, reflecting the overall dynamics of global zirconium raw material consumption. However, imports into Italy later declined to 40–65 kt/year in the 2010s (2.6–6.7%) and to 28–44 kt/year in the 2020s (1.3–2.4% of global imports). In Spain (EU member since 1986), imports increased from 10–20 kt/year in the 1970s (3–5% of global imports) to 125–155 kt/year in the 2000s (7–15%), followed by a decline in the 2010s–2020s (65–140 kt/year, 3–7%). Germany experienced a period of relatively high zircon concentrate imports during 1970–2000 (40–85 kt/year, 6–14% of global imports) and lower import levels thereafter (25–40 kt/year, 1.1–2.7%). France maintained imports at 25–50 kt/year throughout the entire period studied (2–6% of global imports). In the United Kingdom, imports of zirconium raw materials remained at 25–50 kt/year (2–6% of global imports) until 2005, after which they declined to 3–7 kt/year (0.2–1.0%). In the Netherlands, imports range from 15–50 kt/year (1–6% of global imports), although a large share is re-exported through the country's transit trade. A portion of imported zirconium raw materials is also re-exported from Germany and France (up to 20–25% of import volumes).

Japan, which imported 90–190 kt/year in the 1970s–1990s (25–35% of global imports), began reducing its imports after 1997 to 55–65 kt/year (5–9%) in the 2000s and to 20–40 kt/year (1.0–3.3%) in the 2010s–2020s.

A similar trend is observed in the dynamics of zirconium raw material imports into the *United States*, which imported 60–90 kt/year in the 1970s–1990s (10–25% of global imports), followed by a decline to 25–45 kt/year (1.5–3.5%) in the 2000s–2020s (see Fig. 4, *e*, *f*).

For *China*, reliable data on imports are not available prior to 1991. Subsequently, however, imports of zircon concentrate increased rapidly – from 99 kt in 1992 to 1.75 Mt in 2024 (from 14% to 80% of global imports), with an average growth rate of +8.9% per year (see Fig. 4, *e*, *f*).

A gradual increase in import volumes is also observed in *India*, from 3–10 kt/year in the 1990s (0.3–0.7%) to 30–75 kt/year in the 2010s (3–5%) (see Fig. 4, *e*, *f*).

Imports of zircon concentrate into *Malaysia* amounted to 0.5–3.0 kt/year in 1970–1980; subsequently they increased to 30–50 kt/year (see Fig. 4, *e*). However, most of these volumes are re-exported (25–40 kt/year), while domestic consumption remains relatively small (5–10 kt/year).

Whereas *Brazil* was a net exporter of zircon concentrate in the 1950s–1960s, domestic consumption later exceeded national production capacity, resulting in additional imports of 15–23 kt/year (see Fig. 4, *e*).

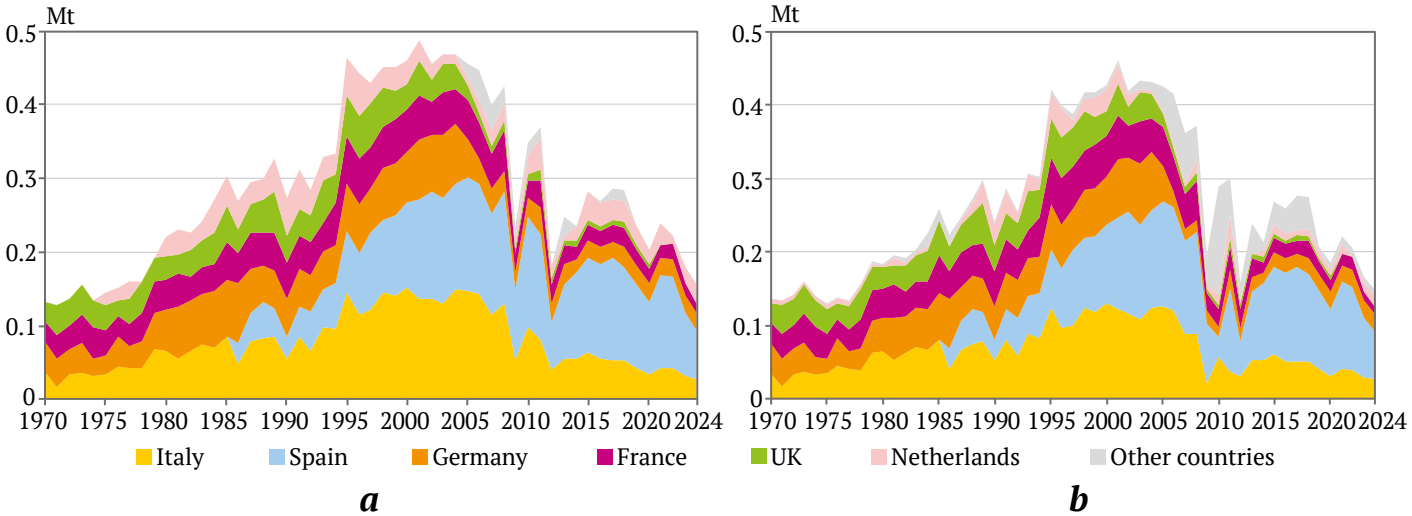

Fig. 8. Dynamics of zirconium raw material imports (*a*) and consumption (*b*) in the European Union countries, 1970–2024
Sources: United Nations Data. URL: https://data.un.org/; TrendEconomy. Open Data Portal. URL: https://trendeconomy.ru/

Changes in global zircon concentrate consumption are primarily driven by demand in the main application sectors: refractories in metallurgy and the glass industry, as well as ceramics in the construction sector. Consequently, there has been a pronounced increase in zircon concentrate consumption in China, associated with the rapid growth of its national economy – from 84 kt (8.7% of the global market) in 1997 to 1.83 Mt (78%) in 2024 (see Fig. 4, *g*, *h*), with an average growth rate of +11.9% per year. Most zirconium raw materials supplied to China are imported, accounting for up to 79% of consumption.

The *United States*, which was initially the world leader in zircon concentrate consumption (159 kt, or 31% of global consumption in 1971), reduced its use to 95–140 kt/year (13–19%) in the 1980s–1990s and to 75–110 kt/year (4–7%) in the 2000s–2020s (see Fig. 4, *g*, *h*). This trend was consistent with the post-industrial development policy of the United States in 1990–2010, which was accompanied by a reduction in industrial production and construction activity. Nevertheless, in the 2020s a process of reindustrialization has emerged in the United States, accompanied by increased consumption of mineral resources, including zirconium raw materials, reaching 100–135 kt/year. Due to the presence of domestic production, U.S. import dependence on zirconium raw materials remains relatively moderate at 18–50% of consumption.

The *European Union*, which led global consumption of zirconium raw materials in 1979–2005 (250–450 kt, or 25–40% of global consumption), has since maintained consumption at a somewhat lower level of 150–250 kt, representing 6–20% of global consumption due to China's dominant role (see Fig. 4, *g*, *h*; Fig. 8, *b*). The leading EU consumers of zirconium raw materials are Spain and Italy (see Fig. 8, *a*). In these countries, the consumption of zircon concentrate has increased as a result of the development of ceramic production using opaque glazes, largely oriented toward export markets. In Spain (EU member since 1986), zirconium raw material consumption amounted to 20–35 kt/year in the 1970s–1980s (2–5% of the global market), increased to 50–95 kt/year in the 1990s (5–10%), and reached 90–130 kt/year in the 2010s–2020s (7–10%). Spain currently ranks fourth globally in zirconium raw material consumption. Consumption in Italy increased from 30–40 kt/year in the 1970s (7–9% of the global market) and 50–60 kt/year in the 1980s (also 7–9%) to 80–120 kt/year in the 1990s–2000s (9–12%). However, since 2007, a decline in ceramic production has resulted in a reduction in zirconium raw material consumption in Italy to 30–50 kt/year (2–3%) (see Fig. 8, *b*). In Germany, consumption dynamics have changed more gradually: 25–40 kt/year in the 1970s (5–9% of the global market), increasing slightly to 45–65 kt/year in the 1980s–1990s (5–9%), followed by a decline after 2006 to 12–25 kt/year (0.9–1.4%). In France, zircon concentrate consumption has remained relatively stable throughout the study period at 20–45 kt/year, corresponding to 1–5% of global consumption. In the United Kingdom, zirconium raw material consumption remained at 25–50 kt/year (2–6% of global imports) until 2005, after which it declined to 3–7 kt/year (0.2–1.0%). Zirconium raw materials consumed in EU countries are supplied almost entirely through imports.

Japan, which experienced rapid growth in the 1960s in the metal-intensive shipbuilding and automotive industries, requiring large volumes of ferrous and non-ferrous metals, was also among the top three global consumers of zircon concentrate (100% supplied by imports). In 1970–1992, consumption amounted to 120–200 kt/year (15–30% of global consumption). Subsequently, against the backdrop of slower economic growth, consumption declined to 50–75 kt/year (4–6%) in the 2000s and 20–40 kt/year (0.9–2.8%) in the 2010s–2020s (see Fig. 4, *g*, *h*).

During its existence, the *USSR* ranked third globally in zirconium raw material consumption in the 1970s–1980s, with 65–96 kt/year (10–15% of global consumption), all of which was produced domestically. Following industrial stagnation in the 1990s, Russia significantly reduced consumption of zirconium raw materials to 8–10 kt/year (see Fig. 4, *g*, *h*).

A smaller but steady increase in zircon concentrate consumption is also observed in India, rising from 10–15 kt/year in the 1970s–1990s (2–3% of the global market) to 35–75 kt/year in the 2000s (3–5%) and 60–120 kt/year in the 2010s–2020s (3–5%) (see Fig. 4, *g*, *h*). India currently ranks fourth globally in zirconium raw material consumption. However, whereas in the 1970s–1990s Indian industry relied primarily on domestic zirconium raw materials (imports accounting for only 0.5–1.1%), by the 2010s the share of imports had increased to 70–85%, making India critically import-dependent [27].

Discussion and conclusions

Global zirconium resources and reserves

The currently available prepared (proven) reserves and forecast resources of zirconium raw materials worldwide (95 Mt + 252 Mt) are sufficient for several decades of global consumption at the current level, assuming an annual growth rate of +3.5%. The complexity of the zirconium mineral resource base lies in the fact that most reserves and resources are associated with endogenic deposit formations in carbonatites and alkaline rocks, whereas the entire his-

torical development of zirconium raw materials has relied on coastal-marine and alluvial placer deposits, composed of loose sediments that are technologically efficient for beneficiation and the production of zircon concentrate. High prices for zirconium raw materials make projects for processing compositionally complex endogenic ores, which require preliminary crushing, economically viable. At the same time, these prices allow a reduction in the cut-off grades of placer deposits, enabling the exploitation of poorer sands and thereby expanding the resource base of this deposit type.

Placer deposits remain the primary source of zirconium raw materials, ensuring the leading positions of Australia and South Africa in global production. High demand for zirconium raw materials has also led to the emergence of new producers, developing placer deposits in Indonesia, Mozambique, Senegal, Kazakhstan, Madagascar, Kenya, Vietnam, and Sierra Leone. A significant increase in zirconium raw material production is possible in Mozambique, Madagascar, and Vietnam, as well as the emergence of new mining operations in Namibia, Tanzania, and Somalia.

The development of endogenic zirconium deposits is complicated by the production of multiple marketable products (zirconium, niobium, and rare-earth compounds), which have different and fluctuating prices and varying demand in commodity markets. Nevertheless, there are projects aimed at developing complex deposits with zircon concentrate as a by-product, including Strange Lake and Thor Lake (Canada), Bear Lodge (USA), Baerzhe, Bozigor, and Tudiling (China), Khalzan-Buregtei (Mongolia), and Katuginskoye, Ulug-Tanzekskoye, and Zashikhinskoye (Russia). Development is also possible for a new technological type of deposit – eudialyte ores, which represent complex niobium-zirconium-rare-earth raw materials. Development projects for such deposits include Nechalacho (Canada), Tanbreez and Kvanefjeld (Greenland), Toongi-Dubbo (Australia), Lovozerskoye (Russia), and Saima (China).

Beneficiation and processing challenges of zirconium raw materials

Unlike the relatively simple gravity beneficiation of sands from placer titanium-zirconium deposits, ores from endogenic complex deposits containing zircon mineralization require preliminary crushing and grinding. Beneficiation (gravity and flotation) uses complex flowsheets to produce individual mineral concentrates with commercial value, including zircon concentrate. For eudialyte deposits, beneficiation is also possible using gravity and flotation methods, while processing of eudialyte concentrate can be carried out using a nitric acid flowsheet, followed by sequential recovery of zirconium and rare earth elements from solution through chemical precipitation [66]. The development of endogenic deposits (both eudialyte and zircon-bearing), in addition to the extra costs associated with crushing and complex beneficiation and processing flowsheets, involves economic risks linked to the production of multiple marketable products with different and variable prices and varying demand in commodity markets [67].

Structure of the global zirconium raw materials trade

In the global zirconium industry, a bipolar structure has formed between producing countries and consuming countries of zirconium raw materials. In international trade, the share of global zircon concentrate exports relative to production volumes is very high, with a clear increasing trend – from 60–80% in the 1970s to 85–98% in the 2010s. The growth rate of global zircon concentrate exports (+2.8% per year) slightly exceeds the growth rate of its production (+2.4% per year), which indicates incomplete reporting of production volumes in some countries (China, the United States, and Australia) and the presence of significant volumes of unrecorded re-exports.

The main suppliers of zircon concentrate to the global market remain the traditional producing countries Australia and South Africa. At the same time, new producing countries have emerged that mine zirconium raw materials in significant quantities, including China, Mozambique, Senegal, Indonesia, Vietnam, Kenya, Madagascar, Sierra Leone, and Kazakhstan. New participants may also appear in the market through the development of placer deposits in Namibia and Tanzania, as well as through projects involving endogenic complex deposits with by-product zirconium in Canada, Greenland, and Russia.

Challenges for the global zirconium industry

The development of the global zirconium raw materials market is highly complex due to rapid growth in consumption, rising prices, and the large share of international trade in this raw material, combined with conflicting interests between producing and consuming countries. In addition, a significant portion of global zirconium reserves is located in complex endogenic deposits, which are difficult to develop both technologically and economically [9, 30, 67, 68]. In most developed industrial countries, zirconium is classified as a critical mineral resource.

In the dynamics of zirconium raw material consumption, the key factor is the rapid increase in demand in China, driven by the rapid growth of its national economy. China will remain the largest

consumer of zirconium raw materials in the future, both through domestic production and – primarily – through imports.

The main risk factor for the global zirconium industry lies in the existence of a group of producing countries (Australia, South Africa, Mozambique, Indonesia and Senegal) and major consuming countries (China, the European Union, the United States, India, and Japan). The share of international trade in zirconium raw materials relative to production has already exceeded 90%, prompting consuming countries to classify this raw material as a critical commodity requiring supply regulation. In most cases, consuming countries have limited or no domestic production of zirconium raw materials. Even in China and the United States, the main consumers of zirconium raw materials, domestic production (for which information is not fully transparent) accounts for only 5–13% and 30–40% of consumption, respectively. The European Union, which is among the global leaders in zirconium raw material consumption, has virtually no domestic mining operations. A substantial volume of transit trade in zirconium raw materials has also emerged (15–20% of global imports), with the largest re-export volumes occurring in the Netherlands, Belgium, Hong Kong, and Malaysia.

Given the spatial separation of production and consumption centers, which has led to the majority of mined raw materials entering international trade, disruptions in the global zirconium raw materials and zirconium products market are inevitable during economic crises and political conflicts, inevitably affecting prices, trade volumes, and supply routes.

In response to growing global demand, the development of new mining operations continues to focus primarily on technologically efficient placer deposits, while projects involving endogenic complex deposits are slowed by risks associated with the production of multiple marketable products with differing prices and market demand.

References

1. Fedoseev S., Tcvetkov P., Sidorov N. Development potential of Russian zirconium industry on world markets. *Journal of Business and Retail Management Research*. 2017;12(1):41–48. URL: https://jbrmr.com/cdn/article_file/content_50624_17-10-04-21-28-12.pdf
2. Comstock B., Barberis P. (Eds.) Zirconium in the nuclear industry. In: *17th International Symposium. STP1543*. West Conshohocken, PA: ASTM International; 2015. https://doi.org/10.1520/stp1543-eb
3. Ting S., Ruoyu L., Xiangning L. et al. The biocompatibility of dental graded nano-glass-zirconia material after aging. *Nanoscale Research Letters*. 2018;13(1):8. https://doi.org/10.1186/s11671-018-2479-4
4. Schulz K.J., DeYoung J.H. Jr., Seal R.R. II, Bradley D.C. Critical mineral resources of the United States – Economic and environmental geology and prospects for future supply. *U.S. Geological Survey Professional Paper*. 2017;1802:797. https://doi.org/10.3133/pp1802
5. Perks C., Mudd G. Soft rocks, hard rocks: the world's resources and reserves of Ti and Zr and associated critical minerals. *International Geology Review*. 2022;64(7):987–1008. https://doi.org/10.1080/00206814.2021.1904294
6. Wang R.C, Che X.D, Wu B., Xie L. Critical mineral resources of Nb, Ta, Zr, and Hf in China. *Chinese Science Bulletin*. 2020;65(33):3763–3777. (In Chinese) https://doi.org/10.1360/TB-2020-0271
7. Hamilton N.T.M. Controls on the global distribution of coastal titanium-zirconium placers. *International Geology Review*. 1995;37(9):755–779. https://doi.org/10.1080/00206819509465426
8. Perks C., Mudd G. Titanium, zirconium resources and production: A state of the art literature review. *Ore Geology Reviews*. 2019;107:629–646. https://doi.org/10.1016/j.oregeorev.2019.02.025
9. Mudd G. Assessing the availability of global metals and minerals for the sustainable century: From aluminium to zirconium. *Sustainability*. 2021;13:10855. https://doi.org/10.3390/su131910855
10. Spandler C., Morris C. Geology and genesis of the Toongi rare metal (Zr, Hf, Nb, Ta, Y and REE) deposit, NSW, Australia, and implications for rare metal mineralization in peralkaline igneous rocks. *Contributions to Mineralogy and Petrology*. 2016;171(121):104. https://doi.org/10.1007/s00410-016-1316-y
11. Xulu S., Phungula P.T., Mbatha N., Moyo I. Multi-year mapping of disturbance and reclamation patterns over tronox's Hillendale mine, South Africa with DBEST and google earth engine. *Land*. 2021;10(7):760. https://doi.org/10.3390/land10070760
12. Bykhovsky L.Z., Remizova L.I., Chebotareva O.S. Zirconium resources of Russia: current state and prospects of the mineral resources base development. *Mineral Recourses of Russia. Economics and Management*. 2017;(2):11–18. (In Russ.)
13. Olivo G.R., Williams-Jones A.E. Hydrothermal REE-Rich eudialyte from the Pilanesberg Complex, South Africa. *Canadian Mineralogist*. 1999;37(3):653–663. URL: https://rruff.info/doclib/cm/vol37/CM37_653.pdf

14. Andersen A. K., Larson P. B., Neill O. K., Clark J. G. Mineral chemistry and petrogenesis of a HFSE(+HREE) occurrence, peripheral to carbonatites of the Bear Lodge alkaline complex, Wyoming. *American Mineralogist*. 2016;101(7):1604–1623. https://doi.org/10.2138/am-2016-5532
15. Laverov N. P., Patyk-Kara N. G. (Eds.) *Placer deposits of Russia and other CIS countries* (*Mineralogeny, industrial types, strategy of mineral resource base development*). Moscow: Nauchny Mir; 1997. 479 p. (In Russ.)
16. Komliev O. O., Zhylkin S. V., Vasylenko S. P. et al. The role of neotectonic activations in the formation of the Ukrainian sub-province of titanium and titanium-zirconium placer deposits (scientific and applied aspects). In: *XIV International Scientific Conference "Monitoring of Geological Processes and Ecological Condition of the Environment"*. Kyiv, 10–3 November 2020. Code 169495. European Association of Geoscientists & Engineers; 2020. https://doi.org/10.3997/2214-4609.202056071
17. Riesgo García M. V., Krzemień A., Manzanedo del Campo M. Á. et al. Rare earth elements mining investment: It is not all about China. *Resources Policy*. 2017;53:66–76. https://doi.org/10.1016/j.resourpol.2017.05.004
18. Van Gorsel J. T. *Bibliography of the geology of Indonesia and surrounding areas*. Edition 7.1. 2020:1–2826. URL: https://www.vangorselslist.com/pdf/BIG_2020_All_7.1.pdf
19. Dong J., Ren J., Sun H. et al. Mineral resources and investment environment in Mozambique. *Geological Bulletin of China*. 2022;41(1):184–195. (In Chinese) https://doi.org/10.12097/j.issn.1671-2552.2022.01.014
20. Gediga J., Morfino A., Finkbeiner M. et al. Life cycle assessment of zircon sand. *International Journal of Life Cycle Assessment*. 2019;24(11):1976–1984. https://doi.org/10.1007/s11367-019-01619-5
21. Ngo Ch. T. Q., Kirichenko Yu. V. Mineral potential of subsea deposits in Vietnamese part of South China Sea. *Russian Mining Industry.* 2020;(1):140–143. (In Russ.)
22. Salikova N. S., Kutsenko N. Y., Zhakupova S. B., Urazbayeva S. E. Economic prospects for development of the titanium-zirconium deposit. *Actual Scientific Research in the Modern World*. 2021;(4–10):69–73. (In Russ.)
23. Sachkov V. I., Nefedov R. A., Amelichkin I. V. et al. Processing of zircon concentrate from the Obukhov Deposit. *Bulletin of Tomsk State University. Chemistry*. 2023;(29):83–92. (In Russ.)
24. Jalloh A. B., Sasaki K., Thomas M. O., Jalloh Y. The geology, mineral resources of Sierra Leone and how the resources can be used to develop the nation. *Procedia Earth and Planetary Science*. 2013;6:131–138. https://doi.org/10.1016/j.proeps.2013.01.018
25. Das S. K. Characteristics of zircon of Chhatrapur Beach Placer Deposit, Ganjam District, Odisha. *Journal of the Geological Society of India*. 2015;86(4):383-390. https://doi.org/10.1007/s12594-015-0326-0
26. Angusamy N., Sahayam J. D., Gandhi M. S., Rajamanickam G. V. Coastal placer deposits of Central Tamil Nadu, India. *Marine Georesources and Geotechnology*. 2005;23(3):137–174. https://doi.org/10.1080/10641190500192102
27. Kain V., Sinha D. K., Singh D., Asnani C. K. Atomic minerals: journey of India to self-sufficiency. *Current Science*. 2022;123(3):293–309. https://doi.org/10.18520/cs/v123/i3/293-309
28. Sabedot S., Wotruba H., Sampaio C. H. et al. Mineral processing of low quality zircon concentrates and preconcentrates. *Transactions of the Institutions of Mining and Metallurgy, Section C: Mineral Processing and Extractive Metallurgy*. 2009;118(2):114–121. https://doi.org/10.1179/174328509X408270
29. Mohanty S., Adikaram M., Sengupta D. et al. Geochemical, mineralogical and textural nature of beach placers, north-east Sri Lanka: Implications for provenance and potential resource. *International Journal of Sediment Research.* 2022;38(2):279–293. https://doi.org/10.1016/j.ijsrc.2022.09.004
30. Khatkov V. Yu., Boyarko G. Yu., Bolsunovskaya L. M. et al. Russian zirconium industry: current issues in raw material supply. *Mining Science and Technology* (*Russia*). 2023;8(2):128–140. https://doi.org/10.17073/2500-0632-2023-02-83
31. Kabanov A. A., Akhmadshin N. Yu. Tuganskoe deposit – the first-born of industrial development of titanium-zirconium placers in Russia. *Gornyi Zhurnal.* 2021;(10):54–64. (In Russ.)
32. Leontev L. I. Prospects for the development of the titanium potential of the Yareg deposit. *Prospect and Protection of Mineral Resources.* 2021;(8):56–60. (In Russ.)
33. Patyk-Kara N. G., Bochneva A. A., Chizhova I. A. et al. Mineral assemblages of titanium-zirconium sands at the central deposit, the East European platform. *Geology of Ore Deposits*. 2018;50:218–239. https://doi.org/10.1134/S1075701508030045 (Orig. ver.: Patyk-Kara N. G., Bochneva A. A., Chizhova I. A. et al. Mineral assemblages of titanium-zirconium sands at the central deposit, the East European platform. *Geologiya Rudnyh Mestorozhdenij*. 2008;50(3):246–270. (In Russ.))
34. Drachev V. G. Technical and economical substantiation of the technology for development of alluvial titanium-zirconium deposit. *Gornyi Zhurnal*. 2006;(8):15–19. (In Russ.)

35. Bykhovsky L.Z., Vasilyev A.T., Zabirko A.G. On the development project for the Beshpagirskoye complex rare metal-titanium placer deposit. *Mineral Resources of Russia. Economics and Management*. 2010;(2):68–75. (In Russ.)
36. Grishkin N.N. The Tarskoye deposit ilmenite-rutile-zircon sands dressability study with production of titanium-containing concentrates. *Obogashchenie Rud*. 2005;(4):47–48. (In Russ.)
37. Gongalsky B., Krivolutskaya N. The Nb-Ta-Zr-REE-Y Katugin deposit. *Modern Approaches in Solid Earth Sciences*. 2019:257–271. https://doi.org/10.1007/978-3-030-03559-4_10
38. Khertek A.K.O. Rare earth metals of Tuva and their deposits. *Natural Resources, Environment and Society*. 2020;(4):24–29. https://doi.org/10.24411/2658-4441-2020-10033
39. Alymova N.V., Vladykin N.V. Ore-Content of rare-metal granites of Zashikhinsky Massif (Irkutsk Region) and minerals concentrating Ta, Nb, Th, Zr, TR. *The Bulletin of Irkutsk State University. Series Earth Sciences*. 2018;25:15–29. (In Russ.) https://doi.org/10.26516/2073-3402.2018.25.15
40. Zozulya D.R., Lyalina L.M., Eby N., Savchenko Ye.E. Ore geochemistry, zircon mineralogy, and genesis of the Sakharjok Y-Zr deposit, Kola Peninsula, Russia. *Geology of Ore Deposits*. 2012;54(2):81–98. https://doi.org/10.1134/S1075701512020079 (Orig. ver.: Zozulya D.R., Lyalina L.M., Eby N., Savchenko Ye.E. Ore geochemistry, zircon mineralogy, and genesis of the Sakharjok Y-Zr deposit, Kola Peninsula, Russia. *Geologiya Rudnykh Mestorozhdenii*, 2012;54(2):99–118. (In Russ.))
41. Kogarko L.N. Features of eudialyte ore formation in high-alkaline magmas of the Lovozero deposit (Kola peninsula). *Doklady Earth Sciences*. 2021;496(2):112–114. https://doi.org/10.1134/S1028334X21020082 (Orig. ver.: Kogarko L.N. Features of eudialyte ore formation in high-alkaline magmas of the Lovozero deposit (Kola peninsula). *Doklady Rossijskoj Akademii Nauk. Nauki o Zemle*. 2021;496(2):128–131. (In Russ.) https://doi.org/10.31857/S2686739721020080)
42. Bagdasarov Yu.A., Pototskiy Yu.P., Zinkova O.N. Baddeleyite-containing stratiform bodies in old carbonate sequences. A possible new genetic type of zirconium deposits. *Reports of the USSR Academy of Sciences. Earth science sections*. 1990;315(6):144–148.
43. Gysi A.P., Williams-Jones Anthony E., Collins P. Lithogeochemical vectors for hydrothermal processes in the Strange Lake peralkaline granitic REE-Zr-Nb deposit. *Economic Geology*. 2016;111(5):1241–1276. https://doi.org/10.2113/econgeo.111.5.1241
44. Sheard E.R., Williams-Jones A.E., Heiligmann M. et al. Controls on the concentration of zirconium, niobium, and the rare earth elements in the Thor Lake rare metal deposit, Northwest Territories, Canada. *Economic Geology*. 2012;107(1):81–104. https://doi.org/10.2113/econgeo.107.1.81
45. Möller V., Williams-Jones A.E. Magmatic and hydrothermal controls on the mineralogy of the basal zone, Nechalacho REE-Nb-Zr deposit, Canada. *Economic Geology*. 2017;112(8):1823–1856. https://doi.org/10.5382/econgeo.2017.4531
46. Constantin M., Matte S. *Mineralogical and geochemical characterisation of the Kipawa syenite complex, Quebec: implications for rare-earth element deposits.* Scientific Presentation 129. Geological Survey of Canada; 2022. 36 p. https://doi.org/10.4095/329212
47. Marshall G.M., Patarachao B., Moran K.E., Mercier P.H.J. Zircon mineral solids concentrated from Athabasca oil sands froth treatment tailings: Surface chemistry and flotation properties. *Minerals Engineering*. 2014;65:79–87. https://doi.org/10.1016/j.mineng.2014.05.016
48. Lohmeier S., Lottermoser B.G., Strauß K. et al. Nearshore marine garnet and magnetite placers in the Erongo and S-Kunene regions, Namibia. *Journal of African Earth Sciences*. 2021;180:104221. https://doi.org/10.1016/j.jafrearsci.2021.104221
49. Abouzeid A.-Z.M., Khalid A.-A.M. Mineral industry in Egypt-Part I: metallic mineral commodities. *Natural Resources*. 2011;2(1):35–53. https://doi.org/10.4236/nr.2011.21006
50. Ndjigui P.-D., Bassanak Ongboye P.R., Ndong Bidzang F. TiO2–Zr–Th–Y–rare-earth elements ore deposit in unconsolidated fine-grained sediments from Tongo Gandima in the Bétaré Oya Gold district, Eastern Cameroon. *Geological Journal*. 2021;56(5):2676–2698. https://doi.org/10.1002/gj.4061
51. Bulatov K.V., Gazaleeva G.I., Shikhov N.V., Nazarenko L.N. Development of a beneficiation scheme for titanium-zirconium sands of the Shokash deposit, North Kazakhstan. *Obogashchenie Rud*. 2023;(6):3–8. (In Russ.) https://doi.org/10.17580/or.2023.06.01
52. Sapargaliev E.M., Azelkhanov A.Zh., Kravchenko M.M. et al. Prospects for the practical value of the integrated development of poor titanium-zirconium placers and weathering crusts in Kazakhstan. *Perm Journal of Petroleum and Mining Engineering*. 2021;21(1):17–22. (In Russ.) https://doi.org/10.15593/2712-8008/2021.1.3
53. Mohanty S., Adikaram M., Sengupta D., et al. Geochemical, mineralogical and textural nature of beach placers, north-east Sri Lanka: Implications for provenance and potential resource. *International Journal of Sediment Research*. 2022;38(2):279–293. https://doi.org/10.1016/j.ijsrc.2022.09.004

54. Hasan A.S.M.M., Hossain I., Rahman Md.A. et al. Chemistry and mineralogy of Zr- and Ti-rich minerals sourced from Cox's Bazar Beach placer deposits, Bangladesh: Implication of resources processing and evaluation. *Ore Geology Reviews*. 2022;141:104687. https://doi.org/10.1016/j.oregeorev.2021.104687
55. Qiu K., Yu H., Wu M. et al. Discrete Zr and REE mineralization of the Baerzhe rare-metal deposit, China. *American Mineralogist*. 2019;104(10):1487–1502. https://doi.org/10.2138/am-2019-6890
56. Kovalenko V.I. The peralkaline granite-related Khaldzan-Buregtey rare metal (Zr, Nb, REE) deposit, Western Mongolia. *Economic Geology*. 1995;90(3):530–547. https://doi.org/10.2113/gsecongeo.90.3.530
57. Sun Z., Qin K., Mao Y. et al. Mineral chemistry of pyrochlore supergroup minerals from the Boziguoer Nb-Ta-Zr-Rb-REE deposit, NW China: Implications for Nb Enrichment by Alkaline Magma Differentiation. *Minerals*. 2022;12(7):785. https://doi.org/10.3390/min12070785
58. Yan S., Shan Q., Niu H.-C., et al. Timing and genesis of the Tudiling trachyte Nb-Ta-Zr-REE deposit in the South Qinling (Central China): Implications for rare metal enrichment in extrusive peralkaline magmatic systems. *Ore Geology Reviews*. 2021;139(Part B):104535. https://doi.org/10.1016/j.oregeorev.2021.104535
59. Schønwandt H.K., Barnes G.B., Ulrich T. Chapter 5 – A description of the world-class rare earth element deposit, Tanbreez, South Greenland. In: de Lima I. B., Leal Filho W. (Eds.) *Rare Earths Industry: Technological, Economic, and Environmental Implications*. Amsterdam: Elsevier; 2015. Pp. 73–85. https://doi.org/10.1016/B978-0-12-802328-0.00005-X
60. Sjöqvist A., Cornell D.H., Andersen T. et al. Three compositional varieties of rare-earth element ore: eudialyte-group minerals from the Norra Kärr alkaline complex, Southern Sweden. *Minerals*. 2013;3(1):94–120. https://doi.org/10.3390/min3010094
61. Tolbert G.E. *The uraniferous zirconium deposits of the Pocos de Caldas Plateau, Brazil*. U.S. Geological Survey Bulletin 1185-C. 1966. 28 p. https://doi.org/10.3133/b1185C
62. Wu B., Wang R.-C., Yang J.-H. et al. Zr and REE mineralization in sodic lujavrite from the Saima alkaline complex, northeastern China: A mineralogical study and comparison with potassic rocks. *Lithos*. 2016;262:232–246. https://doi.org/10.1016/j.lithos.2016.07.013
63. Marker A., Friedrich G., Carvalho A., Melfi A. Control of the distribution of Mn, Co, Zn, Zr, Ti and REEs during the evolution of lateritic covers above ultramafic complexes. *Journal of Geochemical Exploration*. 1991;40(1–3):361–383. https://doi.org/10.1016/0375-6742(91)90048-Y
64. Pulat O., Karakaş M., Yasti M. A. Relationship of ore properties and alteration of the Büyük Kuluncak (Malatya) Nb–U–NTE–Zr–Li deposit. *Bulletin of the Mineral Research and Exploration*. 2022;167(167):127–148. https://doi.org/10.19111/bulletinofmre.973626
65. Wells H.C., Haverkamp R.G. Characterization of the heavy mineral suite in a holocene beach placer, Barrytown, New Zealand. *Minerals*. 2020;10(2):86. https://doi.org/10.3390/min10020086
66. Chanturiya V.A., Minenko V.G., Ryzanceva M.V., Samusev A.L. Complex Processing of eudialyte concentrate. *Tsvetnye Metally*. 2024;(12):47–56. (In Russ.) https://doi.org/10.17580/tsm.2024.12.05
67. Boyarko G.Yu. Basic and associated commercial components of complex mineral raw materials: technological and economic problems of their extraction and selling. *Mineral Recourses of Russia. Economics and Management.* 2024;(5):74–80. (In Russ.)
68. Luo F., Liu W., Xu M. et al. Evolution characteristics and invulnerability simulation analysis of global zirconium ore trade. *Frontiers in Earth Science*. 2025;12:1496579. https://doi.org/10.3389/feart.2024.1496579

Information about the authors

Grigory Yu. Boyarko – Dr. Sci. (Econ.), Cand. Sci. (Geol. and Min.), Professor of the Oil and Gas Engineering Department, National Research Tomsk Polytechnic University, Tomsk, Russian Federation; ORCID 0000-0002-0715-7807, Scopus ID 56350674500, SPIN 8069-7686; e-mail gub@tpu.ru

Liudmila M. Bolsunovskaya – Cand. Sci. (Philolog.), Associate Professor of the Foreign Languages Department, School of Social Sciences, National Research Tomsk Polytechnic University, Tomsk, Russian Federation; ORCID 0000-0002-1499-8970, Scopus ID 56350747600, SPIN 2542-1748; e-mail bolsunovskl@tpu.ru

Received 26.08.2025
Revised 27.12.2025
Accepted 14.01.2026

MINING ROCK PROPERTIES. ROCK MECHANICS AND GEOPHYSICS

Research paper

https://doi.org/10.17073/2500-0632-2025-08-1015
UDC 622.817.3

Comparative analysis of coal permeability models accounting for the stress-strain state of the rock mass

A.I. Manevich[1], K.S. Kolikov[2], N.V. Ledyaev[3], I.V. Losev[1], D.Zh. Akmatov[1], R.V. Shevchuk[1]

[1] *Geophysical Center of the Russian Academy of Sciences, Moscow, Russian Federation*
[2] *University of Science and Technology MISIS, Moscow, Russian Federation*
[3] *JSC SUEK-Kuzbass, Leninsk-Kuznetsky, Russian Federation*
✉ *ai.manevich@yandex.ru*

Abstract

Coal seam permeability is a key parameter controlling degassing efficiency, the intensity of methane emission, and the safety of mining operations. As permeability decreases with depth and is critically dependent on the stress-strain state, its reliable prediction requires models capable of adequately describing the interaction between sorption-induced deformation, poroelastic effects, and fracture aperture closure mechanisms. Owing to the absence of a unified approach for permeability assessment under complex stress-strain conditions, the objective of this study was to systematize and compare the principal empirical and analytical models describing this dependence. To this end, an analytical review of models accounting for sorption-elastic deformation, porosity evolution, effective stress effects, thermoelastic behavior, and cleat system parameters was conducted. Model comparison was performed through numerical simulations of permeability variation over an effective stress range of 0–50 MPa and at depths of up to 1500 m. The models incorporated parameters such as the Biot coefficient, deformation modulus, sorption compressibility, initial permeability, and geometric characteristics of fractures. The results of the parametric calculations demonstrate that, despite conceptual differences, all models exhibit a common trend of nonlinear permeability reduction with increasing effective stress. This behavior reflects the physical processes of pore space compression and fracture aperture reduction. It was established that the most intensive permeability decline occurs within the effective stress range of 5–15 MPa, corresponding to active cleat closure, whereas at depths exceeding 1000 m permeability changes tend to stabilize due to exhaustion of the deformation potential of the fracture structure. Overall, the analysis revealed differing model sensitivities to geomechanical parameters, with the influence of sorption-induced deformation being comparable to that of poroelastic effects. Model selection is shown to be condition-dependent: the Seidle (1992) model is most suitable for accounting for sorption-induced deformation, the Palmer & Mansoori (1998) model for deep coal seams with variable porosity, and the Karkashadze & Hautiev (2015) model for describing elastic deformation effects. The derived relationships can be applied to assess the natural permeability of coal seams in undisturbed rock masses.

Keywords

coal seam, permeability, stress-strain state, sorption-induced deformation, effective stress, permeability models, degassing

Funding

This research was conducted at NUST MISIS with the support of the Russian Science Foundation, Project No. 23-19-00398.

For citation

Manevich A.I., Kolikov K.S., Ledyaev N.V., Losev I.V., Akmatov D.Zh., Shevchuk R.V. Comparative analysis of coal permeability models accounting for the stress-strain state of the rock mass. *Mining Science and Technology* (*Russia*). 2026;11(1):35–45. https://doi.org/10.17073/2500-0632-2025-08-1015

СВОЙСТВА ГОРНЫХ ПОРОД. ГЕОМЕХАНИКА И ГЕОФИЗИКА

Научная статья

Сравнительный анализ моделей зависимости фильтрационных свойств угля от напряженно-деформированного состояния массива

А.И. Маневич[1], **К.С. Коликов**[2], **Н.В. Ледяев**[3], **И.В. Лосев**[1], **Д.Ж. Акматов**[1], **Р.В. Шевчук**[1]

[1] *Геофизический центр РАН, г. Москва, Российская Федерация*

[2] *Университет науки и технологий МИСИС, г. Москва, Российская Федерация*

[3] *АО «СУЭК-Кузбасс», г. Ленинск-Кузнецкий, Российская Федерация*

✉ *ai.manevich@yandex.ru*

Аннотация

Проницаемость угольных пластов – ключевой параметр, определяющий эффективность дегазации, интенсивность метановыделения и безопасность горных работ. Поскольку проницаемость снижается с глубиной и критически зависит от напряжённо-деформированного состояния, для её прогноза необходимы модели, способные адекватно описывать взаимодействие сорбционных деформаций, пороупругих эффектов и механизма закрытия трещин. В связи с отсутствием унифицированного подхода к оценке проницаемости в условиях сложного НДС целью данной работы стали систематизация и сопоставление основных эмпирических и аналитических моделей этой зависимости. Для этого был выполнен аналитический обзор моделей, учитывающих сорбционно-упругие деформации, изменение пористости, влияние эффективного давления, термоупругие эффекты и параметры кливажа. Сопоставление моделей проведено путём численного моделирования изменения проницаемости в диапазоне эффективных напряжений 0–50 МПа и на глубинах до 1500 м. В модели были включены такие параметры, как коэффициент Био, модуль деформации, сорбционная сжимаемость, начальная проницаемость и геометрические характеристики трещин. Результаты вариационных расчётов показали, что несмотря на различия все модели демонстрируют общую тенденцию к нелинейному уменьшению проницаемости с ростом эффективного напряжения. Это отражает физические процессы сжатия порового пространства и закрытия трещин. Установлено, что наиболее интенсивное снижение проницаемости происходит в интервале 5–15 МПа, соответствующем активному закрытию трещин кливажа, тогда как на глубинах свыше 1000 м изменение проницаемости стабилизируется из-за исчерпания потенциала деформации трещинной структуры. Таким образом, анализ выявил различную чувствительность моделей к геомеханическим параметрам, причём влияние сорбционных деформаций оказалось сопоставимым с пороупругими эффектами. Выбор конкретной модели зависит от условий: для учёта сорбционных деформаций оптимальна модель Seidle (1992), для глубоких пластов с изменчивой пористостью – модель Palmer (1998), а для описания упругих деформаций – модель Каркашадзе и Хаутиева (2015). Полученные зависимости применимы для оценки природной проницаемости угольных пластов в ненарушенном массиве.

Ключевые слова

угольный пласт, проницаемость, напряжённо-деформированное состояние, сорбционные деформации, эффективное давление, модели проницаемости, дегазация

Финансирование

Исследование выполнено в НИТУ МИСИС при поддержке Российского научного фонда, проект № 23-19-00398.

Для цитирования

Manevich A.I., Kolikov K.S., Ledyaev N.V., Losev I.V., Akmatov D.Zh., Shevchuk R.V. Comparative analysis of coal permeability models accounting for the stress-strain state of the rock mass. *Mining Science and Technology* (*Russia*). 2026;11(1):35–45. https://doi.org/10.17073/2500-0632-2025-08-1015

Introduction

Accurate prediction of coal seam permeability directly affects the assessment of methane abundance in mine workings and the efficiency of pre-drainage operations. Unsubstantiated estimates of these parameters may, on the one hand, lead to reduced longwall production rates (and, consequently, lower coal output) and, on the other hand, to the manifestation of hazardous gas-dynamic processes in underground mines, posing risks to miner safety and the stability of mine workings [1].

Coal is formed in sedimentary basins where the accumulation of organic matter occurs under a wide range of tectonic settings, from stable platform regions to actively deforming fold-and-thrust belts [2]. Tectonic movements cause redistribution of sedimentary material and changes in pressure and temperature conditions. As a result, coal seams acquire complex structural features, including folding, faulting, and zones of tectonic mélange [2]. These processes are accompanied by the development of tectonic fracture systems, which may either enhance or reduce rock mass permeability depending on their orientation and scale [3, 4]. Fault zones are typically associated with increased fracturing and alterations in the filtration-storage properties of coal. In addition, faults induce stress redistribution within the rock mass, creating specific geomechanical conditions that significantly influence the permeability of the coal-bearing strata [5]. The surrounding host rocks also affect the mechanical behavior of the coal-bearing rock mass, albeit more locally. For example, strong and brittle rocks such as sandstones and limestones may form zones of elevated stress concentration, whereas weaker and more ductile layers (e.g., clay-rich rocks) facilitate stress redistribution [4, 6].

Coal permeability is primarily governed by its fracture density and porosity. A spatially variable stress field involving compression, tension, and shear promotes the formation of faults and microfractures, thereby increasing the volume of void space [4]. However, the influence of the stress-strain state of the coal-bearing rock mass on methane emission from coal seams is not unambiguous. An increase in stress may lead to a reduction in fracture permeability due to cleat closure, whereas stress relief is commonly associated with an increase in fracture aperture and enhanced permeability [5]. At the same time, structural changes in the mineral skeleton of the coal-bearing rock mass may intensify methane desorption from coal micropores [3, 4].

The aim of this study is to perform a comparative analysis of existing empirical and analytical models describing the dependence of coal permeability on the stress-strain state. To achieve this aim, the following objectives were addressed: (1) analysis of the mathematical framework of coal permeability models accounting for the stress-strain state of the coal-bearing rock mass; (2) a systematic analytical review of existing models of this type; (3) numerical simulation of permeability variations over an effective stress range of 0–50 MPa and depths of 0–1500 m to compare model behavior; (4) assessment of model sensitivity to their intrinsic hyperparameters and determination of applicability limits; and (5) development of practical recommendations for selecting permeability models for filtration modeling of coal-bearing rock masses.

Data and methods

The coal matrix exhibits a unique ability to swell during gas adsorption and to contract during desorption. During methane desorption, gas diffuses through the coal matrix into the natural fracture network of coal, commonly referred to as the coal cleat system [3]. Within the matrix of hard coal, fractures of endogenous and exogenous cleat are distinguished, while fracture transmissivity depends on their density, aperture, orientation, persistence, and other parameters [3, 7]. Endogenous cleat forms during coalification and is controlled by internal processes associated with changes in coal composition during its genesis [8]. It is typically represented by two mutually orthogonal cleat sets – the face cleat and the butt cleat [9] (Fig. 1, *a*).

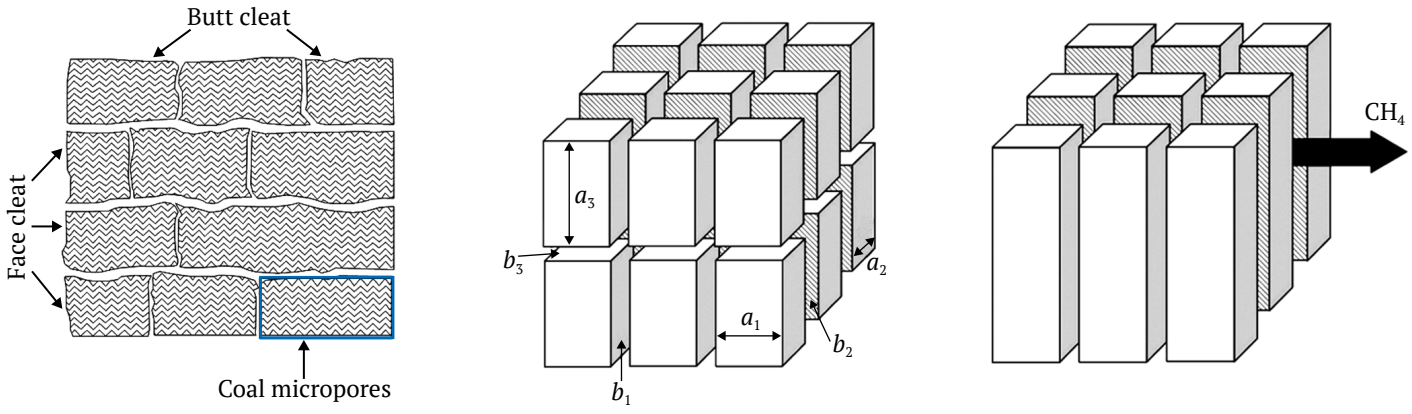

Fig. 1. Coal matrix model [9] and cellular (cubic) permeability model of the coal matrix [10, 14]:
a – coal matrix model; *b* – anisotropic model: a_1, a_2, a_3 – the edge lengths of the cubic cells (intact coal matrix blocks), b_1, b_2, b_3 – the effective fracture apertures associated with the cleat systems; *c* – isotropic model

In general, absolute permeability can be derived from the Navier–Stokes equations for viscous fluid flow. In practice, however, due to limited availability of detailed information, Darcy's law is commonly applied [10]. It is generally assumed that Darcy flow in coal is governed by flow within the cleat system, while the contribution of flow through matrix pores is negligible. Fracture permeability typically ranges from 0.001 to 100 mD, whereas the permeability of coal microblocks is on the order of microdarcies or nanodarcies [9, 11, 12]. Consequently, coal seam permeability is primarily controlled by the cleat system [8]. The presence of cleat results in pronounced permeability anisotropy. Experimental studies indicate that the ratio of permeability along the face cleat to that along the butt cleat varies from 2:1 to 17:1 [11, 13]. In this case, the components of the absolute permeability tensor of coal can be described using a model of a homogeneous impermeable medium intersected by two mutually orthogonal fracture systems [10]:

$$q = -\frac{b_i^3}{12a_i}\frac{1}{\mu}\Delta P, \quad (1)$$

where b_i is the fracture aperture, m, and a_i is the edge length of the cubic cell, m.

Equation (1) is applied to a single cleat system i contributing to the overall flow. Considering the roughness of the fracture-pore space, the parameter b_i is referred to as the effective hydraulic aperture and is typically smaller than the corresponding cell edge a_i. The absolute permeability of the cleat system is determined according to Scheidegger [15]:

$$k_{abs} = -\frac{b_i^3}{12a_i}, \quad (2)$$

or, in ratio form,

$$\frac{k_i}{k_{i_0}} = \left(\frac{b_i}{b_{i_0}}\right)^3, \quad (3)$$

where b_i is the effective fracture aperture, m; k_i is the effective phase absolute permeability of the medium, m^2; b_{i_0} is the initial fracture aperture, m; and k_{i_0} is the initial absolute permeability, m^2.

The stress-strain state of a mined coal seam is primarily controlled by the lateral stress coefficient, mining depth, physico-mechanical properties of the rocks, structural heterogeneities, and sorption-kinetic properties of the rock mass.

Vertical stresses acting within the rock mass give rise to lateral confinement stresses. Several approaches exist for estimating lateral stress [16]: according to A. Heim, lateral stress in the rock mass equals lithostatic pressure, analogous to hydrostatic conditions; according to A.N. Dinnik, lateral stress is defined by the lateral stress coefficient characterizing elastic horizontal response to the weight of overlying strata; according to N. Hast, lateral stress includes, in addition to the Dinnik component, tectonic stresses induced by the regional tectonic stress field. In some parts of the Earth's crust, horizontal tectonic stresses may even exceed lithostatic values, as confirmed by instrumental measurements [16, 17].

Mechanical or thermal loading of coal induces a range of sorption-related effects that result in expansion or contraction of the rock material [6, 9]. As a consequence, an additional and distinct component of the stress-strain state – sorption-induced stress – develops within the coal mass. The magnitude of sorption-induced deformation (and, consequently, stress) depends on gas saturation, gas pressure, temperature, as well as structural and textural characteristics of coal. Coal with high microporosity exhibits greater gas adsorption capacity, which enhances swelling effects. The relationship between stress and sorption-induced deformation in coal can be described using a generalized elasticity law modified to include sorption effects analogous to thermal expansion [18–20]. For a linear elastic medium, this relationship can be expressed as:

$$\sigma_{ij} = C_{ijkl} \times \varepsilon_{ij} + K_s \varepsilon_s \delta_{ij}, \quad (4)$$

where K_s is the sorption modulus characterizing the influence of gas sorption-induced deformation; ε_s is the sorption strain caused by gas adsorption or desorption; δ_{ij} is the Kronecker delta ($\delta_{ij} = 1$ if $i = j$, and $\delta_{ij} = 0$ if $i \neq j$).

In coal permeability models, the dependence of permeability on the stress state is commonly expressed in terms of effective stress. The effective stress tensor is defined as:

$$\sigma_{eff,\,ij} = \sigma_{ij} - \omega P_f \delta_{ij}, \quad (5)$$

where σ_{ij} are the components of the total stress tensor; ω is the Biot coefficient (dimensionless); P_f is the pore fluid pressure, Pa; and δ_{ij} is the Kronecker delta ($\delta_{ij} = 1$ if $i = j$, and $\delta_{ij} = 0$ if $i \neq j$).

Thus, the generalized stress model for a coal-bearing rock mass comprises several principal components: lithostatic stress σ_g, lateral confinement stress σ_r, tectonic stress σ_{tect}, thermal stress σ_{th}, and sorption-induced stress σ_s.

Dependence of coal permeability on the stress-strain state and practical implications

In empirical models describing the dependence of permeability on the stress-strain state, the mean stress within the rock mass is commonly used. Factors related to sorption-induced deformation and pore pressure are typically incorporated at the macroscale.

Below, the principal empirical models are reviewed; for consistency and comparability, they are recast into a unified analytical form.

One of the earliest models of this type was proposed in [21] as an empirical relationship between permeability and mean stress, based on laboratory data obtained from coal samples collected from the Pittsburgh and Virginia coalfields (USA). The distinguishing feature of this model is that it accounts solely for stress-induced changes in fracture aperture resulting from mechanical loading:

$$k_\sigma = k_0\left[e^{(-3\cdot 10^{-3}\cdot\sigma\cdot k_0^{-0,1})} + 2\cdot 10^{-4}\cdot\sigma^{\frac{1}{3}}\cdot k_0^{\frac{1}{3}}\right], \quad (6)$$

where k_σ is stress-dependent permeability, mD; k_0 is permeability at zero stress, mD; and σ is the mean normal stress, Pa.

In [22], an empirical relationship between permeability and effective stress was proposed for coals from the Leigh Creek Basin (Australia):

$$k_\sigma = 1.013\cdot 10^{-0.031\cdot\sigma_{eff}}. \quad (7)$$

This relationship was subsequently generalized into an exponential form that serves as a basis for more advanced permeability models:

$$k_\sigma = k_0\exp(-C_p\cdot\sigma_{eff}), \quad (8)$$

where k_σ is the current coal seam permeability under effective stress, m²; k_0 is the natural (initial) permeability of the coal seam in the absence of applied stresses, m²; C_p is the permeability sensitivity coefficient with respect to effective stress, Pa⁻¹ (typically ranging from 0.01 to 0.1 Pa⁻¹ depending on fracture structure); and σ_{eff} is the effective stress, Pa.

Model [23] accounts for the influence of sorption-induced deformation on fracture aperture variations. In contrast to the previous models, it employs changes in stress and strain rather than their absolute values:

$$k_\sigma = k_0\exp(-3C_p\Delta\sigma_{eff}\cdot S\Delta\varepsilon_s), \quad (9)$$

where $\Delta\sigma_{eff}$ is the change in effective stress, Pa; $\Delta\varepsilon_s$ is the change in sorption strain caused by variations in the amount of adsorbed gas; and S is the permeability sensitivity coefficient with respect to sorption-induced deformation. The parameter S typically varies in the range 0.1–1.0 (other parameters are identical to those in model [22]).

Model [24] also incorporates the effect of sorption-induced deformation on fracture behavior; however, unlike model [23], it uses absolute values of stress and strain:

$$k_\sigma = k_0\exp(-C_p\cdot\sigma_{eff} + (1-\gamma)\Delta\varepsilon_s), \quad (10)$$

where γ is the sorption deformation compensation coefficient, varying between 0 and 1 (other parameters are consistent with models [22, 23]).

Models [25, 26], which further develop model [23], explicitly include coal porosity and sorption-induced deformation within a Darcy-flow framework. These models are based on changes in deformation and stress within the rock mass:

$$k_\sigma = k_0\left(\frac{\varphi}{\varphi_0}\right)^n\exp(-3C_p\Delta\sigma_{eff} + S\Delta\varepsilon_s), \quad (11)$$

where φ is the current coal seam porosity under effective stress (fraction); φ_0 is the initial porosity in the absence of applied stresses (fraction); and n is an empirical exponent typically ranging from 1 to 3 (other parameters correspond to those in model [23]).

Model [27] proposes an alternative formulation to model [22] by explicitly accounting for the deformation properties of the rock. Its distinguishing feature is the use of mean stress and Young's modulus in explicit form:

$$k_\sigma = k_0\cdot 10^{-0.31\cdot 10^{-6}\cdot(\sigma_0-\sigma)\cdot\frac{E}{E_0}}. \quad (12)$$

In a generalized form, the model can be expressed as:

$$k_\sigma = k_0\cdot 10^{-C_p\cdot 10^{-6}\cdot(\sigma_0-\sigma)\cdot\frac{E}{E_0}}, \quad (13)$$

where σ is the current mean normal stress, Pa; σ_0 is the initial mean normal stress, Pa; E is the current Young's modulus of the rock under mean stress, Pa; E_0 is the initial Young's modulus in the absence of applied stresses, Pa; C_p is the permeability sensitivity coefficient with respect to effective stress, Pa⁻¹. The coefficient C_p typically ranges from 0.01 to 0.1 Pa⁻¹, depending on fracture structure.

The mean normal stress is defined as:

$$\sigma = \frac{\sigma_{xx} + \sigma_{yy} + \sigma_{zz}}{3}. \quad (14)$$

Using a lithostatic stress model combined with lateral stress estimated following the Dinnik approach enables evaluation of depth-dependent variations in mean and effective stress:

$$\sigma_z = \rho\cdot g\cdot H,$$
$$\sigma_{x,y} = \sigma_z\cdot\frac{\mu}{1-\mu}, \quad (15)$$

Fig. 2, *a* presents the calculated permeability-effective stress relationships for five models: Gray (1987) [22], Seidle (1992) [23], Palmer & Mansoori (1998) [24], Shi & Durucan (2004) [25, 26], and Karkashadze & Hautiev (2015) [27]. Using the same data, permeability-depth relationships can be derived (Fig. 2, *b*). All models exhibit a common trend of nonlinear permeability reduction with increasing effective stress, reflecting the physical processes of pore space compression and fracture closure within coal seams under external loading.

At the same time, each model incorporates different physical and geomechanical mechanisms, resulting in distinct curve shapes.

The results of the comparative analysis demonstrate significant practical relevance for the coal mining industry. The derived relationships (Fig. 2) can be applied in the development of three-dimensional geomechanical and filtration models of coal-bearing rock masses used to assess degassing efficiency, gas-dynamic behavior of coal seams, and methane abundance in mine workings. Appropriate selection of a permeability model reduces uncertainty in the design of degassing systems, optimizes the placement and parameters of drainage boreholes, decreases the number of ineffective drilling operations, and mitigates the risk of gas-dynamic hazards. The expected economic benefits are associated with increased longwall productivity and reduced costs of degassing operations.

Sensitivity analysis of permeability-stress relationships and discussion of results

Analytical permeability models require data on the microstructural characteristics of coal, reservoir pressure parameters, fluid distribution within the coal-bearing rock mass, and the stress state governing coal deformation. However, at the scale of coal seam permeability modeling, acquiring such detailed information is practically infeasible. In this context, empirical relationships are more appropriate, as they enable coal seam permeability to be described through stress-state parameters. This simplifies the modeling procedure and makes it feasible in practice; however, reliable application of such relationships requires an assessment of model sensitivity and applicability limits.

Based on the analysis performed, the following criteria are proposed for model selection:

– the dominant deformation mechanisms in the seam (sorption-induced, thermoelastic, poroelastic, and structural porosity changes);

– coal seam depth and the expected range of effective stress, which control the shape of the permeability reduction curve;

– microstructural characteristics of the reservoir (presence of a well-developed cleat system and porosity sensitivity to pressure);

– approximate gas saturation and the intensity of sorption processes;

– contrasts in elastic properties among different coal ranks.

To evaluate model sensitivity to stress terms in their governing equations, a set of parametric (variation) calculations was performed by varying the stress values. Model sensitivity is defined as the derivative of permeability with respect to effective stress [28]. It characterizes the rate at which permeability changes as stress increases and is expressed as the following gradient:

$$Sens = \frac{\partial k}{\partial \sigma_{eff}}. \quad (16)$$

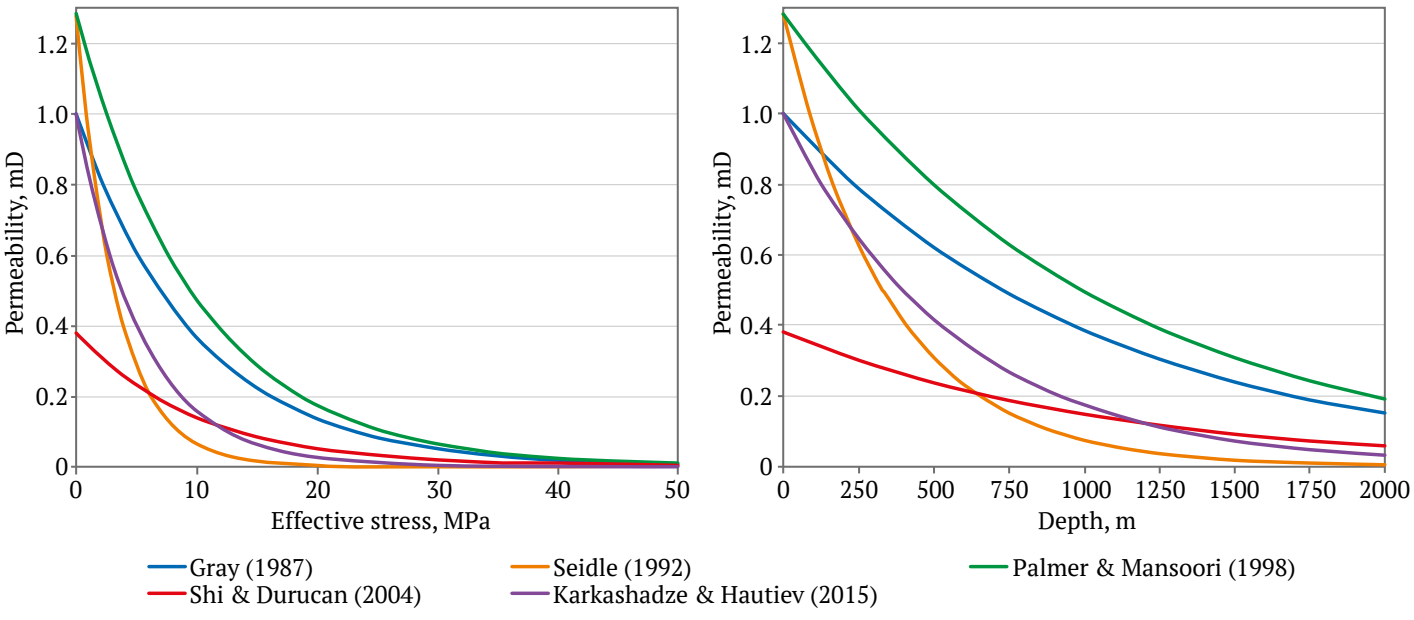

Fig. 2. Permeability as a function of effective stress (*a*) and coal seam depth (*b*) for different model (calculations performed using the following constants: $C_p = 0.1$ Pa^{-1}; $k_0 = 1 \cdot 10^{-12}$ m^2 (1 mD); $\Delta\varepsilon_s = 0.5$; $S = 0.5$; $\gamma = 0.5$; $\varphi_0 = 0.03$; $\varphi = 0.02$; $E_0 = 5 \cdot 10^9$; $E = 3 \cdot 10^9$)

Sensitivity reflects the rate of permeability change in response to stress variations. High (absolute) sensitivity implies a more rapid reduction in permeability with increasing stress, whereas low sensitivity indicates a more gradual change. To determine applicability limits, the sensitivity analysis was carried out for the stress-dependent terms in each model using the parametric calculations described above. The calculation parameters are summarized in Table 1. The full set of results for all models is available as a dataset in the Zenodo repository: https://zenodo.org/records/18441537.

Table 1

Model parameters

No.	Model parameters	Parameter ranges
1	Variable parameters	C_p = 0.01; 0.05; 0.1 Pa^{-1} σ_{eff} = 0–50 MPa $\Delta\sigma_{eff}$ = 0–50 MPa $\Delta\varepsilon_s$ = 0.005; 0.05; 0.5 S = 0.1; 0.5; 1.0 E = 3·10^9; 4·10^9; 5·10^9 Pa γ = 0.1; 0.5; 1.0 φ = 0.025; 0.035; 0.045 n = 1, 2, 3
2	Constants	k_0 = 1·10^{-12} m^2 (1 mD) C_p = 0.1 $\Delta\varepsilon_s$ = 0.5 Σ = 0.5 γ = 0.5 φ_0 = 0.03 E_0 = 5·10^9 σ_0 = 0 MPa

The Gray (1987) model [22] describes permeability as a simple exponential function of effective stress (Fig. 3). This is a baseline model that accounts solely for compression of the pore space as stress increases. Permeability decreases rapidly at low stress levels and gradually stabilizes at higher stresses. The model exhibits moderate sensitivity and is commonly used as a reference for comparison with more advanced formulations. Owing to the absence of additional parameters, it is less suitable for site-specific conditions where sorption-related, thermal, or mechanical deformation effects must be considered.

The Seidle (1992) model [23] predicts a more pronounced reduction in permeability at low effective stress values, which is attributed to the influence of sorption-induced deformation. The model introduces an additional parameter, ε_s, representing sorption strain caused by gas adsorption or desorption (methane or carbon dioxide), as well as the parameter S, which characterizes the sensitivity of the sorption contribution. As a result, permeability decreases more rapidly within the effective stress range of 0–5 MPa. This model is particularly suitable for evaluating in situ coal masses where sorption effects are expected to play a significant role.

The Palmer & Mansoori (1998) model [24] exhibits a smoother permeability decline compared with models [22, 23], owing to its consideration of the combined effects of sorption-induced and thermal deformation. The parameter γ allows the influence of deformation associated with temperature variations and gas sorption to be represented. At low stress levels, the model behavior is similar to that of the Gray

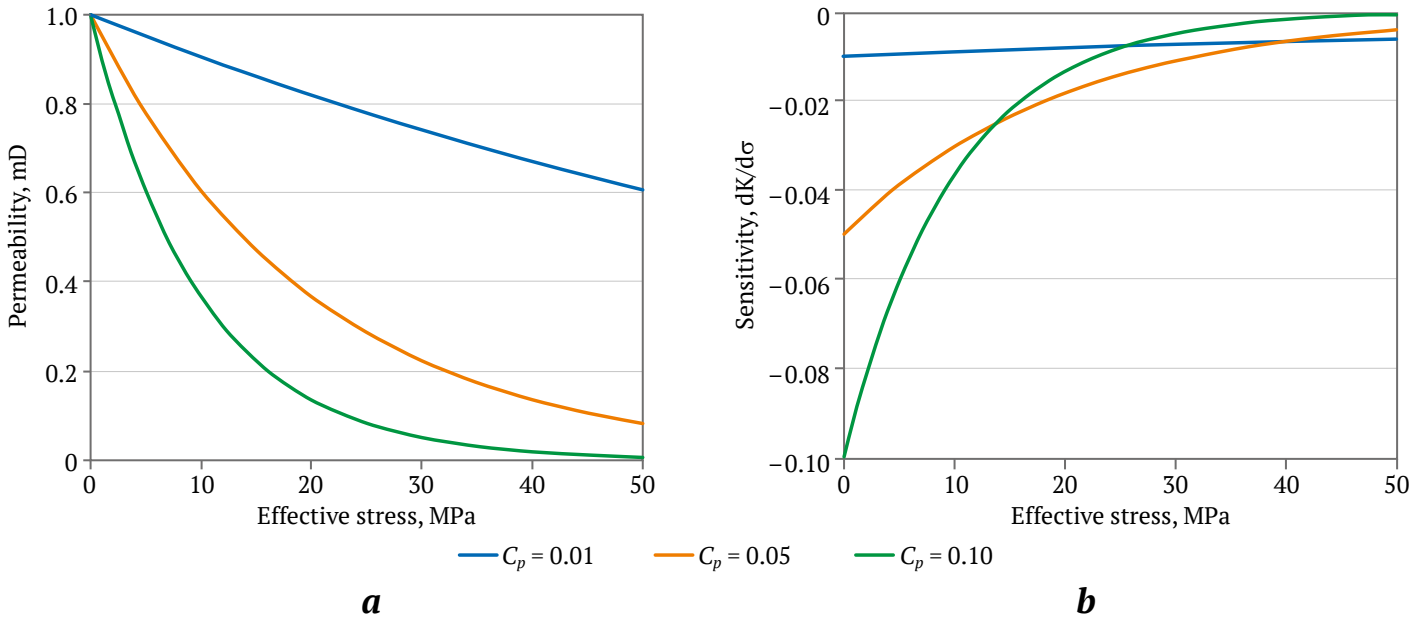

Fig. 3. Sensitivity analysis of the Gray (1987) model [22]. Permeability (*a*) and sensitivity (*b*) as functions of effective stress for different values of the coefficient C_p

model [22]; however, as stress increases, the permeability reduction becomes more gradual. This model is well suited for assessing the natural permeability of coal-bearing rock masses at greater depths, where variations in the geothermal gradient become increasingly important.

The Shi & Durucan (2004) model [25, 26] explicitly incorporates the effect of porosity on permeability. Permeability is expressed as a power-law function of porosity φ, normalized to its initial value φ_0. The model includes the exponent n, which controls the degree of porosity influence, as well as the sorption strain parameter ε_s. Among the models considered, it demonstrates the most uniform permeability reduction, particularly at effective stress levels exceeding 10 MPa. This behavior reflects its dependence on porosity and its comparatively lower stress sensitivity. The model is therefore appropriate for evaluating the natural permeability of rock masses characterized by potentially variable pore structure within the mineral skeleton.

The Karkashadze & Hautiev (2015) model [27] exhibits intermediate behavior between models [22] and [24] (Fig. 4). Its distinguishing feature is the explicit consideration of Young's modulus E, normalized by its initial value E_0 which enables permeability changes induced by elastic deformation of the coal seam to be described. Permeability decreases moderately with increasing effective stress, while the parameter C_p smooths the permeability curve within the intermediate stress range. The model is more sensitive to the mechanical properties of the coal mass, making it suitable for conditions where variations in physico-mechanical properties are significant, particularly in settings where elastic and tectonic stresses contribute substantially to the formation of the stress field.

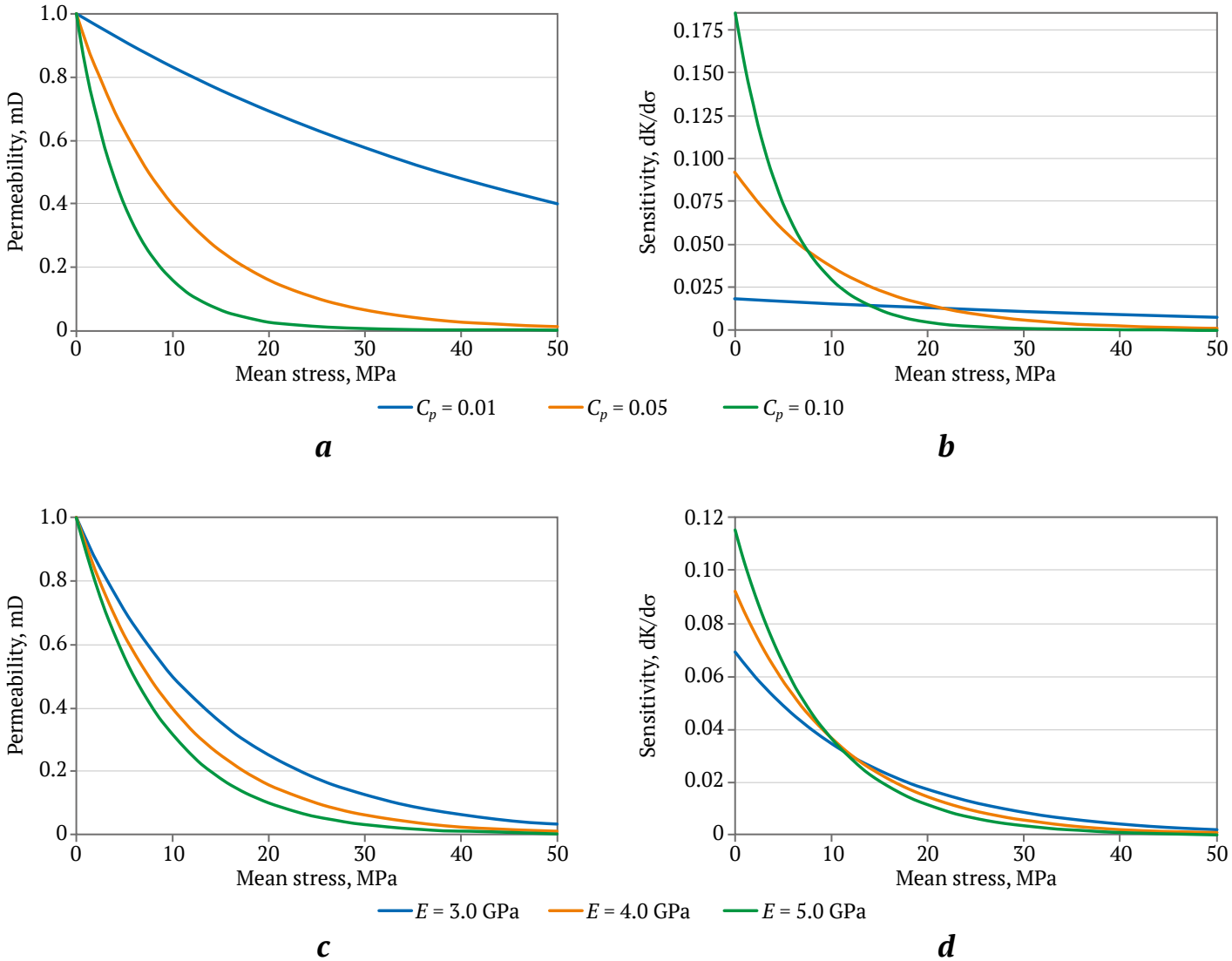

Fig. 4. Sensitivity analysis of the Karkashadze & Hautiev (2015) model [27]. Permeability (*a*) and sensitivity (*b*) as functions of effective stress for different values of the coefficient C_p; permeability (*c*) and sensitivity (*d*) as functions of effective stress for different values of Young's modulus of the rock mass, E

Conclusions

Analytical models of geological medium permeability require consideration of coal microstructural characteristics, reservoir pressure parameters, fluid distribution within the coal-bearing rock mass, and factors governing the stress-strain state. However, under coal seam-scale permeability modeling conditions, acquiring such detailed data is practically infeasible. In this context, a systematic analytical review and analysis of the mathematical frameworks of existing models were conducted, making it possible to identify the parameters that play a decisive role in shaping permeability-stress-strain relationships.

The study demonstrates that a wide range of stress–strain factors influence coal permeability. In accordance with the stated objectives, numerical experiments and sensitivity analyses of the principal empirical models with respect to variations in effective stress were performed. The parametric calculations revealed a common trend across all models: a nonlinear decrease in permeability with increasing effective stress. This behavior reflects the physical processes of pore space compression and fracture closure in coal seams under external loading. At the same time, each model is based on distinct physical and geomechanical assumptions, resulting in differences in curve shape and in the degree of sensitivity to key parameters. A comparative sensitivity analysis of the main empirical and analytical permeability models to changes in the stress-strain state of the coal-bearing rock mass was carried out.

The principal scientific contribution of this study lies in identifying differences in the sensitivity of existing permeability models to the geomechanical parameters of coal-bearing rock masses, as well as in delineating stress-strain ranges in which these models either diverge most strongly or, conversely, converge in their behavior. The following criteria are proposed for model comparison and selection: the nature of dominant deformation mechanisms within the seam; depth of occurrence and the expected range of effective stress; microstructural characteristics of the reservoir; approximate gas saturation and the intensity of sorption processes; and the presence of contrasting elastic properties among different coal ranks.

Within a unified problem formulation, the behavior of the models was examined for variations in effective stress over the range 0–50 MPa and depths up to 1500 m. This approach enabled comparison of their responses to intrinsic geomechanical parameters, including deformation modulus, sorption-induced strain, porosity, and elastic properties. Although the study does not aim to develop a new permeability model, it yields a methodological outcome: zones of increased and reduced sensitivity were identified for each relationship, facilitating informed selection of an appropriate permeability model for specific geomechanical conditions. Model choice should therefore depend on the dominant stress-field formation mechanisms within the coal seam: sorption-induced deformation is best captured by model [23]; deep seams with variable porosity are more adequately described by model [24]; and elastic deformation effects are most effectively represented by model [27]. These relationships can be applied to assess the natural permeability of coal seams in undisturbed rock masses.

Overall, the study provides a comprehensive comparative analysis of permeability models within a unified computational framework. Key zones of model divergence and convergence as functions of geomechanical parameters have been established, forming a scientific basis for their justified selection. The proposed criteria and specific recommendations constitute a practical toolkit for improving the reliability of filtration modeling of coal-bearing rock masses within defined stress and depth ranges.

References

1. Litvinov A.R., Kolikov K.S., Ishkhneli O.G. Accident and traumatism at coal industry enterprises in 2010–2015. *Bulletin of Research Center for Safety in Coal Industry* (*Industrial Safety*). 2017;(2):6–17. (In Russ.)
2. Sen S. Review on coal petrographic indices and models and their applicability in paleoenvironmental interpretation. *Geosciences Journal*. 2016;20(5):719–729. https://doi.org/10.1007/s12303-015-0046-x
3. Pan Z., Connell L.D. Modelling permeability for coal reservoirs: A review of analytical models and testing data. *International Journal of Coal Geology*. 2012;92:1–44. https://doi.org/10.1016/j.coal.2011.12.009
4. Lu S., Shi J., Jiao L. et al. A review of coal permeability models including the internal swelling coefficient of matrix. *International Journal of Coal Science & Technology*. 2024;11:50. https://doi.org/10.1007/s40789-024-00701-0
5. Egorova E.A., Kolikov K.S., Meguid H.A. Coal seam permeability assessment considering geological structure nonuniformity in the roof. *Gornyi Zhurnal*. 2016;(6):56–59. https://doi.org/10.17580/gzh.2016.06.02

6. Connell L.D., Lu M., Pan Z. An analytical coal permeability model for tri-axial strain and stress conditions. *International Journal of Coal Geology*. 2010;84(2):103–114. https://doi.org/10.1016/j.coal.2010.08.011
7. Slastunov S.V., Kolikov K.S., Puchkov L.A. *Extraction of methane from coal seams*. Moscow: Moscow State University Press; 2002. 383 p. (In Russ.)
8. Shilova T., Serdyukov S. Permeability of coking coals and patterns of its change in Leninsky Area, Kuznetsk coal basin, Russia. *Applied Sciences*. 2021;11(9):3969. https://doi.org/10.3390/app11093969
9. Shilova T.V., Rybalkin L.A., Yablokov A.V. Prediction of in-situ cleaved coal permeability. *Journal of Mining Science*. 2020;56:226–235. https://doi.org/10.1134/S1062739120026686
10. Parsons R.W. Permeability of idealized fractured rock. *Society of Petroleum Engineers Journal*. 1966;6(2):126–136. https://doi.org/10.2118/1289-PA
11. Seidle J.P. *Fundamentals of coalbed methane reservoir engineering*. Tulsa, OK: PennWell Books; 2011. 470 p.
12. Sander R., Pan Z., Connell L.D. Laboratory measurement of low permeability unconventional gas reservoir rocks: A review of experimental methods. *Journal of Natural Gas Science and Engineering*. 2017;37:248–279. https://doi.org/10.1016/j.jngse.2016.11.041
13. Gash B.W., Volz R.F., Potter G., Corgan J.M. The effects of cleat orientation and confining pressure on cleat porosity, permeability, and relative permeability. In: *International Coalbed Methane Symposium*. Tuscaloosa, USA: University of Alabama; 1993. Pp. 17–21.
14. Bai M., Elsworth D. *Coupled processes in subsurface deformation, flow and transport*. Reston, VA: American Society of Civil Engineers Press; 2000. 355 p. https://doi.org/10.1061/9780784404607
15. Scheidegger A.E. *The physics of flow through porous media*. 3rd ed. New York: University of Toronto Press; 1960. 353 p.
16. Zubkov A.V. The law of natural stress formation of the earth's crust. *Lithosphere* (*Russia*). 2016;(5):146–151. (In Russ.)
17. Brown E.E., Hoek E. Trends in relationships between measured in situ stresses and depth. *International Journal of Rock Mechanics, Mining Science & Geomechanics*. 1978;15(4):211–215. https://doi.org/10.1016/0148-9062(78)91227-5
18. Langmuir I. The adsorption of gases on plane surfaces of glass, mica and platinum. *Journal of the American Chemical Society*. 1918;40(9):1361–1403. https://doi.org/10.1021/ja02242a004
19. Levine J.R. Model study of the influence of matrix shrinkage on absolute permeability of coalbed reservoirs. *Geological Society Special Publication*. 1996;109:197–212. https://doi.org/10.1144/GSL.SP.1996.109.01.14
20. Karacan C.O. Heterogeneous sorption and swelling in a confined and stressed coal during CO_2 injection. *Energy and Fuels*. 2003;17(6):1595–1608. https://doi.org/10.1021/ef0301349
21. Somerton W.H., Soylemezoglu I.M., Dudley R.C. Effect of stress on the permeability of coal. *International Journal of Rock Mechanics and Mining Sciences & Geomechanics Abstracts*. 1975;12(5-6):129–145. https://doi.org/10.1016/0148-9062(75)91244-9
22. Gray I. Reservoir engineering in coal seams: Part 1 – the physical process of gas storage and movement in coal seams. *SPE Reservoir Engineering*. 1987;2(1):28–34. https://doi.org/10.2118/12514-PA
23. Seidle J.P., Jeansonne M.W., Erickson D.J. Application of matchstick geometry to stress dependent permeability in coals. In: *Society of Petroleum Engineers, SPE Rocky Mountain Regional Meeting*. Casper, Wyoming, USA, May 18–21, 1992. Richardson: SPE; 1992. https://doi.org/10.2118/24361-MS
24. Palmer I., Mansoori J. How permeability depends on stress and pore pressure in coalbeds: a new model. *SPE Reservoir Evaluation & Engineering*. 1998;1(6):539–544. https://doi.org/10.2118/52607-PA
25. Shi J.Q., Durucan S. Drawdown induced changes in permeability of coalbeds: a new interpretation of the reservoir response to primary recovery. *Transport in Porous Media.* 2004;56(1):1–16. https://doi.org/10.1023/B:TIPM.0000018398.19928.5a
26. Shi J.Q., Durucan S.A model for changes in coalbed permeability during primary and enhanced methane recovery. *SPE Reservoir Evaluation & Engineering*. 2005;8(4):291–299. https://doi.org/10.2118/87230-PA
27. Karkashadze G.G., Hautiev A.M.B. Modeling coal bed degassing with wells considering geomechanical stresses. *Mining Informational and Analytical Bulletin*. 2015;(2):235–242. (In Russ.)
28. Saveleva E., Svitelman V., Blinov P., Valetov D. Sensitivity analysis and model calibration as a part of the model development process in radioactive waste disposal safety assessment. *Reliability Engineering & System Safety*. 2021;210:107521. https://doi.org/10.1016/j.ress.2021.107521

Information about the authors

Alexander I. Manevich – Researcher at the Geodynamics Laboratory, Geophysical Center of the Russian Academy of Sciences, Moscow, Russian Federation; ORCID 0000-0001-7486-6104, Scopus ID 57200214238, SPIN 6470-0460; e-mail ai.manevich@yandex.ru

Konstantin S. Kolikov – Dr. Sci. (Eng.), Professor, Head of the Department of Safety and Ecology of Mining Production, Mining Institute, University of Science and Technology MISIS, Moscow, Russian Federation; ORCID 0000-0001-8831-1927, Scopus ID 8946604700, SPIN 6470-0460; e-mail kolikovks@mail.ru

Nikolai V. Ledyaev – Head of the Emergency Resilience Department of Enterprises, JSC "SUEK-Kuzbass", Leninsk-Kuznetsky, Russian Federation; Scopus ID 57864993900, SPIN 9307-6449; e-mail ledyaevnv@suek.ru

Ilya V. Losev – Researcher at the Geodynamics Laboratory, Geophysical Center of the Russian Academy of Sciences, Moscow, Russian Federation; ORCID 0009-0005-0785-4986, Scopus ID 57214669904, SPIN 7963-1926; e-mail locik@mail.ru

Dastan Zh. Akmatov – Cand. Sci. (Eng.), Senior Researcher at the Geodynamics Laboratory, Geophysical Center of the Russian Academy of Sciences, Moscow, Russian Federation; ORCID 0000-0001-6435-464X, Scopus ID 57207911204, SPIN 1687-2529; e-mail dastan.akmatov.1994@mail.ru

Roman V. Shevchuk – Cand. Sci. (Eng.), Senior Researcher at the Geodynamics Laboratory, Geophysical Center of the Russian Academy of Sciences, Moscow, Russian Federation; ORCID 0000-0003-3461-6383; Scopus ID 57206721960, SPIN 5379-1835; e-mail shevchuk.002@mail.ru

Received 05.08.2025
Revised 08.12.2025
Accepted 10.12.2025

MINING ROCK PROPERTIES. ROCK MECHANICS AND GEOPHYSICS

Research paper

https://doi.org/10.17073/2500-0632-2025-12-1065
UDC 622.7:502.174

Potential for using belite sludge from the Achinsk Alumina Refinery to reduce the carbon footprint of aluminum production

V.A. Makarov, **L.T. Koulemou**, **V.G. Mikheev**, **B.M. Lobastov**
Siberian Federal University, Krasnoyarsk, Russian Federation
✉ *vmakarov58s@mail.ru*

Abstract
Certain types of waste from mining and metallurgical industry have the potential to directly absorb carbon dioxide (CO_2) from the atmosphere, as some of them contain minerals capable of carbonation. The paper demonstrates that belite sludges from the Achinsk Alumina Refinery (AAR, RUSAL Achinsk JSC), a byproduct of processing nepheline ores from the Kiya-Shaltyrskoye deposit, possess this property. An investigation of the variability in the mineral composition of the sludges as a function of storage duration in the sludge field (sludge storage facility), across the duration intervals of 0–5, 5–25, 25–50 years revealed a steady decrease in the content of calcium silicates (larnite, wollastonite, merwinite) and an increase in the content of carbonates as the sludge aged from fresh to old. This study examines the factors influencing the rate of sludge carbonation including those observed under conditions typical of an operational sludge storage facility. The electron microscopy (SEM-EDS) analysis of the sludge revealed the porous structure of the silicate particles in the sludge, as well as the extent to which they had been replaced by calcite. An assessment has been conducted of this storage facility's potential for carbon dioxide deposition through the carbonation of silicate minerals in sludge that are chemically unstable under atmospheric conditions. Based on the results of the analysis and literature data on the CO_2 absorption capacity of calcium silicates under atmospheric conditions, it was concluded that larnite has the maximum absorption potential in belite sludges. Based on the conditions at the ARR's belite sludge storage facility, the maximum volume of CO_2 that can be absorbed during complete interaction between larnite and atmospheric air has been calculated. The absorption capacity of one ton of the sludge solely due to larnite (with its content of 32.6%) is 83.3 kg of CO_2, and taking into account wollastonite and merwinite, the total potential reaches 262 kg/t. The scale and dynamics of the process of converting silicates into carbonates in the sludge storage facility will allow the volume of absorbed carbon dioxide to be taken into account in calculations of the carbon footprint of the enterprise's end-use product, aluminum produced from nepheline ore.

Keywords
CO_2 absorption, belite sludge, larnite, wollastonite, merwinite, carbonation, carbon footprint

Acknowledgments
The authors would like to thank Evgeniya Yu. Lokk and Natalia V. Mukhina of RUSAL JSC for their active support and for creating favorable conditions for conducting this research.

For citation
Makarov V.A., Koulemou L.T., Mikheev V.G., Lobastov B.M. Potential for using belite sludge from the Achinsk Alumina Refinery to reduce the carbon footprint of aluminum production *Mining Science and Technology* (*Russia*). 2026;11(1):46–55. https://doi.org/10.17073/2500-0632-2025-12-1065

СВОЙСТВА ГОРНЫХ ПОРОД. ГЕОМЕХАНИКА И ГЕОФИЗИКА

Научная статья

Потенциал использования белитовых шламов Ачинского глиноземного комбината для снижения углеродного следа алюминиевого производства

В.А. Макаров, **Л.Т. Кулему**, **В.Г. Михеев**, **Б.М. Лобастов**
Сибирский федеральный университет, г. Красноярск, Российская Федерация
✉ *vmakarov58s@mail.ru*

Аннотация
Ряд отходов горно-металлургического производства обладает возможностью прямого поглощения углекислого газа CO_2 из атмосферы, поскольку некоторые из них содержат минералы, способные к карбонизации. В статье показано, что такой способностью обладают белитовые шламы Ачинского глино-

земного комбината (АГК, АО «РУСАЛ Ачинск») – отходы переработки нефелиновых руд Кия-Шалтырского месторождения. Изучение изменчивости минерального состава шлама в зависимости от времени его хранения на шламовом поле в возрастных интервалах 0–5, 5–25, 25–50 лет показало устойчивое снижение содержания силикатов кальция (ларнит, волластонит, мервинит) и рост содержания карбонатов в ряду от свежих шламов к лежалым. Рассмотрены факторы, влияющие на скорость карбонизации шламов, в том числе проявляющиеся в условиях действующего шламохранилища. Электронно-микроскопическое изучение шламов (СЭМ-ЭДС) показало пористую структуру силикатных частиц шлама, а также характер замещения их кальцитом. Выполнена оценка потенциала данного хранилища для депонирования углекислого газа за счет карбонизации силикатных минералов шламов, химически неустойчивых в атмосферных условиях. По результатам проведенного анализа и литературным данным по поглощающей способности CO_2 силикатами кальция в атмосферных условиях сделан вывод, что максимальным потенциалом поглощения в белитовых шламах обладает ларнит. Применительно к условиям хранилища белитовых шламов АГК рассчитан предельный объем CO_2, который может быть поглощен при полном взаимодействии ларнита с атмосферным воздухом. Поглотительная способность одной тонны шлама только за счёт ларнита (при его содержании 32,6 %) составляет 83,3 кг CO_2, а с учётом волластонита и мервинита общий потенциал достигает 262 кг/т. Показанные масштабы и динамика процесса преобразования силикатов в карбонаты в объеме шламохранилища позволят учитывать объем поглощенного углекислого газа в расчетах углеродного следа конечной продукции предприятия – алюминия, произведенного из нефелинового сырья.

Ключевые слова
поглощение CO_2, белитовые шламы, ларнит, волластонит, мервинит, карбонизация, углеродный след

Благодарности
Авторы выражают благодарности сотрудникам АО «РУСАЛ» Локк Евгении Юрьевне и Мухиной Наталье Владимировне за активную поддержку и создание благоприятных условий для проведения исследований.

Для цитирования
Makarov V.A., Koulemou L.T., Mikheev V.G., Lobastov B.M. Potential for using belite sludge from the Achinsk Alumina Refinery to reduce the carbon footprint of aluminum production *Mining Science and Technology (Russia)*. 2026;11(1):46–55. https://doi.org/10.17073/2500-0632-2025-12-1065

Introduction

Reducing the carbon footprint of large industrial enterprises is becoming a key factor in their competitiveness. In October 2021, the Russian government approved a strategy for Russia's low-carbon socio-economic development through 2050, which calls for reducing emissions to 70% of the 1990 levels by 2030.

According to experts, CCUS (Carbon Capture, Utilization, and Storage) technologies which encompass a range of methods for capturing, utilizing, and storing carbon dioxide (CO_2) will play a key role in reducing greenhouse gas emissions and addressing climate change [1–3]. The main components of CCUS are: **Capture** – separating CO_2 from industrial emissions (e.g., thermal power plants, cement plants) or directly from the air; **Utilization** – using CO_2 in industry; **Storage** – geological disposal (pumping CO_2 into underground geological formations (former oil and gas fields, saline aquifers)) or mineralization (binding CO_2 into solid carbonates). The latter area is related to the development of technologies for Direct Air Capture (DAC) of CO_2.

Wastes from mining and metallurgical industry have the potential to directly absorb CO_2 from the atmosphere, as many of these materials (tailings, overburden, slag, sludge, etc.) may contain minerals capable of carbonation. In particular, some mining waste (especially ultrabasic and basic rocks) contains calcium, magnesium, and iron silicates (olivine, serpentine, wollastonite, etc.), which are chemically unstable under surface conditions and, when interacting with atmospheric gases, are capable of binding CO_2 into stable carbonates (calcite, magnesite, etc.) [4–6].

The purpose of this study is to demonstrate the potential and feasibility of using belite sludge, a by-product of the Achinsk Alumina Refinery, to absorb carbon dioxide from the atmosphere.

The objectives of the study included examining the variability of the mineral composition of the sludge as a function of its storage duration in the sludge storage facility and assessing the potential of this storage facility for carbon dioxide deposition through the carbonation of the sludge silicate minerals, which are chemically unstable under atmospheric conditions.

The research subject and methods

The Achinsk Alumina Refinery (ARR, RUSAL Achinsk JSC) was commissioned in 1973. Alumina is produced at the refinery by processing nepheline ore from the Kiy-Shaltyrskoye deposit. An important environmental aspect of the alumina production at this facility is the generation of large amounts of waste, belite sludge, which is stored in a sludge storage facility located in the floodplain of the Chulym River (Fig. 1).

The sludge storage facility covers an area of 90 hectares, and the sludge pile is over 100 m high. The total volume of the belite sludge accumulated exceeds 300 million tons.

Research into the properties of the sludge and its potential applications in the national economy began almost as soon as the refinery began operations. Since then, various applications have been identified: production of belite cement and soda ash products, use as soil ameliorant (soil deoxidizer), sorbent, and food additive in poultry feed; pigment for paint production, and others.

Despite the wide range of the belite sludge application properties, the volume of its reuse is insignificant (no more than 20% of the amount delivered to the depositing sites) and is incomparable with the scale and speed of accumulation. At the same time, given the significant volume of this material, it seems appropriate to consider it as a promising candidate for carbon capture, since the magnesium and calcium silicates contained in these sludge dumps are potential materials for binding atmospheric CO_2 into stable carbonates. This technological approach is relevant to combating the greenhouse effect and could be one of the factors in reducing the carbon footprint of the alumina produced at the refinery and, ultimately, of the aluminum produced.

The basis for this study was a quantitative X-ray phase analysis of three randomly selected sludge samples from depositing sites with different storage durations, which revealed a sharp decline in the calcium silicate content in the sludges following prolonged exposure to the atmosphere (Fig. 2). Sludges (samples) collected from different depositing sites were conditionally classified as “old”, “intermediate”, and “fresh”.

The methodology for further research included the selection of 76 samples of sludge of various ages from the surface of the depositing sites, as well as a comparative study of their mineral (X-ray phase analysis, optical and electron microscopy) and chemical (ICP-AES, ICP-MS) composition.

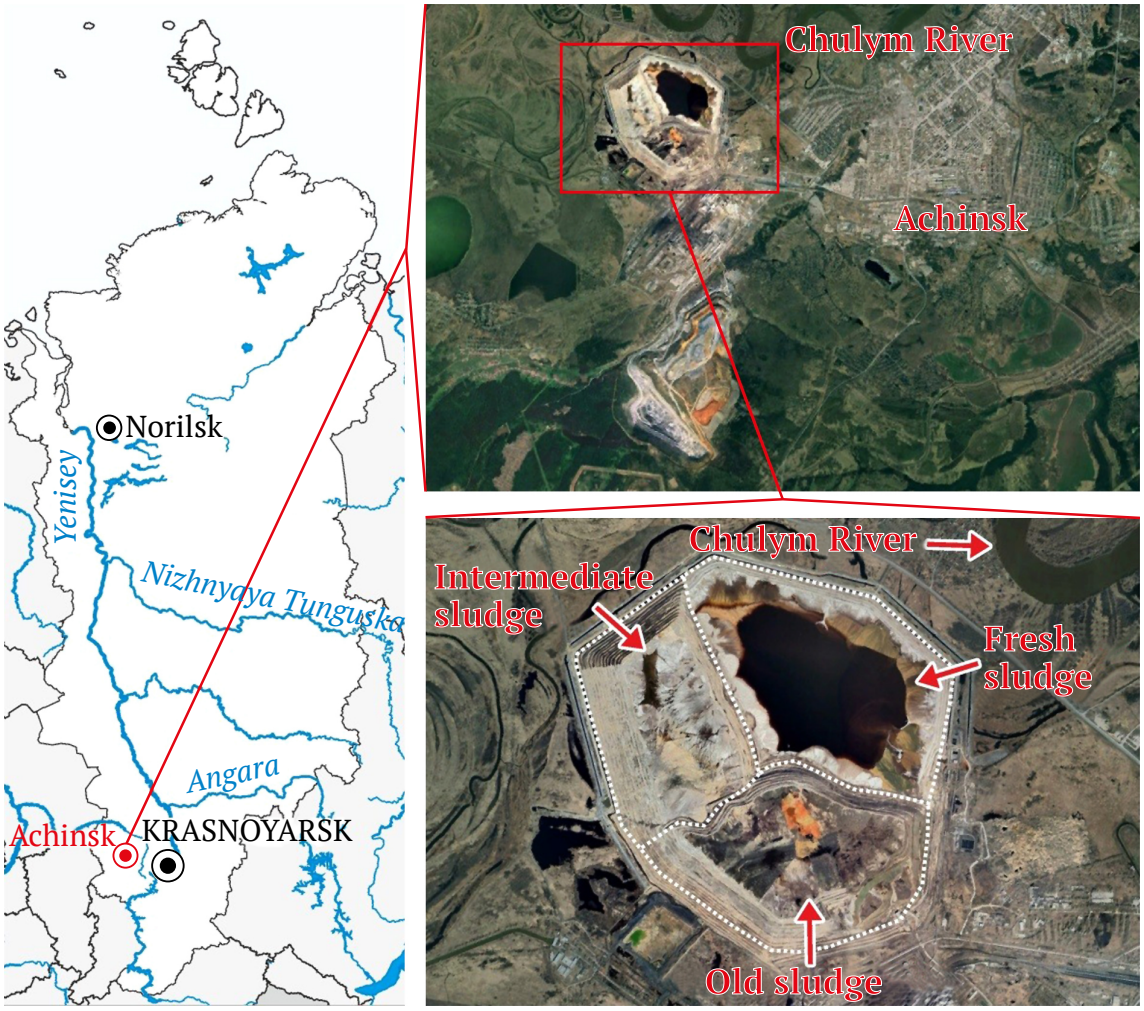

Fig. 1. Location of the ARR’s sludge storage facility and its general view with indicating sludge depositing sites of different ages: fresh sludge (0–5 years of storage); intermediate age sludge (5–25 years of storage); old sludge (25–50 years of storage)

Research findings

Lithologically, the sludge is a loose material with a predominance of sand and silt particles, i.e., the sludge corresponds to silty sand. At depths up to 2.5–4 m, the sludge is generally loose, while at greater depths it becomes cemented due to the interaction of the sludge water with calcium silicates (larnite, wollastonite, and merwinite). In some cases, cementation of the sludge starting from the surface is observed. With increasing depth, the content of coarse-grained sludge (up to the size of coarse sand) increases, while the content of silt (dust-like) fractions decreases.

The sludge storage facility is formed by hydraulicking using a system of sludge pipelines with a recirculating water system. This determines the layered texture of sludge characteristic of sedimentary rocks. The layers dip at angles of 1–5° toward the center of the storage facility. The composition of the sludge and its structural and textural characteristics account for its high porosity and good surface water drainage. Process water supplied to a depositing site via the sludge pipelines has a temperature of about 60 °C, which, together with high humidity and good aeration of the sludge material, leads to the intensive formation of secondary minerals, including in cold season (Fig. 3).

It is noteworthy that the highest contents of calcite, as well as carbon, were found within the interval of 15–30 cm from the surface, which is likely due to specific humidity conditions and the absorption of carbon dioxide from the air.

The chemical composition of the sludge and the features of its variability over time are presented in Table 1.

The table shows that, for most elements, there are no significant changes in the composition of the sludge samples with changing storage duration. The active removal of elements from the surface of sludge dumps is observed for magnesium and sodium only.

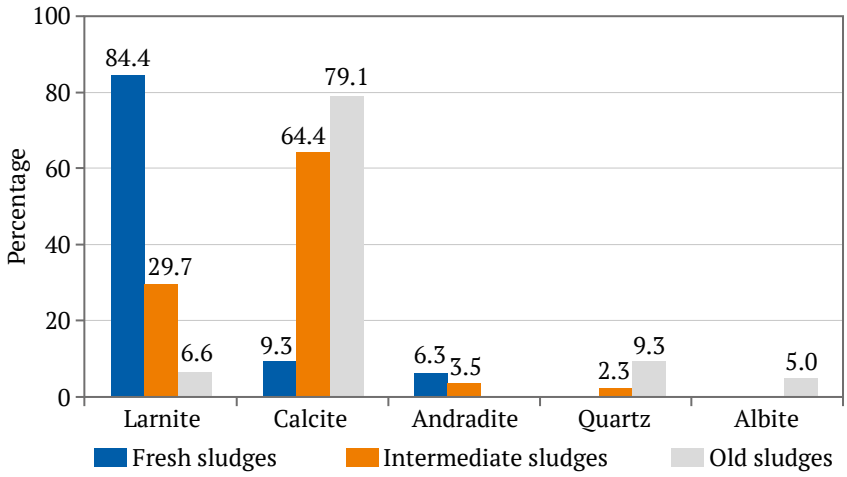

Fig. 2. Trends of variability in the content of larnite and calcite in sludges of different storage duration (randomly selected samples from the surface of the depositing sites): fresh sludge (0–5 years of storage); intermediate sludge (5–25 years of storage); old sludge (25–50 years of storage)

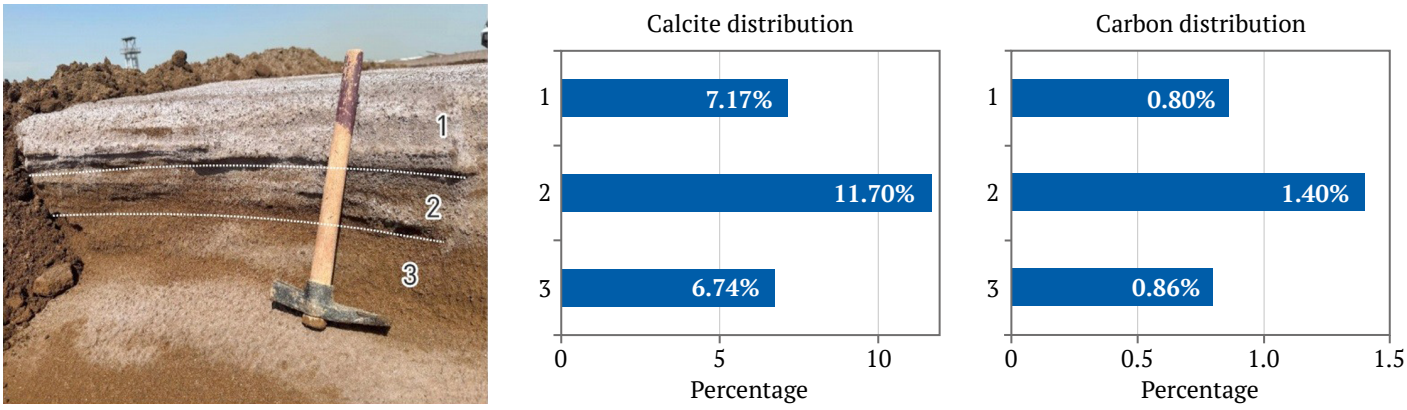

Fig. 3. The formation of a white crust composed of secondary minerals (potassium and sodium salts + carbonates) in the sludge (left). Samples (15-cm-long sample channels) were collected from the sludge near the sludge discharge point from a layer formed two months ago. Graphs showing the distribution of calcite and carbon in samples based on X-ray phase and X-ray fluorescence analyses, respectively are shown on the right

Table 1

Chemical composition of belite sludge based on ICP-AES data* (average contents for 10-sample sets)

Elements, g/t	Sludge category by storage duration**		
	Fresh (FR)	Intermediate (IN)	Old (OL)
As	10.6	9.3	11.2
B	22.0	22.8	20.8
Ba	290.8	298.2	208.6
Ca	297294.0	285448.4	296804.6
Co	8.2	7.6	7.3
Cr	29.3	22.5	25.5
Cu	16.9	30.0	20.5
Li	12.2	10.1	11.8
Mg	10724.1	9314.8	7530.5
Na	11587.7	7140.7	5346.8
Ni	16.6	15.1	14.8
P	1242.6	1119.9	1197.7
Pb	16.4	22.7	17.2
S	1338.3	787.3	889.4
Sb	2.9	2.4	3.1
Sn	1.3	1.2	1.2
Sr	986.4	982.9	907.7
Ti	2032.4	1833.0	1790.5
Zn	46.4	48.3	52.4

* The assays were performed at the laboratory of TsGI Prognoz LLC.
** FR – 0–5 years; IN – 5–25 years; OL – 25–50 years.

X-ray phase analyses of the sludge samples (two samples were analyzed from each depositing site) selected at random from the surface) showed that, in addition to larnite, the samples contained wollastonite and merwinite among the calcium silicates (Table 2).

Table 3 shows that the sum of calcium and magnesium silicates in the fresh sludge-intermediate sludge–old sludge series decreases sequentially: 79.44–76.96–68.9 (%), while the total carbonate content increases: 18.98–27.47–27.09 (%). At the same time, the high carbonate content found in one of the fresh sludge samples (Table 2, sample FR1) reflects the rapid and uneven carbonation of the silicate minerals contained therein. An example of such a high carbonation rate under favorable conditions is shown in Fig. 3.

To assess the features of the processes involved in the replacement of calcium silicates by carbonate, electron microscopic studies were conducted on three samples of sludges of different ages. Fresh, intermediate, and old sludge samples were studied using the SEM-EDS method. Polished microsections were prepared from the epoxy-cemented sample material for the microscopic examination.

SEM-EDS analyses were performed at the Norilsk Nickel–SFU R&D Center using a Tescan Vega III SBH system with an integrated Oxford X-Act system, operating at an accelerating voltage of 20 kV and a probe current of 2.0 nA (on a Faraday cup); spectra were accumulated from point to scale of 300,000 pulses.

Table 2

Mineralogical composition of belite sludge samples of different storage duration*, according to quantitative X-ray phase analysis data, %**

Material	Mineral					
	Larnite Ca_2SiO_4	Wollastonite $CaSiO_3$	Merwinite $Ca_3Mg[SiO_4]_2$	Calcite $CaCO_3$	Vaterite $CaCO_3$	Aragonite $CaCO_3$
Fresh sludge (FR1)	20.8	49.3	2.22	20.9	2.8	3.44
Fresh sludge (FR2)	44.4	34.8	7.36	7.94	2.18	1.15
Intermediate sludge (IN1)	3.8	57.0	12.0	31.5	2.82	3.05
Intermediate sludge (IN2)	16.5	62.5	3.13	12.2	2.35	2.91
Old sludge (OL1)	9.54	58.4	1.7	18.8	5.1	1.89
Old sludge (OL2)	8.97	58.4	0.85	23.50	3.28	1.58

* FR – 0–5 years; IN – 5–25 years; OL – 25–50 years.
** Analyses performed at the Multiple-access Center of the Institute of Non-Ferrous Metals, Siberian Federal University.

Table 3

Average mineral contents in sludges of different storage duration

Material	Mineral					
	Larnite Ca_2SiO_4	Wollastonite $CaSiO_3$	Merwinite $Ca_3Mg[SiO_4]_2$	Calcite $CaCO_3$	Vaterite $CaCO_3$	Aragonite $CaCO_3$
Fresh sludge (FR)	32.6	42.05	4.79	14.2	2.49	2.29
Intermediate sludge (IN)	10.15	59.25	7.56	21.85	2.64	2.98
Old sludge (OL)	9.25	58.4	1.25	21.15	4.19	1.75

In the investigation, standard samples of chemically pure elements and compounds of MAC standards (Micro-Analysis Consultants Ltd, United Kingdom; reg. No. 11192) were used: O – SiO_2, Al – $Al2O_3$, Si – SiO_2, Ca – wollastonite, $CaSiO_3$. Oxygen was determined both directly and by stoichiometry that allowed indirect assessment of the presence of hydroxyl groups and/or water in minerals. The probe current was measured using a MAC cobalt metal standard (reg. No. 9941) every 60 minutes during the study.

The samples were carbon-coated using the Quorum 150 RES automated conductive coating system with thickness control; the coating thickness was 20 nm.

The results of the studies showed that the "fresh" sludge consists mainly of calcium silicates (Fig. 4). Its particle size ranges from the first tens of micrometers to 0.5 mm. The particles shape is irregular, blob-like, or amoeboid; angular, polygonal particles are also observed. Upon closer examination, the following was observed:

– compact particles composed of an aggregate of calcium silicate and certain impurity components;

– particles composed of an extremely fine globular aggregate of calcium silicate, with globule sizes in the range of a few μm;

– particles composed mainly of calcium silicate globules measuring 10–20 μm.

The particles contain a very small amount of calcium carbonate; besides, rounded and irregularly shaped iron particles were occasionally observed (bright spots in Fig. 4).

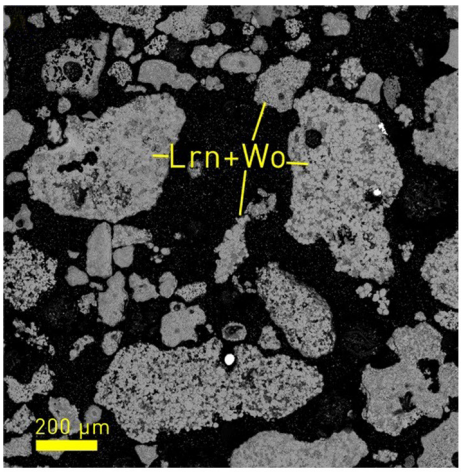

a

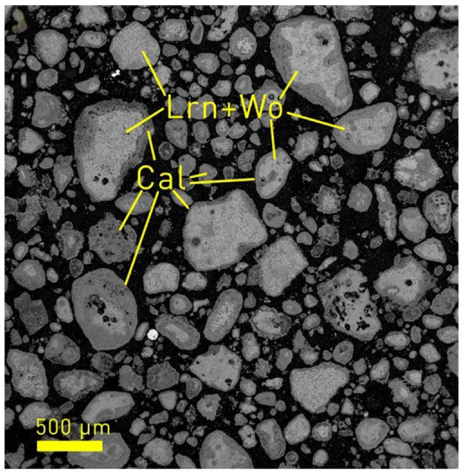

a

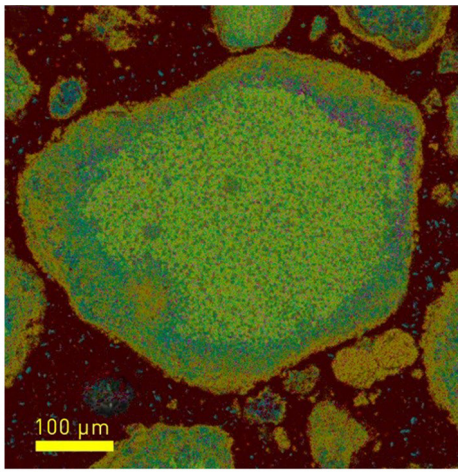

b

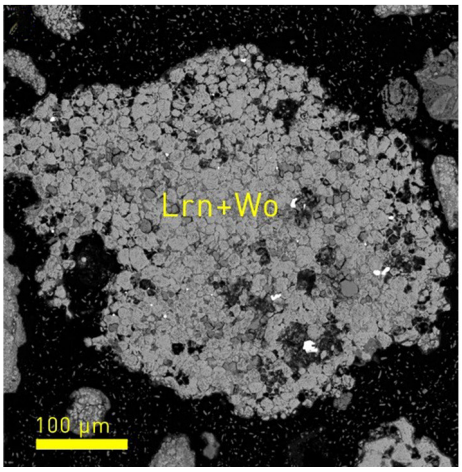

b

Fig. 4. "Fresh" sludge; globular aggregates of calcium silicates are clearly visible: light gray larnite (Lrn) and wollastonite (Wo) with a few bright spots representing iron particles. Photo in back scattered electrons

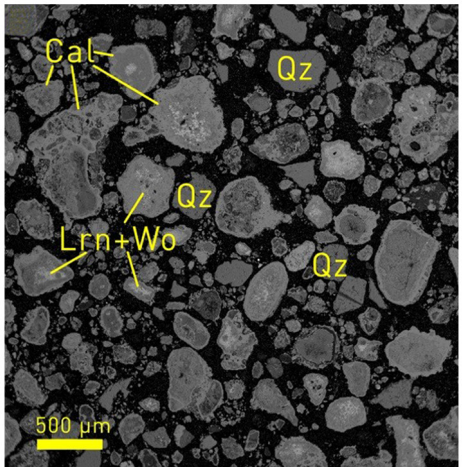

c

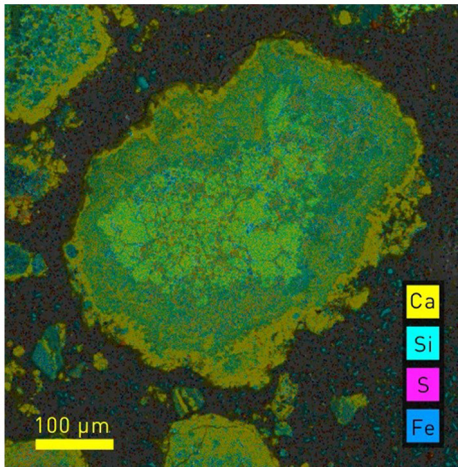

d

Fig. 5. "Intermediate" (*a*, *b*) and "old" (*c*, *d*) sludges; zonal structure of the particles is clearly visible: in the central part, light gray material occurs, presented by calcium silicates larnite Lrn and wollastonite Wo; dark gray calcite Cal develops at the periphery, and a few quartz Qz particles are identified; images *b* and *d* present multi-element maps in pseudo-colors, with symbols shown in the image. Photo in back scattered electrons

In the "intermediate" and "old" sludges, calcium silicate replacement with carbonate was observed. Fig. 5 shows the particle general distribution and features of alteration in particles in "intermediate" and "old" sludges. It is clearly visible that the bright areas in the particle nuclei are very small. This is more common in "intermediate" sludges, where they may be absent at all. Complete replacement of silicates is more commonly observed in "old" sludge, indicating a significantly greater degree of alteration of the initial material. Fig. 5 also shows multi-element maps of individual particles that have undergone varying degrees of alteration: their cores consist of small calcium silicate globules, while a compact crust of calcium carbonate forms along the periphery, appearing darker in backscattered electrons compared to the core.

Findings discussion

The data obtained on the mineral composition of the ARR's belite sludges and the trends in its variability indicate that silicate carbonation processes are occurring in the storage facility under current conditions. Under atmospheric conditions, all silicates (larnite, wollastonite, merwinite), which compose the bulk of the sludge, are capable of absorbing CO_2 to varying degrees.

The stability of these silicates in atmospheric conditions and the rate of carbon dioxide absorption vary and depend on a number of factors, namely: environmental factors, factors related to the nature of the material, and products formed as a result of the reaction [7, 8].

Within the first group of factors, the governing factor is the concentration of CO_2 in the atmosphere (the higher the concentration of carbon dioxide in the air, the faster the reaction). Humidity is also a critically important factor. If the humidity is too low (<~25%), there is not enough water for the hydration reaction and the carbonation process itself to take place (CO_2 must dissolve in water). When humidity is too high (> ~90%), the pores in the material become saturated with water, which slows down gas diffusion. Humidity levels between 50% and 70% are considered optimal [9, 10]. Temperature has a twofold effect on the rate of carbonation.

As the temperature rises, the rate of chemical reaction increases (Van't Hoff's rule). However, elevated temperatures can also reduce relative humidity and CO_2 solubility that in these reactions can lead to the opposite result. The progress in the secondary mineral formation on the surface of the storage facility shown in Fig. 3 indicate a high rate of secondary carbonate formation and the appearance of abnormal carbon contents under a thin surface layer. This is obviously due to the dissolution of carbon dioxide from the air in pore water, where evaporation is minimal and the temperature conditions are optimal for the replacement of calcium silicates.

In general, within moderate ranges, rising temperatures accelerate carbonation. When considering environmental factors in relation to the storage conditions of the ARR's belite sludges, it can be noted that these factors combine in a way that is conducive to carbonation. This relatively high CO_2 content is due to the storage facility being located in an industrial area of the city, with increased humidity caused by both precipitation (movable elements are being carried away, see Table 1) and the evaporation of process water at discharge points at the depositing sites, whose temperatures can range from 60 to 80 °C. Hot process water also serves as a favorable temperature factor for carbonation in winter. At the water discharge point, there is a local thermal anomaly that exists year-round.

The key material-related factors are mineralogical composition, as well as porosity and permeability. The latest two factors determine the access of CO_2 into the material. The more open pores and capillaries there are, the easier it is for CO_2 to penetrate deeply and the higher the carbonation rate. For the ARR's belite sludges, the fine-grained and sandy particle coarseness of the calcium silicates, as well as the high porosity of each individual sludge particle (see Fig. 4), are highly favorable factors. This suggests that the belite sludge storage facility is permeable to atmospheric carbon dioxide, at least in its upper part.

The mineralogical composition of sludge has a significant effect on the rate of carbonation. The predominant silicates in the composition of the ARR's sludges, which determine their carbonation rate, are larnite and wollastonite. The reactions and conditions for carbon dioxide absorption by these minerals are different. For larnite, carbonation occurs in stages through its hydration, resulting in the formation of portlandite and a calcium hydrosilicate ($Ca_2SiO_4 + 3H_2O \rightarrow Ca(OH)_2 + CaO \cdot SiO_2 \cdot aH_2O$), followed by carbonation of portlandite ($Ca(OH)_2 + CO_2 \rightarrow CaCO_3 + H_2O$) and then carbonation of the calcium hydrosilicate ($CaO \cdot SiO_2 \cdot aH_2O + CO_2 \rightarrow CaCO_3 + SiO_2 \cdot bH_2O + H_2O$) [11–13].

The literature indicates that the rate of carbonation of larnite under atmospheric conditions is quite high. However, it is a variable quantity and depends on the formation of a passivating carbonate film on the surface. At the initial stage, the reaction proceeds relatively quickly on the newly

formed surface, since the concentration of CO_2 and the availability of calcium ions are at their highest. As a layer of calcium carbonate ($CaCO_3$) forms on the surface of the larnite particles, this layer begins to act as a barrier. For the reaction to continue, the CO_2 molecules and water must diffuse through this layer, while the calcium ions and silicic acid must diffuse out of it. This diffusion process significantly slows down the overall reaction rate [7, 11]. The phenomena described are clearly observed in belite sludges of different storage durations at the ARR. Fig. 5 shows that large calcium silicate particles are surrounded by a rim of calcium carbonate, while small particles are often completely replaced by carbonate.

The international literature includes studies assessing the dynamics and extent of carbon dioxide uptake by larnite under atmospheric conditions [14, 15]. The observations and experiments described there, conducted on steelmaking waste (slag) – the main mineral of which is larnite (50% of the initial slag) – showed that CO_2 absorption at room temperature amounts to 243 kg per ton of fresh steelmaking slag.

The carbonation rate of wollastonite under atmospheric conditions (0.04% CO_2, 25 °C) is quite low and almost imperceptible. However, under optimized conditions (high CO_2 concentrations, elevated temperature, fine grinding, presence of water), the reaction can proceed quite rapidly. The main difference from larnite is that wollastonite does not require a hydration stage and is carbonatized directly [16, 17].

A study by Canadian researchers assessed the weather resistance of wollastonite and its ability to absorb CO_2 through carbonation under atmospheric conditions. A comparative analysis of CO_2 absorption rates by kimberlite beneficiation tailings from mines in northwestern Canada and wollastonite ore rich in $CaSiO_3$ mined at a deposit in Ontario showed that wollastonite ore is more prone to weathering and carbonation than the kimberlite tailings (which contain slowly weathering hydrated magnesium silicates and aluminosilicates). However, under atmospheric conditions, the process is slow [8, 18, 19].

Based on the analysis conducted and the literature data on the CO_2 absorption capacity of calcium silicates under atmospheric conditions [12, 14, 20], it can be concluded that larnite possesses the highest absorption potential. With regard to the conditions of the ARR's belite sludge storage, it is possible to calculate the maximum volume of the absorbed gas assuming the minerals react completely with atmospheric air (Table 4).

Table 4

Carbon dioxide absorption capacity of one ton of ARR's belite sludge

Masses (of mineral and absorbed CO_2) from 1 ton of sludge		Fresh sludge (FR), test charge, kg
Larnite, CO_2, kg	Larnite Ca_2SiO_4	326.00
	CO_2	83.30
Wollastonite, CO_2, kg	Vollastonite $CaSiO_3$	420.50
	CO_2	159.31
Merwinite, CO_2, kg	Mervinite $Ca_3Mg[SiO_4]_2$	47.90
	CO_2	19.24
Total, kg	CO_2	261.85
	Minerals	794.40

Key findings

1. The main minerals in the ARR's belite sludge are calcium silicates, namely larnite, wollastonite, and merwinite, which are prone to carbonation (absorption of carbon from atmospheric air) to varying degrees.

2. An investigation of the changes in the mineral composition of the sludges as a function of the duration of storage in the sludge storage facility for the duration intervals of 0–5, 5–25, 25–50 years revealed a steady decrease in the content of calcium silicates (larnite, wollastonite, merwinite) and an increase in the content of carbonates as the sludge ages from fresh to old.

3. The main factors having an effect on the rate of sludge carbonation under atmospheric conditions at the existing sludge storage facility are: mineral composition, porous structure of silicate particles in the sludge, and the features of their replacement by calcite. Favorable conditions that influence the rate of carbon dioxide absorption include high surface humidity and a relatively high temperature (60–80 °C) of the recirculating water supplied to a depositing site. The latter is a favorable factor for CO_2 absorption reactions during cold periods.

4. Based on the results of the analysis, it was concluded that larnite has the greatest potential in terms of CO_2 absorption capacity under atmospheric conditions and carbonation rate. Based on the conditions at the ARR's belite sludge storage facility, the maximum amount of CO_2 that can be absorbed during complete interaction between larnite and atmospheric air has been calculated. With a larnite content of 32.6%, one ton of the sludge can absorb 83.3 kg of CO_2.

5. In addition to their various uses in the national economy, the ARR's belite sludge should be considered as a substance that is potentially suitable

for direct absorption of carbon dioxide from the atmosphere. Given the accumulated volume of waste – more than 300 million tons – the potential for carbon dioxide absorption assuming that all calcium silicates are replaced by calcite is quite significant: 80 million tons of CO_2. The scale and dynamics of the process of converting silicates into carbonates in the sludge storage facility will allow the volume of absorbed carbon dioxide to be taken into account in the calculations of the carbon footprint of the enterprise's end-use product, aluminum produced from nepheline ore.

References

1. Ryabov G.A., Petelin S.A., Vivchar A.N. et al. Technologies for capturing carbon dioxide at thermal power plants, its transportation, useful use and storage. In: Klimenko A.V. (Ed.) *Ecology, Energy, Energy Saving*. Iss. 3. Moscow: PJSC Mosenergo; 2022. 32 p. (In Russ.)
2. Osiptsov A.A., Gayda I.V., Grushevenko E.A., Kapitonov S.A. *Carbon capture, utilization and storage (CCUS) technologies – the technological basis for decarbonizing heavy industry in the Russian Federation*. Moscow: Project Center for Energy Transition and ESG; 2022. 79 p. (In Russ.)
3. Zevenhoven R., Back J., Fagerlund J., Sorjonen-Ward P. *Mineral carbonation using mine tailings – A strategic overview of potential and opportunities.* Cheltenham, UK: IEA Greenhouse Gas R&D Programme (IEAGHG); 2022 Jul. 123 p. Report No.: 2022-10.
4. Sanna A., Uibu M., Caramanna G. et al. A review of mineral carbonation technologies to sequester CO_2. *Chemical Society Reviews*. 2014;43(23):8049–8080. https://doi.org/10.1039/c4cs00035h
5. Kusin F.M., Hasan S.N.M.S., Molahid V.L.M. et al. Carbon dioxide sequestration of iron ore mining waste under low-reaction condition of a direct mineral carbonation process. *Environmental Science and Pollution Research*. 2023;30(9):22188–22210. https://doi.org/10.1007/s11356-022-23677-3
6. Ibrahim M.H., El-Naas M.H., Benamor A. et al. Carbon mineralization by reaction with steel-making waste: a review. *Processes*. 2019;7(2):115. https://doi.org/10.3390/pr7020115
7. Santos A., Ajbaryb M., Morales-Florezb V. et al. Larnite powders and larnite/silica aerogel composites as effective agents for CO_2 sequestration by carbonation. *Journal of Hazardous Materials*. 2009;168(2–3):1397–1403. https://doi.org/10.1016/j.jhazmat.2009.03.026
8. Chai Y.E., Chalouati S., Fantucci H., Santos R.M. Accelerated weathering and carbonation (mild to intensified) of natural Canadian silicates (kimberlite and wollastonite) for CO_2 sequestration. *Crystals*. 2021;11(12):1584. https://doi.org/10.3390/cryst11121584
9. Allah P., Nguyen H., Illikainen M. et al. Wet carbonation of wollastonite with pH-modified solutions at ambient conditions: Insights from a geochemical model. *Journal of CO_2 Utilization*. 2025;101:103194. https://doi.org/10.1016/j.jcou.2025.103194
10. Gineika A., Siauciunas R., Baltakys K. Synthesis of wollastonite from AlF_3-rich silica gel and its hardening in the CO_2 atmosphere. *Scientific Reports*. 2019;9(1):18063. https://doi.org/10.1038/s41598-019-54219-6
11. Huijgen W.J.J., Comans R.N.J. C*arbon dioxide sequestration by mineral carbonation: literature review*. Petten: Energy Research Centre of the Netherlands (ECN); 2003 Feb. Report No.: ECN-C--03-016. 52 p.
12. Johnson D.C., MacLeod C.L., Carey P.J., Hills C.D. Solidification of stainless-steel slag by accelerated carbonation. *Environmental Technology*. 2003;24(6):671–678. https://doi.org/10.1080/09593330309385602
13. Montes-Hernandez G., Renard F. Time-resolved in situ Raman spectroscopy of the nucleation and growth of siderite, magnesite, and calcite and their precursors. *Crystal Growth & Design*. 2016;16(12):7218–7230. https://doi.org/10.1021/acs.cgd.6b01406
14. Crouzet C., Brunet F., Montes-Hernandez G. et al. Hydrothermal valorization of steel slags – Part I: coupled H_2 production and CO_2 mineral sequestration. *Frontiers in Energy Research*. 2017;5:29. https://doi.org/10.3389/fenrg.2017.00029
15. Fritz B., Clement A., Montes-Hernandez G., Noguera C. Calcite formation by hydrothermal carbonation of portlandite: complementary insights from experiment and simulation. *CrystEngComm*. 2013;15(17):3392–3401. https://doi.org/10.1039/c3ce26969h
16. Wang T., Tang W., Zhang W. et al. Effect of surface water on wollastonite carbonation: activated dissolution and mass transfer. *Chemical Engineering Journal*. 2024;485:149324. https://doi.org/10.1016/j.cej.2024.149324
17. Coppola A., Scala F., Azadi M. Direct dry carbonation of mining and industrial wastes in a fluidized bed for offsetting carbon emissions. *Processes*. 2022;10(3):582. https://doi.org/10.3390/pr10030582
18. Sipilä J., Teir S., Zevenhoven R. *Carbon dioxide sequestration by mineral carbonation: literature review update 2005–2007.* Turku: Åbo Akademi University, Heat Engineering Laboratory; 2008. Report No.: VT 2008-1. 59 p. URL: https://www.remineralize.org/wp-content/uploads/2015/10/LITR1.pdf

19. Saran R. K., Arora V., Yadav S. CO_2 sequestration by mineral carbonation: a review. *Global NEST Journal*. 2018;20(3):497–503. https://doi.org/10.30955/gnj.002597
20. Bourgeois F., Julcour C. *Rapport bibliographique. Programme "Carboscories"*. Nouméa: CNRT "Nickel & son Environnement"; 2015. 43 p. (In French)

Information about the authors

Vladimir A. Makarov – Dr. Sci. (Geol.-Mineral.), Professor, Head of the Department of Geology of Mineral Deposits and Exploration Methods, Institute of Non-Ferrous Metals and Materials Science, Siberian Federal University, Krasnoyarsk, Russian Federation; ORCID 0009-0005-5971-8070, Scopus ID 57188966055, SPIN 8941-0236; e-mail vmakarov58s@mail.ru

Laurent Thiebo Koulemou – PhD Student, Department of Geology of Mineral Deposits and Exploration Methods, Institute of Non-Ferrous Metals and Materials Science, Siberian Federal University, Krasnoyarsk, Russian Federation; ORCID 0009-0001-1191-5834; e-mail laurentthiebokoulemou1999@gmail.com

Vladimir G. Mikheev – Cand. Sci. (Geol.-Mineral.), Professor, Department of Geology of Mineral Deposits and Exploration Methods, Institute of Non-Ferrous Metals and Materials Science, Siberian Federal University, Krasnoyarsk, Russian Federation; ORCID 0009-0003-2503-6448, SPIN 2100-3262; e-mail vmikheev1938@mail.ru

Boris M. Lobastov – Senior Lecturer, Department of Geology, Mineralogy and Petrography, Institute of Non-Ferrous Metals and Materials Science, Siberian Federal University, Krasnoyarsk, Russian Federation; ORCID 0000-0002-6075-968X, Scopus ID 57211486240, SPIN 4368-7330; e-mail lbm02@ya.ru

Received 15.12.2025
Revised 08.02.2026
Accepted 10.02.2026

MINING ROCK PROPERTIES. ROCK MECHANICS AND GEOPHYSICS

Research paper

https://doi.org/10.17073/2500-0632-2025-02-899
УДК 622.02:004.925.84

Assessing the limits of applicability of photopolymer 3D printing for physical modeling in geosciences

E. V. Kozhevnikov[1], **M. S. Turbakov**[1], **Z. G. Ivanov**[1], **E. P. Riabokon**[1], **P. A. Kamenev**[2]

[1] *Perm National Research Polytechnic University, Perm, Russian Federation*

[2] *Institute of Marine Geology and Geophysics of the Far Eastern Branch of the Russian Academy of Sciences, Yuzhno-Sakhalinsk, Russian Federation*

✉ *kev@pstu.ru*

Abstract

The limited availability of natural core material and its unsuitability for repeated use in laboratory experiments create a need for alternative ways of producing specimens for geomechanical investigations. Against this background, 3D-printed rock replicas are attracting increasing interest. Among the available approaches, 3D-LCD printing is a readily accessible and precise stereolithographic technology based on the layer-by-layer curing of liquid photopolymers through a liquid-crystal display. The aim of this study was to experimentally evaluate the physical and mechanical properties of materials produced by this method and to compare them with those of natural rocks. To address this aim, a set of tests was performed, including microstructural analysis, nondestructive testing based on elastic-wave velocity measurements, and uniaxial compression tests. The results showed that the printed specimens were characterized by a high degree of isotropy in their elastic properties and by stable mechanical parameters under varying post-curing and storage conditions. The inclination of the printed layers relative to the loading direction was also found to have a significant effect on compressive strength and Young's modulus: the highest strength values were obtained at an orientation angle of 60° (up to 162 MPa), whereas the lowest were recorded at 30° (up to 120 MPa). Comparison with test data for natural silicites, silicified dolomites, and opoka, a carbonate-siliceous sedimentary rock, showed comparable mechanical properties and similar deformation behavior within the elastic range (up to 20 MPa). Thus, 3D-LCD rock replicas can be used for the physical modeling of geotechnical processes and for laboratory studies of failure behavior; however, differences in failure mechanisms during plastic deformation must be taken into account.

Keywords

3D printing, photopolymer printing, rock replicas, uniaxial compression, anisotropy, Young's modulus, geomechanics, elastic properties, 3D-LCD technology

Funding

This study was supported by the Russian Science Foundation, Project No. 23-19-00699, https://rscf.ru/project/23-19-00699/

For citation

Kozhevnikov E. V., Turbakov M. S., Ivanov Z. G., Riabokon E. P., Kamenev P. A. Assessing the limits of applicability of photopolymer 3D printing for physical modeling in geosciences. *Mining Science and Technology* (*Russia*). 2026;11(1):56–69. https://doi.org/10.17073/2500-0632-2025-02-899

СВОЙСТВА ГОРНЫХ ПОРОД. ГЕОМЕХАНИКА И ГЕОФИЗИКА

Научная статья

Исследование границ применимости фотополимерной 3D-печати для физического моделирования в геонауках

Е.В. Кожевников[1], М.С. Турбаков[1], З.Г. Иванов[1], Е.П. Рябоконь[1], П.А. Каменев[2]

[1] *Пермский национальный исследовательский политехнический университет, г. Пермь, Российская Федерация*

[2] *Институт морской геологии и геофизики ДВО РАН, г. Южно-Сахалинск, Российская Федерация*

✉ *kev@pstu.ru*

Аннотация

Дефицит природного кернового материала и невозможность его многократного использования в лабораторных экспериментах обусловливают необходимость поиска альтернативных способов получения образцов для геомеханических исследований. В связи с этим всё более востребованным становится применение реплик горных пород, изготовленных методами 3D-печати. Одним из таких методов выступает 3D-LCD-печать – доступная и точная технология стереолитографии, основанная на послойном отверждении жидких фотополимеров через жидкокристаллический дисплей. В связи с этим целью настоящей работы являлось: экспериментальная оценка физико-механических характеристик материалов, получаемых данным методом, и их сопоставление с параметрами природных горных пород. Для решения поставленных задач был проведён комплекс испытаний, включающий микроструктурный анализ, неразрушающие исследования на основе измерения скорости упругих волн и испытания на одноосное сжатие. Испытания показали, что напечатанные образцы характеризуются высокой изотропией упругих свойств и стабильностью механических параметров при изменении условий постотверждения и хранения. Показано также, что наклон слоёв относительно направления нагружения существенно влияет на предел прочности и модуль Юнга: максимальные значения прочности достигаются при угле ориентации 60° (до 162 МПа), минимальные – при 30° (до 120 МПа). Сравнение с данными испытаний природных силицитов, окремнённых доломитов и опок выявило соизмеримость механических характеристик и сходство деформационного поведения в области упругих деформаций (до 20 МПа). Таким образом, 3D-LCD-реплики горных пород могут быть использованы для физического моделирования геотехнических процессов и оценки параметров разрушения в лабораторных условиях, однако требуют учёта различий в механизмах разрушения при пластическом деформировании.

Ключевые слова

3D-печать, фотополимерная печать, реплики горных пород, одноосное сжатие, анизотропия, модуль Юнга, геомеханика, упругие свойства, 3D-LCD-технология

Финансирование

Исследование выполнено при финансовой поддержке Российского научного фонда, проект № 23-19-00699, https://rscf.ru/project/23-19-00699/

Для цитирования

Kozhevnikov E. V., Turbakov M. S., Ivanov Z. G., Riabokon E. P., Kamenev P. A. Assessing the limits of applicability of photopolymer 3D printing for physical modeling in geosciences. *Mining Science and Technology* (*Russia*). 2026;11(1):56–69. https://doi.org/10.17073/2500-0632-2025-02-899

Introduction

To overcome the shortage of core material and enable its repeated use in research, investigators have proposed using approximate copies of rock specimens, that is, replicas produced by 3D additive manufacturing technologies [1, 2]. This approach is increasingly employed in the mining [3] and oil and gas industries [4] to investigate the mechanical properties and permeability of rocks in relation to their internal structure and loading conditions. A key advantage of such replicas is that they allow the required number of specimens to be produced for a wide range of studies, including destructive tests [5, 6].

A variety of technologies are currently available for fabricating 3D rock models. The choice of printing method and material depends on the purpose of the study [7]. Specimens may be produced by material extrusion using thermoplastic filament (FDM/FFF), by stereolithography (SLA) based on the layer-by-layer curing of liquid photopolymer resin, by binder jetting of gypsum [8] or cement–silica–water mixtures [9], or by binder jetting of quartz sand using specific binder systems, including cyanoacrylate adhesive [11] and furfuryl alcohol- and phenolic resin-based binders [12]. Thus, these 3D-printing methods differ primarily in the type of material used [12].

In experimental studies involving the physical modeling of rocks, materials with physical and mechanical properties similar to those of natural rocks, such as gypsum and sand-cement mixtures, are generally preferred. However, existing mineral-based printing methods offer low resolution and do not allow the internal structure of specimens to be reproduced [13]. Specimens produced by material extrusion using thermoplastic filament (FDM/FFF) are rarely suitable as rock replicas because of their low printing resolution and because their structure and material properties differ markedly from those of natural rocks [14].

Stereolithographic 3D printing (SLA), based on the layer-by-layer curing of photopolymer resins, provides the highest print quality and is widely used in both industrial applications and research [15]. Depending on the method used to expose the photopolymer resin, SLA techniques are classified as laser-based [16], digital light processing (DLP) [17], and liquid-crystal-display-based stereolithography (LCD) [18]. SLA offers the highest printing resolution, making it possible to reproduce with high accuracy the microscale heterogeneities inherent in the original objects; for this reason, it is widely used to fabricate porous and fractured rock replicas [19]. LCD-based printing is the most accessible and fastest stereolithographic method and is therefore particularly promising for the production of rock replicas for geomechanical investigations, as it allows a high degree of replication to be achieved at minimal cost and within a short time frame [20].

Thus, an analysis of previous studies has shown that 3D-LCD printing is the most promising method for producing accurate rock replicas. The aim of this study was to experimentally evaluate the applicability of this method to the fabrication of rock replicas for investigating their geomechanical characteristics and to determine the limits of its applicability in physical modeling. To achieve this aim, the following objectives were pursued:

– to examine the microstructure of 3D-LCD replicas and assess its influence on their elastic and mechanical properties;

– to carry out comparative uniaxial compression tests on the replicas and natural rocks;

– to investigate the effect of layer orientation during printing on the Young's modulus of the specimens.

1. Theoretical background

A considerable number of studies have examined the mechanical properties of materials produced by 3D-LCD printing and have shown that these properties are influenced most strongly by printing conditions [21–23] and curing conditions [24, 25]. However, all other factors being equal, the defining feature of 3D-LCD printing is the inherent heterogeneity associated with the layered structure of the fabricated parts [26, 27]. This layered structure gives rise to anisotropy in mechanical properties depending on layer orientation, owing to the heterogeneity inherent in each layer and the presence of interlayer interfaces.

A review of the literature has shown that the results of experimental studies on the effect of layer orientation are often contradictory. Independent research groups investigating the effect of print orientation on the tensile and compressive strength of printed parts have concluded that specimens with layers parallel to the tensile loading direction exhibit the highest Young's modulus and strength [28–30]. Under compression, however, some studies have reported that specimens with inclined layers exhibit the best mechanical properties [31, 32]. Li and Tang [28] attributed this behavior to weaker bonding between adjacent layers, suggesting that layer inclination affects interlayer bond strength. They also noted that strength is influenced by printing-related defects, such as irregular edges, air bubbles, and foreign inclusions.

Other studies [21, 25, 33] have experimentally shown that the strength of specimens with layers oriented parallel to the tensile load is lower than that of specimens in which the layers are oriented perpendicular to the load. The authors of [22] attribute this to the effect of the laser path during curing. Study [34] showed that specimens loaded in tension along the layering direction exhibit the highest Young's modulus, whereas specimens with inclined layers demonstrate greater strength and deformation. It has also been established that reducing the layer thickness improves both strength and elastic properties [33]. In specimens with layers perpendicular to the load, Young's modulus is slightly higher, whereas strength is noticeably lower at any layer thickness. A reduction in layer thickness increases the brittleness of the material, resulting in greater stiffness and lower strength.

Thus, despite the available studies on the effect of layer orientation on the strength of parts produced by 3D-LCD printing, a substantial gap remains in understanding how mechanical properties vary with loading direction. Most studies have focused primarily on tensile strength, whereas comparatively few have examined compressive strength, and the reported findings are often contradictory. These inconsistencies hinder understanding of the failure mechanisms involved and of the factors governing changes in strength as a function of layer orientation. This limited understanding of material behavior also constrains the use of 3D-LCD printing for the fabrication of rock replicas in geomechanical investigations.

The present study addresses these issues. Its novelty lies in establishing the relationship of the mechanical properties of 3D-LCD rock replicas to print orientation and material microstructure, as well as in defining the limits of applicability of such replicas for physical modeling. Based on the results of the experimental program and comparative analysis, the study concludes that 3D-LCD printing is suitable for the physical modeling of geotechnical processes.

2. Methodology

2.1. Specimen fabrication

Digital specimen models were designed with an initial length of 70 mm and diameter of 35 mm, corresponding to a length-to-diameter ratio of 2 : 1, consistent with the specimen geometry specified in ASTM D7012-23. The models were exported in STL format for subsequent print preparation. Using dedicated software, the specimens were arranged on the build platform corresponding to the movable platform of the 3D printer. The models were then sliced layer by layer at different layer inclinations (Fig. 1, *a*), with three specimens prepared for each print orientation. Angles of 90°, 60°, 30°, and 0° correspond to the angle between the layer plane and the specimen axis. All specimens were printed with supports and oriented along the printer's Y-axis.

The specimens were printed on an Anycubic Photon Mono X printer using LCD-based stereolithography (see Fig. 1, *a*). A layer exposure time of 2 s was identified in preliminary tests as optimal for achieving high print quality while maintaining an adequate printing rate. The layer thickness was 50 μm, the standard setting for this printer model. Anycubic Basic Resin Black was used as the printing resin; the black color was selected to minimize the effect of stray light on print quality.

After printing, the specimens were cleaned in an ultrasonic bath containing isopropyl alcohol. This yielded cylindrical specimens with a nominal diameter of 35 mm and a length of 70 mm (Fig. 1, *b*, *c*). These dimensions were selected for the following reasons.

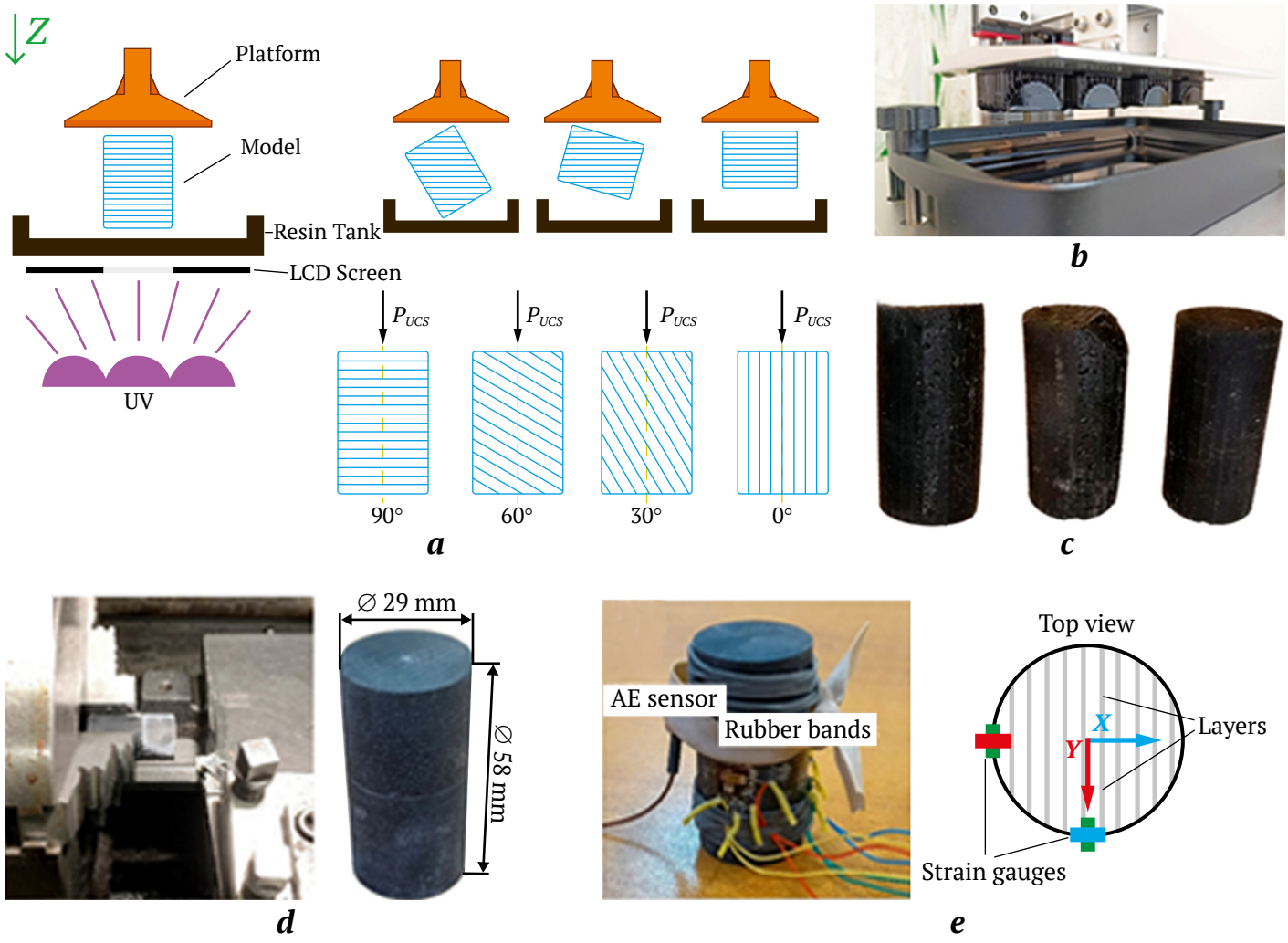

Fig. 1. Specimen fabrication: *a* – schematic illustration of specimen printing at different layer orientations; *b* – printing of the specimens; *c* – printed specimens; *d* – specimen machining; *e* – finished specimen fitted with axial and lateral strain gauges and acoustic emission (AE) sensors

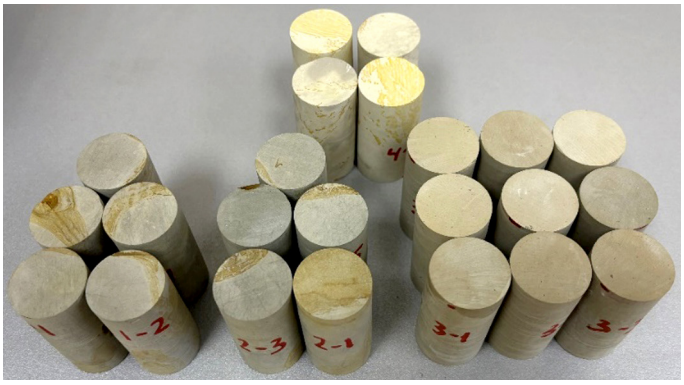

Fig. 2. Cylindrical specimens of silicites (1, 2), silicified dolomites (3), and opoka (4) for uniaxial compression tests

First, the limited build area of the Anycubic Photon Mono X printer does not allow a large number of large specimens to be fabricated simultaneously. However, the simultaneous fabrication of a batch of specimens printed at the same orientation is critical for ensuring within-batch uniformity.

Second, owing to the specific features of the technology, namely the layer-by-layer curing of the resin and the separation of each printed layer from the LCD screen, increasing specimen size increases the contact area with the screen and, consequently, substantially increases the separation force. This may lead to premature delamination of the replicas, detachment of the supports, as well as layer sagging and deviations of the actual layer thickness and inclination from the specified values.

Specimens printed with parallel and inclined layers (see Fig. 1, *c*) exhibited deviations from the cylindrical shape because of layer sagging during printing. Because of these visible defects, they were machined on a lathe to obtain the correct cylindrical geometry (Fig. 1, *d*). Machining yielded specimens with parallel end faces, a diameter of 29 mm, and a length of 58 mm, preserving the 2 : 1 length-to-diameter ratio required for testing.

The finished specimens were post-cured in a UV chamber. Before and after machining, they were stored in a dark place to minimize exposure to ambient light. The temperature and humidity during storage corresponded to normal room conditions, and all specimens were kept in the same environment, thereby excluding any influence of storage conditions on the test results [25, 33, 35].

2.2. Natural rocks

Because the rock replicas were regarded as homogeneous materials, natural rocks with a homogeneous fine-crystalline structure were selected for comparison, namely silicites (microcrystalline quartz), silicified dolomites, and opoka, a carbonate-siliceous sedimentary rock. To evaluate mechanical properties over a wide strength range and to investigate anisotropy, specimens representing different lithotypes were selected. Silicites were assigned to Groups 1 and 2, silicified dolomites to Group 3, and opoka to Group 4.

The specimens were cut perpendicular to bedding (Groups 1 and 3) and parallel to bedding (Groups 2 and 4). Cylindrical specimens measuring 30 mm in diameter and 60 mm in length were prepared for the mechanical tests (Fig. 2).

2.3. Uniaxial compression testing procedure

Uniaxial compression tests were carried out using a Rock Mechanics Test System 816. To measure axial and lateral strains, strain gauges were bonded to the lateral surface of the specimens, and the data were recorded using the system's data acquisition unit. Two pairs of strain gauges were positioned with reference to the printer axes. An acoustic emission (AE) sensor was also attached to the central portion of the lateral specimen surface to record signals during loading. The sensor arrangement is shown in Fig. 1, *e*.

During loading, data from the load cell, strain gauges, and the AE recording system were continuously recorded on a computer. An A-Line 32D measuring system was used to record AE signals. The specimens were loaded to failure at a constant rate of 0.1 MPa/s, in accordance with ASTM D7012-23.

2.4. Nondestructive methods for strength assessment

The nondestructive methods employed in this study included measurements of the propagation velocities of longitudinal and transverse elastic waves. Changes in these velocities over time reflect changes in the mechanical properties of the material and make it possible to assess anisotropy in both the replicas and the natural rocks. Such methods are particularly important for strength assessment in photopolymer resins because these materials undergo property changes during post-processing, including ultraviolet irradiation and storage, and also possess a layered structure [25, 33]. Elastic-wave velocity measurements were performed using an Ultrazvuk instrument (EcogeosProm LLC, Russia).

3. Results

3.1. Changes in mechanical properties during processing

Stabilization of elastic-wave velocity was used as the criterion for determining the sufficient duration of post-curing UV exposure. The relationships between elastic-wave velocity and UV post-curing time are shown in Fig. 3. After 1 min of exposure, elastic-wave velocity increased sharply relative to the untreated specimen and then changed only slightly, indicating

that 1 min was sufficient for surface hardening. Four minutes of UV exposure was sufficient to achieve complete polymerization of the material, as longer exposure produced no further changes in mechanical properties. This is confirmed by the constancy of elastic-wave velocity after 8 min of treatment: UV radiation no longer penetrated into the interior of the specimen, and prolonged irradiation was therefore unnecessary.

Storage time was also found to have no effect on internal polymerization of the material under room conditions in a dark place. The velocities of longitudinal and shear waves remained unchanged after 14 days of storage (see Fig. 3).

3.2. Anisotropy

Specimen anisotropy was evaluated in the axial and radial directions, that is, parallel and perpendicular to the printed layers, respectively (Fig. 4). These directions are sufficient for analysis because layered materials exhibit the greatest differences in mechanical properties along them [25]. Ultrasonic measurements showed that wave velocities measured across and along the layers were identical within experimental error. The identical Young's and shear moduli (see Fig. 3) indicate a high degree of isotropy in the elastic properties of the 3D-LCD specimens, as determined by nondestructive testing.

Nondestructive testing is effective for assessing the stability of replica properties during storage and in long-term test programs, as well as for evaluating the effect of ambient curing on the material. Ultrasonic methods are useful as an auxiliary tool for the indirect assessment of elastic properties; however, they do not provide information about the actual behavior of the material under loading up to failure. Another limitation of these methods is that elastic-wave velocity depends on density and on the presence of heterogeneities and voids, including artificially created cracks and pores. In addition, such methods are applicable only to undamaged specimens of regular shape.

Importantly, specimens produced by 3D-LCD printing do not exhibit initial anisotropy. This ensures clarity in the interpretation of results, high reproducibility of the experimental data, and the possibility of fine adjustment of test parameters.

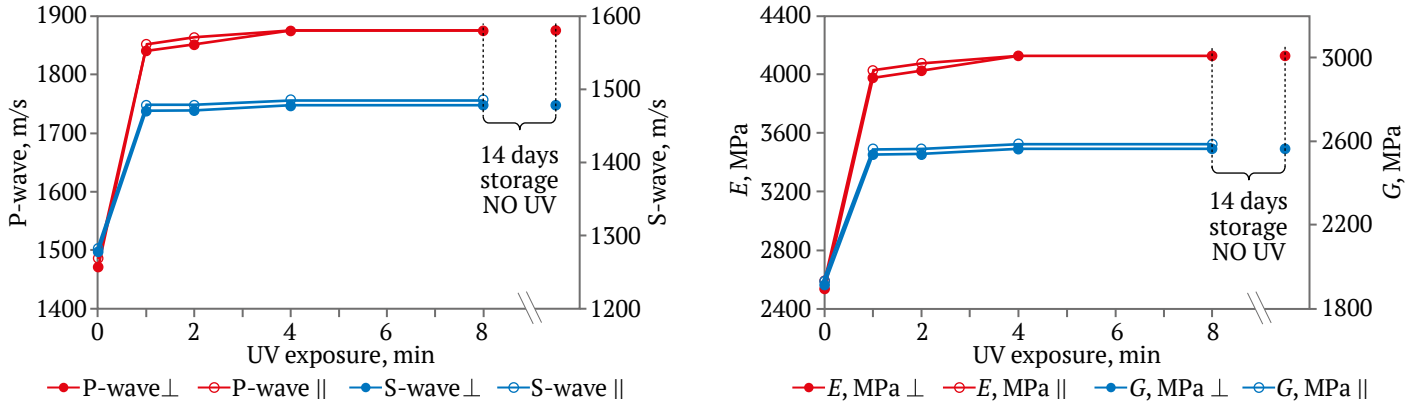

a ***b***

Fig. 3. Effect of post-curing UV exposure time on elastic-wave velocity (*a*) and on the calculated values of Young's modulus and shear modulus (*b*)

a ***b***

Fig. 4. Measurement of elastic-wave velocity in the axial (*a*) and radial (*b*) directions

3.3. Uniaxial compression test results

The uniaxial compression tests showed that the highest strength was exhibited by specimens with layers oriented at 60° to the loading vector, with an average compressive strength of 158 MPa (maximum 162 MPa, minimum 156 MPa). The lowest strength was observed in specimens with a layer inclination of 30°, for which the average value was 138 MPa, with a maximum of 140 MPa and a minimum of 120 MPa (Fig. 5). Specimens with layers oriented parallel (0°) and perpendicular (90°) to the loading direction showed similar strength values, averaging 146 and 147 MPa, respectively.

The tests yielded stress-strain curves and cumulative AE signal plots (see Fig. 5). The stress-strain curves indicate elasto-viscoplastic behavior of the specimens. Under loading up to 20 MPa, all specimens exhibited a quasi-elastic deformation zone, highlighted in blue in Fig. 5, in which stress varied linearly with strain. In this zone, no AE signals exceeding the 40 dB filter threshold were recorded, indicating either a very low level of internal damage or its complete absence.

This quasi-elastic deformation zone is of the greatest engineering interest because structural elements retain their mechanical properties within the elastic range. Young's modulus values for specimens with different layer orientations were determined from the slope of the stress-strain curve in this region. The stress-strain relationships in the quasi-elastic zone are described by the following equations:

$$\sigma_0 = 4272.2\varepsilon_\alpha + 0.5489; \quad (1)$$

$$\sigma_{30} = 4060.8\varepsilon_\alpha + 0.4588; \quad (2)$$

$$\sigma_{60} = 3892.7\varepsilon_\alpha + 0.5892; \quad (3)$$

$$\sigma_{90} = 4006.8\varepsilon_\alpha + 0.4912, \quad (4)$$

where σ is stress, MPa (the subscript corresponds to the angle between the layers and the loading vector), and ε_α is axial strain.

The coefficients on the right-hand side of the equations correspond to Young's modulus values and range from 3893 MPa for specimens with a layer inclination of 60° to 4272 MPa for specimens with layers parallel to the loading direction. These values indicate a fairly high degree of uniformity in elastic properties at stresses up to 20 MPa.

The highest Young's modulus was recorded for specimens with layers parallel to the loading vector, whereas the lowest was found for specimens with a layer inclination of 60°. Overall, Young's modulus tended to decrease as the layer orientation increased relative to the specimen axis (Eqs. (1)–(4)). At the same time, the modulus of specimens with layers perpendicular to the load (90°) was comparable to that of specimens with a layer inclination of 30°.

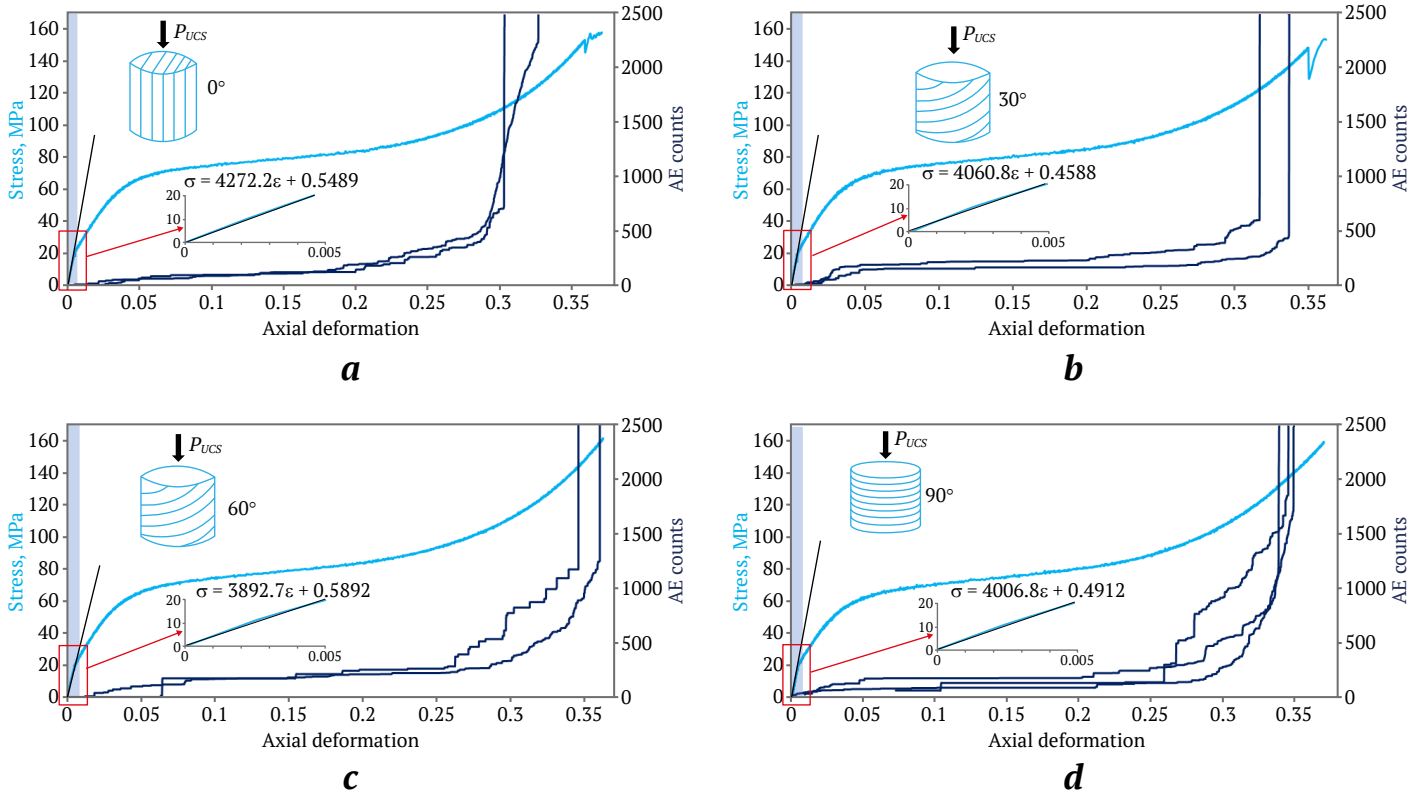

Fig. 5. Stress-strain curves and cumulative AE signal plots for specimens with layer inclinations of 0° (*a*), 30° (*b*), 60° (*c*), and 90° (*d*). The light blue line represents stress, and the dark blue line represents the cumulative number of AE signals. The quasi-elastic deformation zone is highlighted in blue

Specimens with layer orientations of 0° and 30° combined relatively low strength with a high Young's modulus in the quasi-elastic deformation zone, indicating greater stiffness but relatively brittle failure. By contrast, specimens with a layer inclination of 60°, although exhibiting the highest strength, showed the lowest Young's modulus values and therefore lower stiffness. This mismatch between strength and elastic modulus suggests that different failure mechanisms operate depending on layer orientation.

A comparative analysis of the AE data and uniaxial compression results (see Fig. 5) showed that, despite the similar overall shape of the stress-strain curves, the failure mechanisms differed among specimens with different layer inclinations relative to the loading vector. Combined analysis of the AE signals and compression curves makes it possible to determine with high accuracy the deformation stage reached by a specimen at a given load level. The comparison further showed that the duration of each deformation stage depended on the layer inclination relative to the loading vector. For example, the longest elasto-viscoplastic stage was observed in specimens with layers perpendicular to the load (Fig. 5, *d*), whereas the shortest occurred in specimens with a layer inclination of 30° to the loading axis (Fig. 5, *b*). Thus, the combined analysis of AE and uniaxial compression data showed that geomechanical studies must take into account the fact that the failure mechanisms of rock-specimen replicas printed by the 3D-LCD method vary with layer orientation.

3.4. Uniaxial compression of rocks

The results of the uniaxial compression tests on the natural rocks are presented in Fig. 6 as stress-strain curves.

All natural rock specimens exhibited a compaction zone at the initial stage of loading, in which stress increased nonlinearly with strain (see Fig. 6). This zone is associated with the presence of relaxation microcracks oriented perpendicular to the principal stress and, as a rule, parallel to bedding. Closure of such cracks under loading occurs without failure, as confirmed by the absence of acoustic emission activity. As the microcracks close, the material becomes denser and stiffer, which is reflected in an increasing slope of the stress-strain curve.

Because of the nonuniform stress distribution, some microcracks remain unclosed, and new ones may also form. Once the strain reaches 0.001, stress redistribution causes a sharp increase in AE activity. Further loading promotes closure of both relaxation microcracks and newly formed microcracks, so that the specimen becomes nearly fully compacted and then enters a linear deformation stage.

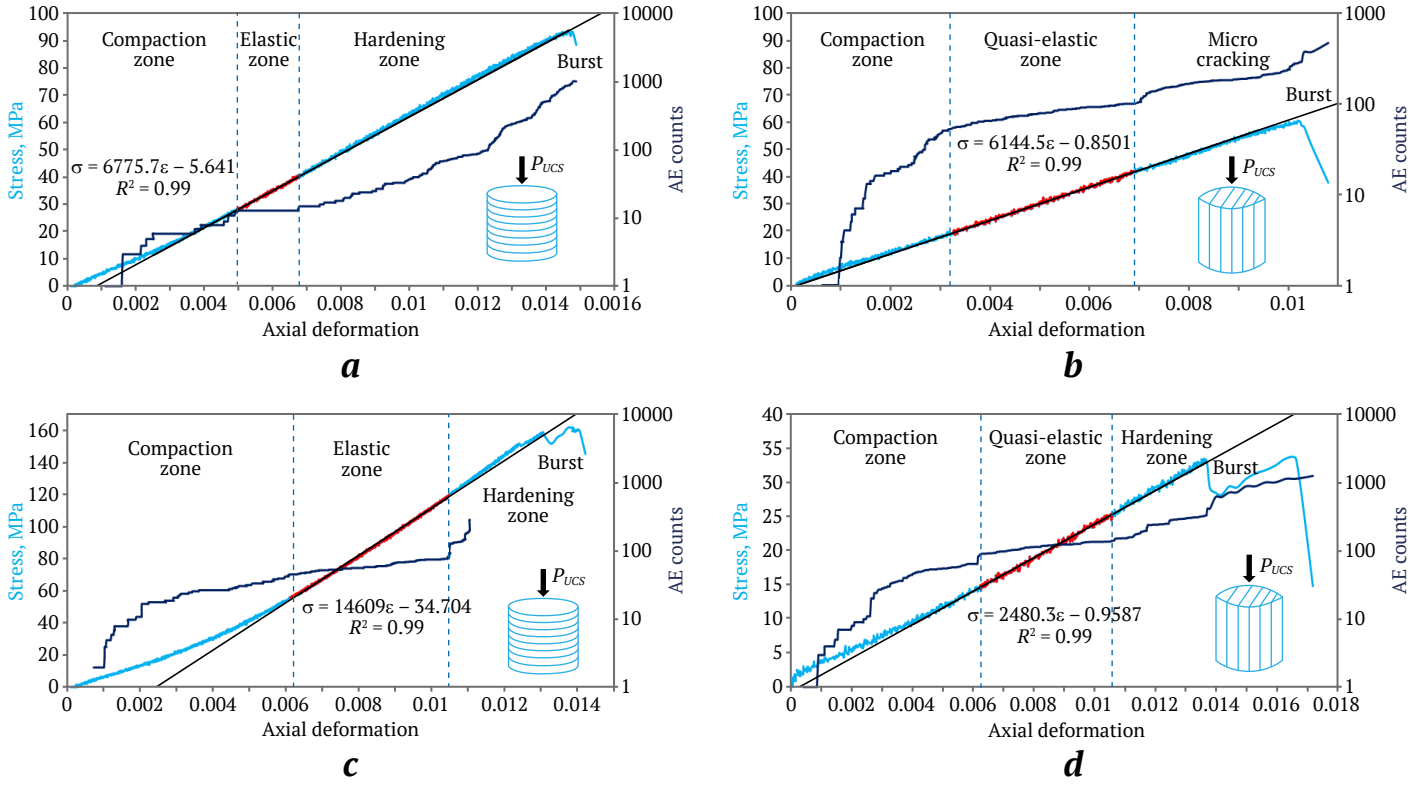

Fig. 6. Stress-strain curves and cumulative AE count plots for natural rock specimens:
silicites cut perpendicular to bedding (*a*); silicites cut parallel to bedding (*b*); silicified dolomites (*c*); opoka (*d*).
The light blue line represents stress, and the dark blue line represents cumulative AE counts.
The red line indicates the linear elastic or quasi-elastic segment used to calculate Young's modulus

In all specimens, the linear segment of the stress-strain curve is characterized by a linear increase in stress with strain and by the absence, or low intensity, of AE activity. The lowest AE intensity was observed in silicite specimens drilled perpendicular to bedding (Fig. 6, *a*). In silicite specimens with the bedding plane parallel to the loading vector, as well as in opoka, AE activity remained relatively high despite the linearity of the stress-strain curve in this region(Fig. 6, *b*, *d*).

The tangents to the stress-strain curves in the linear elastic or quasi-elastic segment are described by the following equations:

$$\sigma_1 = 6775.7\varepsilon_\alpha - 5.64; \quad (5)$$

$$\sigma_2 = 6144.5\varepsilon_\alpha - 0.85; \quad (6)$$

$$\sigma_3 = 14609.0\varepsilon_\alpha - 34.70; \quad (7)$$

$$\sigma_4 = 2480.3\varepsilon_\alpha - 0.95. \quad (8)$$

The subscript corresponds to the specimen group. The coefficients on the right-hand side of the equations represent the Young's moduli of the specimens.

Beyond the elastic or quasi-elastic segment, the intensity of microcracking increased, as reflected in a marked rise in cumulative AE counts. In specimens shown in Fig. 6, *a*, *c*, and *d*, this stage was accompanied by hardening, as indicated by the increasing slope of the stress-strain curve. In contrast, in silicite specimens drilled parallel to bedding, microcracking led to degradation of the mechanical properties, as indicated by the descending branch of the curve (Fig. 6, *b*). After the strength limit was exceeded, all specimens failed.

The highest uniaxial compressive strength was observed in specimens drilled perpendicular to bedding, namely 117 MPa for silicites and 186 MPa for silicified dolomites. The lowest strength was recorded in specimens drilled parallel to bedding, namely 86 MPa for silicites and 51 MPa for opoka. Specimens with bedding perpendicular to the load also exhibited the greatest total strains (see Fig. 6, *a*, *c*), which is attributable to the orientation of relaxation cracks perpendicular to the loading vector.

4. Discussion

Effect of 3D-LCD printing features and layer orientation on anisotropy. Because the LCD-based 3D-printing method is inherently layer-by-layer, it results in a layered internal structure in the finished parts. Such a structure may give rise to anisotropy in the properties of the printed specimens depending on layer angle and orientation. However, the present study showed that these features do not affect the uniformity of the elastic properties measured by non-destructive methods or under uniaxial compression in the stress range up to 20 MPa. Anisotropy associated with layer angle and orientation becomes apparent only above this threshold.

Comparison of rocks and replicas. Despite differences in layer angle and orientation, the rock replicas exhibit relative uniformity, as evidenced by the similar shape of their stress-strain curves. In natural rocks, by contrast, anisotropy is controlled by bedding and has a pronounced effect on mechanical behavior under loading.

To assess whether the replicas could be used as analogs of natural rocks, materials spanning a broad strength range were selected, namely homogeneous high-strength rocks (silicites and silicified dolomites) and weak opoka. The test results showed that even rocks with a high degree of structural uniformity exhibit pronounced anisotropy in their mechanical properties.

Comparative analysis of the stress-strain curves showed that the Young's moduli of the replicas are lower than those of silicified dolomites and silicites, but higher than that of opoka. At the same time, the elastic deformation range of the replicas coincides with the elastic deformation range of the natural rocks (Fig. 7).

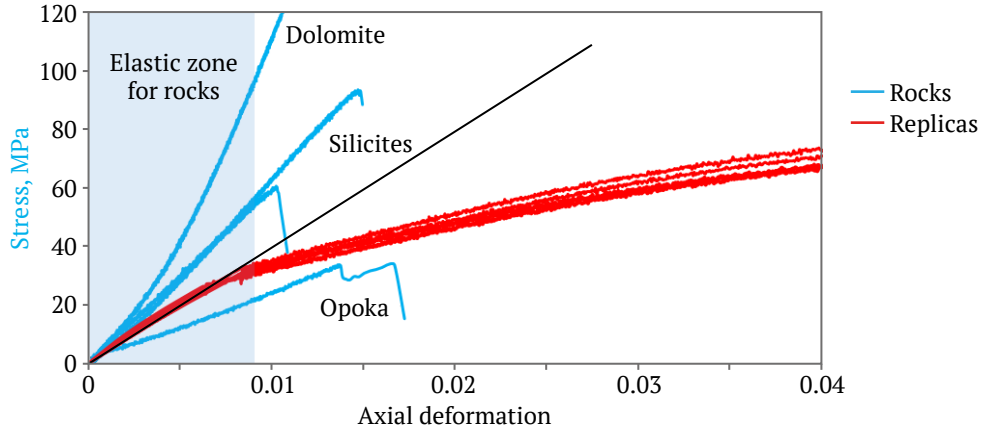

Fig. 7. Stress-strain curves for rocks (blue line) and replicas (red line). The shaded area indicates the elastic deformation zone of the rocks. The black line is tangent to the stress-strain curves of the replicas

Thus, the replicas may be regarded as analogs of natural rocks, but only within the stress range that does not exceed the elastic limit.

At stresses above 40 MPa, microdamage begins to develop in the replicas, and, because of their structural features, the stress-strain curves start to diverge. The greater strains observed in the replicas compared with the natural rocks are attributable to the predominance of cohesive bonding and the very low level of internal friction. Because internal friction is essentially absent, the layers slide relative to one another without substantial resistance. This behavior is related to the polymeric nature of the resin, which contains no solid particles.

Nevertheless, the replicas exhibit uniaxial compressive strength values comparable to those of natural rocks and, in some cases, even higher. Depending on layer inclination, the compressive strength of the replicas ranges from 138 to 162 MPa, whereas that of the natural rocks ranges from 51 to 186 MPa. At the same time, the replicas accumulate substantial strain before failure, reaching values of up to 0.37, and the specimens assume a barrel-shaped form (Fig. 8, *b*). In natural rocks, strain remains barely noticeable even after failure (Fig. 8, *d*, *e*) and does not exceed 0.015.

Micrographs of the fracture surfaces (Fig. 9) show that the replica has a smooth fracture surface, indicating that nothing impedes interlayer sliding or the propagation of microcracks. The fine-grained structure of the natural rocks, by contrast, provides high cohesion and substantial internal friction because of their granular texture. This impedes smooth crack propagation, so the fracture surfaces of the rocks are irregular and rough (Fig. 9, *b*).

The failure pattern of the natural rock specimens does not show a pronounced dependence on bedding angle, unlike that of the replicas. Silicites drilled perpendicular and parallel to bedding exhibit a similar type of failure characterized by extensive fragmentation and longitudinal macrocracks propagating toward the specimen ends (Fig. 10, *a*, *b*). Despite differences in strength and bedding angle, silicified dolomites and opoka (Fig. 10, *c*, *d*) both exhibit high brittleness, as reflected in pronounced fragmentation. The abundance of cracks at the specimen ends indicates that brittle failure predominates over ductile deformation.

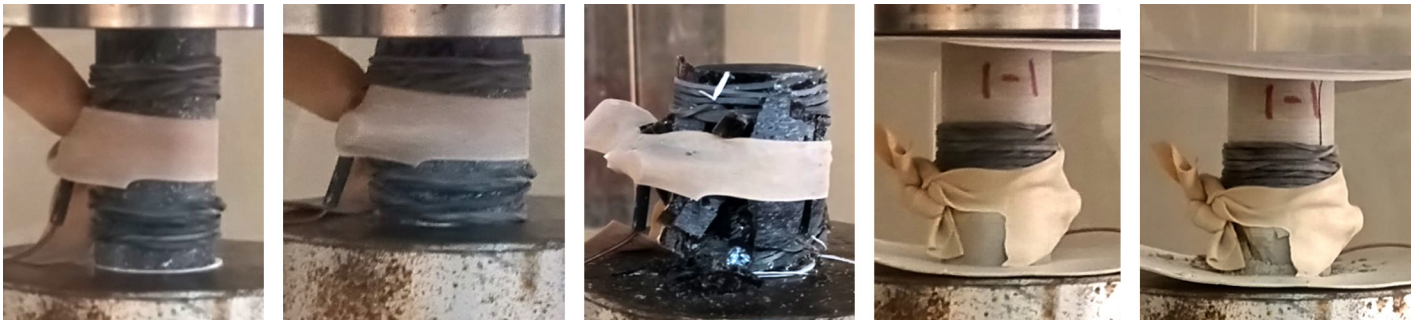

a ***b*** ***c*** ***d*** ***e***

Fig. 8. Photographs of specimens under load:
replica and natural rock specimen before loading (*a*, *d*); replica before failure (*b*); failed replica and rock specimen (*c*, *e*)

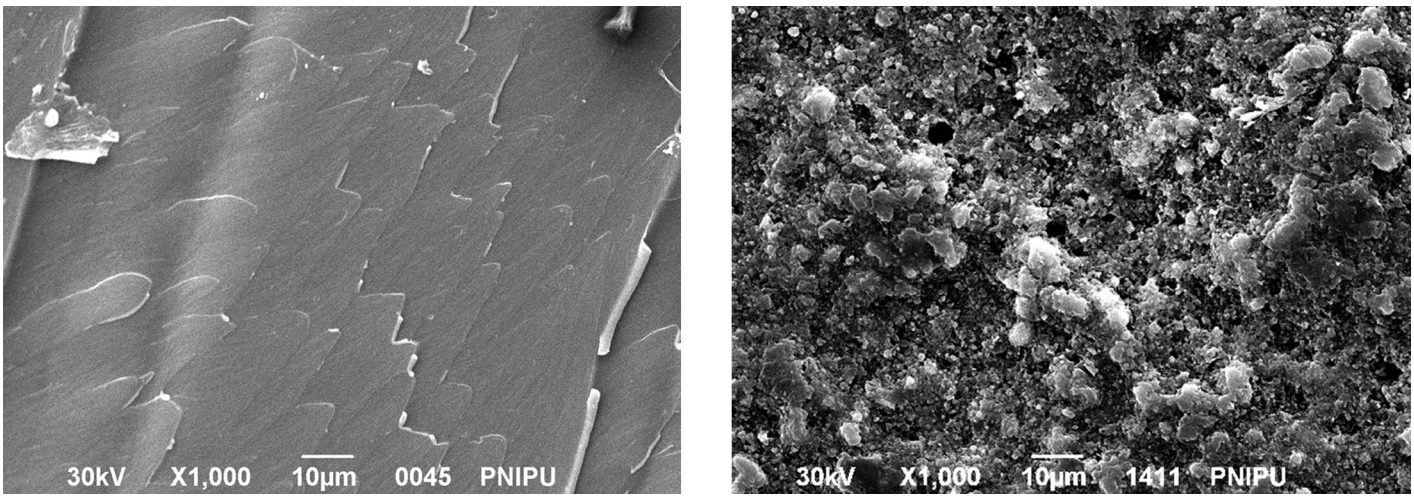

a ***b***

Fig. 9. Micrographs of specimen fracture surfaces: *a* – replica; *b* – silicite

a *b* *c* *d*

Fig. 10. Natural rock specimens after uniaxial compression testing. Specimens drilled perpendicular (*a*, *c*) and parallel (*b*, *d*) to bedding

In replicas with a layer orientation of 0°, numerous cracks are also observed at the specimen ends; however, unlike those in natural rocks, these cracks result from delamination and are characteristic only of this specimen group. In replicas with layer inclinations of 60° and 90°, in which prolonged hardening stages were previously observed, no longitudinal brittle cracks were found at the specimen ends, confirming that failure in these specimens is predominantly ductile.

Thus, the present study showed that the 3D-LCD printing method is suitable for producing and investigating the geomechanical characteristics of rock-like specimens under low loads that do not lead to internal damage. Replicas fabricated by 3D-LCD printing are not complete analogs of natural rocks and cannot fully replace studies of real rocks, especially in investigations involving failure. To use the 3D-LCD method for producing rock replicas in studies involving failure, the issue of internal friction, which is absent in the material, must first be addressed. Nevertheless, the use of this replication method under purely elastic loading makes it possible to evaluate the geomechanical characteristics and behavior of rocks with different structural features, which can be varied over a wide range.

5. Practical applications

The results of this study have high practical potential and can be directly used in laboratory geomechanical testing in the mining, oil and gas, and construction industries. The findings confirm that 3D-LCD printing technology enables the cost-effective batch production of rock replicas with reproducible physical and mechanical properties. This makes it possible to replace scarce core material and substantially reduce the costs associated with field drilling, transportation, and storage of expensive specimens.

The use of 3D rock replicas improves the efficiency of experimental studies by eliminating the costly and time-consuming procedures involved in sampling and preparing natural specimens. The economic

benefit is achieved through reduced testing costs and shorter testing times, as well as through the possibility of repeatedly reproducing identical specimens for parallel experiments.

Practical implementation of the proposed approach makes it possible to create physical models of rock masses for assessing excavation stability, calculating drilling parameters, predicting fracture development, and evaluating the filtration properties of reservoir rocks. In addition, the results may be used in the development of digital testbeds and in the verification of numerical geomechanical models. Thus, the use of 3D-LCD rock replicas helps reduce experimental costs, improve the accuracy of engineering predictions, and accelerate the design stage in the mining and oil and gas industries.

3D-LCD printing technology can be effectively used not only for fabricating rock specimen replicas but also for laboratory-scale physical modeling of various mining objects, including the assessment of the stability of mine workings and underground structures, the calculation of the load-bearing capacity of supports and pillars, and the optimization of their shape and arrangement. This opens up new opportunities for the rapid and cost-effective evaluation of design solutions in mining and construction.

Conclusion

The results of the experimental study confirmed the applicability of 3D-LCD printing for producing rock replicas suitable for physical modeling of geomechanical behavior under elastic loading. The aim of the study was achieved, and all the stated objectives were fully accomplished.

The study showed that the optimal post-curing time for the photopolymer material is 4 min, which ensures complete polymerization without further changes in mechanical properties. The resulting specimens were shown to exhibit isotropy of elastic properties: differences in the propagation velocities of longitudinal and transverse waves in the axial and radial directions did not exceed the measurement error. For the printed replicas, Young's modulus determined from nondestructive testing and uniaxial compression tests falls within the range of 3.89–4.27 GPa, which is comparable to the corresponding values for natural silicites and silicified dolomites.

The effect of printed-layer orientation on specimen strength was established experimentally: the highest strength was recorded at an angle of 60° (average 158 MPa), whereas the lowest was observed at 30° (138 MPa). The mechanical tests were accompanied by acoustic emission monitoring, which made it possible to identify differences in failure mechanisms as a function of layer orientation.

Comparison with the results obtained for natural rocks revealed similar patterns of deformation behavior under elastic loading, confirming the suitability of 3D-LCD replicas for modeling geomechanical processes. The scientific novelty of the study lies in the quantitative determination of the relationships between elastic modulus, compressive strength, and layer orientation angle, as well as in the experimental confirmation of the isotropy and stability of the elastic properties of photopolymer replicas. These findings expand the scope of 3D-LCD printing in geotechnical research and demonstrate its high reproducibility and cost-effectiveness.

References

1. Johnson P. R., Copeland P. M., Ayodele A. O. et al. In-vacuum performance of a 3D-printed ion deflector. *Vacuum*. 2020;172:109061. https://doi.org/10.1016/j.vacuum.2019.109061
2. Dong D., Su H., Li X. et al. Microstructures and mechanical properties of biphasic calcium phosphate bioceramics fabricated by SLA 3D printing. *Journal of Manufacturing Processes*. 2022;81:433–443. https://doi.org/10.1016/j.jmapro.2022.07.016
3. Khimulia V., Karev V., Kovalenko Y., Barkov S. Changes in filtration and capacitance properties of highly porous reservoir in underground gas storage: CT-based and geomechanical modeling. *Journal of Rock Mechanics and Geotechnical Engineering*. 2024;16(8):2982–2995. https://doi.org/10.1016/j.jrmge.2023.12.015
4. Riabokon E., Gladkikh E., Turbakov M. et al. Effects of ultrasonic oscillations on permeability of rocks during the paraffinic oil flow. *Geotechnique Letters*. 2023;13(3):151–157. https://doi.org/10.1680/jgele.22.00137
5. Hodder K. J., Sanchez-Barra A. J., Ishutov S. et al. Increasing density of 3D-printed sandstone through compaction. *Energies*. 2022;15(5):1813. https://doi.org/10.3390/en15051813
6. Wu H., Ju Y., Han X. et al. Size effects in the uniaxial compressive properties of 3D printed models of rocks: an experimental investigation. *International Journal of Coal Science & Technology*. 2022;9:83. https://doi.org/10.1007/s40789-022-00556-3

7. Cheng P., Wang K., Peng Y. et al. A novel 3D printed continuous ramie fiber reinforced variable stiffness biocomposite honeycomb structure. *Vacuum*. 2023;215:112301. https://doi.org/10.1016/j.vacuum.2023.112301
8. Wu Z., Zhang B., Weng L. et al. A new way to replicate the highly stressed soft rock: 3D printing exploration. *Rock Mechanics and Rock Engineering*. 2020;53:467–476. https://doi.org/10.1007/s00603-019-01926-1
9. Wang Y., Wang L., Zhang W., Ma G. Size effect of fractured rock mass based on 3D printed model testing. *Rock Mechanics and Rock Engineering*. 2022;55:7005–7020. https://doi.org/10.1007/s00603-022-03013-4
10. Zhang K., Zhang K., Ye J. et al. An improved sand 3D printing method for better reproduction of high-strength and high-brittleness rock mechanical properties is proposed. *Journal of Materials Research and Technology*. 2023;26:5037–5054. https://doi.org/10.1016/j.jmrt.2023.08.204
11. Sharafisafa M., Shen L. Experimental investigation of dynamic fracture patterns of 3D printed rock-like material under impact with digital image correlation. *Rock Mechanics and Rock Engineering*. 2020;53:3589–3607. https://doi.org/10.1007/s00603-020-02115-1
12. Song R., Wang Y., Ishutov S. et al. A comprehensive experimental study on mechanical behavior, microstructure and transport properties of 3D-printed rock analogs. *Rock Mechanics and Rock Engineering*. 2020;53:5745–5765. https://doi.org/10.1007/s00603-020-02239-4
13. Shi D., Hou Y., Gao G. Effect of printing parameters on properties of 3D printing sand samples. *China Foundry*. 2023;20:553–562. https://doi.org/10.1007/s41230-023-3002-9
14. Morettini G., Palmieri M., Capponi L., Landi L. Comprehensive characterization of mechanical and physical properties of PLA structures printed by FFF-3D-printing process in different directions. *Progress in Additive Manufacturing*. 2022;7:1111–1122. https://doi.org/10.1007/s40964-022-00285-8
15. Izdebska-Podsiadły J. Chapter 3 – Classification of 3D printing methods. In: Izdebska-Podsiadły J. (Ed.) *Polymers for 3D Printing*. William Andrew (Elsevier); 2022. Pp. 23–34. https://doi.org/10.1016/B978-0-12-818311-3.00009-4
16. Vidhu N., Gupta A., Salajeghe R. et al. A computational model for stereolithography apparatus (SLA) 3D printing. *Progress in Additive Manufacturing*. 2023;9:1605–1619. https://doi.org/10.1007/s40964-023-00525-5
17. Yu Z., Li X., Zuo T. et al. High-accuracy DLP 3D printing of closed microfluidic channels based on a mask option strategy. *The International Journal of Advanced Manufacturing Technology*. 2023;127:4001–4012. https://doi.org/10.1007/s00170-023-11769-4
18. Saitta L., Tosto C., Pergolizzi E. et al. Liquid Crystal Display (LCD) printing: a novel system for polymer hybrids printing. In: *Macromolecular Symposia. Progress on Polymers and Composites Products and Manufacturing Technologies – POLCOM 2020*. 2021;395(1):2000254. https://doi.org/10.1002/masy.202000254
19. Chen S., Zhang J., Yin D. et al. Visualizing experimental investigation on gas-liquid replacements in a microcleat model using the reconstruction method. *Deep Underground Science and Engineering*. 2023;2(3):295–303. https://doi.org/10.1002/dug2.12044
20. Katheng A., Prawatvatchara W., Chaiamornsup P. et al. Comparison of mechanical properties of different 3D printing technologies. *Scientific Reports*. 2025;15:18998. https://doi.org/10.1038/s41598-025-03632-1
21. Dulieu-Barton J.M., Fulton M.C. Mechanical properties of a typical stereolithography resin. *Strain*. 2000;36(2):81–87. https://doi.org/10.1111/j.1475-1305.2000.tb01177.x
22. Puebla K., Arcaute K., Quintana R., Wicker R. B. Effects of environmental conditions, aging, and build orientations on the mechanical properties of ASTM type I specimens manufactured via stereolithography. *Rapid Prototyping Journal*. 2012;18(5):374–388. https://doi.org/10.1108/13552541211250373
23. Chen Q., Zou B., Lai Q. et al. Influence of irradiation parameters on the curing and interfacial tensile strength of HAP printed part fabricated by SLA-3D printing. *Journal of the European Ceramic Society*. 2022;42(14):6721–6732. https://doi.org/10.1016/j.jeurceramsoc.2022.07.019
24. Rehbein T., Johlitz M., Lion A. et al. Temperature- and degree of cure-dependent viscoelastic properties of photopolymer resins used in digital light processing. *Progress in Additive Manufacturing*. 2021;6:743–756. https://doi.org/10.1007/s40964-021-00194-2
25. Shirinbayan M., Zirak N., Saddaoui O. et al. Effect of build orientation and post-curing of (meth) acrylate-based photocurable resin fabricated by stereolithography on the mechanical behavior from quasi-static to high strain rate loadings. *The International Journal of Advanced Manufacturing Technology*. 2022;123:1877–1887. https://doi.org/10.1007/s00170-022-10336-7

26. Lee J.H., Prud'homme R.K., Aksay I.A. Cure depth in photopolymerization: experiments and theory. *Journal of Materials Research*. 2001;16:3536–3544. https://doi.org/10.1557/JMR.2001.0485
27. Lee E.-D., Sim J.-H., Kweon H.-J., Paik I.-H. Determination of process parameters in stereolithography using neural network. *KSME International Journal*. 2004;18:443–452. https://doi.org/10.1007/BF02996109
28. Li Y., Teng Z. Effect of printing orientation on mechanical properties of SLA 3D-printed photopolymer. *Fatigue & Fracture of Engineering Materials & Structures*. 2024;47(5):1531–1545. https://doi.org/10.1111/ffe.14265
29. Monzón M., Ortega Z., Hernández A. Anisotropy of photopolymer parts made by digital light processing. *Materials*. 2017;10(1):64. https://doi.org/10.3390/ma10010064
30. Farkas A.Z., Galatanu S.-V., Nagib R. The influence of printing layer thickness and orientation on the mechanical properties of dlp 3d-printed dental resin. *Polymers*. 2023;15(5):1113. https://doi.org/10.3390/polym15051113
31. Saini J., Dowling L., Kennedy J., Trimble D. Investigations of the mechanical properties on different print orientations in SLA 3D printed resin. *Proceedings of the Institution of Mechanical Engineers, Part C: Journal of Mechanical Engineering Science*. 2020;234(11):2279–2293. https://doi.org/10.1177/0954406220904106
32. Keßler A., Hickel R., Ilie N. In vitro investigation of the influence of printing direction on the flexural strength, flexural modulus and fractographic analysis of 3D-printed temporary materials. *Dental Materials Journal*. 2021;40(3):641–649. https://doi.org/10.4012/dmj.2020-147
33. Pandzic A. Influence of Layer height, build orientation and post curing on tensile mechanical properties of SLA 3D printed material. In: Katalinic B. (Ed.) *32nd DAAAM International Symposium on Intelligent Manufacturing and Automation*. Vienna, Austria: DAAAM International; 2021. Pp. 0200–0208. https://doi.org/10.2507/32nd.daaam.proceedings.030
34. Cosmi F., Dal Maso A. A mechanical characterization of SLA 3D-printed specimens for low-budget applications. *Materials Today: Proceedings*. 2020;32(Part 2):194–201. https://doi.org/10.1016/j.matpr.2020.04.602
35. Quagliato L., Kim S.Y., Ryu S.C. Quasi-ductile to brittle transitional behavior and material properties gradient for additively manufactured SLA acrylate. *Materials Letters*. 2022;329:133121. https://doi.org/10.1016/j.matlet.2022.133121

Information about the authors

Evgenii V. Kozhevnikov – Cand. Sci. (Eng.), Associate Professor at the Department of Oil and Gas Technologies, Perm National Research Polytechnic University, Perm, Russian Federation; ORCID 0000-0002-6084-0795, Scopus ID 55531698200, SPIN 3914-7370; e-mail kev@pstu.ru

Mikhail S. Turbakov – Cand. Sci. (Eng.), Associate Professor at the Department of Oil and Gas Technologies, Leading Researcher at the Laboratory of Natural Gas Hydrates, Perm National Research Polytechnic University, Perm, Russian Federation; ORCID 0000-0002-9336-5847, Scopus ID 36443127500, ResearcherID A-5611-2014, SPIN 1613-8284; e-mail msturbakov@pstu.ru

Zakhar G. Ivanov – Laboratory Assistant at the Department of Oil and Gas Technologies, Perm National Research Polytechnic University, Perm, Russian Federation; ORCID 0009-0001-7957-8280, Scopus ID 59022877200, SPIN 1511-2857; e-mail zakharivanov@pstu.ru

Evgenii P. Riabokon – Cand. Sci. (Eng.), Senior Lecturer at the Department of Oil and Gas Technologies, Perm National Research Polytechnic University, Perm, Russian Federation; ORCID 0000-0003-0555-3977, Scopus ID 56006175100, SPIN 8783-5060; e-mail riabokon@pstu.ru

Pavel A. Kamenev – Cand. Sci. (Eng.), Senior Researcher at the Laboratory of Geochemistry and Regional Geology, Institute of Marine Geology and Geophysics of the Far Eastern Branch of the Russian Academy of Sciences (IMGG FEB RAS), Yuzhno-Sakhalinsk, Russian Federation; ORCID 0000-0002-9934-5855, Scopus ID 57193337193, SPIN 6271-5797; e-mail p.kamenev@imgg.ru

Received 10.02.2025
Revised 05.12.2025
Accepted 10.12.2025

TECHNOLOGICAL SAFETY

Research paper

https://doi.org/10.17073/2500-0632-2025-08-1022
UDC 622.4

Methodological framework for designing ventilation control systems for complex mine ventilation networks

L. Yu. Levin, M. A. Semin ✉, S. V. Maltsev, A. V. Zaitsev
Mining Institute, Ural Branch of the Russian Academy of Sciences, Perm, Russian Federation
✉ *seminma@inbox.ru*

Abstract
As ventilation networks in modern mines expand, airflow distribution control becomes increasingly complicated due to three factors: insufficient control depth combined with unsynchronized operating schedules of individual mine sectors; increasingly complex aerodynamic interactions between working areas and control devices; and growing system inertia. This highlights the need for a unified approach to designing ventilation control systems for complex networks, so that the conditions under which their implementation is technically feasible and economically justified can be assessed in advance. To achieve this objective, two key tasks were addressed: identifying the appropriate spatial depth and temporal scale of ventilation control. The methodology was based on a mathematical framework for analyzing aerodynamic interactions in branched networks with numerous fans, shafts, levels, and diagonal connections. The framework includes the use of aerodynamic influence matrices, their graphical analysis, clustering, and decomposition of the network into subsystems. Dimensional analysis was also applied to estimate the characteristic times of various dynamic processes in mines. As a result, principles for designing control systems were proposed, including the selection of the control level with regard to the number of air consumers and their operating schedules, as well as matching the control time scale to the characteristic times of ventilation and mining processes. It was shown that the duration of production cycles permits ventilation control to be applied at that level, opening a promising direction for further research. It was also established that, in complex ventilation networks, control algorithms should be designed primarily to maintain the required airflow rate, whereas control based on gas concentration is less effective.

Keywords
mine ventilation, ventilation on demand, mine ventilation networks, ventilation control, aerodynamic influence, spatial depth of control, temporal scale of control

Funding
This study was supported by the Russian Science Foundation, grant No. 19-77-30008P.

For citation
Levin L. Yu., Semin M. A., Maltsev S. V., Zaitsev A. V. Methodological framework for designing ventilation control systems for complex mine ventilation networks. *Mining Science and Technology* (*Russia*). 2026;11(1):70–79. https://doi.org/10.17073/2500-0632-2025-08-1022

ТЕХНОЛОГИЧЕСКАЯ БЕЗОПАСНОСТЬ

Научная статья

Методологические аспекты создания систем управления проветриванием сложных вентиляционных сетей современных рудников

Л. Ю. Левин, М. А. Семин ✉, С. В. Мальцев, А. В. Зайцев
Горный институт УрО РАН, г. Пермь, Российская Федерация
✉ *seminma@inbox.ru*

Аннотация
По мере развития вентиляционных сетей современных рудников управление воздухораспределением осложняется воздействием трёх факторов: недостаточной глубиной регулирования и несинхронностью графиков работы отдельных участков; усложнением аэродинамических связей между рабочими зонами и регуляторами; ростом инерционности системы. Это обусловливает необходимость разработки единого подхода к созданию систем управления вентиляцией в сложных сетях, позволяюще-

го заранее оценить условия, при которых внедрение таких систем будет экономически оправданным и технически реализуемым. Достижение указанной цели предполагало решение двух ключевых задач: определение пространственной глубины управления и временного масштаба управления. Основой методологии послужил разработанный математический аппарат для анализа аэродинамических связей в разветвлённых сетях с большим числом вентиляторов, стволов, горизонтов и диагональных соединений. Он включает использование матриц аэродинамического влияния, их графический анализ, кластеризацию и декомпозицию сети на подсистемы. С помощью метода размерностей получены оценки характерных времен различных динамических процессов в рудниках. В результате предложены принципы проектирования систем управления, предусматривающие выбор уровня регулирования с учётом числа потребителей и их производственных графиков, а также согласование временного масштаба регулирования с характерными временами аэрологических и горнотехнологических процессов. Показано, что длительность технологических циклов допускает применение регулирования вентиляции на их уровне, что открывает перспективное направление для дальнейших исследований. Установлено, что для сложных вентиляционных сетей алгоритмы управления должны быть в первую очередь ориентированы на поддержание требуемого расхода воздуха, тогда как регулирование по концентрации газов менее эффективно.

Ключевые слова
рудничная вентиляция, вентиляция по требованию, вентиляционные сети, управление проветриванием, аэродинамическое влияние, пространственная глубина управления, временной масштаб управления

Финансирование
Исследование выполнено при финансовой поддержке Российского научного фонда (проект № 19-77-30008П).

Для цитирования
Levin L. Yu., Semin M. A., Maltsev S. V., Zaitsev A. V. Methodological framework for designing ventilation control systems for complex mine ventilation networks. *Mining Science and Technology* (*Russia*). 2026;11(1):70–79. https://doi.org/10.17073/2500-0632-2025-08-1022

Introduction

As large mineral deposits are developed, mine ventilation networks tend to become highly branched over time. They may include several hundred or even thousands of mine workings, numerous working areas, underground levels, and pressure sources. As the network expands, the nonproductive use of fresh air, that is, so-called air leakage, also increases. Delivering the required volume of fresh air to each working area becomes progressively more difficult, while ensuring this in an energy-efficient manner becomes even more challenging. As a result, mine ventilation costs steadily increase with mining depth, the expansion of the workings network, and rising production rates. Under such conditions, the share of power consumption attributable to ventilation may reach 50% of the total energy used in mining operations [1–3]. Ventilation thus becomes such a costly production process that its optimization can no longer be neglected if a mining enterprise intends to remain profitable.

The number of shafts in mines is usually minimized for economic reasons. However, their air-carrying capacity is limited by the permissible air velocity, which, according to safety regulations, must not exceed 15 m/s. This naturally reduces the maximum allowable airflow through shafts and, in turn, requires more rational and efficient air distribution throughout underground workings.

Energy-efficient ventilation of underground mines requires the use of airflow control systems. The most widespread of these is ventilation on demand (VoD), which provides dynamic adjustment of air supply depending on the current operating conditions [4, 5]. For each shift, a required airflow rate is specified, and the system achieves it by varying the rotational speed of the main fans, adjusting the door opening, and using other control means. This approach has proven effective in relatively small mines with one or several working areas. In such cases, it is generally possible to rely on fairly simple control algorithms for fan installations and ventilation doors.

However, in branched ventilation networks serving numerous air consumers, the effective use of ventilation control systems remains an open issue. There are known cases where simple control schemes that distribute airflow only among the main mine districts fail to deliver appreciable energy savings [6]. This is primarily due to insufficient control depth and the limited overlap between the operating schedules of development and production districts. In this context, control depth refers to the hierarchical level at which ventilation regulators are installed, that is, the extent to which ventilation doors are positioned beyond the shaft station and the main drifts to redistribute airflow among individual sectors of the network. For example, in the Verkhnekamsk potash mines, if ventilation doors are installed only on the main ventilation drifts near the shaft station and regulate only the overall airflow by direction, the system cannot accurately redistribute airflow among panels and blocks within the same direction. Consequently, a significant portion of the potential benefit is lost.

The growing complexity of airflow distribution control in developing ventilation networks cannot be explained by this factor alone. Two additional aspects are also of major importance.

First, aerodynamic interactions between working areas and control devices become increasingly complex. In practice, a ventilation network cannot always be represented as a simple system of several parallel airways, each controlled by a separate fan or door. Working areas are often connected in series or by diagonal links, so that a single control device may affect several air consumers to different extents [7].

Second, ventilation system inertia increases. The greater the total length of the main ventilation airways and the more complex the network, the longer it takes for a new airflow distribution to become established after the control settings have been changed. This limits the performance of the control system, which must operate on a time scale consistent with the transition of the network to a new steady state. In large networks, the control system is physically unable to respond to short-term fluctuations in airflow rate or gas concentration; such variations must therefore remain outside the control range.

This raises an important question: can a unified approach be developed for designing ventilation control systems in complex networks that would make it possible to assess in advance the conditions under which their implementation would be technically feasible and economically justified? Addressing this question requires a conceptual reappraisal of ventilation control, especially in mines with complex ventilation networks. In the present study, complexity is understood specifically in terms of controllability, that is, the presence of one or more of the following factors:

– a large number of ventilation control devices, including fans and ventilation doors;

– numerous working areas connected in parallel, in series, or through diagonal connections, with unsynchronized operating schedules;

– long airways, which increase system inertia.

The **aim** of this study is to develop and substantiate methodological principles for designing ventilation control systems for complex mine ventilation networks while accounting for these factors.

To achieve this aim, two **key objectives** must be addressed:

1. To identify the appropriate spatial depth of control, that is, to determine the hierarchical level at which ventilation regulators should be installed to effectively influence airflow in working areas.

2. To determine the appropriate temporal scale of control, that is, to identify the characteristic times of transient processes that may serve as targets for automatic regulation.

The first objective concerns the placement of negative regulators at underground levels. The key question is where they should be installed in order to exert a significant influence on airflow in the working area and, ultimately, to enable the system to achieve appreciable power savings.

Whereas the first objective relates to the spatial structure of the network, the second concerns its dynamics. More specifically, it requires estimating the characteristic times of unsteady aerological processes and comparing them with the response time of the control system.

Some dynamic processes are so rapid that they cannot be regulated by means of ventilation doors or fans, as any such attempt would destabilize the system. These include gas emission from the rock mass [8], the aerodynamic effects produced by moving mining equipment [9], and similar phenomena. Other processes are much slower, for example thawing of the rock mass [10], for which periodic manual adjustment of ventilation windows, once a week or once a month, is sufficient. It is therefore essential to identify processes whose duration is comparable to, but not shorter than, the response time of the control system and to use them as the basis for automatic regulation.

The development of a unified approach to mine ventilation control systems has been discussed in earlier studies. Significant contributions were made in [11–13], which established the theoretical foundations for automated airflow distribution control. In particular, [11] introduced the term *automated ventilation control system*. The authors of [12] were the first to emphasize the need to account for the different inertia of aerodynamic and gas-dynamic processes arising from different rates of disturbance propagation, and they also proposed a classification of ventilation networks into easy-to-control and difficult-to-control systems. In [13], an optimality criterion for ventilation network control was formulated, and methods for solving the corresponding optimal control problem were proposed.

The present study builds on the definition of complex ventilation systems proposed by S.V. Maltsev[1], while substantially extending it in the context of control tasks.

It should also be noted that the above studies considered optimal airflow distribution control pri-

[1] Maltsev S.V. Research and development of methods for determining the aerodynamic parameters of complex ventilation systems in underground mines. [Diss. ... Cand. Sci. (Eng.)] Perm; 2020. 148 p. (In Russ.)

marily through computer models of ventilation networks. The present study, by contrast, focuses on the application of automatic control theory. Thus, despite the extensive theoretical foundation already available, the methodology for designing ventilation control systems for mines with complex ventilation networks has not yet been addressed as a distinct subject in its own right.

Determining the spatial depth of ventilation control

Ventilation networks in modern mines are highly branched structures in which the airflow is split not once or twice, but many times. This is especially evident in potash mines (Fig. 1), where a *central ventilation system* is typically used.

Air entering through the intake shaft is first distributed among the main mine districts, then routed into the intake panel drifts, including the haulage and conveyor drifts, and subsequently into the block workings. If ventilation doors are installed only on the return drifts of the main directions, it becomes impossible to regulate airflow distribution among the individual branches within those directions, that is, at the panel and block levels.

This is due to the mining method used. At the Verkhnekamsk deposit, room-and-pillar mining with mechanized extraction by continuous miners is employed. Under these conditions, many production faces, often several dozen, operate simultaneously in different panels and on asynchronous schedules. On average, downtime at each face may reach 10 h per day. However, because a single ventilation door supplies air to several faces at once, it is practically impossible to reduce the total airflow rate in the mine [6].

By contrast, installing doors at every panel within a given direction would substantially increase their number and, consequently, the cost of implementing the ventilation control system. In addition, doors would have to be installed on all parallel branches, that is, all panels within that direction, in order to eliminate parallel aerodynamic connections. Otherwise, air would short-circuit through the branch not equipped with a flow-restricting device, effectively reducing the potential energy-saving effect to zero.

Thus, the placement of ventilation doors should be determined with reference to two key factors:

– the number of air consumers served by a single automatic ventilation door;

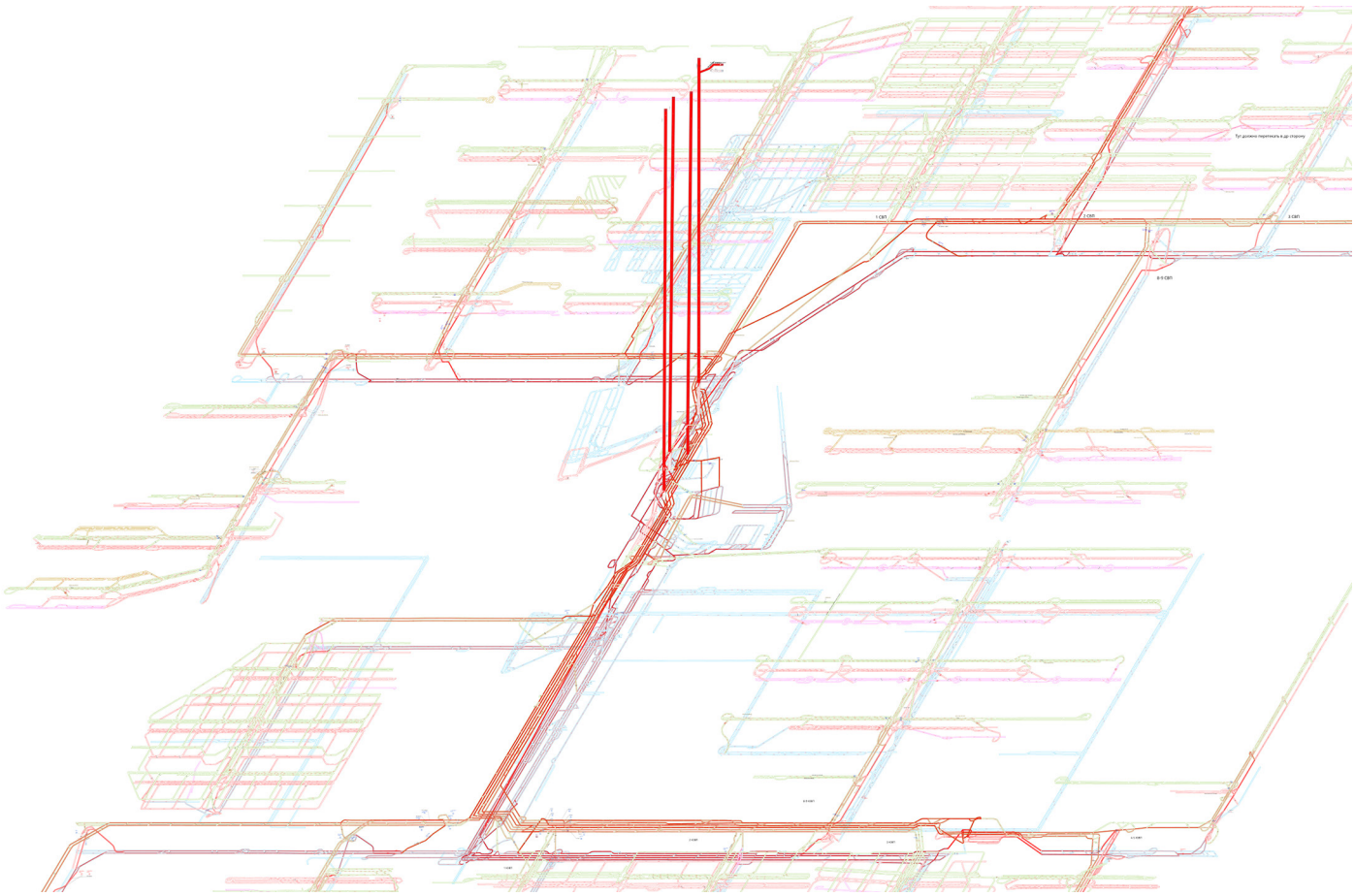

Fig. 1. Fragment of the ventilation network of a potash mine in the Verkhnekamsk deposit (generated using the Aeroset software package)

– the degree of overlap between the operating schedules of these air consumers.

If the number of consumers is large and their schedules are substantially out of phase, appreciable power savings are unlikely to be achieved. In such cases, the doors should be installed one hierarchical level lower, after the next airflow split into individual sectors, and the number of air consumers served by each automatic door should then be reassessed.

Ideally, one ventilation door should serve one consumer. In practice, however, this is not always feasible because of the large number of working areas, their high mobility, the rapid advance of the mining front, continual changes in active locations, and the influence of additional disturbing factors near individual working areas, such as auxiliary fans or moving mining equipment. Accordingly, identifying a compromise solution usually requires comparing the capital cost of installing ventilation doors with the savings in operating costs achieved through lower fan power demand.

This situation is not typical of the potash mines of the Starobin deposit, where longwall mining with caving is predominantly used. In the main directions of the ventilation networks at these mines, there are relatively few high-capacity working areas, namely longwalls, which makes it possible to achieve substantial power savings [5].

A different situation arises when ventilation control systems are designed for mines with a *flank ventilation system*. Examples include the copper-nickel mines in northern Krasnoyarsk Krai, which typically have 5–7 shafts, 2–4 main fan installations, and numerous underground levels. Fig. 2 shows the ventilation network of one such mine, including three main fans, seven shafts, and more than ten underground levels.

Whereas in mines with a central ventilation system the topological relationship between individual air consumers and ventilation doors can still be identified with reasonable clarity, in mines with a flank ventilation system it becomes much more difficult to trace airflow paths, determine which workings exert the strongest influence on particular air consumers, and establish where ventilation doors should be installed.

This complexity is primarily due to the large number of ventilation raises, inclines, connecting ramps, and other workings that create numerous diagonal connections and make the overall airflow pattern difficult to interpret. In this context, it is difficult to determine the required control depth and the corresponding arrangement of ventilation doors across underground levels.

To solve this problem, the present study proposes the use of aerodynamic influence matrices. These matrices make it possible to quantify how a change in the i-th control parameter affects the airflow rate at the j-th consumer.

If a tentative set of ventilation doors has been selected and the suitability of their locations needs to be assessed, an aerodynamic influence matrix may be calculated in the form

$$I_{ij} = \frac{R_{0j}}{Q_{0i}} \frac{\Delta Q_i}{\Delta R_j}, \quad (1)$$

where R_{0j} is the initial aerodynamic resistance of the j-th door, N·s^2/m^8; Q_{0i} is the initial airflow rate at the i-th consumer, m^3/s; ΔQ_i is the change in the total airflow rate at the i-th consumer in response to a change in the resistance of door j, m^3/s; ΔR_j is the change in door resistance, N·s^2/m^8.

The coefficients of the aerodynamic influence matrix in Eq. (1) make it possible to identify which ventilation doors have a strong effect on the airflow rate at a given air consumer while causing only minimal disturbance elsewhere in the network. This is determined by both the magnitude and the sign of the corresponding matrix elements.

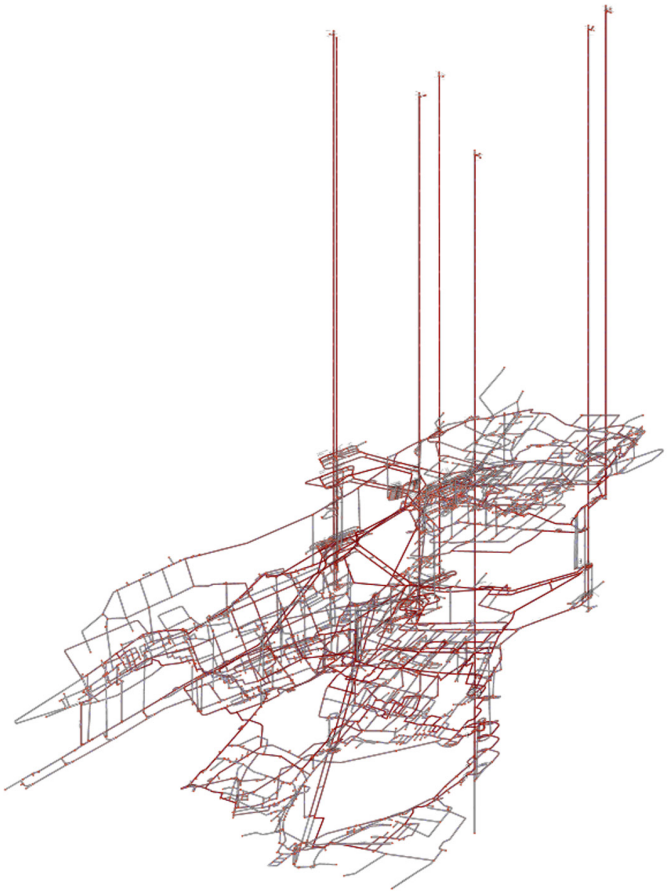

Fig. 2. Ventilation network of a copper-nickel mine in Krasnoyarsk Krai

A similar matrix may be constructed to evaluate the effect of the main fan installations on the airflow rates at the air consumers:

$$I_{ij} = \frac{n_{0j}}{Q_{0i}} \frac{\Delta Q_i}{\Delta n_j}, \quad (2)$$

where n_{0j} is the initial impeller rotational speed of the j-th fan installation, rpm, and Δn_j is the change in the impeller rotational speed of the j-th fan installation, rpm.

Mathematically, Eqs. (1) and (2) represent the Jacobian of the ventilation network. They are closely related to the sensitivity matrices used in stability analysis of mine ventilation networks [14, 15], but in this case they are expressed in normalized dimensionless form, which allows direct comparison of matrix elements for workings with substantially different airflow rates.

These matrix coefficients are not fixed; rather, they depend on the initial airflow rates Q_{0i}, aerodynamic resistances R_{0j}, and fan rotational speeds n_{0i}. Consequently, if the mine ventilation regime for which matrices (1) and (2) were derived changes substantially, their numerical values may also change appreciably. In addition, qualitative changes may occur, especially in parts of the network containing diagonal connections, reflecting the variable nature of aerodynamic interactions and highlighting potentially vulnerable zones susceptible to ventilation instability.

The corresponding matrix was constructed to assess the effectiveness of the selected ventilation-door locations in the copper-nickel mine shown in Fig. 2. For six aggregated air consumers, that is, mining districts comprising several working areas, matrix (1) identified the ventilation doors with the greatest influence on their ventilation (Fig. 3).

The blue and light-blue cells correspond to cases where $I_{ij} < 0$, that is, where an increase in ventilation-door resistance leads to a decrease in the airflow rate at the given consumer. At the same time, the matrix also contains elements for which $I_{ij} > 0$. In such cases, increasing door resistance causes the airflow rate to increase at some air consumers located on airways parallel to the corresponding door.

The ventilation door exerting the strongest negative influence was identified for each air consumer. This information was then used to assign control functions among the doors so as to ensure the required airflow rate at each consumer.

An approach of this kind, conceptually close to clustering methods widely used in data analysis, often reveals distinct clusters in the matrices, that is, groups of air consumers and doors that are closely interconnected but only weakly connected to the rest of the mine. In such cases, the control system of a complex mine can be organized as several mutually independent subsystems, which greatly simplifies its practical implementation.

Such clusters can be identified, for example, by introducing a threshold value for $|I_{ij}|$ (Fig. 4). Once all cells with values below this threshold are removed, it becomes clear which ventilation doors should be assigned to control which air consumers. At the same time, the need for some doors may be called into question, as in the case of doors 1, 7, and 9 in the mine considered here.

This matrix-based approach was applied in the development of ventilation control systems for three copper-nickel mines in Krasnoyarsk Krai. Because these mines use full-seam mining combined with drill-and-blast development, work shifts are highly synchronized. This makes it possible to distinguish several relatively large districts containing multiple working areas; in the mine considered above, six such districts were identified (see Figs. 3 and 4). In such cases, dynamic intrashift airflow distribution control can deliver substantial average daily energy savings, which ranged from 10.9 to 20.1% across the three mines studied.

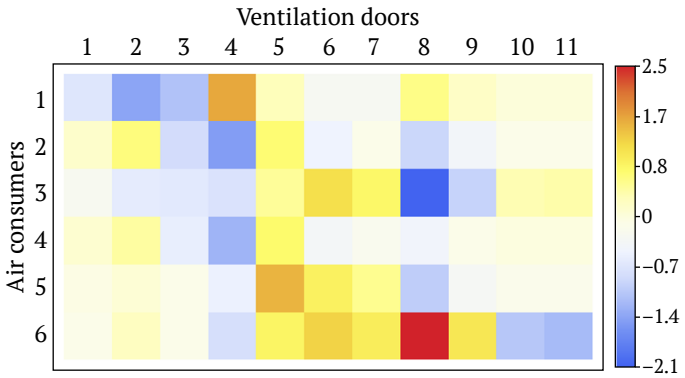

Fig. 3. Aerodynamic influence matrix for air consumers (production districts) in the copper-nickel mine

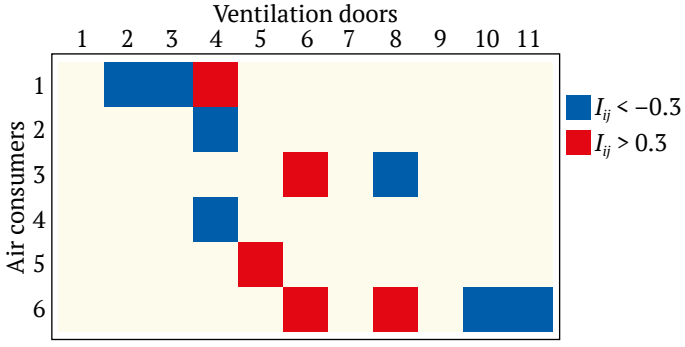

Fig. 4. Binarized aerodynamic influence matrix for air consumers in the copper-nickel mine

Determining the temporal scale of ventilation control

Aerological processes in the mine atmosphere are inherently unsteady and differ substantially in their characteristic time scales.

Fast processes. The fastest processes, such as the passage of a shock wave during drilling-and-blasting operations or methane outbursts, as well as the propagation of an acoustic wave during the rapid opening or closing of stoppings, are characterized by the following time scale:

$$\tau_1 = \frac{L}{c}, \quad (3)$$

where L is the length of the main airway in the ventilation network, m, and c is the speed of sound in air, m/s. For L = 10 km, this gives $\tau \approx 30$ s.

On such a short time scale, the airflow distribution in the network obviously cannot reach a steady state. Establishing a new distribution requires the repeated passage of acoustic disturbances [16]. The characteristic time required for the ventilation network to reach a steady airflow distribution can be estimated using the equation proposed in [17]:

$$\frac{\rho L}{S}\frac{dQ}{dt} = H - RQ^2, \quad (4)$$

where ρ is the air density, kg/m^3; S is the cross-sectional area of the working, m^2; Q is the airflow rate, m^3/s; H is the pressure drop, Pa; R is the aerodynamic resistance, N·s^2/m^8.

In this case, the characteristic time

$$\tau_2 = \frac{\rho LQ}{SH} \quad (5)$$

is on the order of tens of minutes.

Intermediate time scales. The characteristic times of production cycles depend on the specific type of operation. They may be on the order of:

– minutes, during the movement of load-haul-dump machines or haul trucks used to re-enter dead-end workings after blasting, as well as during the operation of continuous miner systems, for example in the Verkhnekamsk potash mines;

– hours, during post-blast ventilation of blind headings, maintenance operations, and similar activities.

In the general case, the time parameter τ_3, which reflects the cyclicity of production operations in working areas, should be determined individually. The same applies to τ_4, which characterizes shift duration (production, maintenance, or shutdown).

Slow processes. The longest-term variations are associated with thermal processes in the rock mass, including thawing, as well as seasonal changes in natural ventilation pressure, and may persist for weeks or months. Their characteristic time may be estimated from [18] as:

$$\tau_5 = \frac{R^2}{a}, \quad (6)$$

where R is the characteristic transverse dimension of the mine working, typically on the order of several meters, m, and a is the thermal diffusivity of the rock ($\approx 10^{-6}$ m^2/s).

Associated unsteady processes. Other processes also occur in mines, including the release of dust, methane, and hydrogen sulfide from the rock mass, as well as emissions from diesel-powered equipment. Their temporal behavior is sometimes correlated with equipment operation, but in many cases follows a different pattern. For example, gas emission from the rock in potash and coal mines may vary over time as a result of random processes, with characteristic fluctuation times on the order of minutes [8, 11].

This raises an important question: which parameter should be used to control ventilation doors and fans? Some authors [19–21] propose relying on direct gas analyzer readings at the working face. However, in mines with complex ventilation networks, this approach may be impractical because many gas-emission processes vary on time scales much shorter than the response time of the control system. In such cases, a more reliable control criterion is compliance with the required airflow rates determined in accordance with approved procedures. Since these values are relatively stable over time, they can serve as a sound basis for the design of automated ventilation control systems.

Thus, all unsteady processes occurring in mine ventilation networks can be classified according to their characteristic times. This makes it possible to place them on a common time scale together with the characteristic response time of the ventilation control system, τ_y. The response time, however, should not be shorter than τ_2, the time required for a steady airflow distribution to become established after changes have been introduced into the network (Fig. 5).

Within this time scale, it is possible to identify the range of characteristic times over which unsteady processes can and should be regulated by the ventilation control system. Processes whose time scales fall outside this range are either not amenable to effective control or are not worth regulating from an economic or operational standpoint.

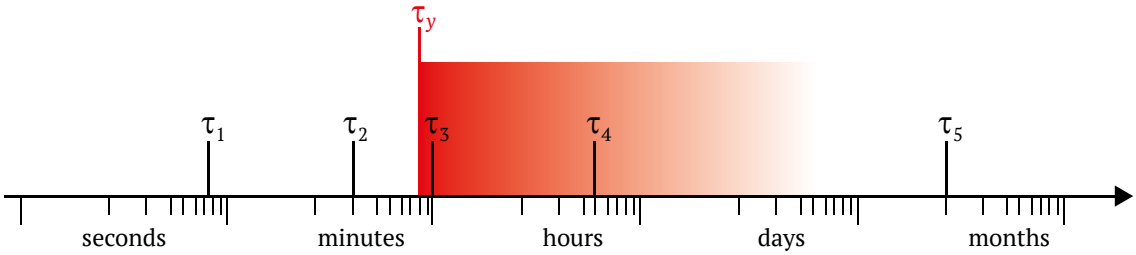

Fig. 5. Characteristic time scales of the main processes and control response time

Fig. 5 shows, in particular, that the primary objects of control are production processes associated with operations in working areas, as well as transitions between different shift states, namely production, maintenance, and shutdown. The latter, referred to as dynamic intershift control [22], most often serves as the basic implementation level of ventilation on demand in mines. It is based on fixed setpoints, that is, airflow rates specified at the dispatcher workstation and usually assumed to remain unchanged within each shift. This approach ensures a high level of reliability and operational stability, as repeatedly confirmed in practice [5, 23, 24].

At the same time, processes characterized by the time scales of production cycles within a shift, such as vehicle entry and exit, truck loading and unloading, and similar operations, may also be sufficiently long to permit regulation in some cases. This opens up a promising avenue for future research, namely the development of intrashift ventilation control methods. Their implementation would increase the flexibility of ventilation-on-demand systems, better align air supply with the actual pattern of production operations, and thereby create additional potential for energy savings.

Conclusion

The main scientific and practical findings of the study can be summarized as follows.

1. Three main factors were identified that increase the complexity of airflow distribution control as the ventilation network develops: insufficient spatial control depth combined with unsynchronized mining schedules in different districts; increasingly complex aerodynamic interactions between individual working areas and airflow control devices; and growing system inertia, which lengthens the response time to disturbances.

2. Methodological principles were proposed for designing ventilation control systems for mines with complex ventilation networks: when selecting the control level, it is necessary to take into account the number of air consumers served by a single automatic door and the extent to which their operating schedules overlap, while the temporal scale of ventilation control should be matched to the characteristic times of ventilation and mining processes.

3. A new mathematical framework was developed for analyzing aerodynamic interactions in networks with large numbers of fans, shafts, levels, and diagonal connections. The framework is based on aerodynamic influence matrices, their graphical analysis, clustering, and the decomposition of the network into mutually independent subsystems.

4. It was shown that the characteristic times of production cycles such as vehicle entry and exit, loading, and unloading may be sufficiently long to permit ventilation control at the level of these processes, thereby opening a promising direction for further research.

5. In complex ventilation networks, control algorithms should primarily be aimed at maintaining the required airflow rate, whereas control based on gas concentration is less suitable because of its rapid variability in response to gas emission from the rock mass.

References

1. de Souza E. Cost saving strategies in mine ventilation. *CIM Journal*. 2018;9(2).
2. de Vilhena Costa L., da Silva J. M. Cost-saving electrical energy consumption in underground ventilation by the use of ventilation on demand. *Mining Technology: Transactions of the Institutions of Mining and Metallurgy*. 2020;129(1):1–8. https://doi.org/10.1080/25726668.2019.1651581
3. Pinsker O.V., Mukhortikov S.G., Kvitkov V.V. et al. Evaluation of the efficiency of fan speed control of local ventilation of coal mines. *Mining Equipment and Electromechanics*. 2024;(4):27–36. (In Russ.) https://doi.org/10.26730/1816-4528-2024-4-27-36

4. Acuña E.I., Alvarez R.A., Hurtado J.P. Updated ventilation on demand review: implementation and savings achieved. In: *Proceedings of the 1st International Conference of Underground Mining*. October 19–21, 2016, Santiago, Chile.
5. Semin M.A., Grishin E.L., Levin L.Y., Zaitsev A.V. Automated ventilation control in mines. Challenges, state of the art, areas for improvement. *Journal of Mining Institute*. 2020;246:623–632. (In Russ.) https://doi.org/10.31897/PMI.2020.6.4
6. Bublik S.A., Zaitsev A.V., Maltsev S.V., Semin M.A. Analysis of the efficiency of dynamic ventilation control systems in potash mines. *Gornoe Ekho*. 2021;(3):81–89. (In Russ.) https://doi.org/10.7242/echo.2021.3.15
7. Kozyrev S.A., Osintseva A.V. Optimizing arrangement of air distribution controllers in mine ventilation system. *Journal of Mining Science*. 2012;48(5):903–910. https://doi.org/10.1134/S1062739148050153 (Orig. ver.: Kozyrev S.A., Osintseva A.V. Optimizing arrangement of air distribution controllers in mine ventilation system. *Fiziko-Texhnicheskiye Problemy Razrabbotki Poleznykh Iskopaemykh*. 2012;(5):135–143. (In Russ.)
8. Brady D. The role of gas monitoring in the prevention and treatment of mine fires. In: Aziz N. (Ed.) *Coal 2008: Coal Operators' Conference*. University of Wollongong & the Australasian Institute of Mining and Metallurgy; 2008. Pp. 202–208.
9. Levin L., Semin M., Maltsev S. et al. Numerical analysis of the impact of variable borer miner operating modes on the microclimate in potash mine working areas. *Computation*. 2025;13(4):85. https://doi.org/10.3390/computation13040085
10. Hoholov Y.A., Solovyev D.E. The temperature schedule of everfrost rock mass during drifting works. *Mining Informational and Analytical Bulletin*. 2009;(4):177–182. (In Russ.)
11. Puchkov L.A., Bakhvalov L.A. *Methods and algorithms for automatic ventilation control in coal mines*. Moscow: Nedra; 1992. 399 p. (In Russ.)
12. Mester I.I., Zasukhin I.N. *Automation of monitoring and control of mine ventilation*. Moscow: Nedra; 1974. 240 p. (In Russ.)
13. Tsoi S.V. *Automatic control of mine ventilation systems*. Alma-Ata: Nauka; 1975. (In Russ.)
14. Hu L.M., Jiang S.G., Dong S.B. Selection and application of ventilation system's sensitive branches based on the sensitivity. *Advanced Materials Research*. 2014;1010–1012:1471–1474. https://doi.org/10.4028/www.scientific.net/AMR.1010-1012.1471
15. Zhou L., Bahrami D. A derivative method to calculate resistance sensitivity for mine ventilation networks. *Mining, Metallurgy & Exploration*. 2022;39(4):1833–1839. https://doi.org/10.1007/s42461-022-00630-z
16. Zhou A., Wang K. A transient model for airflow stabilization induced by gas accumulations in a mine ventilation network. *Journal of Loss Prevention in the Process Industries*. 2017;47:152–160. https://doi.org/10.1016/j.jlp.2017.03.006
17. Kazakov B., Shalimov A., Grishin E. Modeling moving air nonstationary processes and diffusion heat and admixtures on tunnels ventilation jets with using program complex "Aeronetwork". *Izvestija Tulskogo Gosudarstvennogo Universiteta. Nauki o Zemle*. 2010;(2):64–69. (In Russ.)
18. Galkin A.F. Calculation of the Fourier criterion in predicting the thermal regime of thawed and frozen dispersed rocks. *Arctic and Antarctica*. 2022;(3):1–10. https://doi.org/10.7256/2453-8922.2022.3.38555
19. Puchkov L., Kaledina N. *Methane dynamics in mined-out areas of mines*. Moscow: Moscow State Mining University; 1995. 313 p. (In Russ.)
20. Jahir T., Mohamed M. *Using gas monitoring and personnel & vehicle tracking to maximize the benefits of ventilation-on-demand in underground mining operations*. Conspec Controls Limited; 2011. 7 p.
21. Kashnikov A.V., Kruglov Yu.V. Fuzzy logic-based determination of ventilation parameters in active mining areas. *Mining Informational and Analytical Bulletin*. 2023;(5):68–82. (In Russ.) https://doi.org/10.25018/0236_1493_2023_5_0_68
22. Grishin E.L., Nakaryakov E.V., Trushkova N.A., Sannikovich A.N. Experience in implementation of dynamic mine ventilation control. *Gornyi Zhurnal*. 2018;(8):103–108. (In Russ.) https://doi.org/10.17580/gzh.2018.08.15
23. Kumar M., Maity T., Kirar M.K. Energy savings by optimizing the speed of the primary ventilation fans in Indian underground coal mines based on VOD and TOU tariffs. *Energy Efficiency*. 2024;17(8):105. https://doi.org/10.1007/s12053-024-10282-1
24. Acuña E.I., Feliú A. Considering ventilation on demand for the developments of the New Level Mine Project, El Teniente. In: Hudyma M., Potvin Y. (Eds.) *Deep Mining 2014: Proceedings of the Seventh International Conference on Deep and High Stress Mining*. Perth: Australian Centre for Geomechanics; 2014. Pp. 813–821. https://doi.org/10.36487/ACG_rep/1410_59_Acuna

Information about the authors

Lev Yu. Levin – Dr. Sci. (Eng.), Corresponding Member of the Russian Academy of Sciences, Head of the Aerology and Thermophysics Department, Director, Mining Institute of the Ural Branch of the Russian Academy of Sciences, Perm, Russian Federation; ORCID 0000-0003-0767-9207, Scopus ID 56358515000, SPIN 6447-8130; e-mail aerolog_lev@mail.ru

Mikhail A. Semin – Dr. Sci. (Eng.), Scientific Secretary, Mining Institute of the Ural Branch of the Russian Academy of Sciences, Perm, Russian Federation; ORCID 0000-0001-5200-7931, Scopus ID 59727932700, ResearcherID S-8980-2016, SPIN 8353-4907; e-mail seminma@inbox.ru

Stanislav V. Maltsev – Cand. Sci. (Eng.), Head of the Mine Ventilation Sector, Aerology and Thermophysics Department, Mining Institute of the Ural Branch of the Russian Academy of Sciences, Perm, Russian Federation; ORCID 0009-0002-9887-1455, Scopus ID 57215839650, SPIN 6952-9875; e-mail st.v.maltsev@ya.ru

Artem V. Zaitsev – Dr. Sci. (Eng.), Deputy Director, Mining Institute of the Ural Branch of the Russian Academy of Sciences, Perm, Russian Federation; ORCID 0000-0002-2314-0482, Scopus ID 57213120380, SPIN 8246-2359; e-mail artem.v.zaitsev@yandex.ru

Received 28.08.2025
Revised 22.10.2025
Accepted 23.10.2025

MINING MACHINERY, TRANSPORT, AND MECHANICAL ENGINEERING

Research paper

https://doi.org/10.17073/2500-0632-2024-12-873
UDC 622.232.7

Stochastic mathematical model for rock cutting force generation

V.P. Kondrakhin ✉, **V.O. Gutarevich**
Donetsk National Technical University, Donetsk, Russian Federation
✉ *vkondrakhin52@mail.ru*

Abstract
A mathematical model describing the formation of dynamic load components acting on the working units of mining machines during rock cutting is an essential component of the digital twin of a mining shearer and is used for engineering analysis, design calculations, process simulation, and machine-parameter optimization. The application of various numerical methods to cutting-force modeling, including FEM and DEM, is constrained by the need to identify a large number of parameters, typically 10 to 20, many of which are difficult to determine either analytically or experimentally. A stochastic mathematical model of the rock cutting process has been developed by representing the process as a flow of random events, namely elementary loading events and fracture events associated with the failure of a certain volume of rock mass, that is, chip formation events. The interval between elementary loading events in time or space is treated as a random variable. The closest agreement with experimental data obtained from tests of a shearer cutting a full-scale coal-cement block was achieved with a model based on a truncated exponential distribution of the interval between successive fracture events. For each elementary loading event, the maximum cutting force at which chip formation occurs is determined analytically from the known expected value of the cutting force. For the cutting force acting on an individual pick, the modeling error does not exceed 7% for the expected value and standard deviation and 15% for the maximum value. Good agreement was also confirmed between the histograms of the force distribution and the spectral density plots obtained from full-scale and computational experimental data. The proposed model contains no more than three parameters requiring identification and can be used as a component of the digital twin of a mining shearer. The same approach is also applicable to mathematical modeling of the cutting of hard soils using the working tools of earthmoving machines and to modeling the operating processes of crushing machines.

Keywords
mathematical model, cutting force, rock, flow of events, chip formation, probability distribution, histogram, spectral density

For citation
Kondrakhin V.P., Gutarevich V.O. Stochastic mathematical model for rock cutting force generation. *Mining Science and Technology* (*Russia*). 2026;11(1):80–89. https://doi.org/10.17073/2500-0632-2024-12-873

ГОРНЫЕ МАШИНЫ, ТРАНСПОРТ И МАШИНОСТРОЕНИЕ

Научная статья

Стохастическая математическая модель формирования усилия резания горных пород

В.П. Кондрахин ✉, **В.О. Гутаревич**
Донецкий национальный технический университет, г. Донецк, Российская Федерация
✉ *vkondrakhin52@mail.ru*

Аннотация
Математическая модель формирования динамических составляющих нагрузок на рабочие органы горных машин при резании горных пород является необходимой составной частью цифрового двойника горного комбайна и используется для инженерного анализа, расчетов, симуляции рабочих процессов и оптимизации параметров машины. Применение для моделирования силы резания различных вариантов метода конечных элементов (FEM, DEM и др.) ограничено необходимостью идентифицировать большое количество параметров (примерно 10–20), определение которых расчетным или экспериментальным путем затруднено. Разработана стохастическая математическая модель процесса резания горной породы, основанная на представлении процесса в виде потока случайных событий – единич-

ных актов нагружения и разрушения некоторого объема горного массива (сколов). Интервал между единичными актами нагружения во времени или в пространстве рассматривается как случайная величина. Установлено, что наилучшую сходимость с данными экспериментальных исследований очистного комбайна на угле-цементном блоке обеспечивает модель с усеченным показательным законом распределения интервала между единичными актами разрушения. В единичном акте нагружения максимальное значение силы резания, при котором происходит скол, определяется расчетным путем исходя из известного среднего значения силы резания. Погрешность моделирования силы резания на отдельном резце не превышает: по математическому ожиданию и среднеквадратическому отклонению – 7 %, по максимальному значению – 15 %. Подтверждено хорошее соответствие гистограмм распределения и графиков спектральной плотности усилия, полученных при обработке данных натурного и вычислительного экспериментов. Предложенная модель содержит не более трех параметров, требующих идентификации, и может быть использована как составная часть цифрового двойника горного комбайна. Данный подход целесообразно применять при математическом моделировании процесса резания прочных грунтов рабочими органами землеройных машин, а также для моделирования рабочего процесса дробильных машин.

Ключевые слова
математическая модель, сила резания, горная порода, поток событий, скол, закон распределения, гистограмма, спектральная плотность

Для цитирования
Kondrakhin V.P., Gutarevich V.O. Stochastic mathematical model for rock cutting force generation. *Mining Science and Technology* (*Russia*). 2026;11(1):80–89. https://doi.org/10.17073/2500-0632-2024-12-873

Introduction

For simulation-based modeling and optimization to be used more widely in mining-machine research and design, a sufficiently general yet relatively simple mathematical model is needed to describe the dynamic load components acting on working units during the cutting of a wide range of rocks. Such a model is an essential part of the integrated mathematical model, or digital twin, of a mining shearer and can be used for engineering analysis, design calculations, process simulation, and machine-parameter optimization [1].

Mean load levels acting on cutting tools and the energy demands of operating processes in mining shearers and drilling machines have already been studied in detail [2–4].

Considerable research attention has been devoted to mathematical modeling of rock cutting with allowance for dynamic load components. The cutting process is cyclic in nature: rock is separated from the rock mass in discrete portions, or chips, and this separation is accompanied by fracture of the newly formed core and disintegration of the detached volume [4, 5]. Studies [6, 7] analyzing cutting-force oscillograms showed that, over the duration of a single chip formation event, the cutting force varies linearly and can therefore be represented as a triangular pulse. This conclusion is supported by numerous experimental studies of rock cutting reported by different authors [8–10].

Reference [11] describes a model in which the pressure distribution in the contact zone between the pick and the rock is governed by elastic deformation beneath the pick and by irreversible deformation associated with rock crushing in this region due to the formation of a pre-fractured surface zone. Under this model, the occurrence of rock chipping at discrete moments in time is one of the causes of the oscillatory variation of the cutting-force components.

Numerous studies have modeled the rock cutting process using different numerical methods [12–14]. These include the finite element method (FEM) [15], the boundary element method (BEM) [14], the discrete element method (DEM) [16–18], and combined approaches such as FDEM [14]. These methods make it possible to simulate rock cutting processes with varying degrees of accuracy. At the same time, their application to mining-machine calculations remains problematic. Methods of this type involve a large number of parameters, typically about 10 to 20, many of which are difficult to determine either analytically or experimentally. Some can only be estimated through parameter identification, that is, model calibration. This is a labor-intensive procedure that requires a substantial amount of experimental data. In addition, implementation of such models usually relies on expensive commercial software packages such as ANSYS, LS-DYNA, and ABAQUS, most of which are developed by foreign vendors.

The rock cutting process is inherently random because the structure and mechanical properties of rock vary randomly along the cutting path [4–6]. A mathematical model of rock cutting must therefore be stochastic. Determining the parameters of such models requires extensive experimental data, which makes it essential to minimize the number of parameters that must be measured or identified. A reasonable compromise is therefore needed between the

number of factors included in the model, the feasibility of estimating their parameters reliably, and the accuracy required to reproduce the random dynamic load components.

As is well established [3, 4], the load acting on a cutting tool during coal and rock cutting is resolved into three components: cutting force, feed force, and side force. For modeling dynamic processes in mining shearer power systems, the dynamic components of the cutting force are of primary importance. These components generate dynamic loads in the machine drive, and their spectra contain significant frequency components up to 40–50 Hz [4, 19, 20]. For most practical purposes, therefore, there is no need to reproduce the spectral composition of the cutting force acting on the cutting tool with high accuracy above 40–50 Hz.

It is also important to note that, in the formation of random dynamic loads in mining shearer power systems, the exact form of the cutting-force distribution for an individual pick is of little practical importance. According to the central limit theorem, the distribution of the load generated by several picks, reaching several dozen in modern shearers, approaches a normal distribution regardless of the distribution law governing the load acting on each individual pick.

These considerations provide a basis for developing sufficiently simple algorithmic models capable of reproducing, with the required accuracy, the random loads arising during coal and rock cutting.

The objective of this study is to improve the design quality and operating efficiency of mining shearers by developing an easy-to-use stochastic mathematical model of rock cutting as a component of the integrated mathematical model, or digital twin, of a mining shearer for engineering analysis, design calculations, process simulation, and machine-parameter optimization.

To achieve this objective, the following tasks were undertaken:

– a stochastic mathematical model of the cutting process was developed in the form of a flow of random events, namely elementary loading events and the corresponding chip formation events associated with rock fracture, requiring identification of only two or three parameters instead of the 10–20 parameters typically required by models based on different variants of the finite element method;

– experimental studies of the cutting process were carried out using a shearer cutting a full-scale coal-cement block, and realizations of cutting force for a radial pick were obtained under different operating conditions;

– statistical processing of the experimental data was performed, the model parameters were identified, and the adequacy of the model with respect to the real process was established.

Theory. Mathematical model

In this paper, rock cutting by a mining-machine tool is modeled as a flow of random events, namely elementary loading events involving individual volumes of rock mass. Each event ends with an element separating from the rock mass and subsequently disintegrating. The interval between successive elementary loading events in time or space is treated as a random variable.

The forces Z_i, generated by the interaction between the cutting tool and the rock during the i-th elementary loading event are represented, in the general case, by triangular pulses with random parameters:

$$\begin{cases} Z_i = C_{ps,i} \cdot \Delta x_i(t) & \text{for } \Delta x_i(t) \le \dfrac{P_{chip,i}}{C_{ps,i}}, \\ Z_i = 0 & \text{for } \Delta x_i(t) > \dfrac{P_{chip,i}}{C_{ps,i}}, \end{cases} \quad (1)$$

where $\Delta x_i(t)$ is the elastoplastic deformation of the rock volume involved in the given elementary loading event; $C_{ps,i}$ is the linearized pseudo-stiffness[1] coefficient of the rock, characterizing the resistance of the material being fractured to penetration by the cutting tool; and $P_{chip,i}$ is the force at which brittle fracture occurs and the rock volume under consideration separates from the rock mass.

The idealized graphical form of relationship (1) is shown in Fig. 1.

In the general case, the parameters $C_{ps,i}$ and $P_{chip,i}$ depend on the properties of the rock being cut, the geometry of the cutting tool, and the cutting conditions. The parameters should, in principle, be treated as random variables that vary from one elementary loading event to the next. The statistical characteristics of $C_{ps,i}$ are established either during parametric identification of the proposed mathematical models or through dedicated cutting experiments. The parameter $P_{chip,i}$, however, is handled differently because reliable and widely accepted procedures are available for calculating the mean load acting on a pick. Accordingly, in each elementary loading event, $P_{chip,i}$ is selected so that the simulation reproduces the prescribed mean load level.

[1] The prefix *pseudo-* is used to emphasize the elastoplastic nature of the resulting deformations.

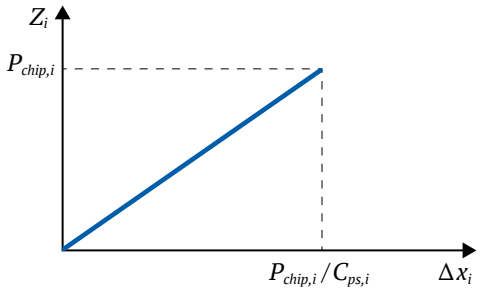

Fig. 1. Idealized dependence of force Z_i on deformation Δx_i in an elementary loading event

When modeling cutting forces, the appropriate independent variable is the distance traveled by the pick between the onset of two successive fracture events. The intensity of the random event flow, λ, is defined as the average number of chips formed per meter of cutting path. The literature reports λ values for coal and certain rock types [4]. As an approximation, λ can be estimated from cutting-force oscillograms by counting the average number of peaks per unit pick travel.

For modeling cutting forces in coal, the following relationship is proposed. It was obtained by generalizing our experimental results for cutting a coal-cement block with ZR4-80 picks mounted on the RKU-13 shearer and the data reported in [4]:

$$\lambda = \frac{584000}{2920 + Z_{mean}},\ \text{m}^{-1}, \qquad (2)$$

where Z_{mean} is the mean cutting force, N.

To reduce the number of model parameters requiring identification, event flows were considered in which the time intervals, or equivalently the path intervals Δl, follow one-parameter distributions. For a Poisson event flow, the interval between events is a random variable with an exponential distribution described by the density function

$$f(\Delta l) = \lambda \exp(-\lambda \Delta l). \qquad (3)$$

Another one-parameter distribution considered here is the Rayleigh distribution, written as

$$f(\Delta l) = \frac{\Delta l}{\sigma_0^2} \exp\left(-\frac{\Delta l^2}{2\sigma_0^2}\right), \qquad (4)$$

where σ_0 is the distribution parameter determined from the expression $\sigma_0 = 0.798/\lambda$.

To assess whether these distributions are suitable for the problem under study, cutting-force oscillograms obtained in experimental tests of the RKU-13 shearer on a test rig with a coal-cement block were analyzed [20, 21]. Fig. 2 shows, as an example, the histogram of the interval distribution between successive chip formation events during cutting of the coal-cement block with a ZR4-80 pick mounted on the RKU-13 shearer.

Statistical analysis of the experimental data shows that the distribution of intervals between elementary events is fairly complex and is not well described by standard theoretical distributions. To adapt the exponential distribution to real cutting conditions, the possible range of the random variable Δl must be bounded from below and above in such a way that its mean value, equal to $1/\lambda$, remains unchanged. The lower bound of the interval range, l_{lower}, is determined from $l_{lower} = 1/(\lambda K_{lower})$, where K_{lower} is the ratio of the mean interval to the minimum distance between successive events. This parameter can be estimated from the oscillogram as the minimum spacing between cutting-force peaks, assuming the cutting speed is approximately constant. For cutting a coal-cement block, $K_{lower} = 2.0$.

The upper bound, lupper, is determined by requiring the expected value of the truncated distribution to be equal to $1/\lambda$. The probability density function of a random variable bounded both below and above is given by

$$f_a(l) = \frac{f(l)}{\int_{l_{lower}}^{l_{upper}} f(l)\, dl} = \frac{\lambda \exp(-\lambda l)}{\exp(-\lambda l_{lower}) - \exp(-\lambda l_{upper})}. \qquad (5)$$

Setting the expected value of this random variable equal to $1/\lambda$ yields the following transcendental equation for determining the upper bound, l_{upper}:

$$l_{lower} \exp(-\lambda l_{lower}) = l_{upper} \exp(-\lambda l_{upper}). \qquad (6)$$

The trivial solution $l_{upper} = l_{lower}$ is disregarded, and the equation is solved numerically. For example, $\lambda = 68\ \text{m}^{-1}$ and $K_{lower} = 2.0$ yield $l_{lower} = 7.4$ mm and $l_{upper} = 25.9$ mm. As shown in Fig. 2, these boundary values cover virtually the entire range of variation of the random variable Δl.

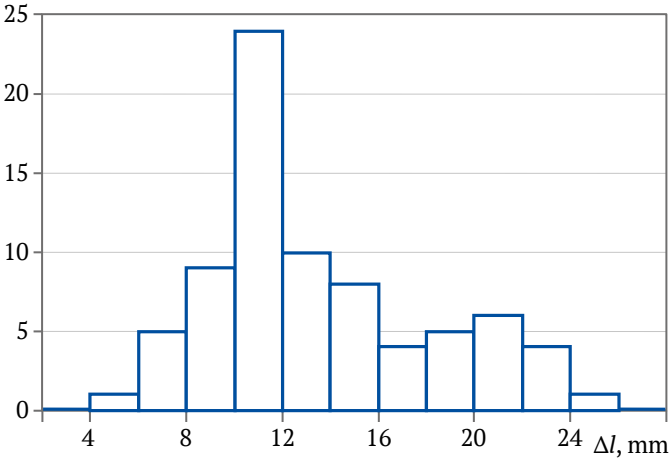

Fig. 2. Histogram of intervals between successive chip formation events based on full-scale experimental data ($n = 77$)

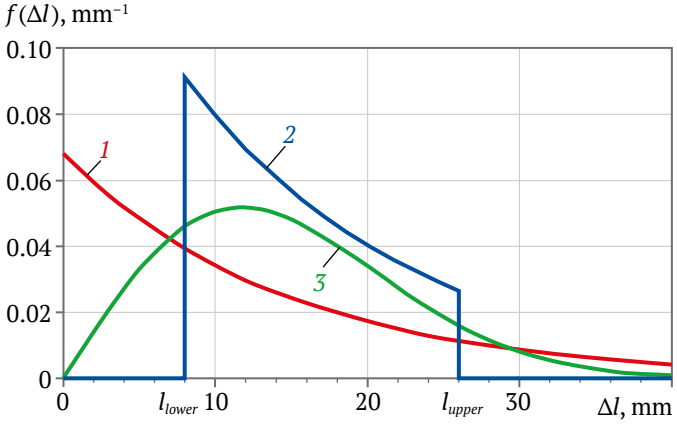

Fig. 3. Probability density functions of the intervals between successive chip formation events: *1* – exponential; *2* – truncated exponential; *3* – Rayleigh

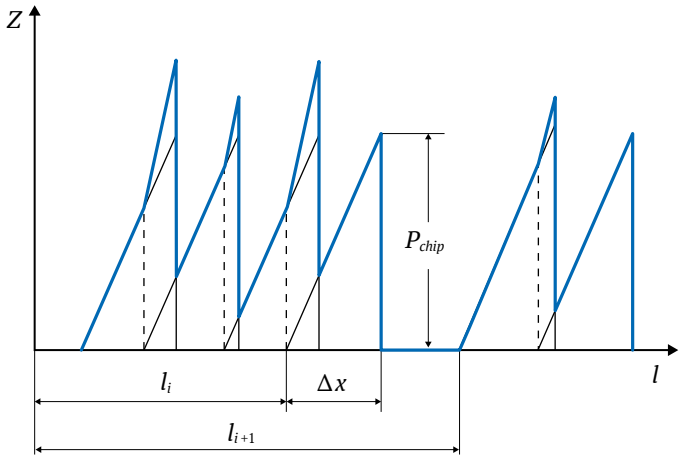

Fig. 4. Summation of the forces generated in the individual elementary fracture events

Fig. 3 presents the probability density functions of the random variable Δl for the three cases considered above.

For the **first case**, the interval between successive chip formation events in the numerical simulation is generated as the random variable[2] [22]

$$\Delta l_i = -\lambda^{-1}\ln(1-\nu), \tag{7}$$

where ν is a random variable uniformly distributed over the interval [0, 1].

In the **second case**, only values Δl_i obtained from Eq. (7) that satisfy the inequality

$$l_{lower} < \Delta l_i < l_{upper}, \tag{8}$$

are retained.

In the **third case**, the interval between successive chip formation events follows a Rayleigh distribution. In the numerical simulation, this interval is determined from the following expression [21]

$$\Delta l_i = \sigma_0\sqrt{\xi_1^2+\xi_2^2}, \tag{9}$$

where ξ_1 and ξ_2 are realizations of independent normally distributed random variables with zero mean and unit variance.

For all cases, the pick position at the onset of the *i*-th elementary event is determined from

$$l_i = l_{i-1} + \Delta l_i. \tag{10}$$

The elastoplastic deformation of the rock volume involved in a given elementary loading event is then

$$\Delta x_i(t) = l(t) - l_i,$$

where $l(t)$ is the distance traveled by the pick by time t, that is, the pick coordinate.

The maximum deformation of the elementary rock volume at the moment of brittle fracture is $\Delta X = P_{chip,i}/C_{ps,i}$. To simplify the model, $C_{ps,i}$ and $P_{chip,i}$ are assumed to be deterministic. For a prescribed mean cutting force, these quantities are taken to be the same for all elementary loading events and are denoted by C_{ps} and P_{chip}.

The mean cutting force, which can be determined by established methods [2–4], is used as the reference quantity for determining the required model parameters.

At any instant, the cutting force acting on the pick is defined as the sum of the forces generated in the individual elementary fracture events

$$Z(t) = \sum_{i=N_1}^{N_2} Z_i, \tag{11}$$

where N_1 and N_2 are the sequence numbers of the first and last elementary fracture events that have started but have not yet ended. The summation procedure for the forces generated in the individual elementary fracture events is illustrated in Fig. 4.

For the proposed cutting-force model, the expected value of a realization of the random process over an arbitrary length L is determined as the ratio of the area enclosed by the polygonal line shown in Fig. 4 to the length L. This area is equal to the sum of the areas of the elementary triangles, whose number N is equal to the number of elementary loading events that occur over the trajectory segment under consideration. The area of each triangle is $S_{tri} = 0.5P_{chip}^2/C_{ps}$. Accordingly, the expected value of the cutting force is

$$Z_{cut} = \frac{S_{tri}N}{L} = \frac{0.5P_{chip}^2 N}{C_{ps}L}.$$

[2] Bakalov V.P. Digital Simulation of Random Processes: A Textbook. Moscow: MAI Publishing House; 2001. 84 p.

Since $\lambda = N/L$, the final expression for determining the parameters of an elementary fracture event from the known mean value, that is, the expected value, of the cutting force can be written as

$$P_{chip} = \sqrt{\frac{2Z_{cut}C_{ps}}{\lambda}}. \quad (12)$$

The generalized flowchart of the algorithm used to simulate rock cutting force is shown in Fig. 5.

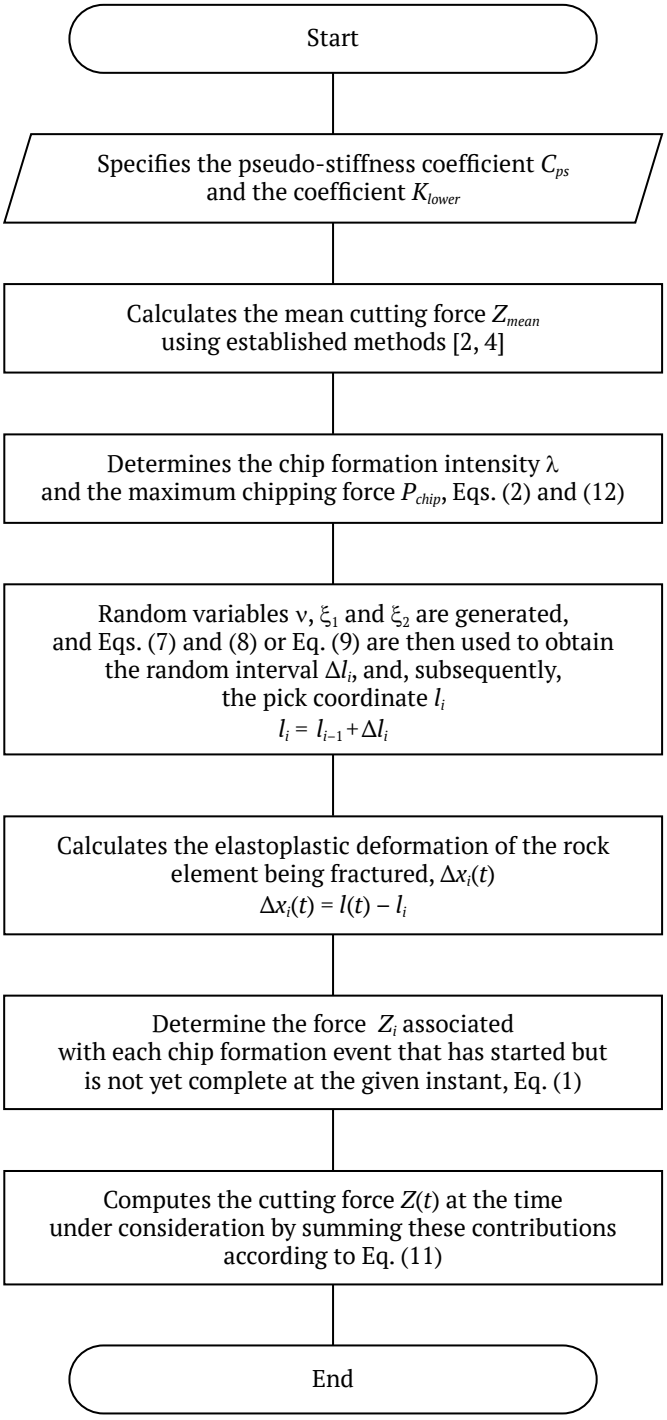

Fig. 5. Generalized flowchart of the rock cutting force simulation algorithm

Results

The proposed simulation model includes two main input parameters, λ and C_{ps}, which can be determined either through dedicated experiments or through parametric identification of the mathematical models developed for specific mining machines. In addition, the second variant of the model, which uses a truncated exponential distribution for the intervals between successive chip formation events, includes one additional parameter, K_{lower}.

Experimental studies of the cutting process were carried out on an RKU-13 shearer equipped with strain-gauge instrumented holders for measuring the three components of the interaction force between a radial pick and the rock [20]. Measurements were taken during cutting of a full-scale coal-cement block with a mean cutting resistance of 210 N/mm at different machine travel speeds.

To reproduce the experimental conditions as closely as possible in the simulation, the mean cutting force was set equal to its experimental value. During a single cut, this mean cutting force varied from zero to a maximum and then back to zero according to a sinusoidal law. With a total duration of 0.75 s for one cut, segments of the realizations from the time interval 0.175–0.575 s were analyzed. Oscillograms from five successive cuts, both in the full-scale and in the computational experiment, were joined together to form a composite realization 2 s in duration. For spectral analysis, the composite realizations were assembled from the original records after trend removal. The resulting composite realizations possess the property of stationarity and are sufficiently long in time to make the ergodicity assumption more justified. These realizations were subjected to statistical analysis, which yielded estimates of the expected value, standard deviation, distribution histograms, and spectral density of the random process.

The cutting force was simulated using the algorithm described above for three variants of the proposed model, corresponding to different distributions of the random variable representing the intervals between successive chip formation events: exponential in variant 1, truncated exponential in variant 2, and Rayleigh in variant 3. The closest agreement with the full-scale experimental data was obtained for variant 2. Fig. 6 shows fragments of oscillograms from the full-scale and computational experiments for this variant.

The table presents the statistical results for variants 2 and 3 obtained from the full-scale and computational experiments under two operating conditions with substantially different mean cutting forces.

Fig. 7 compares cutting-force histograms obtained in the full-scale and computational experiments for variant 2 of the model.

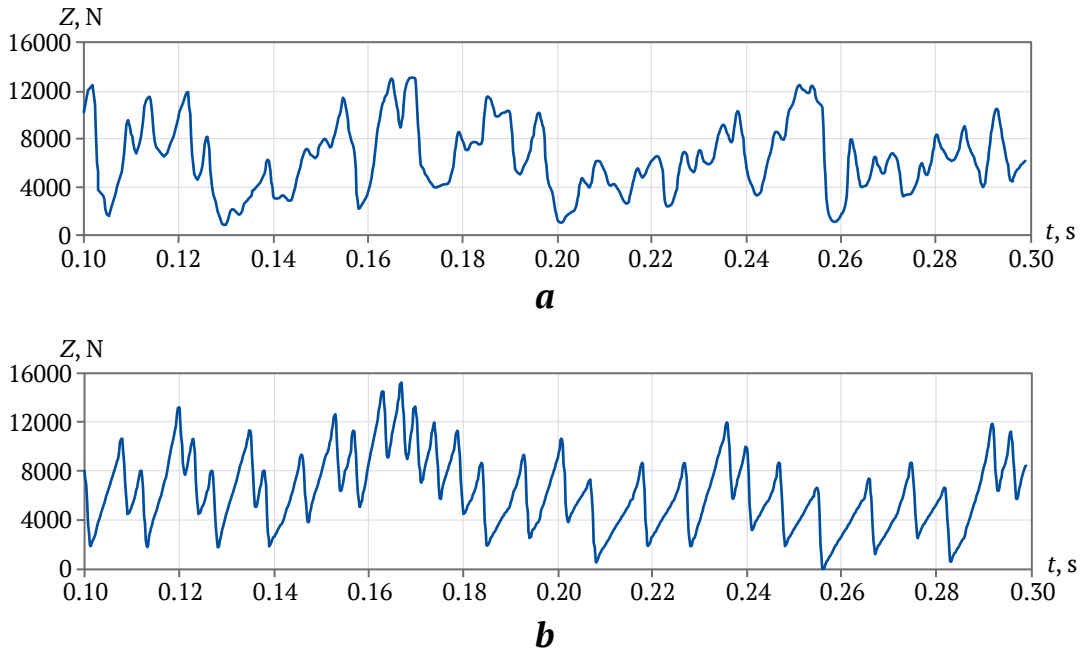

Fig. 6. Fragments of oscillograms from the full-scale experiment (*a*) and the computational experiment (*b*)

Table

Cutting force, kN, in computational and full-scale experiments

Experiment		Model		
		Expected value	Standard deviation	Maximum value
Experiment 1		5.67	2.99	15.5
Variant 2 of the model	Value	5.94	2.79	15.7
	Error, %	4.80	−6.70	1.3
Variant 3 of the model	Value	6.02	3.31	17.7
	Error, %	6.20	10.70	14.1
Experiment 2		3.25	1.76	9.17
Variant 2 of the model	Value	3.35	1.88	10.5
	Error, %	3.10	6.80	14.5
Variant 3 of the model	Value	3.42	2.08	11.8
	Error, %	5.20	18.00	28.6

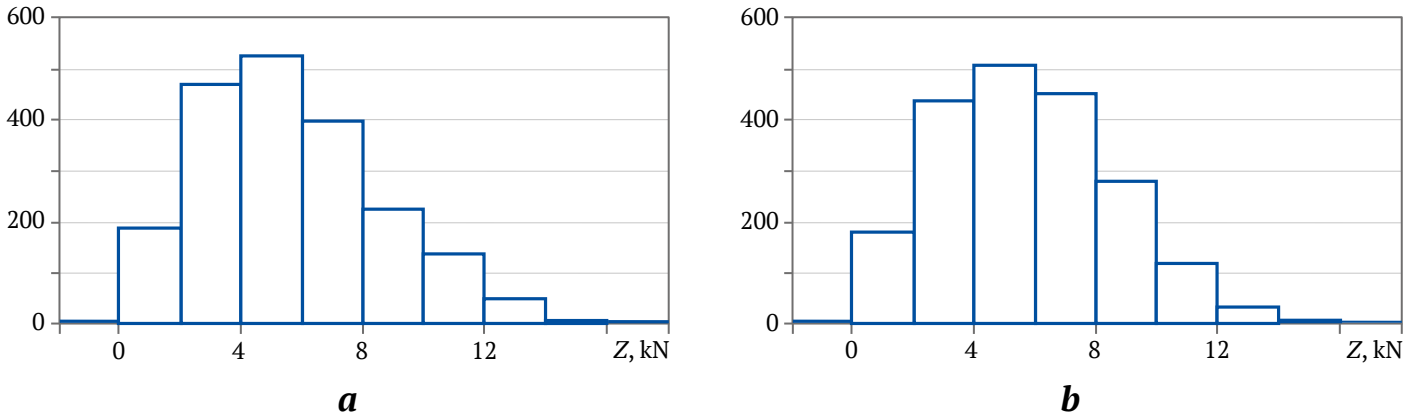

Fig. 7. Histograms of the cutting-force in the full-scale experiment (*a*) and the computational experiment (*b*) at a mean load level of 5.67 kN

Fig. 8 shows plots of the estimated normalized spectral densities of composite cutting-force realizations obtained in the full-scale and computational experiments.

As shown in Fig. 8, the variance of the random cutting-force process is distributed similarly over the 0–100 Hz frequency range in the full-scale and computational experiments.

Discussion and conclusions

Analysis of the table shows that the smallest errors are obtained for variant 2 of the model, not exceeding 7% for the expected value and standard deviation and 15% for the maximum value. Variant 3 of the model also provides acceptable accuracy, with the corresponding errors reaching 18% and 29%, respectively.

Variant 2 of the developed model shows good agreement between the simulated and experimental cutting-force histograms, as illustrated in Fig. 7. As shown in Fig. 8, the spectral composition of the cutting force obtained in the computational experiment is also in close agreement with the experimental data.

The model validation shows that the developed stochastic model of cutting-force formation, specifically variant 2, agrees well with the experimental data in terms of the statistical characteristics, the distribution histogram, and the spectral composition at two representative mean load levels. Variant 3 yields somewhat larger errors, but it has an important advantage in that it requires only two parameters, λ and C_{ps}.

The modeling error of the developed mathematical model does not exceed the corresponding errors reported for different finite-element-based approaches and expensive commercial software packages, most of which have been developed abroad. For example, according to [16], the error of 3D DEM simulation for the standard deviation of sandstone cutting force exceeds 22%.

Given the simplicity of the proposed mathematical model and its acceptable level of agreement with real processes, the validated approach appears suitable for developing a stochastic mathematical model of cutting in hard soils by the working units of earthmoving machines, as well as for modeling the operating process of crushing machines [22].

Thus, three variants of a stochastic mathematical model of rock cutting have been developed. They involve only a small number of parameters, namely two or three, do not require expensive commercial software, and provide an adequate representation of the real process.

Of the three variants, the simulation model represented by variant 2 best satisfies the adequacy requirements. In this variant, the intervals between elementary loading events follow a truncated exponential distribution. The error in modeling the cutting force acting on an individual pick does not exceed 7% for the expected value and standard deviation and 15% for the maximum value. Good agreement is also observed between the distribution histograms and the spectral density plots obtained from the processing of full-scale and computational experimental data.

The proposed mathematical model of rock cutting can be used as a component of the integrated mathematical model, or digital twin, of a mining shearer for engineering analysis, design calculations, process simulation, and structural and parametric optimization at the design stage. The proposed representation of rock fracture as a flow of random events, namely elementary fracture events, also appears suitable for mathematical modeling of cutting in hard soils by the working units of earthmoving machines and for modeling the operating process of crushing machines.

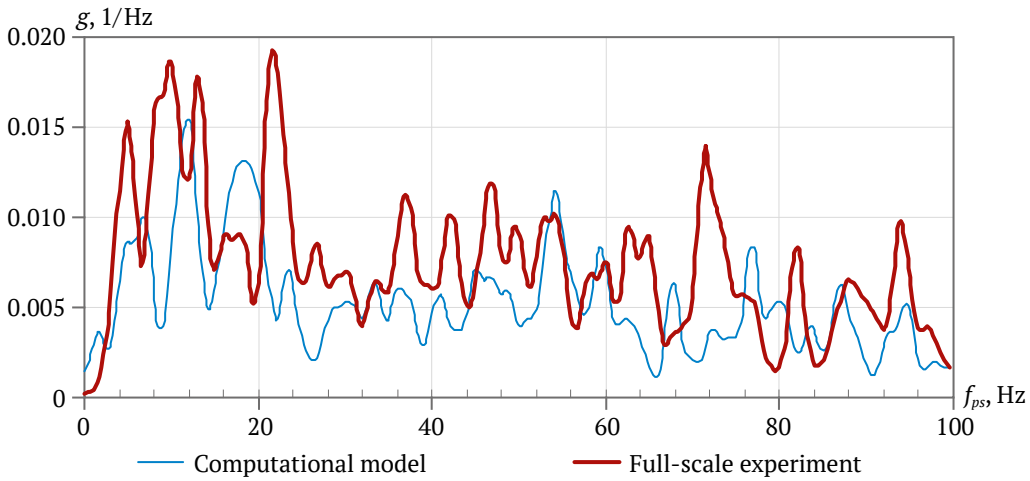

Fig. 8. Estimated normalized spectral densities of composite cutting-force realizations for the computational model and the full-scale experiment

References

1. Artemov I.V., Nosyrev M.B. The digital twin technology and its application for mining industry. *Mine Surveying and Subsurface Use*. 2024;(5):38–43. (In Russ.) https://doi.org/10.56195/20793332_2024_5_38_43
2. Linnik Yu.N., Linnik V.Yu. *Destruction of coal seams during mining by shearer machines*. Moscow: INFRA-M Publ., 2022. 356 p. (In Russ.)
3. Gorbatov P.A., Petrushkin G.V., Lysenko N.M. et al. *Mining machines for underground coal mining*. Donetsk: Nord Kompyuter Publ.; 2006. 669 p. (In Russ.)
4. Pozin E.Z., Melamed V.Z., Ton V.V. *Destruction of coals by shearer machines*. Moscow: Nedra Publ.; 1984. 288 p. (In Russ.)
5. Pozin E.Z., Khurgin Z.Ya., Burdin V.E. et al. *Modeling of the coal fracture process by cutting tools*. Moscow: Nauka Publ.; 1981. 181 p. (In Russ.)
6. Vasilyev L.M. Investigation of the spalling process of a single chip element in rock cutting. *Fiziko-Tekhnicheskie Problemy Razrabotki Poleznykh Iskopaemykh.* 1976;(6):41–46. (In Russ.)
7. Gabov V.V., Zadkov D.A., Nguyen K.L. Features of elementary burst formation during cutting coals and isotropic materials with reference cutting tool of mining machines. *Journal of Mining Institute*. 2019;236:153–161. https://doi.org/10.31897/PMI.2019.2.153
8. Gabov V.V., Chekmasov N.V., Burak A.Ya., Shishlyannikov D.I. Studies of formation process elementary spalls off at destruction of potash salts cross cuts. *Mining Equipment and Electromechanics*. 2011;(8):42–43. (In Russ.)
9. Zhabin A.B., Polyakov A.V., Averin E.A. et al. Ways of development for the theory of rock and coal destruction by picks. *Ugol'*. 2019;(9):24–28. (In Russ.) https://doi.org/10.18796/0041-5790-2019-9-24-28
10. Kondrakhin V.P., Khitsenko A.I. Identification of rock cutting force. *Naukovi Pratsi Donetskoho Derzhavnoho Tekhnichnoho Universytetu. Seriya: Hirnycho-Enerhomekhanichna*. 2002;(51):124–129. (In Russ.) URL: http://ea.donntu.ru/handle/123456789/19113
11. Krasnyk V. Designing cutting tools of mining machines for coal auger mining. *Mining of Mineral Deposits*. 2016;10(3):13–19. (In Russ.) https://doi.org/10.15407/mining10.03.013
12. Joodi B., Sarmadivaleh M., Rasouli V., Nabipour A. Simulation of the cutting action of a single PDC cutter using DEM. *Petroleum and Mineral Resources*. 2012;81:143–150. https://doi.org/10.2495/pmr120131
13. Zhang Q.-Q, Han Zh.-N., Ning Sh.-H. Numerical simulation of rock cutting in different cutting mode using the discrete element method. *Journal of GeoEngineering*. 2015;10(2):35–43. https://doi.org/10.6310/jog.2015.10(2).1
14. Su O., Akcin N.A., te Kamp L. Modeling of cutting forces acting on a conical pick. In: *2nd International Conference on Computational Methods in Tunnelling (EURO:TUN 2009)*. Bochum, Germany: Aedificatio Publishers; 2009.
15. Carrapatoso C.M., Lautenschläger C.E.R., Righetto G.L. et al. Rock cutting analysis employing finite and discrete element methods. *Journal of Mechanics Engineering and Automation*. 2016;6(2):100–108. https://doi.org/10.17265/2159-5275/2016.02.006
16. Rojek J., Onate E., Labra C., Kargl H. Discrete element simulation of rock cutting. *International Journal of Rock Mechanics & Mining Sciences*. 2011;48:996–1010.
17. Kalogeropoulos A, Michalakopoulos T. Numerical simulation of the rock cutting process using the discrete element method. In: Anagnostou G., Benardos A., Marinos V.P. (Eds.) *Expanding Underground – Knowledge and Passion to Make a Positive Impact on the World*. London: CRC Press; 2023. https://doi.org/10.1201/9781003348030-76
18. Moon T., Oh J. A study of optimal rock-cutting conditions for hard rock TBM using the discrete element method. *Rock Mechanics and Rock Engineering*. 2012;45:837–849. https://doi.org/10.1007/s00603-011-0180-3
19. Boyko N.G., Ignatov V.I. Computer simulation of forces acting on a cutter during rock mass destruction. *Izvestiya Vuzov. Gornyi Zhurnal*. 1983;(7):77–79. (In Russ.)
20. Gorbatov P.A., Kondrakhin V.P., Krivchenko Yu.A., Motin N.N. *Measurement of cutting force components on cutters of mining shearers. Mechanization of mining operations*. Kemerovo: KuzPI Publ.; 1988. Pp. 23–28. (In Russ.)

21. Gorbatov P.A., Kondrakhin V.P. Methodology for experimental determination of external load on the working units of a shearer. *Izvestiya Vuzov. Gornyi Zhurnal*. 1989;(9):88–91. (In Russ.)

22. Kondrakhin V., Martyushev N., Klyuev R. et al. Mathematical modeling and multi-criteria optimization of design parameters for the gyratory crusher. *Mathematics*. 2023;11(10):2345. https://doi.org/10.3390/math11102345

Information about the authors

Vitaly P. Kondrakhin – Dr. Sci. (Eng.), Professor at the Department of Transport Systems and Logistics named after I.G. Shtokman, Donetsk National Technical University, Donetsk, Russian Federation; ORCID 0000-0001-5655-2160, Scopus ID 6506839592, SPIN 9628-3575; e-mail vkondrakhin52@mail.ru

Viktor O. Gutarevich – Dr. Sci. (Eng.), Head of the Department of Transport Systems and Logistics named after I.G. Shtokman, Donetsk National Technical University, Donetsk, Russian Federation; ORCID 0000-0002-6294-5232, Scopus ID 55633624800, ResearcherID A-2783-2016, SPIN 6436-6484; e-mail viktor.gutarevich@mail.ru

Received 18.12.2024
Revised 24.10.2025
Accepted 18.12.2025

MINING ROCK PROPERTIES. ROCK MECHANICS AND GEOPHYSICS

Research paper

https://doi.org/10.17073/2500-0632-2025-07-1104
UDC 622.281 (574.32)

Formation of inelastic deformation zones based on numerical modeling

V.F. Demin[1], **N.G. Valiev**[2], **D.R. Akhmatnurov**[1] ✉, **R.A. Mussin**[1], **N.M. Zamaliyev**[1]
[1] *Abylkas Saginov Karaganda Technical University, Karaganda, Republic of Kazakhstan*
[2] *Ural State Mining University, Yekaterinburg, Russian Federation*
✉ *d.akhmatnurov@gmail.com*

Abstract
Comprehensive consideration of the geomechanical and structural characteristics of the rock mass is a prerequisite for ensuring the safety and efficiency of underground mining operations. The key parameters that must be incorporated into computational models include the physical, mechanical and strength properties of rocks, their degree of fracturing, as well as the initial and mining-induced stress state of the rock mass. This study investigates geomechanical criteria for determining support parameters of development workings under conditions of plastic deformation. The methodological framework is based on a combination of theoretical analysis, finite element numerical modeling using the RS2 software package (Rocscience), and generalization of experimental data on the properties of host rocks. This approach enabled a detailed analysis of the stress-strain state of the rock mass at various stages of mining operations, including the roadway junction where a new roadway is driven from an existing excavation and its subsequent development. The modeling results established the spatial boundaries of deformation zones: the depth of developed inelastic deformation reaches 0.6–0.7 m from the excavation boundary, while the elastoplastic deformation zone extends to 1.8–1.9 m. Stress analysis showed that in the abutment pressure zone ahead of the excavation face, stresses reach values of 20.48 MPa, which is about 25% higher than the in-situ stress level at a depth of 600 m. Analysis of the Factor of Safety (FoS) revealed local zones with FoS < 1 in the junction zone, indicating the need for reinforcement of the support system. The results provide a scientifically substantiated basis for predicting the geomechanical state of the rock mass and for selecting rational support parameters, thereby improving excavation stability, reducing maintenance requirements, and enhancing industrial safety in underground coal mining.

Keywords
mining, underground mining, development workings, rock support, parameters, geomechanics, geomechanical processes, rock bolting, modeling, analytical modeling, stress-strain state, rock pressure, rock mass, methodology, relationships, finite element method

Funding
This study was supported by the Science Committee of the Ministry of Science and Higher Education of the Republic of Kazakhstan under the targeted funding program for the implementation of a scientific and scientific-technical program, IRN BR24992803.

For citation
Demin V.F., Valiev N.G., Akhmatnurov D.R., Mussin R.A., Zamaliyev N.M. Formation of inelastic deformation zones based on numerical modeling. *Mining Science and Technology* (*Russia*). 2026;10(1):90–102. https://doi.org/10.17073/2500-0632-2025-07-1104

ЦИФРОВЫЕ ТЕХНОЛОГИИ И ИСКУССТВЕННЫЙ ИНТЕЛЛЕКТ

Научная статья

Формирование зон неупругих деформаций на примере цифрового математического моделирования

В.Ф. Демин[1], **Н.Г. Валиев**[2], **Д.Р. Ахматнуров**[1] ✉, **Р.А. Мусин**[1], **Н.М. Замалиев**[1]
[1] *Карагандинский технический университет имени Абылкаса Сагинова, г. Караганда, Республика Казахстан*
[2] *Уральский государственный горный университет, г. Екатеринбург, Российская Федерация*
✉ *d.akhmatnurov@gmail.com*

Аннотация
Комплексный учет геомеханических и структурных характеристик горного массива является обязательной основой для обеспечения безопасности и эффективности подземных горных работ. Критически важными параметрами, подлежащими включению в расчетные модели, выступают физико-механиче-

ские и прочностные свойства пород, степень их трещиноватости, а также исходное и техногенно-измененное напряжённое состояние массива. Исследование направлено на геомеханическое обоснование параметров крепления подготовительных выработок в условиях развития пластических деформаций. Методическая база основана на сочетании теоретического анализа, численного моделирования методом конечных элементов в программном комплексе RS2 (Rocscience) и обобщения экспериментальных данных о свойствах вмещающих пород, что позволило детально проанализировать напряжённо-деформированное состояние массива на различных стадиях проведения горных работ, включая засечку новой выработки и её последующее развитие. В результате моделирования установлены пространственные границы зон деформирования: глубина развитых неупругих деформаций составляет 0,6–0,7 м от контура выработки, область упругопластического деформирования достигает 1,8–1,9 м. Анализ напряжённого состояния показал, что в зоне опорного давления перед забоем напряжения достигают 20,48 МПа, что на 25 % превышает природный уровень на глубине 600 м. С применением коэффициента запаса прочности FoS выявлены локальные участки с FoS < 1 в районе засечки, количественно подтверждающие необходимость усиления крепи. Полученные результаты позволяют сформировать научно обоснованный подход к прогнозированию геомеханического состояния массива и выбору рациональных параметров крепи, что способствует повышению устойчивости выработок, снижению объемов ремонтных работ и увеличению уровня промышленной безопасности при подземной разработке угольных месторождений.

Ключевые слова
горное дело, подземные горные работы, горные выработки, крепь, параметры, геомеханика, геомеханические процессы, анкерная крепь, моделирование, аналитическое моделирование, напряжённо-деформированное состояние, горное давление, массив горных пород, методика, зависимости, метод конечных элементов

Финансирование
Исследование выполнено при поддержке Комитета науки Министерства науки и высшего образования Республики Казахстан в рамках программно-целевого финансирования по реализации научной и научно-технической программы ИРН BR24992803.

Для цитирования
Demin V.F., Valiev N.G., Akhmatnurov D.R., Mussin R.A., Zamaliyev N.M. Formation of inelastic deformation zones based on numerical modeling. *Mining Science and Technology* (*Russia*). 2026;10(1):90–102. https://doi.org/10.17073/2500-0632-2025-07-1104

Introduction

To ensure efficient mineral deposit development, it is necessary to account for the physical, mechanical and strength properties of rocks, the degree of fracturing, and the stress state of the rock mass. This makes it possible to identify deformation patterns and zones of increased stress that affect the stability of mine workings and working conditions [1, 2].

The roof, ribs, and floor rocks of development workings in coal mines of the Karaganda coal basin are characterized by relatively low uniaxial compressive strength, failing in the range of 20–37 MPa, and are classified as weak and unstable rocks. When exposed over distances exceeding one meter, they tend to collapse and are also prone to slaking and floor heave.

Since the stability of underground mine workings remains one of the most critical factors determining the operational efficiency of coal mines in the Karaganda basin of the Republic of Kazakhstan, it is necessary to conduct applied scientific studies aimed at determining support parameters in zones of roof arch formation and performing predictive geomechanical assessment of the deformation state of the host rock mass in coal seams, taking into account their stress-strain conditions [3, 4].

At present, the development of this scientific field in the coal industry of Kazakhstan is associated with assessing the formation of inelastic deformation zones using numerical modeling [5, 6]. The practical value of such research lies in the implementation of its results for testing advanced geotechnical solutions in coal mines of the Karaganda basin.

The aim of this study is to provide a geomechanical justification of support parameters for mine workings based on the investigation of the stress-strain state of near-excavation zones of the coal-bearing rock mass under various operating conditions.

The main objectives are:

– analysis of the current state of technological schemes for driving and maintaining mine workings, including their stability and defect development;

– identification of the deformation features of the rock mass surrounding development workings;

– substantiation of support parameters for mine workings, taking into account mining-induced geotechnical factors, for the development of effective support technologies.

The concept underlying this study is that geomechanical forecasting of the development of inelastic deformation and stress redistribution zones in mining-disturbed rock masses surrounding an excava-

tion can serve as the basis for determining the technological parameters of support systems for development workings, thereby ensuring their stability.

This study presents an integrated methodology that combines geomechanical characterization of the rock mass, prediction of deformation for various support schemes depending on seam depth, geometry, and lithological properties, and numerical modeling. The application of deformation-state assessment for stabilizing excavation boundaries in coal mines will reduce repair volumes and significantly improve operational safety, efficiency, and the timeliness of longwall panel preparation.

The present study relies on numerical methods for modeling support technologies aimed at stabilizing the coal-bearing host rock mass surrounding mine workings, with particular emphasis on the stress-strain state under rock pressure conditions.

The methodological approach involves constructing a computational model of the unstable rock volume separated from the rock mass by weakening contacts, which represents the spatial configuration of the excavation, surrounding rock layers, and coal seam.

One of the most common manifestations of rock pressure is the failure of the rock mass surrounding an underground excavation [7, 8]. Such failure may extend over significant areas of the rock mass, causing the collapse of rock fragments into the excavation under their own weight. When the failure zone is smaller, rock pressure manifests itself in the spalling of individual rock blocks. Another form of manifestation is the deformation of the excavation boundary during operation. In most cases, both forms occur simultaneously, with the most hazardous being dynamic manifestations such as rock bursts, sudden outbursts, and brittle rock spalling [9, 10]. Rock mass failure near underground structures occurs when a specific combination of stress-strain parameters reaches a critical level[1] [2, 11].

Stresses in the host rock mass surrounding the excavation [12, 13] that exceed the creep threshold gradually decrease over time due to the development of plastic deformation in the rocks. As stresses decrease, the rate of rock deformation also declines, which in turn reduces the rate of displacement of the excavation boundary. Conversely, an increase in stresses initiates a new phase of displacement.

Within the inelastic deformation zone, the integrity of the rock mass is disrupted, resulting in microdefects that develop into macrofractures. The growth of such deformation (dilatancy) leads to an increase in rock volume, which may exceed the displacements caused by elastic deformation by an order of magnitude. This phenomenon constitutes the main cause of rock displacement in the near-excavation zone of mine workings under active rock pressure conditions[2] [14].

Therefore, it is essential to determine the extent of inelastic deformation in rocks at the limit state, taking into account the size of the inelastic deformation zone and the degree of rock loosening in the post-failure region [15].

Research significance

The mining industry of Kazakhstan is one of the leading sectors of the national economy. Intensive exploitation of the mineral resource base presents mining enterprises with a number of complex challenges related to ensuring the stability and safety of underground excavations. Of particular importance is the monitoring of rock mass displacements around mine workings, which becomes critically significant when deposits are mined at greater depths, where rock pressure increases substantially [16, 17].

The geological conditions of Kazakhstan are characterized by considerable diversity of rock mass types, including coal, iron ore, polymetallic, and other deposits. The Karaganda coal basin, one of the largest in the country, is distinguished by complex seam structures, significant mining depths, and high geomechanical loads. These conditions require the application of modern modeling methods to assess the stress-strain state of the rock mass. These issues become especially important in the context of increasing requirements for mining safety and the need to minimize risks associated with failure of the near-contour rocks surrounding underground excavations.

Typical manifestations of rock pressure around an advancing excavation include the abutment pressure zone, the stress concentration zone ahead of the face that develops into a fractured rock zone, and zones of compression and crushing of the rock mass in the immediate vicinity of the excavation face.

Geomechanical characteristics of the rock mass: theoretical background

Driving an underground excavation disturbs the equilibrium state of the rock mass and causes a redistribution of stresses in the surrounding rock. In this case, the stress intensity at the excavation boundary is significantly higher than in the undisturbed rock mass. Elevated stresses at the excavation bounda-

[1] Zhurov V.V. Improvement of the methodology for calculating support parameters of mine workings taking into account mining and technological factors. [Cand. Sci. (Eng.) Dissertation]. Karaganda: Karaganda State Technical University; 2010. 115 p.

[2] Demin V.F., Sitnikov R.S., Steflyuk Yu.Yu., et al. Device for supporting excavation contours in unstable rocks. Patent 31419, Republic of Kazakhstan; IPC E21D 21/00. Published August 15, 2016, Bulletin No. 9.

ry lead to the formation of an inelastic deformation zone around it [16, 17]. The structure of this zone and the nature of rock deformation within it depend on several factors, including the depth of the excavation, the rock type and its physical, mechanical and technological properties, the size of the excavation, the type and characteristics of the support system, and the dip angle of the host rocks. Manifestations of rock pressure observed in driven workings include displacements of the rock mass in the near-excavation zone [7].

The primary focus of this study is the determination of displacements of the excavation boundary based on experimentally obtained data on rock properties and the stress-strain state of the rock mass.

Several studies have proposed recommendations for reducing the rock mass loosening coefficient associated with dilatancy, which can be achieved by adjusting support parameters, excavation geometry, and controlling the rate of rock deformation.

To achieve the research objective, a comprehensive research methodology was applied, combining theoretical analysis, numerical modeling, and experimental investigations. Such an approach is necessitated by the complex nonlinear nature of deformation in coal-bearing rock masses, where the stress-strain state of the near-excavation zone is governed by the combined influence of mining conditions, physical and mechanical rock properties, and support system parameters.

Numerical modeling was used to predict excavation boundary deformation and to analyze stress redistribution, theoretical methods were applied to generalize and interpret the identified patterns, and experimental investigations were carried out to verify the calculated results and refine the initial parameters of the model.

To establish geomechanical patterns occurring in development workings driven in coal seams, analytical studies were performed to determine roof deformation along the axis of the development working.

The analysis considers the features of stress redistribution and the formation of deformation zones in the rock mass depending on the properties of the host rocks and the parameters of the excavation. The analysis was performed on the basis of numerical modeling that accounts for the geomechanical characteristics of the rock mass and the support schemes in order to identify patterns in the evolution of the stress-strain state and potential zones of instability.

The following mathematical model describes manifestations of rock pressure around a driven excavation associated with rock mass displacements in the near-excavation zone. The total displacement of the rock mass in the excavation U_{tot} is composed of elastic U_1 and inelastic U_2 components:

$$U_{tot} = U_1 + U_2. \quad (1)$$

Elastic deformation is determined by the following equations [7]:

$$\frac{\partial X_x}{\partial x} + \frac{\partial X_y}{\partial y} + X = 0,$$

$$\frac{\partial X_y}{\partial x} + \frac{\partial Y_y}{\partial y} + Y = 0,$$

$$X_x = \lambda\theta + 2\mu\frac{\partial u}{\partial x}, \quad (2)$$

$$Y_y = \lambda\theta + 2\mu\frac{\partial v}{\partial y},$$

$$X_y = \mu\left(\frac{\partial v}{\partial x} + \frac{\partial u}{\partial y}\right),$$

where X, Y, X_x, Y_y are the displacement vectors and their projections on the coordinate axes; μ is Poisson's ratio; ν is the viscosity coefficient, N/m^2; u is the deformation rate, m/day; λ is the lateral pressure coefficient; r, θ are the polar coordinates of the points.

Inelastic deformation of rocks in the plastic failure zone is determined by the following equation [8]:

$$U_2 = \frac{S_d}{P_{exc}}(K_l - 1), \quad (3)$$

where S_d is the area of the inelastic deformation zone, m^2; P_{exc} is the excavation perimeter, m; K_l is the rock mass loosening coefficient in the post-failure deformation zone.

Numerical modeling of the stress-strain state of the rock mass was carried out using the RS2 (Rocscience) software package, which implements the finite element method (FEM). The choice of this software is determined by its specialization for geomechanical analysis of underground excavations, the ability to account for complex excavation geometry, layered rock mass structure, nonlinear deformation behavior of rocks, and the implementation of various strength criteria and boundary conditions typical of underground mining conditions. The finite element method implemented in RS2 allows adequate representation of stress redistribution and deformation development in the near-excavation zones of the rock mass, which is critically important for analyzing excavation stability and substantiating support parameters.

The modeling procedure included the following stages:

– construction of the computational geometric model of the underground excavation under specified mining conditions;

– assignment of physical and mechanical rock properties and development of the geological model of the studied rock mass section;

– generation of a triangular FEM mesh with local mesh refinement in the near-excavation zone;

– performing calculations under specified boundary conditions and adopted criteria for evaluating the stress-strain state of the rock mass;

– interpretation and analysis of the obtained results to assess deformation and stress distribution within the excavation influence zone.

Numerical modeling approach

To provide a more comprehensive analysis of the formation mechanism of inelastic deformation zones around a mine excavation during its advance, numerical modeling was performed using the RS2 software package. In this study, a model was developed that takes into account the geological conditions at the roadway junction, followed by the driving of the excavation along the coal seam at a depth of 600 m below the surface.

The model conditions included the rocks of the excavation floor, represented by argillites and siltstones, as well as the roof of the coal seam, composed of siltstones and sandstones. Particular attention was given to the analysis of the stress-strain state of the rock mass, including the identification of zones of inelastic deformation that arise as a result of changes in rock pressure and the interaction between the rock mass and the excavation boundary. The overall numerical model is shown in Fig. 1.

The model was structured in stages, which made it possible to analyze in detail the evolution of the stress-strain state of the rock mass at each stage of excavation development.

The initial stage of modeling involves the excavation of the first roadway, which serves as the junction point from which the new roadway is driven. At this stage, particular attention was paid to the analysis of the formation of initial zones of stress redistribution around the roadway junction, which provides the basis for further modeling.

At the next stage, the junction between the workings was simulated. This stage is important for studying the interaction between zones of stresses and deformations, as well as for assessing the stability of the junction and the influence of its parameters on the overall condition of the rock mass.

In subsequent stages of modeling, the coal seam was excavated progressively. Each stage involved coal extraction with a step of 0.75 m. This approach made it possible to identify the dynamics of changes in stresses and deformations in the rock mass and to evaluate the development of inelastic deformation zones.

To improve the accuracy of the obtained results, the finite-element mesh was significantly refined in the areas directly adjacent to the excavation under consideration.

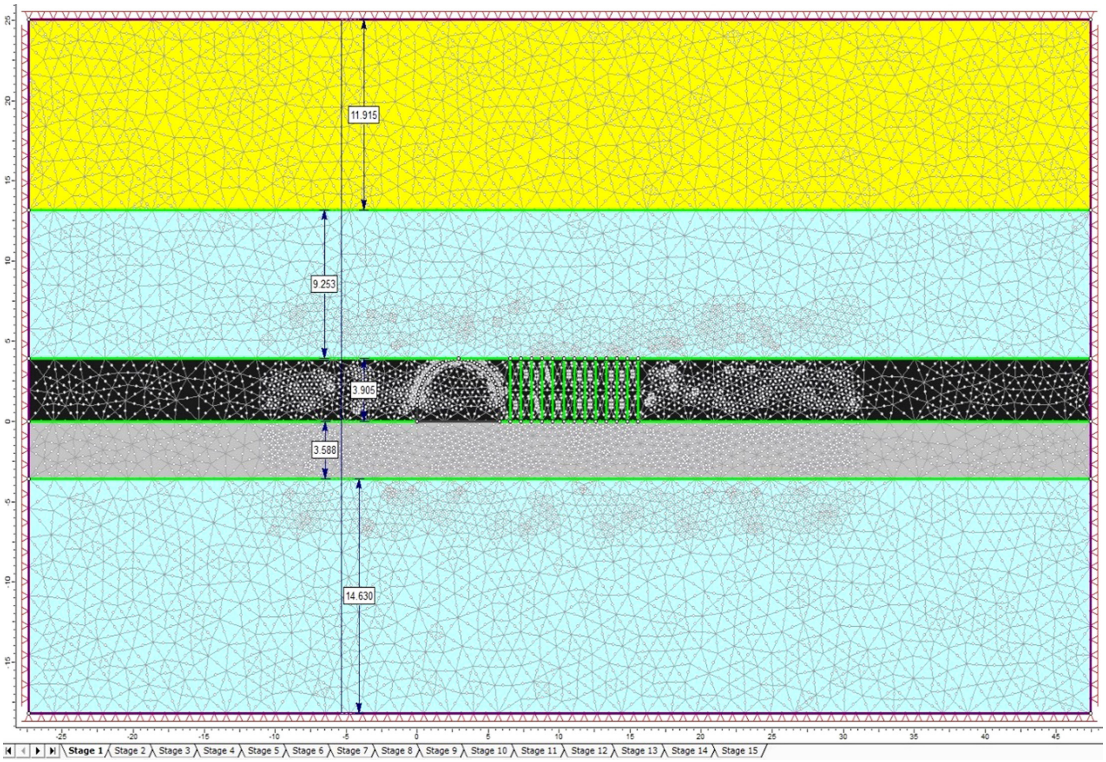

Fig. 1. Numerical model of excavation development

To determine the initial parameters of the acting stresses and to compare them with the stress-strain state of the rock mass during mining operations, the first stage assumed the absence of any mining activities. As shown in Fig. 2, the stresses in the rock mass correspond to the calculated stress parameters of the undisturbed rock mass at the considered depth:

$$\sigma_\gamma = \gamma \cdot H = 0.0273 \cdot 600 \approx 16.4 \text{ MPa},$$

where γ is the average unit weight of the overlying rocks, kN/m^3; H is the depth, m.

Fig. 3 shows the distribution of the maximum principal stresses σ_1 in the undisturbed coal-bearing rock mass prior to excavation, obtained from numerical modeling. The color scale reflects the increase in vertical stress values with depth, which corresponds to the natural geostatic stress state of the rock mass and confirms the correctness of the initial boundary conditions specified in the model.

Analysis of the stress field indicates that, in the absence of excavation, the distribution of σ_1 is quasi-linear and is formed primarily under the influence of the self-weight of the overlying rock strata. The absence of local stress concentrations and sharp stress gradients indicates that the rock mass is in an equilibrium state, which allows this model to be considered as the baseline (reference) state for subsequent analysis of mining-induced disturbances.

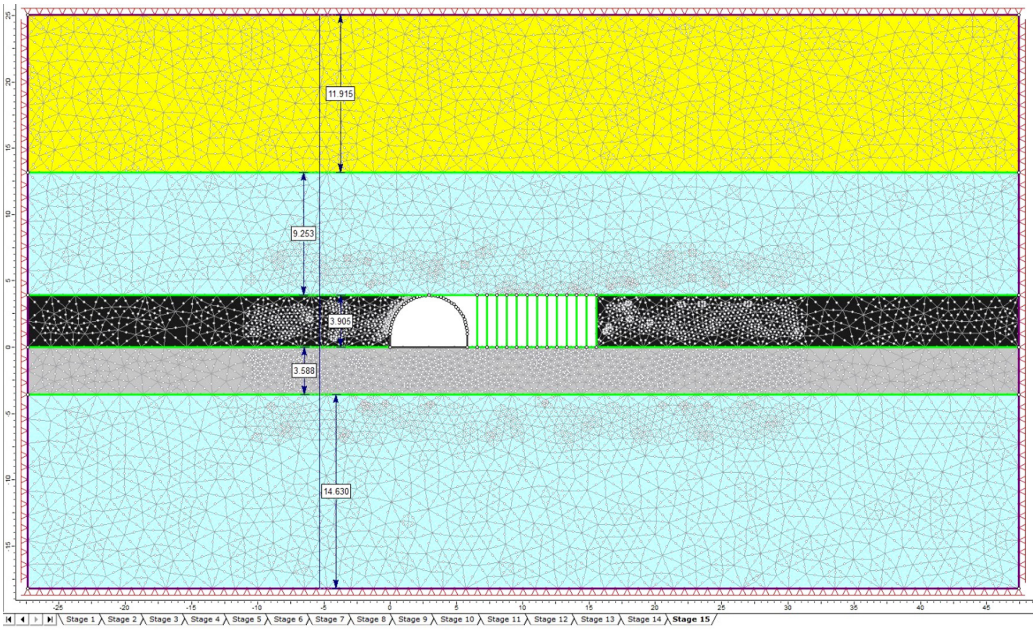

Fig. 2. Numerical model at the final stage of excavation

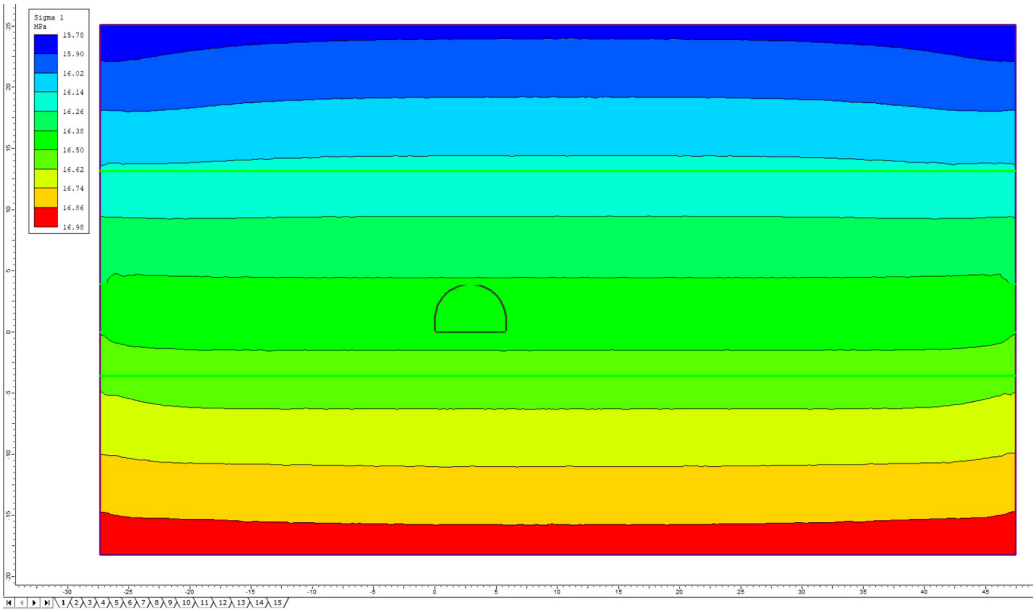

Fig. 3. Distribution of principal stresses in the undisturbed rock mass

Results and discussion

The distribution of stresses at different stages of roadway development is shown in Figs. 4–7.

Fig. 4 illustrates the distribution of the maximum principal stresses σ_1 in the near-excavation rock mass surrounding the roadway from which the new roadway is driven. The obtained stress distribution reflects the results of numerical modeling and makes it possible to identify zones of stress concentration and redistribution that arise due to the disturbance of the rock mass continuity during roadway development.

Analysis of the stress distribution shows that a pronounced zone of increased compressive stresses forms in the near-excavation region of the roadway roof and sidewalls. These stresses significantly exceed the background stresses of the undisturbed rock mass. The maximum values of σ_1 are concentrated near the junctions of the excavation boundary with the sidewalls, which is caused by the geometric effect of excavation and the redistribution of loads within the rock mass. In the roadway floor, by contrast, a zone of reduced stresses is observed, associated with unloading of the rock mass and the development of tensile and shear deformations.

Fig. 5 presents the distribution of the maximum principal stresses σ_1 in the rock mass during the driving of a new roadway from an existing roadway. The results obtained by numerical modeling characterize the changes in the stress-strain state of the rock mass in the roadway junction zone.

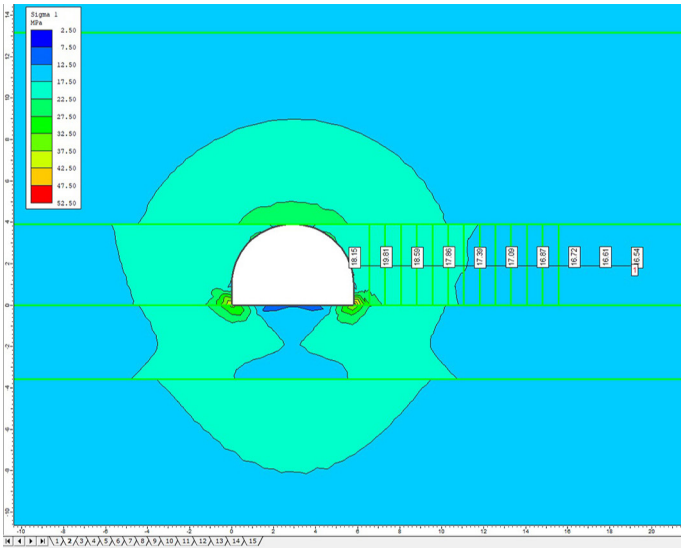

Fig. 4. Distribution of principal stresses in the near-excavation rock mass of the roadway from which the new roadway is driven

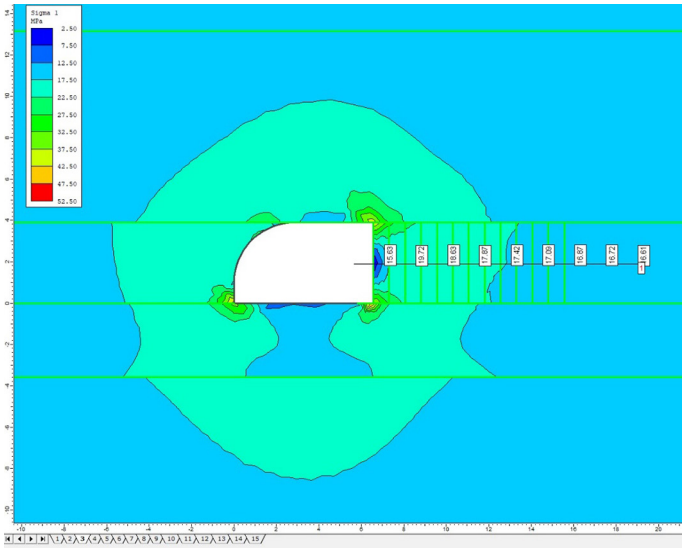

Fig. 5. Distribution of principal stresses during the formation of a new roadway at the roadway junction

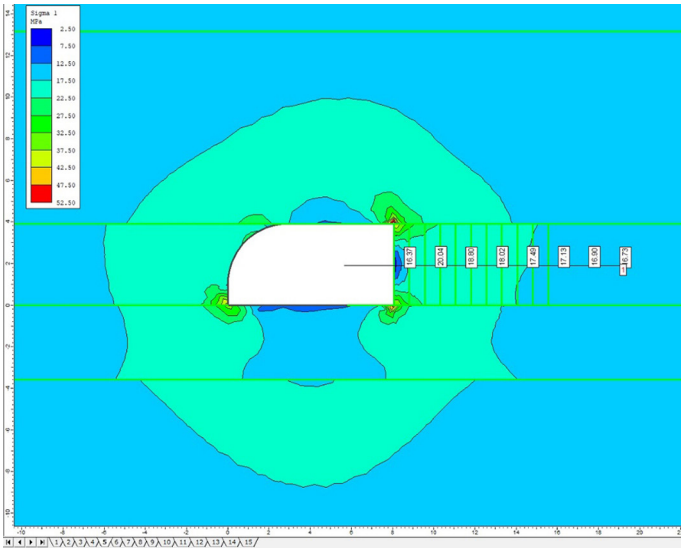

Fig. 6. Distribution of principal stresses during mining operations at +1.5 m from the roadway junction

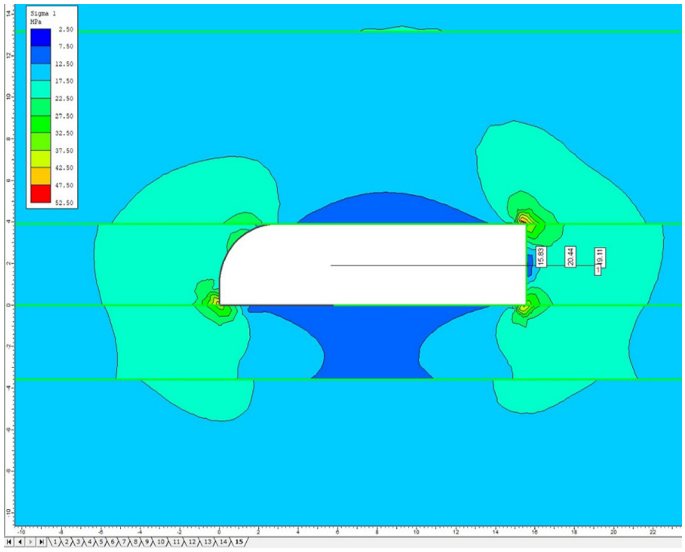

Fig. 7. Distribution of principal stresses during mining operations at +9 m from the roadway junction

Fig. 6 illustrates the distribution of the maximum principal stresses σ_1 in the near-excavation rock mass at the stage of mining operations at a distance of +1.5 m from the roadway junction zone. This stage of modeling reflects the evolution of the stress-strain state of the rock mass after the initial formation of the roadway junction and makes it possible to assess the spatial evolution of stresses as the excavation face advances away from the junction.

Fig. 7 shows the distribution of the maximum principal stresses σ_1 in the rock mass at the stage of mining operations at a distance of +9 m from the roadway junction zone, which corresponds to the stage at which the roadway reaches a quasi-stationary stress state.

The obtained results indicate that at this distance the influence of the roadway junction zone on the overall stress field significantly decreases. The stress state of the rock mass becomes more symmetrical relative to the roadway axis, while the local stress concentrations previously recorded in the near-excavation zone of the junction transform into extended zones of moderate compressive stresses.

A stable zone of reduced σ_1 values forms in the roadway roof, which corresponds to a developed unloading zone, whereas zones of elevated stresses remain in the side parts of the rock mass, defining the boundaries of the active influence of mining operations. In the roadway floor, the stress state becomes more uniform, indicating a reduction in the intensity of deformation processes compared with the initial stages of mining.

A comparison of the stress distributions at distances of +1.5 m and +9 m from the roadway junction shows that the main geomechanical effects associated with stress concentration are localized within a limited zone beyond the junction of the roadways. Outside this zone, the stress state of the rock mass stabilizes and is determined mainly by the mining depth and the physical and mechanical properties of the rocks.

As follows from the interpretation of the principal stress distribution, an abutment pressure zone forms in front of the excavation face during mining operations. Within this zone, stresses increase and reach 20.48 MPa, which is approximately 25% higher than the in-situ stress level characteristic of the undisturbed rock mass. This increase is associated with stress redistribution around the excavation caused by the local disturbance of rock mass continuity. From the standpoint of rock mechanics, such an increase in stress may affect roadway stability, especially in the presence of weak structural elements in the rock mass.

In addition, the interpretation presented in Figs. 5–7 reveals a zone of reduced stresses at the excavation face, indicating the presence of an unloading zone with a depth of up to 0.7 m. This phenomenon suggests possible loosening of the rock mass as well as partial destruction of the rock structure. Such unloading zones are typical of areas where local stress redistribution occurs as a direct result of mining operations.

The presence of such a zone must be taken into account because the loosened rock mass has reduced load-bearing capacity. This may lead to an increase in the volume of rock fall and complicate mining operations. To minimize these risks, special measures should be applied, such as reinforcement of the support system, grouting, or additional monitoring of the rock mass condition using geophysical methods.

To assess the extent of inelastic deformation zones and to identify areas susceptible to plastic deformation or complete failure, the most informative parameter for interpretation is the Factor of Safety (FoS). FoS allows a quantitative assessment of how close the current stress state of the rock mass is to its failure limit.

In software such as RS (e.g., Rocscience RS2 or RS3), the calculation of the FoS value is based on complex algorithms that account for the strength parameters of the rock mass. These calculations include physical and mechanical properties of rocks such as compressive strength, elastic modulus, cohesion, and internal friction angle, which determine the resistance of the rock mass to deformation and failure.

The main criterion for the development of inelastic deformation zones is the exceedance of the calculated stresses over the strength limits of the rock mass, which may lead to local failures, plastic deformation, and structural changes in the rock mass.

The application of FoS in data interpretation makes it possible not only to predict the behavior of the rock mass under loading but also to develop effective stabilization measures, such as selecting an optimal support system, modifying excavation parameters, or implementing compensatory engineering measures. Thus, the analysis of inelastic deformation zones using FoS becomes a key element in assessing the stability of underground mine workings. The distribution of the defined inelastic deformation zones is shown in Fig. 8.

The use of the Factor of Safety (FoS) in interpreting the results of numerical modeling makes it possible not only to quantitatively assess the stability of the near-excavation rock mass but also to identify potentially hazardous zones where inelastic deformation may develop. Unlike the analysis of individual stress components, the FoS distribution provides an integrated characterization of the stress-strain state of the rocks while accounting for their strength properties.

As shown in Fig. 8, local zones with reduced FoS values (FoS < 1) are formed in the roadway junction zone, confined to the near-excavation regions of the roadway roof, floor, and sidewalls. These areas correspond to zones where the rock mass transitions into an inelastic state and represent potential sites for the development of failure, delamination, and intensive deformation.

Moving away from the excavation boundary deeper into the rock mass, a gradual increase in FoS values is observed, indicating a reduction in the influence of mining operations and the transition of the rock mass to a stable state. The spatial location of the boundaries of the inelastic deformation zones makes it possible to determine their depth of propagation and to use these data to substantiate the required length and arrangement of the support elements.

Analysis of the FoS distribution is a key element in the geomechanical justification of support parameters for underground mine workings. It enables rational selection of support types and parameters, prediction of the effectiveness of stabilization measures, and evaluation of the need for additional compensating solutions in the roadway junction zone.

The application of the proposed geomechanically justified approach to analyzing the stress-strain state of the near-excavation rock mass and selecting support parameters not only improves the stability of underground workings but also produces a cumulative economic effect by reducing operational and maintenance costs.

The main sources of economic benefit include:

– reduction in the volume of repeated support installation and roadway repairs due to decreased intensity of inelastic deformation in the roof and floor;

– reduction in downtime of longwall and transportation equipment caused by excavation deformation and floor heave;

– reduction in the loss of roadway cross-section, which helps maintain the design dimensions and avoid unplanned widening or floor trimming;

– optimization of support parameters, including rational selection of bolt length and installation density, which reduces excessive consumption of support materials while maintaining the required stability level;

– improved industrial safety, leading to a reduced probability of accidents and associated financial losses.

Additional economic benefits are achieved through the possibility of predictive control of geomechanical processes. The use of numerical modeling and FoS analysis allows potentially unstable zones to be identified in advance and preventive engineering measures to be implemented, which is significantly less costly than eliminating the consequences of developed deformation.

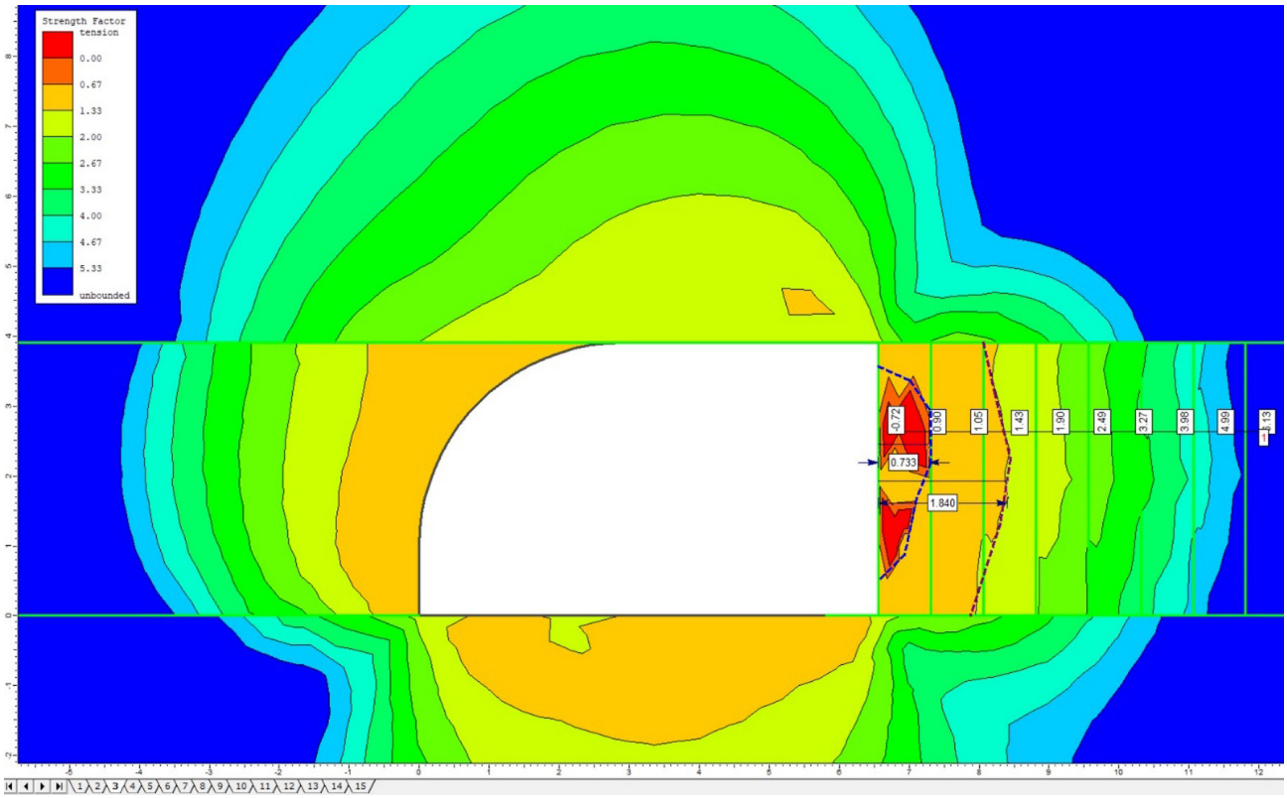

Fig. 8. Distribution of inelastic deformation zones at the roadway junction

The economic effect is achieved through the simultaneous reduction of capital and operating costs while increasing the reliability and service life of underground mine workings. The obtained results can serve as a basis for subsequent technical and economic calculations in the design and operation of underground excavations under similar mining and geological conditions.

Practical implications

For the considered computational model of the rock mass, it has been established that the inelastic deformation zone is localized in the near-excavation region of the excavation face and extends approximately 0.6–0.7 m into the rock mass. This zone is characterized by the maximum concentration of stresses and the development of intense plastic deformation caused by the redistribution of rock pressure during roadway driving. Within this region, the rocks lose their load-bearing capacity, accompanied by the destruction of their structural integrity and the formation of fragmented material, indicating the transition of the rock mass to a limit state.

Beyond the zone of developed inelastic deformation, within a depth interval of 0.7–1.8 (up to 1.9) m, a region of elastoplastic behavior of the rock mass is formed. In this interval, intensive fracturing processes occur, during which the rocks exist in a transitional state between elastic and plastic deformation. Although the overall stability of the rock mass is preserved, the development of fractures leads to a gradual decrease in its deformation stiffness and load-bearing capacity, which must be taken into account when determining the parameters of the support system.

At depths exceeding 1.8–1.9 m, the rock mass is characterized predominantly by an elastic state and at the considered moment is only weakly affected by mining operations. In this zone, the rocks retain high strength and their ability to sustain the acting stresses without developing significant deformation. At the same time, the possible evolution of the stress-strain state should be considered over the long term under the influence of time-dependent factors such as stress relaxation, rock creep, temperature effects, and further development of mining operations.

The obtained model of deformation distribution reflects the zonal character of rock mass stability disturbance, which requires a differentiated approach to stabilization. The zone of developed inelastic deformation requires the application of active and combined support methods that ensure stress redistribution and limit rock failure. In contrast, within the elastoplastic behavior zone it is advisable to use rock bolts designed to stitch fractured rock and enhance the overall integrity of the rock mass.

To ensure the safety and stability of underground workings, it is recommended to organize systematic geomechanical monitoring of the rock mass condition using instrumental and geophysical methods, as well as to adjust support parameters as mining and geological conditions evolve.

Future development of the mathematical model

Within the framework of further development of the proposed mathematical model, several interrelated directions may be identified to increase its predictive reliability and expand its practical application under conditions of intensely deforming coal-bearing rock masses. These directions are based on integrating modern concepts of rock mechanics, the capabilities of numerical modeling, and the needs of mining production for substantiating support parameters.

Consideration of nonlinear deformation and failure kinetics. The current model operates with separate zones of elastic and inelastic behavior, whose boundary is determined empirically through the area S_d. For a more accurate description of the transition of the rock mass to the limit state, it is necessary to explicitly introduce a strength criterion into the system of equations. This would make it possible to calculate the configuration of the inelastic deformation zone not as a predefined parameter but as a function of the acting stresses and the rheological properties of specific rocks.

Particular importance should be given to the time factor and loading rate, since the strength and deformation characteristics of coal and host rocks of the Karaganda basin demonstrate pronounced rheological dependence. Modification of the strain-rate component u in equations (2) through the introduction of creep parameters or modeling of viscoplastic flow would allow prediction of displacement development not only during roadway driving but also during long-term roadway operation.

Structural-geological parameterization of the loosening coefficient. The loosening coefficient K_l in equation (3) is a key parameter but currently remains a generalized quantity. Its physical meaning can be significantly refined by relating it to quantitative characteristics of rock mass disturbance, including volumetric fracture density; orientation of fracture systems relative to the excavation boundary; roughness of fracture surfaces; granulometric composition of fragmented rock.

Such parameterization would allow differentiation of the loosening degree for the roof, floor, and sidewalls of the roadway, where different failure mechanisms dominate (spalling, shear, or floor heave). A further step could involve developing nomograms or analytical relationships linking K_l with the Rock Quality Designation (RQD) index, geophysical imaging data, or results of discrete element modeling (DEM), thereby enabling the transition from generalized estimates to specific mining-geological conditions of the site.

Development of a calibrated database and digital twin models for roadway development. The maximum practical benefit of the model can be achieved through its integration into an engineering decision-support system. For this purpose, it is necessary to create a library of calibration relationships based on both existing and future finite-element modeling sessions, as well as data from instrumental monitoring at real mining sites. These relationships should establish quantitative links between model parameters S_d and K_l and a set of controllable mining factors, including mining depth; span width; type and installation spacing of rock bolts; time delay between excavation and support installation. In the future, such a database may serve as the basis for creating digital twins of standard roadway development schemes. This will allow rapid scenario calculations of displacement and Factor of Safety values for different support configurations during the design stage, thereby optimizing engineering decisions in terms of stability, material consumption, and economic efficiency.

Development of the model along these directions will not only deepen the theoretical understanding of the processes governing the formation of inelastic deformation zones, but will also directly contribute to solving applied engineering problems. The result will be a more justified selection and adaptive management of support parameters, minimization of repair work volumes, and consequently an increase in the industrial safety and economic efficiency of underground coal mining.

Conclusions

Based on numerical modeling of the stress-strain state of a coal-bearing rock mass using the RS2 software package, considering the example of roadway development at a depth of 600 m, quantitative parameters and patterns of the formation of inelastic deformation zones were established, as well as their influence on the stability of underground workings and the selection of support parameters.

The performed geomechanical analysis confirmed that as the rate of rock deformation increases, the apparent strength limit of the rocks and the accumulation of elastic energy also increase, which, provided that permissible stress levels are maintained, reduces the probability of the formation of extensive failure zones in the near-excavation rock mass. However, a critical threshold was identified: when the calculated stresses exceed the strength characteristics of the rocks (for the studied conditions, stresses in the abutment pressure zone reach 20.48 MPa, which is about 25% higher than the background level), accelerated deformation leads to intensified loosening of the rock mass and the development of intense inelastic deformation within a zone 0.6–0.7 m from the excavation boundary.

A clear zonal pattern of rock mass deformation around the excavation was identified: a zone of developed inelastic deformation (0–0.7 m), a region of elastoplastic behavior with active fracturing (0.7–1.9 m), and a zone of predominantly elastic rock mass behavior (beyond 1.9 m). To reduce dilatancy caused by the relative displacement of fracture surfaces within the failure zone, it is recommended to control the deformation rate by installing support immediately after rock exposure, which is confirmed by modeling performed with an excavation advance step of 0.75 m.

Mining-geological conditions were found to have a determining influence: with increasing mining depth (600 m in the considered case), the initial stress state increases proportionally ($\sigma_\gamma \approx 16.4$ MPa) and, accordingly, the potential for the development of inelastic deformation increases. At the same time, as the distance from the excavation boundary increases (beyond 1.9 m), the influence of mining operations decreases, the probability of dilatancy is significantly reduced, and the rock mass transitions to an elastic state, which is confirmed by the symmetry of the stress field at a distance of +9 m from the roadway junction.

To further reduce the degree of rock mass loosening and increase roadway stability, the need for a rational selection of the roadway cross-sectional shape is substantiated, which minimizes stress concentration and ensures a more uniform redistribution of stresses in the near-excavation rock mass. A reduction in local stress maxima, in turn, leads to a decrease in the size of failure zones.

It was established that directed modification of the structural characteristics of the rock mass is an effective tool for controlling its strength properties. Weakening leads to an expansion of failure zones, whereas active strengthening of the near-excavation rock mass by injection grouting or chemical stabilization increases the strength limit and deformation

stiffness. When the achieved strength of the treated rock mass exceeds the acting stress level, the development of destructive processes and dilatancy is prevented, ensuring a stable state of the roadway and improving the safety of mining operations.

The implementation of a geomechanically justified approach based on analysis of the Factor of Safety (FoS) and the results of numerical modeling not only increases roadway stability but also generates a cumulative economic effect. Its sources include a reduction in the volume of repair and restoration work, decreased equipment downtime, reduced losses of the useful cross-section of roadways, optimization of support parameters and consumption of support materials, and an increase in industrial safety through early identification of zones with FoS < 1.

References

1. Djaksimuratov K.M., O'telbayev A.A., O'razmatov J.I., Mnajatdinov D.M. Properties of coal, processes in coal mining companies, methods of coal mining in the world. *Journal NX*. 2021;7(10):231–236. URL: https://repo.journalnx.com/index.php/nx/article/view/3681/3548
2. Batyrkhanova A., Tomilov A., Zhumabekova A., Abekov U., Demin V. Developing technological schemes of driving workings with controlled resistance of contours. *Naukovyi Visnyk Natsionalnoho Hirnychoho Universytetu*. 2019;(3):22–28. https://doi.org/10.29202/nvngu/2019-3/2
3. Akhmatnurov D., Zamaliyev N., Mussin R., Demin V., Tolovkhan B., Ganyukov N., Skrzypkowski K., Korzeniowski W., Stasica J., Rak Z. Geomechanical modeling of the Northern Katpar Deposit (Kazakhstan): Assessing the Impact of Rock Mass Disturbance on Stability Safety Factor. *Mining*. 2025;5(4):73. https://doi.org/10.3390/mining5040073
4. Budi G., Rao K.N., Mohanty P. Field and numerical modelling on the stability of underground strata in longwall workings. *Energy Geoscience*. 2023;4(1):1–12. https://doi.org/10.1016/j.engeos.2022.07.003
5. Xiong Y., Kong D., Wen Z. et al. Analysis of coal face stability of lower coal seam under repeated mining in close coal seams group. *Scientific Reports*. 2022;12(1):1–14. https://doi.org/10.1038/s41598-021-04410-5
6. Nehrii S., Nehrii T., Zolotarova O., Volkov S. Investigation of the geomechanical state of soft adjoining rocks under protective constructions. *Rudarsko-Geološko-Naftni Zbornik*. 2021;36(4):61–71. https://doi.org/10.17794/rgn.2021.4.6
7. Lama B., Momayez M. Review of non-destructive methods for rock bolts condition evaluation. *Mining*. 2023;3(1):106–120. https://doi.org/10.3390/mining3010007
8. Tsay B.N., Sudarikov A. E. *Mechanics of underground structures*. Karaganda: KarGTU; 2007. 159 p. (In Russ.)
9. Taran I. Interrelation of circular transfer ratio of double-split transmissions with regulation characteristic in case of planetary gear out-put. *Naukovyi Visnyk Natsionalnoho Hirnychoho Universytetu*. 2012;(3):78–85.
10. Huang W., Liu S., Gao M. et al. Improvement of reinforcement performance and engineering application of small coal pillars arranged in double roadways. *Sustainability*. 2022;15(1):292. https://doi.org/10.3390/su15010292
11. Demin V.F., Demina T.V., Kaynazarov A.S., Kaynazarova A.S. Evaluation of the workings technological schemes effectiveness to increase the stability of their contours. *Sustainable Development of Mountain Territories*. 2018;10(4):606–617. (In Russ.) https://doi.org/10.21177/1998-4502-2018-10-4-606-616
12. Shashenko A., Gapieiev S., Solodyankin A. Numerical simulation of the elastic-plastic state of rock mass around horizontal workings. *Archives of Mining Sciences*. 2009;54(2):341–348.
13. Nemova N.A., Stakhanov D., Hasan B., Zhumabekova A.E. Technological solutions development for mining adjacent rock mass and pit reserves taking into account geomechanical assessment of the deposit. *Naukovyi Visnyk Natsionalnoho Hirnychoho Universytetu*. 2020;(2):17–24. https://doi.org/10.33271/nvngu/2020-2/017
14. Smoliński A., Malashkevych D., Petlovanyi, M. et al. Research into impact of leaving waste rocks in the mined-out space on the geomechanical state of the rock mass surrounding the longwall face. *Energies*. 2022;15(24):9522. https://doi.org/10.3390/en15249522
15. Sotskov V., Saleev I. Investigation of the rock massif stress strain state in conditions of the drainage drift over-working. In: Pivnyak G., Bondarenko V., Kovalevs'ka I., Illiashov M. (Eds.) *Mining of Mineral Deposits*. CRC Press; 2013. Pp. 197–201. https://doi.org/10.1201/b16354-35
16. Yang H., Han C., Zhang N. et al. Research and application of low density roof support technology of rapid excavation for coal roadway. *Geotechnical and Geological Engineering*. 2020;38:389–401. https://doi.org/10.1007/s10706-019-01029-2

17. Bondarenko V., Symanovych G., Koval O. The mechanism of over-coal thin-layered massif deformation of weak rocks in a longwall. In: Bondarenko V., Kovalevs'ka I., Illiashov M., Pivnyak G. (Eds.) *Geomechanical Processes During Underground Mining*. CRC Press; 2012. Pp. 41–44. https://doi.org/10.1201/b13157-8

Information about the authors

Vladimir F. Demin – Dr. Sci. (Eng.), Professor of the Department of Mineral Deposits Development, Abylkas Saginov Karaganda Technical University, Karaganda, Republic of Kazakhstan; ORCID 0000-0002-1718-856X, Scopus ID 57212219714; e-mail vladfdemin@mail.ru

Niyaz G. Valiev – Dr. Sci. (Eng.), Deputy Chairman of the Academic Council, Head of the Mining Department, Ural State Mining University; General Director, Mining Industry Association of the Urals, Yekaterinburg, Russian Federation; ORCID 0000-0002-5556-2217, Scopus ID 55749527900, SPIN 3886-5864; e-mail Niyaz.Valiev@m.ursmu.ru

Denis R. Akhmatnurov – PhD, Head of the Methane Energy Laboratory, Abylkas Saginov Karaganda Technical University, Karaganda, Republic of Kazakhstan; ORCID 0000-0001-9485-3669, Scopus ID 57194187849, SPIN 1396-9321; e-mail d.akhmatnurov@gmail.com

Ravil A. Mussin – PhD, Associate Professor of the Department of Mineral Deposits Development, Abylkas Saginov Karaganda Technical University, Karaganda, Republic of Kazakhstan; ORCID 0000-0002-1206-6889, Scopus ID 7005446397; e-mail R.A.Mussin@mail.ru

Nail M. Zamaliyev – PhD, Associate Professor of the Department of Mineral Deposits Development, Abylkas Saginov Karaganda Technical University, Karaganda, Republic of Kazakhstan; ORCID 0000-0003-0628-2654, Scopus ID 57194194006; e-mail nailzamaliev@mail.ru

Received 06.07.2025
Revised 29.01.2026
Accepted 01.02.2026